

**School of Chemical and Petroleum Engineering
Department of Chemical Engineering**

**Metal-based Nanocatalysts for Oxidative Degradation of Aqueous
Organic Pollutants in Contaminated Water**

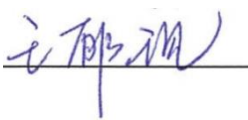
Yuxian Wang

**This thesis is presented for the Degree of
Doctoral of Philosophy
of
Curtin University**

August 2015

Declaration

To the best of my knowledge and belief this thesis contains no material previously published by any other person except where due acknowledgement has been made. This thesis contains no material which has been accepted for the award of any other degree or diploma in any university.

Signature: 

Yuxian Wang

Date: 12-Aug-2015

Acknowledgement

First, I want to express my sincere gratitude to Prof. Shaobin Wang for his instructive guidance and continuous encouragement. Prof. Shaobin Wang acts as the role model for me in the world of science. Though he is busy, his door is always open for me. Without his edification I cannot complete this journey in such a short time. And it is such a great honor to be his student.

Equally, I owe my heartfelt gratitude to my co-supervisor, Dr. Hongqi Sun. I am very grateful for him to give me innovative ideas, instill me new knowledge and revise my manuscripts. Truly, without his painstaking efforts in polishing my manuscripts, it has been not possible for me to publish those papers. Also special thanks should be given to him for holding some of the wonderful group parties.

I would like to thank Prof. Shaomin Liu who has given me instructive suggestions on my studies, career and personal life.

I am thankful to Xiaoguang Duan. Thank you for giving me supports during the hard times and thank you for your help for preparing the manuscripts and thesis.

I also express my gratitude to my friends, Guanliang, Yilin, Jian Kang, Chi, Ping, Xiaochen, Chen, Yu, Jijiang, Huayang, Zana, Stacey and Leon. Thank you so much for your help during the experiments and understanding whenever I used your chemicals.

I am also thankful to the lab technicians, Jimmy, Roshanak and Andrew who gave me technical supports when I needed help.

I would like to express to my truthful thanks to Cooperative Research Centre for

Contamination Assessment and Remediation of the Environment (CRC CARE) for supporting my PhD scholarship,

I would like to thank my parents for their financial support for my undergraduate period, for their guidance when I am upset and for their love when I feel cold.

Last, but not the least, I would like to thank Feiyu Suo, with love. Thanks for your understand and spiritual supporting. Without her care and love, I cannot withstand the pressure and go further.

ABSTRACT

Among the available wastewater remediation technologies, advanced oxidation processes (AOPs) have received increasing research attention for degradation of toxic aqueous organic pollutants due to their high degradation efficiency, complete mineralization capability and eco-friendly nature. Compared with other AOPs such as Fenton reactions and catalytic ozonation, AOPs employing sulfate radicals for decomposition of organic contaminants have been proven to be more cost-effective. Therefore, the purpose of this research focused on the development of various efficient metal-based catalysts and the employment of these catalysts for degradation of aqueous organic pollutants by sulfate radicals based AOPs (SR-AOPs). In this research, various types of metal-based catalysts such as 1D MnO_2 in nanowires, nanotubes or nanorods, 3D hierarchically structured MnO_2 , magnetically separable 3D hierarchical structured $\text{MnO}_2/\text{ZnFe}_2\text{O}_4$ hybrids, nano- Fe^0 encapsulated in carbon spheres and magnetically separable Co_3O_4 loaded on core/shell structured Fe_3O_4 /carbon sphere have been synthesized via different techniques such hydrothermal, sol-gel and impregnation methods. The as-synthesized catalysts have been characterized and tested for activation of peroxymonosulfate (PMS) to generate sulfate radicals for the degradation of aqueous phenol solutions. It was found that the catalytic activities of the as-synthesized materials depend on their surface areas, exposed active facets and crystalline structures. Experimental results demonstrated that phenol degradation efficiency was influenced by phenol initial concentration, reaction temperature, catalyst loading and oxidant loading, etc. Kinetic studies revealed that, for all the catalysts, catalytic oxidation of phenol could be described by a first order kinetic model. In addition, generation and evolution processes of free radicals were investigated by electron paramagnetic resonance (EPR) spectra. It was found that the generation and evolution processes of the free radicals depend on the types of the catalysts. While radical quenching tests unveiled that both the generated hydroxyl and sulfate radicals could be responsible for the oxidation of phenol.

Publications by the Author

1. **Wang Y**, Sun H, Ang HM, Tadé MO, Wang S. 3D-hierarchically structured MnO₂ for catalytic oxidation of phenol solutions by activation of peroxymonosulfate: Structure dependence and mechanism. *Appl. Catal., B.* 2015;164(0):159-67.
2. **Wang Y**, Sun H, Duan X, Ang HM, Tadé MO, Wang S. A new magnetic nano zero-valent iron encapsulated in carbon spheres for oxidative degradation of phenol. *Appl. Catal., B.* 2015;172–173(0):73-81.
3. **Wang Y**, Sun H, Ang HM, Tadé MO, Wang S. Facile Synthesis of Hierarchically Structured Magnetic MnO₂/ZnFe₂O₄ Hybrid Materials and Their Performance in Heterogeneous Activation of Peroxymonosulfate. *ACS Appl. Mater. Interfaces.* 2014;6(22):19914-23.
4. **Wang Y**, Indrawirawan S, Duan X, Sun H, Ang HM, Tadé MO, et al. New insights into heterogeneous generation and evolution processes of sulfate radicals for phenol degradation over one-dimensional α -MnO₂ nanostructures. *Chem. Eng. J.* 2015;266(0):12-20.
5. **Wang Y**, Sun H, Ang HM, Tadé MO, Wang S. Magnetic Fe₃O₄/carbon sphere/cobalt composites for catalytic oxidation of phenol solutions with sulfate radicals. *Chem. Eng. J.* 2014;245(0):1-9.
6. **Wang Y**, Zhou L, Duan X, Sun H, Tin EL, Jin W, et al. Photochemical degradation of phenol solutions on Co₃O₄ nanorods with sulfate radicals. *Catal. Today.* In press.
7. **Wang Y**, Sun H, Ang HM, Tadé MO, Wang S. Synthesis of magnetic core/shell carbon nanosphere supported manganese catalysts for oxidation of organics in water by peroxymonosulfate. *J. Colloid Interface Sci.* 2014;433(0):68-75.
8. **Wang Y**, Xie Y, Sun H, Xiao J, Cao H, Wang S. Facile Synthesis of γ -MnO₂ on Reduced Graphene Oxide as 2D/2D Nano-Hybrids for Catalytic Ozonation. *J. Hazard. Mater.* 2016;301(0):56-64.
9. Sun H, **Wang Y**, Liu S, Ge L, Wang L, Zhu Z, et al. Facile synthesis of nitrogen doped reduced graphene oxide as a superior metal-free catalyst for oxidation. *Chem. Commun.* 2013;49(85):9914-6.
10. Sun H, Zhou G, **Wang Y**, Suvorova A, Wang S. A New Metal-Free Carbon Hybrid for Enhanced Photocatalysis. *ACS Appl. Mater. Interfaces.* 2014;6(19):16745-54.10.

11. **Wang Y**, Xie Y, Sun H, Xiao J, Cao H, Wang S. Catalytic Ozonation of Phenolics over Hierarchical Shape-Controlled Calcium Manganites. Submitted.
12. Oral presentation on Magnetic Supported Manganese Oxide for Phenol Degradation on CHEMECA 2014.
13. Oral presentation on Novel g-C₃N₄ supported ZVI for Activation of PMS for Phenol Degradation on IWA Young Water Professionals 2014.

Content

Declaration	i
Acknowledgement	ii
Abstract	iv
Publications by the Author	v
Content	vii

Chapter 1: Introduction	1
1.1 Current issues and remediation methods in water resources	1
1.2 Research objectives	4
1.3 Thesis organization	5
References	8
Chapter 2: Literature Review	10
2.1 Introduction	10
2.2 Adsorption	14
2.3 Wet air oxidation process	17
2.4 Catalytic wet air oxidation process	19
2.5 Advanced oxidation processes (AOPs) for pollutants at low concentrations	23
2.5.1 Classical Fenton reaction	23
2.5.2 Modified Fenton/ Fenton-like Reactions	25
2.5.3 Photocatalytic oxidation	28
2.5.4 Ozonation/catalytic ozonation	32
2.5.4.1 Catalytic ozonation process	34
2.5.4.2 Homogeneous catalytic ozonation	34
2.5.4.3 Heterogeneous catalytic ozonation	36
2.5.5 Sulfate radical-based advanced oxidation processes	39
2.5.5.1 Energy induced sulfate radical oxidation	40
2.5.5.2 Homogeneous sulfate radical oxidation	42
2.5.5.3 Heterogeneous sulfate radical oxidation	43
2.5.6 Other advanced oxidation processes	45
2.6 Development of heterogeneous catalysts for peroxymonosulfate activation	46
2.6.1 Metal-based heterogeneous catalysts	46
2.6.2 Metal-free heterogeneous catalysts	51
2.7 Conclusions	52
References	54

Chapter 3: 3 D-hierarchically Structured MnO₂ for Catalytic Oxidation of Phenol Solutions by Activation of Peroxymonosulfate: Structure Dependence and Mechanism	77
3.1. Introduction	78
3.2. Experimental Section	80
3.3. Results and discussion.....	83
3.3.1. Characterization of the hierarchical materials	83
3.3.3. PMS activation processes on MnO ₂	95
3.4 Conclusions	101
References	102
Chapter 4: New Insights into Heterogeneous Generation and Evolution Processes of Sulfate radicals for Phenol Degradation over One-dimensional α-MnO₂ Nanostructures	106
4.1 Introduction	107
4.2 Materials and Methods	108
4.3 Results and Discussion.....	109
4.3.1 Characterization of 1D MnO ₂ materials	109
4.3.2 Catalytic oxidation of phenol.....	114
4.3.3 Activation of PMS and evolution processes of sulfate radicals.....	121
4.4 Conclusions	128
References	129
Chapter 5: Facile Synthesis of Hierarchically Structured Magnetic MnO₂/ZnFe₂O₄ Hybrid Materials and Their Performance in Heterogeneous Activation of Peroxymonosulfate	132
5.1 Introduction	133
5.2 Experimental Section	133
5.3 Results and Discussion.....	135
5.3.1 Characterization of the hierarchical materials.	135
5.3.2 Catalytic oxidation of phenol.....	140
5.3.3 Activation processes of PMS and mechanism of phenol degradation.	146
5.4 Conclusions	153
References	154
Chapter 6: A New Magnetic Nano Zero-valent Iron Encapsulated in Carbon Spheres for Oxidative Degradation of Phenol	158
6.1 Introduction	159
6.2 Experimental Sections.....	160
6.3 Results and Discussion.....	161
6.3.1 Physicochemical properties of the materials.....	161
6.3.2 Catalytic oxidation of phenol.....	166
6.3.3 Mechanism of enhanced reusability	173
6.3.4 Mechanism of PMS activation and phenol degradation.....	178
6.4 Conclusions	183
References	184

Chapter 7: Magnetic Fe₃O₄/carbon sphere/cobalt composites for catalytic oxidation of phenol solutions with sulfate radicals	188
7.1 Introduction	189
7.2 Experimental Sections.....	189
7.3 Results and Discussion.....	191
7.3.1 Characterization of the composites	191
7.3.2 Adsorption and heterogeneous catalytic phenol degradation	198
7.3.3 Effects of reaction parameters on phenol degradation	201
7.4 Conclusions	206
References	207
Chapter 8: Conclusions and Perspectives	210
8.1 Conclusions	210
8.1.1 Catalytic activation of PMS utilizing 3D hierarchical structured manganese oxides.....	210
8.1.2 Catalytic activation of PMS utilizing 1D manganese oxides in different shapes.....	211
8.1.3 Hierarchically structured magnetic ZnFe ₂ O ₄ /MnO ₂ hybrid materials	211
8.1.4 Magnetic nano-Fe ⁰ encapsulated in carbon sphere catalysts	212
8.1.5 Magnetic Fe ₃ O ₄ /carbon sphere/cobalt composites.....	212
8.2 Perspective of Future Works	213

Chapter 1: Introduction

1.1 Current issues and remediation methods in water resources

As one of the crucial resources for sustaining the human beings and other living creatures on the Earth, water, especially the fresh water, is highly demanded not only for maintaining the human and creatures' lives, but also for industrial and agricultural uses for the production of the daily necessities.

Water resources seem to be abundant on the Earth, however, the fresh drinking water is scarce. Statistic data illustrated that, although our planet is covered by 71% of the water with the total volume of 1.4 billion cubic kilometers, more than 97.5% of the planet's surface water is saline.(1) And among the remaining 2.5% of the freshwater, around 68% is stored in form of glaciers and ice caps in polar areas. Only less than 0.3% of the freshwater exists in groundwater and surface water such as lakes, rivers and reservoirs which could be ready for human activities.(2) Therefore, proper use of the fresh water and the treatment of the wastewater are imperative for the sustainable development of human society.

According to the United Nations World Water Development Report 2012 (WWDR4) published by the United Nations Educational, Scientific and Cultural Organization (UNESCO), the applications of fresh water could be classified into agricultural, industrial and domestic uses.(3) Agriculture plays the dominant role in consuming fresh water which accounts for more than 70% of the global fresh water usage. (4) Fresh water was mainly used for irrigation in agriculture to sustain the growth of the crops. The increasing population would stimulate the demand for irrigation water to satisfy the corresponding increase in food production requirements. Industrial use contributes to around 25% of the total fresh water usage. Fresh water is consumed a lot in industry to produce energy, chemicals, paper products, oils and metals, etc. In these industries, water is widely applied for the purposes such as cooling, washing,

solvent and transportation. Since industrial revolution, the water consumption in the industry has been increasingly enhanced. While the rest 5% of the fresh water used could be accounted for domestic usage for drinking, hygiene and food production. In the similar trend, urbanization and population explosion also result in the larger requirement of the fresh water.

Population explosion and rapid urbanization and rising industrialization not only increase the consumption of the fresh water and pressure to the scarce fresh water resources, but also result in discharging vast amount of pollutants into the water body. The discharged toxic pollutants from industrial, agricultural and domestic wastewater to the water body have attracted intensive public concerns in the recent years. Among these discharged pollutants, aqueous organic pollutants are the major components.(5) Within these organic pollutants in the contaminated water, most of them are detrimental to both human beings and the nature environment with resistance to self-degradation.(6) For example, fertilizers and pesticides (including herbicides and insecticides) are widely used by farmers to ensure the anticipated production by the crops.(7) Most of these fertilizers and pesticides are in the organic forms and the runoff of these organic compounds to the surface water will not only impose harmful effects to the living creatures, but also break the ecological equilibrium. For the industries, the discharged organic pollutants mainly consist of the reaction byproducts, such as polychlorinated biphenyls (PCBs), polycyclic aromatic hydrocarbons (PAHs) and dibutylphthalate (DBP), and the concentrations of these organic pollutants varies in accordance with the different purposes of the industries.(8) Therefore, considering the fact that the global fresh water resources are limited for human beings to survive, it is urgent and crucial to preserve these fresh water resources and find ways to remediate the contaminated water containing toxic organic pollutants.

To regulate the organic pollutants discharged into the water body, many countries not only identified the types of the hazardous organic pollutants, but also issued some relevant regulations to limit the discharging concentrations of these toxic organic

pollutants. The U.S. Environmental Protection Agency (EPA) listed over 400 hazardous organic compounds as the potential pollutants present in the waste/contaminated water. And in many countries, the maximum discharging thresholds for phenol and its derivative compounds are less than 1 mg/L. For Australia, the maximum concentration of phenol and 4-methyl phenol is 0.5 mg/L and 0.01 mg/L, respectively.(9, 10) Nevertheless, despite of the strict regulations, the release of these toxic organic pollutants still results in some severe environmental and health problems.

Phenol and its phenolic derivatives are major organic pollutants detected in the contaminated water discharged from industries such as pharmaceutical, petrochemical and chemical processes. The current phenol production rate is about 6 million ton/y with a significant increasing trend. Moreover, EPA's data illustrated that the ranking of the phenol waste among all 400 hazardous organic pollutants was 21st in the year of 2005.(11) The structure of phenol is shown in Fig. 1.1. Similar to other toxic organic compounds, phenol and its derivatives are toxic even at a low concentration. The exposure to phenol by inhalation, ingesting and skin/eye contacting may lead to severe problem. Phenol also affects the liver, lungs, kidneys, and vascular system. It was reported that the ingestion of 1 g phenol may lead to the fatal to the adults.(12) Therefore, it is imperative to develop effective techniques for treating and removal these phenolic organic pollutants from waste water.

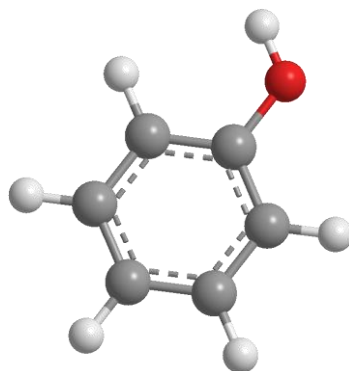


Figure. 1.1 Phenol chemical structure.

In order to remove the phenolics from contaminated water, several technologies have been developed such as thermal treatments, physico-chemical treatments and biological processes. For thermal treatments, incineration is widely employed for treatment of the toxic organics. Although it is simple and less expensive, incineration will generate considerable amount of other hazardous compounds and therefore cause the secondary pollution.(13) Physico-chemical treatments mainly includes adsorption, reverse osmoses, precipitation and flocculation. Most of the physico-chemical treatments are cost-effective, however, they cannot completely destroy the organic pollutants and then post-treatments are required.(14) Biological processes stand for an eco-friendly strategy for removal of organic pollutants within contaminated water. Nevertheless, they are not applicable for treatment of non-biodegradable contaminated water. Furthermore, they usually require a long treatment time for micro-organisms to degrade the pollutants.(13)

Recent years, advanced oxidation processes (AOPs) such as catalytic ozonation, Fenton reactions, wet air oxidation and photocatalytic oxidation have been gradually developed and attracted extensive attention as promising alternatives to conventional treatment technologies. By utilizing chemicals as the oxidants to generate reactive species, AOPs possess the capability of complete decomposition of the organic pollutants and transfer them into mineral acids, carbon dioxide and water. Due to high efficiency, nonselective degradation and complete decomposition, AOPs are the most suitable technologies to decompose toxic organic pollutant such as phenol and its derivatives.

1.2 Research objectives

The major objective of the research is to synthesize and develop several types of metal-based nanocatalysts for oxidative degradation of aqueous organic pollutants in contaminated water. These novel nanomaterials will be employed as the heterogeneous catalysts for activating peroxymonosulfate (PMS) to produce reactive species for

oxidative degradation of phenol which is utilized as the model organic pollutant in contaminated water. To this end, the following studies were carried out.

1. Synthesize magnetic or non-magnetic metal-based catalysts based on transition metals of either Co, Mn or Fe.
2. Investigate the catalytic activity and the stability/recyclability of the catalysts in terms of phenol degradation.
3. Study the reaction kinetics and the activation energy for each catalyst.
4. Determine the influences of reaction parameters such as catalyst loading, reaction temperature, oxidant loading and initial concentration on degradation efficiency.
5. Identify the reactive species generated during the catalytic degradation processes and probe the dominant reactive species responsible for degradation.

1.3 Thesis organization

This thesis includes eight chapters, including introduction, literature review, results and discussion (published papers), conclusion and suggestions for future research.

Chapter 1 — Introduction — mainly describes the background and motivation of this study, including current issues in water resources, water pollution as well as the strategies for treatment of the contaminated water. This chapter also presents the research objectives and the organization of the thesis.

Chapter 2 — Literature Review — provides a comprehensive review of techniques, with particular attention on advanced oxidation processes (AOPs) for treatment of phenolics in previous studies. Moreover, various types of catalysts used for AOPs investigated by other researches are reviewed.

Chapter 3 — 3D-hierarchically structured MnO₂ for catalytic oxidation of phenol solutions by activation of peroxymonosulfate: Structure dependence and mechanism. Applied Catalysis B: Environmental, 164 (2015) 159-167 — presents the study of

MnO₂ in 3D-hierarchically structure and its catalytic activity in phenol oxidation. The as-prepared catalysts demonstrated excellent catalytic activity for activating PMS to degrade phenol. Catalytic degradation of phenol was influenced by reaction temperature. The kinetic studies suggested that the heterogeneous catalytic reactions followed a first-order kinetics. The mechanism of catalytic reaction for PMS activation was investigated by electron paramagnetic resonance (EPR) spectra showing that both of •OH and SO₄^{-•} are produced in the activation processes, and SO₄^{-•} plays a more critical role in phenol oxidation.

Chapter 4 — *New insights into heterogeneous generation and evolution processes of sulfate radicals for phenol degradation over one-dimensional α -MnO₂ nanostructures*. *Chemical Engineering Journal*, **266** (2015) 12-20 — presents the study of the several 1D MnO₂ catalysts and their catalytic activities for phenol degradation. It was found that 1D MnO₂ nanowires showed the best catalytic efficiency. And it was revealed that in the evolution process of reactive species, generation of sulfate radicals was initiated by hydroxyl radicals produced at the initial stage and the sulfate radicals were the major reactive species responsible for the catalytic phenol oxidation.

Chapter 5 — *Facile synthesis of hierarchically structured magnetic MnO₂/ZnFe₂O₄ hybrid materials and their performance in heterogeneous activation of peroxymonosulfate*. *ACS Applied Materials & Interfaces*, **6** (2014) 19914-23 — describes the synthesis of the 3D magnetically separable ZnFe₂O₄/MnO₂ nanocomposites in different shapes and compared their catalytic activities in activating PMS for phenol decomposition. It was found that ZnFe₂O₄/MnO₂ with microsphere/nanosheet hierarchical structure possessed a higher BET surface area and thus a better catalytic activity than urchin-like catalysts. A first-order kinetic model was used to evaluate the kinetic parameters, and the activation energies for microsphere/ nanosheet hierarchical structure and urchin-like structure were calculated to be 41.7 and 49.4 kJ/mol, respectively. Catalyst stability tests suggested that deactivation of the catalysts occurred because of the blockage of active sites by the reaction intermediates.

Chapter 6 — *A new magnetic nano zero-valent iron encapsulated in carbon spheres for oxidative degradation of phenol. Applied Catalysis B: Environmental, 172-173 (2015) 73-81* — describes the synthesis of Fe/Fe₃C@CS nanocomposites via a modified hydrothermal method followed by self-reduction under nitrogen atmosphere. The novel ZVI-based nanocomposites showed a superior catalytic activity in activation of PMS for phenol degradation. The kinetic studies suggested that, in the heterogeneous systems, catalytic oxidation of phenol followed first order kinetics and the apparent activation energy was 16.3 kJ/mol. Moreover, Fe₃C catalysis for PMS activation was observed for the first time. The catalyst deactivation mechanism was also investigated and it was found that Fe₃C has a better catalytic stability than Fe⁰ in catalytic reaction. Magnetic separation capability was also remained even after five runs.

Chapter 7 — *Magnetic Fe₃O₄/carbon sphere/cobalt composites for catalytic oxidation of phenol solutions with sulfate radicals. Chemical Engineering Journal, 245 (2014), 1-9* — presents the study of the core/shell structured magnetic carbon sphere loaded with cobalt oxides and the evaluation of the catalytic activity for PMS activation for phenol degradation. It was revealed that catalytic degradation of phenol was influenced by initial phenol concentration, catalyst loading and reaction temperature.

Chapter 8 — *Conclusions and perspectives* — this chapter summarizes research results and put up with some suggestions for further research in this area.

References

1. Vörösmarty CJ, Green P, Salisbury J, Lammers RB. Global water resources: vulnerability from climate change and population growth. *Science*. 2000;289(5477):284-8.
2. Oki T, Kanae S. Global hydrological cycles and world water resources. *Science*. 2006;313(5790):1068-72.
3. WWDR U. World water development report 4—managing water under uncertainty and risk. 2012.
4. Hanjra MA, Qureshi ME. Global water crisis and future food security in an era of climate change. *Food Policy*. 2010;35(5):365-77.
5. Wang S, Sun H, Ang H-M, Tadó M. Adsorptive remediation of environmental pollutants using novel graphene-based nanomaterials. *Chem. Eng. J.* 2013;226:336-47.
6. Wang S. A Comparative study of Fenton and Fenton-like reaction kinetics in decolourisation of wastewater. *Dyes Pigm.* 2008;76(3):714-20.
7. Larson SJ, Capel PD, Goolsby DA, Zaugg SD, Sandstrom MW. Relations between pesticide use and riverine flux in the Mississippi River basin. *Chemosphere*. 1995;31(5):3305-21.
8. Vargas M-C, Ramírez NE. Phenol oxidation of petrol refinery wastewater catalyzed by Laccase. *CT.F.* 2002;2:23-30.
9. Saputra E, Muhammad S, Sun H, Ang H-M, Tadó MO, Wang S. A comparative study of spinel structured Mn_3O_4 , Co_3O_4 and Fe_3O_4 nanoparticles in catalytic oxidation of phenolic contaminants in aqueous solutions. *J. Colloid Interface Sci.* 2013;407(0):467-73.
10. Verheyen V, Cruickshank A, Wild K, Heaven MW, McGee R, Watkins M, et al. Soluble, semivolatile phenol and nitrogen compounds in milk-processing wastewaters. *J. Dairy Sci.* 2009;92(7):3484-93.
11. Downing RS, Kunkeler PJ, van Bekkum H. Catalytic syntheses of aromatic amines. *Catal. Today*. 1997;37(2):121-36.
12. Busca G, Berardinelli S, Resini C, Arrighi L. Technologies for the removal of phenol from fluid streams: A short review of recent developments. *J. Hazard. Mater.* 2008;160(2–3):265-88.
13. Liotta LF, Gruttadauria M, Di Carlo G, Perrini G, Librando V. Heterogeneous

catalytic degradation of phenolic substrates: Catalysts activity. J. Hazard. Mater. 2009;162(2-3):588-606.

14. Danis TG, Albanis TA, Petrakis DE, Pomonis PJ. Removal of chlorinated phenols from aqueous solutions by adsorption on alumina pillared clays and mesoporous alumina aluminum phosphates. Water Res. 1998;32(2):295-302.

Every reasonable effort has been made to acknowledge the owners of copyright material. I would be pleased to hear from any copyright owner who has been omitted or incorrectly acknowledged.

Chapter 2: Literature Review

2.1 Introduction

Due to the decrease of the amount and the deterioration of the quality along with and the increasing demands for water resources throughout the world, water resource preservation and wastewater treatment have received worldwide attention. Industrialization and urbanization have resulted in discharging a large amount of wastewater containing various types of pollutants into the water body and have caused severe pollution in the past few decades. Among these pollutants, aqueous toxic and hazardous organic pollutants including organic dyes, endocrine disrupting chemicals (EDCs), aromatic compounds, agrochemicals and sulfur- and nitrogen-containing compounds have brought harmful effects to both human beings and aquatic creatures.(1) Among these discharged organic pollutants, phenol and its derivatives have received increasing attention in the past few years due to their strong toxicity and recalcitrance to natural degradation. Since phenol shows strong toxicity even at a low concentration (2), countries around the world have set the maximum threshold allowed for phenol discharge, for instance 0.5 mg/L for Australia wastewaters.(3) Therefore, the development of efficient, convenient and cost-effective wastewater treatment technologies are highly required.

Conventional wastewater treatment methods employing filtration, adsorption, physico-chemical processes (flocculation, ozonation and chlorination) and biodegradation have demonstrated their effectiveness for treatment of majority of anthropogenic pollutants.(4) However, no single method mentioned above achieves efficient degradation for removal of refractory toxic chemicals such as phenols, dyes, pesticides, organic solvents and domestic chemicals.(4) Despite the fact that biodegradation is very effective for treatment of municipal and domestic wastewater, it is not feasible to treat industrial wastewater containing toxic pollutants due to the biomass poison-

ing.(5) Wet air oxidation process is widely utilized for treating wastewater having chemical oxygen demand (COD) greater than 20 g/L, however due to its incomplete degradation and generation of high concentration of toxic byproducts, further treatments are still required. (6, 7) Moreover, physico-chemical wastewater treatment technologies such as flocculation, adsorption and reverse osmosis also require post treatment to prevent secondary pollution.(8)

In the recent years, advanced oxidation processes (AOPs), for example Fenton reaction, photocatalysis, catalytic ozonation and various other chemical oxidation, have attracted intensive research interests for decomposing the organic contaminants due to their high efficacy of complete degradation to inorganic compounds such as H₂O and CO₂.(9) Among these AOPs, previous investigations have demonstrated that Fenton/Fenton-like reactions utilizing hydroxyl radicals (OH[·]) could decompose organic contaminants efficiently.(10, 11) And homogeneous Fe²⁺/H₂O₂ system has been proven to be the most effective for degradation of aqueous organic pollutants.(10, 12, 13) However, these processes suffer from shortcomings like metal leaching, pH adjustment, production of large quantity of sludge and cost-intensive operation. (14)

Compared to Fenton reaction, the emerging catalytic ozonation process utilizing various reactive species such as [·]OH, ¹O₂ and [·]O₂⁻ for aqueous organic pollutants degradation becomes an efficient alternative.(15, 16) Although traditional ozonation process possessed an excellent ability for removal of aqueous organic pollutants, the oxidation reaction is selective and cannot fully mineralize organic contaminants into inorganic forms.(15) By introducing catalysts, controlled decomposition of ozone could be achieved and the generated active free radicals would be responsible for efficient mineralization of the persistent organic contaminants.(16) Additionally, the pH requirements for oxidation reactions could be adjusted in accordance with the properties of catalysts. (17, 18)

As another promising alternative to Fenton reactions, sulfate radical based AOPs

(SR-AOPs) have attracted intensive attention.(19-21) Sulfate radicals ($\text{SO}_4^{\cdot-}$), which can be generated by activation of either persulfate (PS) or peroxymonosulfate (Ox-one, PMS), have a higher redox potential than hydroxyl radicals ($E_0=3.1\text{V}$ vs. $E_0=2.7\text{V}$) and are more desirable for persistent organic pollutants (POPs) degradation.(22) In addition to the high activity, the initiators of sulfate radicals are less expensive and more environmentally benign. (23) More importantly, the sulfate radicals can be generated in both heterogeneous and homogeneous catalysis, metal leaching problem leading to secondary pollution can be thus minimized. In the past few years, studies have been carried out in relation to the activation of sulfate radicals by UV radiation(24), heat(25) and metal catalysts(26). Various types of homogeneous and heterogeneous catalysts have been developed for the generation of sulfate radicals. Studies have suggested that cobalt based materials demonstrated the best catalytic efficiency for activating PMS to produce sulfate radicals.(27, 28) Nevertheless, employing cobalt based catalysts would inevitably result in leaching or loss of cobalt ions into the reaction solution and thus leading to the secondary pollution caused by the toxicity of cobalt ions.(29, 30)

Compared with cobalt ion/oxide, manganese oxides are less toxic and more environmentally benign. In our previous studies, manganese oxides at different chemical states showed a good catalytic ability for PMS activation to produce sulfate radicals.(31) Though metal leaching problem can be minimized when nanosized manganese oxides are employed for heterogeneous catalysis, if no proper recovery, the nanosized particles would still bring in secondary contaminants to the environment.

Utilization of magnetic separation technology for recovering catalysts has attracted considerable attention. Compared with traditional separation technologies such as centrifugation and filtration, magnetic separation provides a much easier and cost-effective process by simply applying an external magnetic field.(32, 33) Recently, magnetite (Fe_3O_4) nanoparticles have been frequently used as the magnetic core in various fields, owing to their outstanding magnetic and electrochemical

properties. (34-37). However, their prone to aggregation characteristics resulted from high surface area to volume ratio, strong dipole–dipole attraction between particles, and limited functional groups for selective binding hinder their further applications.(33) To overcome such drawbacks, barrier materials such as SiO₂ or carbon nanotubes (CNT) have been investigated to prevent self-aggregation and to isolate from attached functional components.(32, 38) More recently, carbon coated magnetite nanospheres (Fe₃O₄/C) have been employed because of their low cytotoxicity and highly modifiable surface (39, 40). We recently synthesized such magnetic carbon nanospheres and used them as support for cobalt based catalyst.(41) It was found that the as-synthesized cobalt based magnetic carbon nanospheres showed excellent catalytic performance for activation of PMS for phenol degradation.

More recently, nanocarbon materials including graphene, graphene oxide/reduced graphene oxide and carbon nanotubes (CNTs) have been utilized as promising alternatives for the metal-based catalysts to completely avoid metal ion leaching problem. Due to their large theoretical surface area, unique electronic property, outstanding thermal conductivity and sp² hybridized carbon configuration, various studies have revealed that these nanocarbon materials have promising catalytic activity for energy and environmental applications.(42, 43) Fullerene, graphene oxide, graphene nanoplates, single-walled carbon nanotubes (SWCNTs) and multi-walled carbon nanotubes (MWCNTs) have been demonstrated to be catalytic active for PMS activation.(29, 30, 44-46)

In consideration of the current freshwater situation, the well-being of the current generation and the development of the future generations, it is highly imperative to select proper wastewater treatment to degrade aqueous organics cost-effectively, completely, and eco-friendly. Moreover, in order to improve the degradation efficiency and to prevent further contamination, facile synthesis of novel catalysts with high catalytic activity, excellent recyclability and low toxicity of catalysts is in high demand.

2.2 Adsorption

Adsorption process is a simple and effective operation to remove various types of pollutants from the environment and has attracted research attention for a long time. Compared with other environmental remediation technologies, adsorption does not result in the production of any reaction residues and thus can prevent the harmful and toxic substance brought by the secondary pollution.(47) For adsorbents employed in the adsorption process, the surface area, pore volume, surface charge and surface functionalities are the critical factors influencing their adsorption capability.

Adsorption process is normally resulted from the electrostatic or non-electrostatic interactions between the adsorbent surface and the adsorbate.(48) Electrostatic interactions occur when adsorbate is an electrolyte which can be dissociated in aqueous solution. And the electrostatic interaction could be attractive or repulsive depending on the adsorbent's charge density, adsorbate's chemical characteristics and the ionic strength of the solution. While the non-electrostatic interactions are always attractive and are determined by the van der Waals force, hydrogen bonds and hydrophobic interactions. (48)

In the past few decades, different types of the porous materials have been developed and their adsorption capabilities have been investigated. Porous materials such as activated carbon (49), clay minerals (50, 51), zeolites (52), biomaterials (53), industrial solid wastes (54) and some novel carbonaceous-based materials such as graphene, graphene oxide and carbon nanotubes (55, 56) have been widely applied for adsorptive removal of heavy metals, dye products and organic pollutants from wastewater and demonstrated high removal efficiency. Due to the superior adsorption capacity and thermal/structural stability, carbonaceous-based materials have arouse significant research interests among these porous materials.

Activated carbon (AC) has been widely utilized as the adsorbent for adsorption of both organic and inorganic waste compounds from water. Production of activated carbon is simple since it can be generated from various low-cost materials such as cereals, nut shell, municipal wastes and fruit waste. (49) According to the statistic data, more than 80% of the world production of AC is used as an adsorbent in the liquid phase applications.(57) The adsorption capacity of AC for organic compounds is dominated by its pore size distribution, surface functionality and contents of mineral matters. (48)

As one of the new members of the carbon materials, carbon nanotubes (CNTs) have received considerable attention in the adsorption-related applications due to their unique structure and physico-chemical properties.(56) Compared with activated carbon, CNTs have a far more well-defined and uniform structure at nanoscale, which are completely different from AC. Moreover, CNTs not only possess large specific surface area, but also chemically stable with robust surface for physical adsorption.(58) Due to these superior features, extensive studies have been conducted for the adsorption of heavy metal ions (59, 60), radionuclides (61, 62), small molecules (63, 64) and organic chemicals (65, 66) on various CNTs such as single-walled CNTs, multi-walled CNTs, close- or open ended CNTs. For ACs, the adsorption capacity is quantified by the parameters such as pore size distribution and adsorption energy distribution, however, for CNTs, the adsorption capacity is mainly related with well-defined adsorption sites. (56) Depending on the pollutants adsorbed, there are four possible adsorption sites existing on CNTs (67, 68): (i) interstitial channels between individual nanotubes in the bundles; (ii) the hollow interior of individual nanotubes; (iii) the grooves on the edge of the nanotube bundle and the exterior surface of the outermost nanotubes; and (iv) the curved surface of individual nanotubes on the outside of the nanotube bundles.

Apart from activated carbon and CNTs, graphene-based materials including graphene nanosheets (GN) and graphene oxide (GO) have attracted significant research inter-

ests due to their large theoretical specific surface area and the surface functional groups.(44, 55, 69) In the recent years, several investigations have been performed by utilizing graphene-based materials as adsorbents for removal of pollutants from air and aqueous solution.(70-73) Dyes are stable and non-biodegradable organic pollutants discharged from textile, dyeing, tannery and paper industries. Several GO, GN and their composites have been developed and employed for dye adsorption.(74-77) Dyes usually exist in aqueous solution in forms of ions. And the major interaction between graphene-based materials and dyes is dominated by cationic-anionic force.(55) Studies revealed that GO possesses excellent adsorption capacity for cationic dyes such as methylene blue and crystal violet, but low affinity for anionic dyes such as methyl orange and orange II.(71, 77) While GN and its composites demonstrate high adsorption capacity for both cationic and anionic dyes due to the π - π stacking.(78) Apart from adsorption of various types of dyes, graphene-based nanomaterials have been utilized for some persistent aromatic pollutants which are not only harmful to aquatic life, but also toxic to human beings. Researches have been carried out for the adsorption of phenolic compound, pesticides, drugs and humic acids on GO and GN.(70, 79-81) And studies revealed that hydrophobic effect, π - π bonds, hydrogen bonds and covalent and electrostatic interactions may determine the adsorption capacity of organic pollutants on the surface of the nanosized carbon materials.(82) While among these interactions, the π - π interaction between the carbon surface and the organic pollutants plays a crucial role in the adsorption capacity.

To conclude, removal of organic pollutants by adsorption is a facile, eco-friendly and cost-effective technology among the various available treatment technologies. By employment of materials with large surface area or high surface functionalities, pollutants can be effectively attached on the adsorbent surface and thus leading to no secondary pollution. However, in the adsorption process, organic pollutants within the wastewater are just adsorbed rather than destroyed, and further treatment is still required for the degradation of the contaminants as well as collection and separation of these adsorbents. Therefore, other treatment technologies are still required to ef-

fectively mineralize the aqueous organic pollutants.

2.3 Wet air oxidation process

Chemical oxygen demand (COD) is one of the features of water quality to measure amount of organic compounds in water. Higher COD value indicates a larger amount of organics in the water. If COD of the waste water is too high, incineration might be feasible for the treatment; if COD is relatively low, wastewater treatment technologies such as chemical oxidations and biological treatment will be feasible to employ. However, when the COD of the wastewater situates in a medium range, neither incineration or chemical oxidation could be applied. Therefore, it is imperative to investigate technologies for the treatment of this kind of water. Being as one of the most attractive and successful wastewater treatment technologies, wet air oxidation process (WAO) is suitable for processing wastewater streams in which the COD value is low to incinerate and too high for chemical/biological treatment.(83) And the preferred COD for WAO is between the range of 20,000 and 200,000 mg/L. (84) WAO is most employed in the aqueous phase to oxidize the soluble or suspended organic/inorganic wastes with high temperature (398-573K) and pressure (0.5-20MPa) under the presence of the oxygen-containing gas (usually air).(85) In the WAO process, oxidation potential is improved by enhancing the solubility of the molecular oxygen under the condition of high temperature and pressure. Furthermore, the elevated temperature favors the increase of reaction rates and the production of free radicals.

It has been proven that WAO could be utilized for the treatment of variety of wastewater including sludge waste, petroleum refining waste, textile waste, petrochemical waste and majority of the organic compounds existed in wastewater could be destroyed.(7) Process flow diagram of WAO used in industries is shown in **Fig. 2.1**.(86) In this process, the organic pollutants can be oxidized to carbon dioxide,

water and some low molecular weight organic compounds such as carboxylic acids, alcohols and acetaldehydes. And 75-90% of COD removal could be reached for WAO process.(83) The degree of the oxidation usually depends on the feed composition, retention time and process conditions.(85) WAO normally cannot result in the complete mineralization of the organic/inorganic contaminants, however, these contaminants have been transferred into the forms with significantly reduction in toxicity and chemical oxygen demand. (85) Moreover, WAO usually leads to the formation of off-gas and liquid effluents which require further treatment. (83)

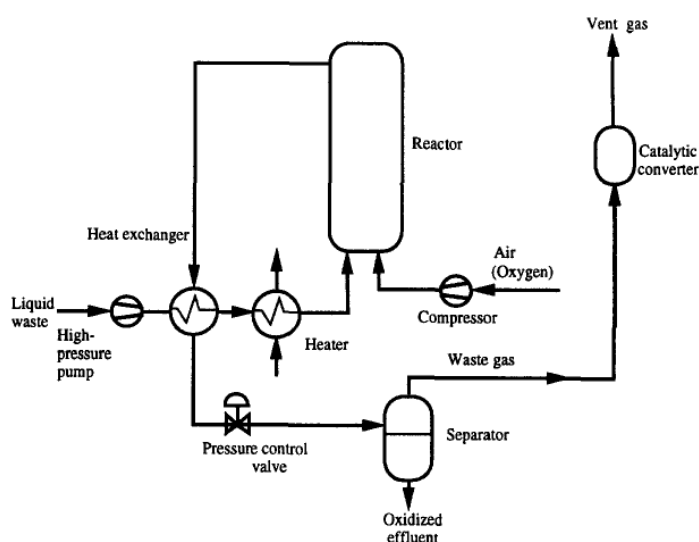
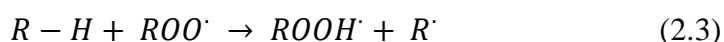
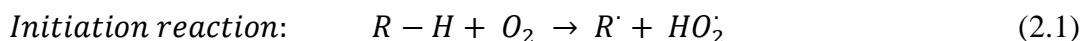


Figure 2.1. Process flow diagram of WAO used in industries. (86)

In order to investigate the mechanisms of WAO, several studies have been carried out using carboxylic acids and phenol as target pollutants.(87, 88) Taking the degradation mechanism of carboxylic acid as the example, it was found that during the oxidation of the aqueous organic pollutants, hydroperoxides and oxy-radicals were generated within the free radical chain reactions. And two major steps were included in the free radical chain reactions. Firstly, hydrogen atoms were abstracted from α , β and γ -CH₂ groups within the carboxylic acids by the dissolved oxygen and leading to the formation of free radicals. Simultaneously, these generated free radicals reacted immediately with O₂ to form peroxy radicals. Secondly, these peroxy radicals can abstract

H atoms from other carboxylic groups and therefore resulting in the decarboxylation of these groups and formation of CO₂. Within the generation of free radicals, the processes of radicals initiation, propagation and termination occur, which are shown in the following equations.(6)



Wet air oxidation process is widely employed in industries due to its minimal air pollution discharges since most of the contaminants remain in the aqueous phase. However, the major disadvantages of WAO lie in the partial decomposition of the contaminants and high capital costs. Since the process is carried out under high temperature and pressure, the materials used for constructing equipment need to be strengthened to withstand severe operation conditions and thus increase the construction cost. Moreover, during the operation, large amount of power is required for compressed air production and high pressure liquid pumping. It was reported that WAO process becomes economical when concentration of the organic/inorganic pollutants to be oxidized situated between the ranges of 1-20 wt%. Within this concentration range, the amount of aqueous pollutant is sufficient to react with oxygen to produce enough heat to keep the desired operating conditions in the reaction without external energy source.(89) Due to these disadvantages, WAO is normally used as a pretreatment technology of wastewater, which requires additional treatments.

2.4 Catalytic wet air oxidation process

In order to overcome the disadvantages of WAO, catalytic wet air oxidation process (CWAO) was developed. Compared with the conventional WAO, CWAO could not only achieve a higher oxidation rate and a better mineralization of the organic pollutants, but also reduce the capital cost and energy requirements. With the aid of catalysts, aqueous organic contaminants can be fully mineralized into innocuous inorganic compounds such as water and carbon dioxide. “Zero discharge” can be achieved in the CWAO process. The refractory acetic acid and ammonia which cannot be completely destroyed at WAO could be totally mineralized within the help of catalysts, moreover, leading to no detectable level of NO_x or SO_x in the discharged effluent gas.(86) Furthermore, CWAO process is allowed to control the degradation rate of the organic pollutants. In accordance with the type and amount of the organic compounds dissolved in the wastewater, the process can be designed either to reduce the organic compounds’ concentration to form biodegradable intermediates or completely mineralized them. In addition, with the presence of catalysts, free radical chain reactions can occur at a much lower temperature and pressure condition. Moreover, the retention time for the liquid phase within the oxidation reactor can be significantly reduced. The less severe reaction condition and the reduced volume of reactor not only avoids the stress corrosion cracking of the construction materials, but also significantly reduces both the capital and operating costs.(90)

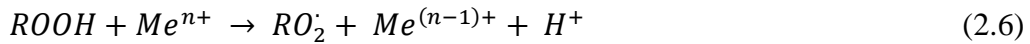
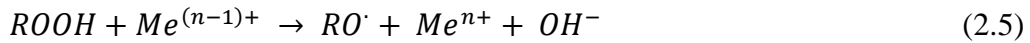
In the past few decades, various heterogeneous catalysts such as metal oxides and supported metal oxides have been employed for CWAO process for the treatment of aqueous organic pollutants. And the following table presents the some of the reported heterogeneous catalysts.

Table 2.1. Some of the reported heterogeneous catalysts for CWAO.

Catalyst	Pollutants	Ref.
Cu/Al	Phenol, p-cresol	(91, 92)
Cu	Phenol	(91)
Cu-Zn	Phenol	(93)
Mn/Al	Phenol	(91)
Mn-Zn-Cr	Industrial wastes	(94)
Co	Alcohols, amines	(95)
Co-Bi	Acetic acid	(96)
Co-Ce	Ammonia	(97)
Ru/CeO ₂	Alcohols, phenol	(98)

In CWAO, heterogeneous catalysts can be classified into two streams: noble metals and metal oxides. (99) And in the most cases, in order to improve their reactivity and stability, a noble metal is loaded onto another metal oxide or supporting materials. In terms of catalytic activity, it was found that, although Cu, Zn, Co, Mn and Bi oxide mixtures demonstrated excellent catalytic activity, metal ion leaching problem arising from the dissolution of the catalysts was observed. (94, 96-98) While studies revealed that utilization of precious metal oxides depositing on a stable support as the heterogeneous catalysts can minimize the leaching of the active ingredient. (100, 101) In addition, compared with transition metal oxide catalysts, noble metal catalysts such as Ru, Pt, Rh and Ir demonstrated higher degradation efficiency of acetic acid. (102, 103)

Following equations show the mechanism of the CWAO with the presence of heterogeneous catalysts.(104) And the redox potential of the metal ion couple ($Me^{n+}/Me^{(n-1)+}$) determines catalytic performance of the catalysts. (105)



Apart from insoluble heterogeneous catalysts, homogeneous catalysts employing transition metal ions have been developed as the alternative to further improve the reaction rate and degradation efficiency. Homogeneous Cu^{2+} system has been demonstrated to be the most effective for organic decomposition. (86) However, further treatments such as separation and purification are required for the homogeneous catalytic systems. **Fig. 2.2** describes the simplified triangular reaction scheme for CWAO using heterogeneous/homogeneous catalysts.

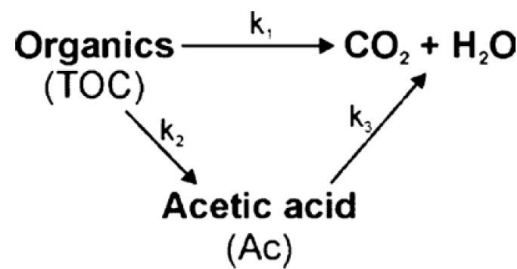


Figure 2.2. Simplified triangular reaction scheme for CWAO using heterogeneous/homogeneous catalysts.

To conclude, catalytic wet air oxidation process is a promising wastewater treatment technology which oxidizes the organic pollutants into more biodegradable forms or completely destroy them. Moreover, compared with conventional wet air oxidation process, CWAO is much more cost-effective by utilizing less energy and requiring less capital and operating costs. Metal oxide catalysts or transition metal ions have been proven to be catalytically active as heterogeneous or homogeneous catalysts, respectively. For these catalysts, leaching may result in the loss of the active sites and bring about problem for further treatments. In order to reduce leaching, metal oxides are incorporated into the lattice of the support materials such as Al, Si and

some noble metals. However, poisoning and blockage of the active sites by reaction intermediates, loss of surface area of the supporting material and coking on catalyst surface can result in the loss of catalytic activity. Therefore, for further studies, research attention should be focused on the investigation of more stable and durable catalysts with equal or higher catalytic activity.

2.5 Advanced oxidation processes (AOPs) for pollutants at low concentrations

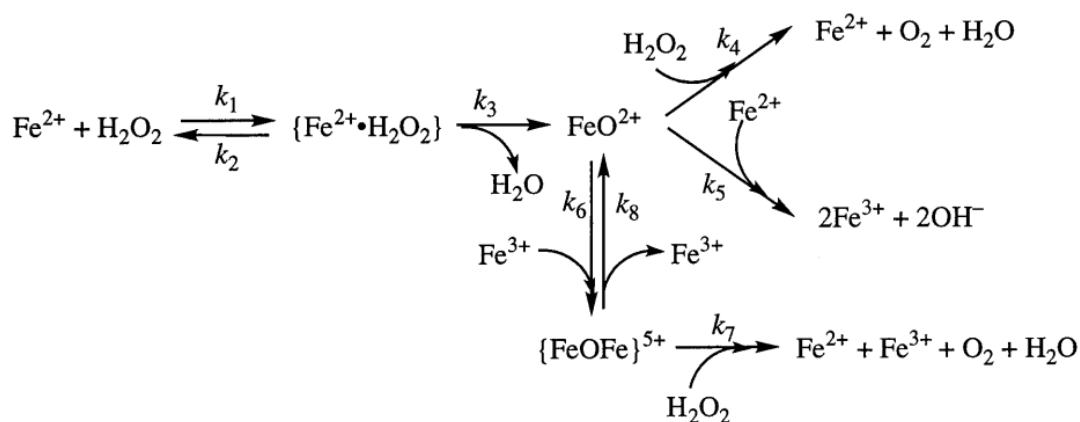
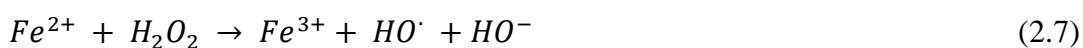
One of the important technologies for wastewater treatment is the AOP method which has the potential to completely mineralize the harmful aqueous organic pollutants at low levels. In AOPs, reactions follow a specific oxidation pathway for generation of free radicals such as hydroxyl or sulfate radicals which not only obtain high redox potentials but also are non-selective to the contaminants. Owing to the complete degradation capability of the AOPs, the final products of the toxic contaminants are carbon dioxide, water and other inorganic residues such as sulfate and chloride ions depending on the chemical composition of the precursors. However, since the final concentrations of these residues are low, their existence can be considered environmentally acceptable. Typical AOPs include Fenton/Fenton-like reactions, photocatalysis, ozonation/catalytic ozonation and sulfate radicals induced oxidation reactions.

2.5.1 Classical Fenton reaction

Conventionally, classical Fenton reaction was the oxidation of organic substrates by homogeneous reaction of iron (II) and hydrogen peroxide (H_2O_2). This kind of reaction was firstly discovered by H.J.H Fenton more than 100 years ago by observing the oxidation of tartaric acid by hydrogen peroxide with the addition of Fe^{2+} . Although Fenton reaction was discovered for more than a century, not until in late 1960s,

it has been widely utilized as an effective oxidation technique for treatment of toxic organic pollutants such as phenolic compounds(106, 107), aromatic amines(108), dyes(10, 13, 109), and pesticides(110, 111).

In Fenton reactions, hydrogen peroxide decomposes into hydroxyl radicals and hydroxide ions under the catalytic effect of Fe^{2+} within the aqueous acidic medium. The oxidation of Fe^{2+} will generate Fe^{3+} which may further catalyze H_2O_2 to produce more hydroxyl radicals. The produced hydroxyl radicals are not only a non-selective oxidants, but also of a high oxidation potential of 2.7 V and will take the responsibility of oxidizing toxic organic pollutants into nontoxic inorganic forms. The following equations illustrate the detailed reaction mechanism of Fenton reaction. And **Scheme 2.1** presents the chain mechanisms of Fe^{2+} regeneration. (112)



Scheme 2.1. Chain mechanisms of Fe^{2+} regeneration (112).

It has been revealed that Fenton reactions are influenced by hydrogen peroxide concentration, pH value, reaction time and the ratio of Fe^{2+} to H_2O_2 . Furthermore, the initial concentration of target pollutant as well as the reaction temperature will affect the oxidation efficiency of Fenton reaction.(10)

Although Fenton reactions have the advantages such as cost-effective, simple reactor requirement, and high efficiency of organic pollutants mineralization(4), they still suffer from several drawbacks such as low pH requirement, metal leaching problem, production of sludge and difficulties in transportation and storage of hydrogen peroxide.(113) These disadvantages place the bottleneck for the further application of Fenton reaction. In order to circumvent these drawbacks mainly resulting from the homogenous reaction, heterogeneous Fenton systems have been investigated. In a heterogeneous Fenton reaction system, iron species (mostly Fe^{3+}) are usually anchored on the supporting materials to confine leaching under acidic reaction conditions.(12, 17, 114-119). Heterogeneous iron-based catalysts using mesoporous materials (12), activated carbons (117), graphene (118), MWCNT (119), natural and synthetic zeolites, clays and silica (116, 120), nafion films (114) and aluminates (121) as the host matrix have been developed for Fenton reactions. Furthermore, some iron-based materials, such as magnetite, ferrihydrite, maghemite, hematite, zero-valent iron and lepidocrocite have been proven to be catalytically active for Fenton reactions. (122)

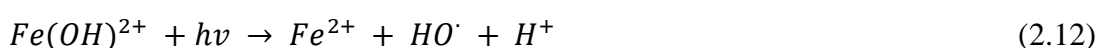
Apart from iron and iron oxides based catalyst, some non-ferrous metal catalysts have been also investigated for heterogeneous Fenton reactions. It has been revealed that elements with multiple redox states such as copper (123, 124), manganese (125), chromium (126), cerium (127) and cobalt (128) can effectively convert hydrogen peroxide into hydroxyl radicals through the conventional Fenton reaction pathways.

2.5.2 Modified Fenton/ Fenton-like Reactions

Though heterogeneous Fenton reaction can minimize the metal leaching and reduce the dependence on pH, the reaction rate between the heterogeneous catalyst and hydrogen peroxides is at least 3-orders of magnitude slower than the classical homogeneous Fenton reaction. (4) Therefore, various modifications have been developed to enhance the efficiency through the synergistic effect.

(A) Photo-Fenton Reactions

As one of the photochemical processes, photo-Fenton has been demonstrated to be a highly effective process for decomposition of various pollutants under ultraviolet (UV) or solar light irradiations.(129-132) The pioneer study by Zepp and his co-workers revealed that $[\text{Fe}(\text{OH})]^{2+}$ ion, which is the pre-eminent form of Fe(III), is the key factor contributing to the photo-Fenton reaction.(130) Moreover, under the irradiation of UV or solar light, the hydrogen peroxide itself could generate hydroxyl radicals.(129) Therefore, overall hydroxyl radical production is enhanced by improving the decomposition of H_2O_2 . Additionally, the iron sludge waste produced by photo-Fenton reaction was drastically reduced. The following equations describe the reactions involved during the photo-Fenton reaction. (4)



Additionally, the presence of colored substances such as organic dyes could also immensely improve the production rate of the hydroxyl radicals and thus enhance the catalytic oxidation efficiency.(133, 134) Under visible light irradiation, iron(III) will be reduced to iron(II) due to the intermolecular electron transfer from the excited dye states. And the reduced iron(II) will trigger the hydrogen peroxide to generate hydroxyl radicals for degradation.(4) Below equations describe the photo-Fenton reactions with participation of dyes. Fig. 2.3 schematically shows the mechanism.

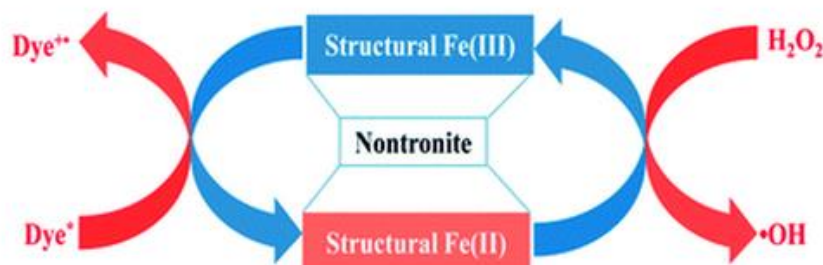


Figure 2.3 Mechanism of photo-Fenton process (134).

(B) Sono-Fenton reactions

The synergistic effect of ultrasound and Fenton reaction has also been investigated. In sono-Fenton reactions, the sound waves with a high frequency (20 kHz-1 MHz) could decompose water and dissolved oxygen molecules into highly reactive hydroxyl radicals by creating transient or stable acoustic cavitation in the reaction solution. (135) Moreover, hydrogen peroxide could be generated in situ during the reaction. The generation process of reactive radicals during the sono-Fenton reaction is shown as below.



Where))) stands for the ultrasonic irradiation. Researches have revealed that compared with classical Fenton reactions, the catalytic degradation efficiency of sono-Fenton reaction is dramatically improved by using water and oxygen as the additional precursors for generation of hydroxyl radicals.(136-138)

Apart from integrating light irradiations to the Fenton reaction, studies have also been conducted to investigate the synergistic effect of Fenton reaction with other sources such as electro-Fenton reactions (139, 140), sono-photo-Fenton reactions (135) and sono-electro-Fenton reactions(141).

To conclude, these Fenton-like reactions can produce less sludge waste, withstand a wider pH range and be more effective. These advantages of Fenton-like reactions circumvent the drawbacks of the classical Fenton reactions and make them versatile for feasible applications.

2.5.3 Photocatalytic oxidation

Over the past four decades, photocatalytic process has demonstrated great potentials for wastewater treatment because it is cost-effective, eco-friendly and will discharge “zero” waste. By employing heterogeneous catalysts such as TiO_2 , ZnO and CdS , and ultraviolet or visible light irradiation, the in situ produced reactive radicals within the photocatalytic oxidation process could effectively degrade the toxic organics in wastewater into less toxic substances, and deactivate microorganism.(142, 143) Mineralization efficiency of the persistent organic pollutants in photocatalytic oxidation process is controlled by the irradiation source, oxidizing agent and the activity of semiconductor photocatalyst. Among these factors, a semiconductor photocatalyst plays the dominant role to influence the degradation efficiency.

In photocatalytic process, photons from the irradiation source are absorbed by the surface of the photocatalyst. When the photons with the energy greater than the band gap energy of the photocatalyst, the electrons in the valence band could be excited to conduction band (CB) and leave a positive hole (h_v^+) in VB. The produced positive holes could either oxidize water to generate hydroxyl radicals or directly oxidize the toxic pollutants. The electrons in the conduction band take the responsibility of reducing the oxygen adsorbed on the photocatalyst. For photons with the energy lower

than the band gap energy of the photocatalyst, the absorption of these photons will only lead to the energy dissipation in the forms of the heat.(144) **Fig. 2.4** shows the schematic diagram of photocatalytic redox reaction. (144) The mechanism of the chain oxidative-reductive reactions occurring at the photoactivate surface of TiO₂ catalyst was illustrated as follows. (145)

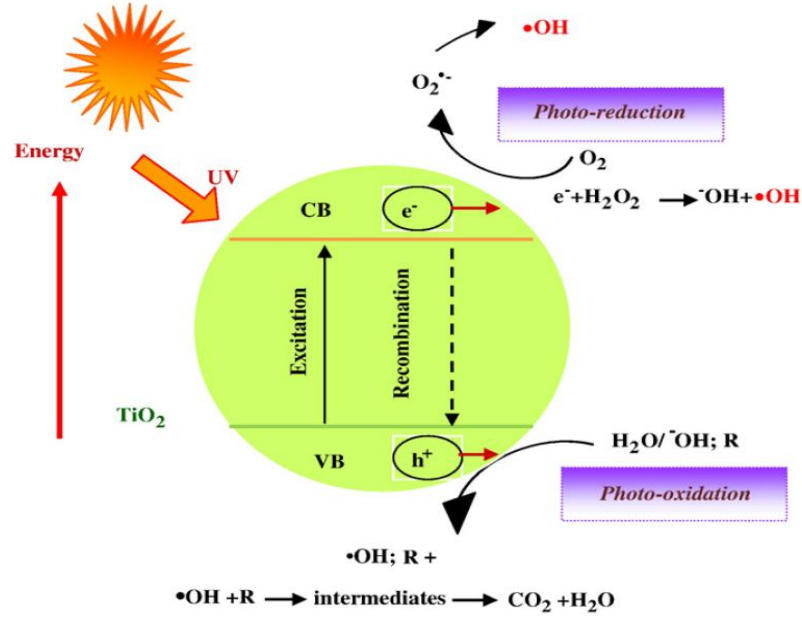
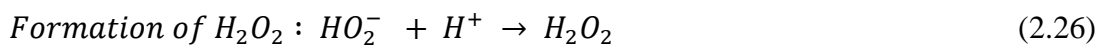
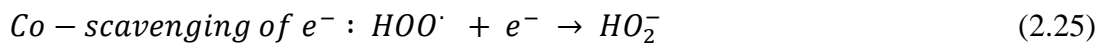
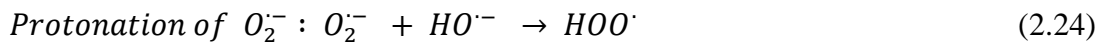
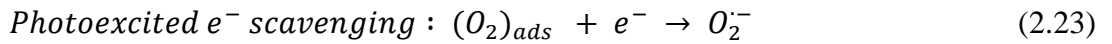
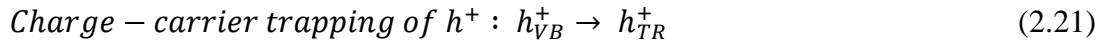
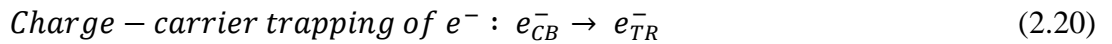
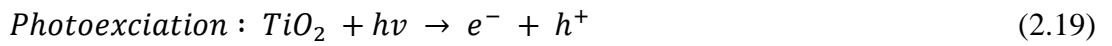
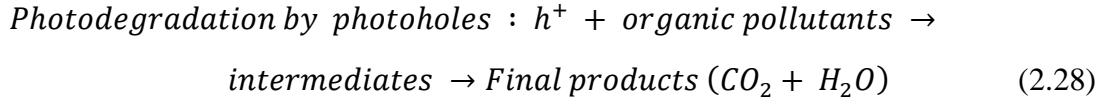
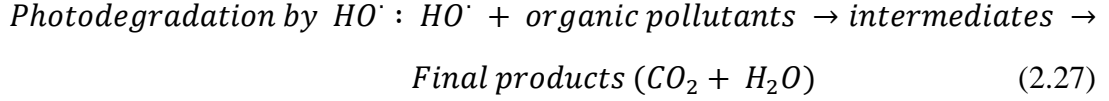


Figure 2.4. Schematic diagram of photocatalytic process (144).





Where e_{CB}^- and e_{TR}^- stands for the electrons in the conduction band and the valence band electrons which are trapped at the catalyst surface, respectively. h_{VB}^+ and h_{TR}^+ present the photo holes in valence band and surface trapped conduction band holes, respectively. Noted that in this chain oxidative-reductive reaction process, without the presence of electron scavengers, the photoexcited electron will instantly recombine with the valence band hole and dissipate in the form of heat and lose their reactivity.(144) Therefore, the participation of electron scavengers will significantly reduce the electron-hole recombination process and thus enhance the efficiency of photocatalysis. Researches have revealed that the presence of dissolved oxygen also has the capability of impeding the recombination of electron-hole pairs by production of a superoxide radical. (146, 147) Moreover, as shown in Eqs. 2.22-2.24, the produced superoxide radical will further react with a hydroxyl radical to be protonated to hydroperoxyl radical (HOO^\cdot) which is also reported to have strong electron scavenging ability.(148-150)

Dissolved oxygen and water molecules play significant roles for improving the degradation efficiency of photocatalysis by prolonging the electron-hole pair recombination process. And the photocatalytic activity is equally important for efficacy of toxic organic pollutants decomposition. With the observation of the above oxidative-reductive reactions occurring during the photocatalytic reactions, it was found that the catalytic activity of the photocatalysts depends on the following aspects: (1) trapping ability of the photons; (2) band gap energy; (3) generation of electron-hole pairs; and (4) ability of separation of electron-hole pairs with recombination.

Metal-based semiconductor materials such as metal oxides (151-153), metal sulfides (154-156) and noble metals(157) have been widely employed as the photocatalysts for degradation a variety of persistent organic pollutants (POPs) in aqueous solutions. Among these photocatalysts, extensive studies have been carried out on TiO_2 or TiO_2 based materials due to their low cost, excellent ability for photon absorption, desirable physical and chemical properties and structural flexibility to form a composite with other materials.(158-160) Rutile and anatase forms of TiO_2 have been widely investigated as photocatalysts and Degussa P-25 containing anatase and rutile phases in the ratio of 3:1 has been proven to obtain the highest catalytic activity among the TiO_2 materials. (161)

Recently, metal-free materials such as graphitic carbon nitride and graphene have been developed as promising alternatives to toxic or precious metals and their oxides. Studies have revealed that these metal-free photocatalysts demonstrate excellent degradation efficiency for decomposition of aqueous organic pollutants within contaminated water.(162-165) Because of its unique structure and outstanding electron transfer ability, graphene, carbon nanotube and reduced graphene oxide demonstrated exceptional photocatalytic activity in degradation of rhodamine B under visible light.(163) Carbon quantum dots (CQDs) is an effective photocatalyst under near-infrared-light (NIR) and showed selective oxidation capability of oxidizing benzyl alcohol to benzaldehyde. (164) Due to the stable structure and low cost, carbon nitride has aroused numerous research attention as a fascinating metal-free photocatalyst for treatment of toxic aqueous organic pollutants.(162) Nonporous and mesoporous graphitic carbon nitride were synthesized by Cui et al. from thermal-induced polymerization method. (166) It was found that only graphitic carbon nitride with mesoporous structure could effectively degradation phenol or 4-chlorophenol. At current stage, the photocatalytic activity of carbon nitride was limited due to its high excitation energy and the low charge mobility. However, by doping or integrating other semiconductor materials, its activity can be significantly improved.(167, 168)

It was reported that irradiation sources, and the activity of a catalyst, the categories of the pollutants, and the pH of the medium solution would work together affecting the photocatalytic degradation efficiency. Researches show that pH of the solution can significantly influence both the surface charge and ionization or speciation (pKa) of the organic pollutants. Therefore, solution pH plays a key role to affect adsorption and photocatalytic degradation of the pollutants. (169, 170) The following table summarizes the optimum pH values for photocatalytic degradation of phenol and its derivatives.

Table 2.2. Optimum pH values for photocatalytic degradation phenol and its derivatives. (144)

Pollutant	Light source	Photocatalyst	Optimum pH	Ref.
4-Nitrophenol	Solar	ZnO	6.0	(171)
Phenol	Solar	ZnO	5.0-7.0	(172)
4-Chlorophenol	UV	TiO ₂	5.0	(173)
2-Phenyl phenol	UV	ZnO	12.0	(174)
2-Chlorophenol	UV	Co-TiO ₂	9.0	(175)
4-Fluorophenol	UV	ZnO/TiO ₂	7.0	(176)
Phenol	UV	TiO ₂	5.0	(177)
m-Nitrophenol	UV	TiO ₂	8.9	(178)
4-Chlorophenol	UV	N-TiO ₂	3.0	(150)

2.5.4 Ozonation/catalytic ozonation

Ozone has been widely utilized for wastewater treatment in order to improve the odor, taste, color and to remove the organic compounds. As a powerful oxidizing agent with a redox potential of 2.08 V, ozone has demonstrated efficient oxidation and disinfection.(179) In addition, ozone also demonstrates its efficiency in inactivating microorganisms including viruses, bacteria and some forms of algae. And the inactivation ability of ozone to various microorganisms follows increasing order of cysts, viruses and bacteria.(180) In practice, ozone has been applied for treatment of effluent from various industries such as textile dye production, shale oil processing, pesticides and pharmaceutical production, municipal wastewater treatment and pulp

and paper production. (181-185)

Studies have demonstrated that there are two routes existing in the ozonation process, the direct molecular ozone reaction and indirect reaction involving decomposition of ozone molecules and generation of more powerful hydroxyl radicals for the oxidation. (15, 16) The following equations present the chain reactions of the ozone decomposition process. (15)



The decomposition of ozone in the indirect reaction follows the pseudo first-order kinetic law which is shown as follows. (186)

$$-\left(\frac{d[O_3]}{dt}\right)_{pH} = k'[O_3] \quad (2.34)$$

Where k' is the pseudo first-order reaction constant for a given pH value. From this pseudo first order kinetic law, it is observed that the solution pH value plays a crucial role to influence the decomposition of ozone by affecting the generation of hydroxyl radicals. Relevant studies suggest that ozone decomposition could be enhanced if the solution pH is basic. (15, 16) When $pH < 3$, decomposition of ozone will not be effective for formation of hydroxyl radicals and thus direct molecular ozone reaction occurs. For $7 < pH < 10$, the typical half-life time ozone is from 15 to 25 min. Within this pH range, combination of direct and indirect reaction happens. When solution pH is greater than 10, most of the molecular ozone will decompose and indirect reac-

tion will dominate the degradation process.

Although ozone is effective for degradation of multiple bonds such as C=C and C=N within the organic pollutants, the formed aldehydes and carboxylic acids cannot be further oxidized by ozone to achieve total mineralization. Moreover, ozone reacts rather slowly and selectively with some organic compounds such as inactivated aromatics. Additionally, the relatively low solubility and stability of ozone in water together with its high cost limit its wider application in wastewater treatment.

2.5.4.1 Catalytic ozonation process

As mentioned above, in ozonation process the degradation efficiency was significantly influenced by solution pH value and complete mineralization of the organic pollutants cannot be achieved. Recently, catalytic ozonation process has been proven to be an efficient strategy for removal of aqueous organic pollutants.(15, 16, 187) With a catalysts, controlled decomposition of ozone was achieved and the generated hydroxyl radicals are not only more powerful than molecular ozone, but also non-selective for degradation. In addition, in some recent studies, the synergistic effects of ozone together with UV or hydrogen peroxide have been investigated and the degradation efficiency was found to be enhanced. Generally, catalytic ozonation process can be classified into homogeneous catalytic ozonation and heterogeneous catalytic ozonation in accordance with the form of catalysts.

2.5.4.2 Homogeneous catalytic ozonation

Transition metal ions such as Mn(II), Fe(II), Fe(III), Co(II), Cu(II), Cd(II), Cr(III) and Zn(II) have demonstrated a high catalytic activity for homogeneous catalytic ozonation.(188-190) Table 2.3 lists several homogeneous catalysts employed for catalytic ozonation process and their corresponding organic pollutants studied.

Table 2.3. Homogeneous catalysts employed for catalytic ozonation process and their corresponding organic pollutants studied.

Catalyst	Organic compound	Ref.
Mn(II)	Carboxylic acid (oxalic, pyruvic, sulfosalicylic, propionic), dichlorophenol, dinitrotoluene	(188, 189, 191,
Mn(II), Fe(II), Fe(III), Cr(III)	Humic substances	(188)
Mn(II), Fe(III), Fe(II)	Chlorobenzenes	(189)
Mn(II), Fe(II)	Simazine	(193)
Co(II), Cu(II)	Oxalic acid, pyruvic acid	(194,
Ce(III)	Phenol	(196)
Ni(II), V(V), Mn(VI)	Dinitrobenzene	(197)
Mn(IV)	Propionic acid	(195)
Mn(II), Fe(II), Zn(II), Co(II), Ni(II)	Azo dyes	(190)

Although the detailed reaction mechanism of homogeneous catalytic ozonation is still unclear, the major steps involved in the homogeneous catalytic ozonation have been proposed. In the first place, ozone is decomposed by metal ions and thus leads to the formation of free radicals such as hydroxyl radicals and superoxide radicals. Then complexes will be formed between the metal ion catalyst and the organic pollutant molecules. In the final step, the generated free radicals attack the metal-organic complexes, and the organic pollutants will be subsequently oxidized to form innocuous carbon dioxide and water while the metal ion catalyst will be released from the complexes. (198, 199) Studies have revealed that the concentration of the metal ions as well as the pH of the solution would influence both the reaction mechanism and the degradation efficiency.(194, 200)

However, despite of its high efficiency in decomposition and mineralization, utilizing transition ions as homogeneous catalysts will result in many problems. These transition metals especially Co and Ce are high toxic for both human beings and the envi-

ronment. Cobalt has been recognized as a priority heavy metal pollutants which can cause several health problems such as pneumonia, asthma and other lung-related problems.(201) If these transition metal ions cannot be well recovered, the secondary pollutant will be caused. Therefore, in order to minimize the influence brought by transition metal ions, development of heterogeneous catalysts is in highly demand.

2.5.4.3 Heterogeneous catalytic ozonation

Compared with the transition metal ions as the catalysts for homogeneous catalytic ozonation, the catalysts used in the heterogeneous catalysis are in the solid phase. Metal oxides, supported metal oxides on minerals and metal-free materials have been employed as the heterogeneous catalysts. And Table 2.4 summarizes the variable heterogeneous catalysts and the studied organic pollutants.

Table 2.4. Heterogeneous catalysts and the studied organic pollutants.

Catalyst	Organic compound	Ref.
MnO ₂	Carboxylic acid, phenol	(200, 202-204)
Al ₂ O ₃	Carboxylic acid	(205)
TiO ₂	Oxalic acid, naproxen	(206, 207)
FeOOH	p-Chlorobenzoic acid	(208)
CeO ₂	Aniline, dyes	(204)
Co ₃ O ₄ /Al ₂ O ₃	Pyruvic acid	(209)
CuO/Al ₂ O ₃	Oxalic acid	(195)
NiO/Al ₂ O ₃	Oxalic acid	(210)
MnO _x /Al ₂ O ₃	Phenazone, ibuprofen, phenytoin, di-phenhydramine	(211)
Co/CeO, Mn/CeO	Phenolic wastewater	(212)
Activated carbon	Oxalic acid	(17)

Metal oxide catalysts are most widely employed for heterogeneous catalytic ozonation process due to their low-cost, availability and high catalytic activity.(16) Among

these metal oxide catalysts, MnO_2 has been reported to be the most efficient metal catalyst in decomposition.(213) And it is known that in aqueous solution, the decomposition of the ozone increase with the increase of the solution pH. In some researches, it was reported that the catalytic activity of MnO_2 increased with the decrease of pH, which could be ascribed to the combination effect of homogeneous and heterogeneous catalytic ozonation.(214) And the homogenous reaction occurs at low pH range will inevitably bring in metal leaching problem which is still a shortcoming that needed to be solved. In order to reduce the metal leaching problem, some matrix are designed to load these active metal oxides. In a recent work, supported cobalt oxide catalyst on alumina was synthesized and employed as the heterogeneous catalyst for catalytic ozonation of pyruvic acid at acidic pH.(209) Fig. 2.5 illustrates the mechanism of catalytic ozonation in presence of metal on supports. It was found that despite the fact that excellent catalytic efficiency was observed for catalytic degradation of pyruvic acid, some cobalt ions were still detected in the reaction solution. And metal leaching problem is inevitable for metal-based catalysts under acidic pH conditions. In order to avoid this problem, recently, some metal-free catalysts such as activated carbon and carbon nanotubes were utilized for catalytic ozonation.(17, 215) It was found that for these metal-free catalysts, the basic centers take the responsibility for decomposition of the ozone to produce active free radicals.

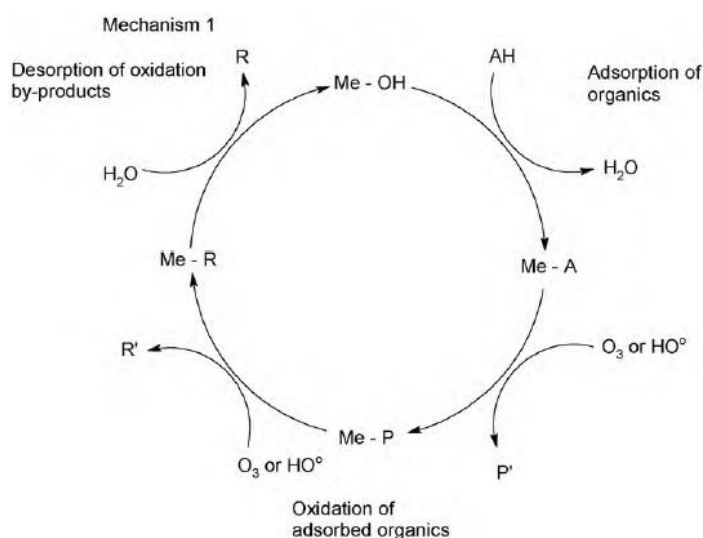


Figure 2.5. Mechanism of catalytic ozonation in the presence of metal on supports. (AH- organic acid; P, R - adsorbed primary and final by-products; P', R'- primary and final by-products in solution) (187)

Catalytic oxidation on these heterogeneous catalysts mainly arises from the catalytic decomposition of ozone and the enhanced formation of hydroxyl radicals. Literatures reveal that the catalytic activity is mainly affected by temperature and pH of the solution.(15, 16) The solubility and stability of ozone in water are influenced by solution temperature. The pH of the solution also has significant influence on the stability of ozone in water. It was found that the decomposition constant of ozone increases when solution pH value is increased. Additionally, pH of the reaction solution also has immense influence on the surface properties and the surface active sites of the catalysts. Kasprzyk et al., found that pH value has direct effect on the surface charge which would influence the adsorption capacity of the organic molecules on the catalyst's surface.(15)

Similar as homogeneous catalytic ozonation, the detailed reaction mechanisms for heterogeneous reaction still remain controversial and unclear. However, studies have agreed on the active sites for the decomposition of ozone. For metal oxides, ozone decomposition occurs on the Lewis center and/or the non-dissociated hydroxyl groups attached on the surface of metal oxides. (216, 217) For metal oxide loaded on the solid support, ozone decomposition takes place on oxidized/reduced form of the deposited metal. (194) For metal-free catalysts, as mentioned above, ozone decomposes on the basic centers of the catalysts. (17)

To sum up, for catalytic ozonation process, with the contribution of homogeneous/heterogeneous catalysts, the degradation efficiency of aqueous organic pollutants is significantly increased and therefore leading to the higher mineralization of these organic pollutants. In addition, the usage of ozone could be reduced compared with ozonation alone. However, for metal-based catalysts, leaching and fouling of the cat-

alysts surface might lead to the loss or deactivation of the active sites. While for metal-free catalysts, the stability for successive use still needs to improve. Therefore, more investigations have to perform to increase stability and durability of the catalysts.

2.5.5 Sulfate radical-based advanced oxidation processes

As mentioned above, in advanced oxidation process, Fenton/Fenton-like reactions and catalytic ozonation processes utilizing hydroxyl radicals demonstrate excellent degradation efficiency for removal of organic pollutants in contaminated water. However, the generation of the free radicals in these two processes usually requires acidic pH condition and thus leading to leaching problem to the metal-based homogeneous or heterogeneous catalysts. In the past decade, advanced oxidation processes employing sulfate radical have attracted worldwide attention. Sulfate radicals not only have a higher standard redox potential than hydroxyl radicals (3.1V vs. 2.7V), but also can be easily generated under neutral pH by the homogeneous or heterogeneous activation. (69, 113, 218) In addition, sulfate radicals are more selective for the oxidation reactions including electron-transfer process than hydroxyl radicals which can participate in various reactions with equal tendency.(219) Moreover, compared with other free radicals, sulfate radicals are more applicable for solutions containing carbonate or phosphate buffers. (220) Therefore, AOPs utilizing sulfate radicals demonstrate a higher efficiency than hydroxyl radicals in terms of both decomposition and mineralization of aqueous organic pollutants.

Sulfate radicals can be generated either from persulfate (PS) or peroxymonosulfate (PMS), which is the symmetrically substituted or mono-substituted derivative of hydrogen peroxide by sulfo moiety.(221) Persulfate ion ($S_2O_8^{2-}$) can be chemically or thermally activated by catalysts or external energy sources to produce sulfate radicals.(220) Moreover, due to its high stability in the subsurface, high aqueous solubility and excellent degradation efficiency at a relative low cost, AOPs utilizing persul-

fate oxidation have become one of the promising alternative for remediation of contaminated water. PMS is known for its commercial name of Oxone with the composition of $2\text{KHSO}_5 \cdot \text{KHSO}_4 \cdot \text{K}_2\text{SO}_4 \cdot \text{KHSO}_5$. In aqueous solution, the effective component within Oxone is the peroxymonosulfate ions which might directly result in the generation of sulfate radicals for organic compounds decomposition. Compared with the length of oxygen-oxygen bond inside the hydrogen peroxide (1.497 Å), the length of oxygen-oxygen bond within peroxymonosulfate ion is shorter (1.460 Å). Moreover, there is a hydrogen atom and SO_3 group on the left and right side of this oxygen-oxygen bond, respectively and thus favoring the formation of sulfate group during the activation process.(222) For both PS and PMS, although their active species $\text{S}_2\text{O}_8^{2-}$ and HSO_5^- have strong redox potentials (2.01V and 1.82V), direct reaction using PS or PMS alone for decomposition of pollutants are slow. However, by chemical or thermal activation, the produced sulfate radicals could rapidly and efficiently degrade various organic pollutants.

2.5.5.1 Energy induced sulfate radical oxidation

For PMS and PS, sulfate radicals can be generated by the external power source such as heat, ultraviolet irradiation and ultrasound. And Fig. 2.6 describes the sulfate radical formation process from PMS (1) and PS (2) under external energy source, respectively.

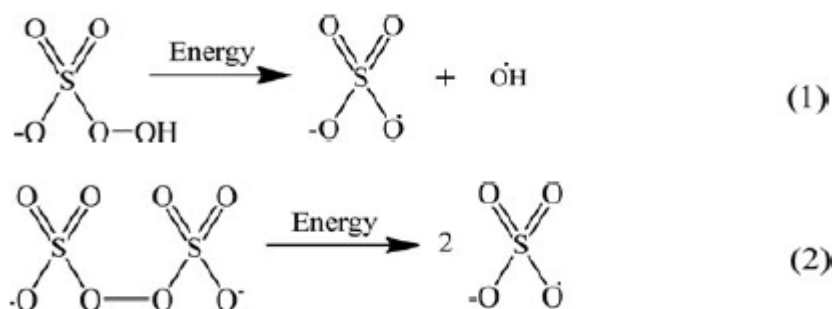


Figure 2.6. Formation of sulfate radicals under external energy source for PMS (1) and PS (2). (221)

Thermal activation of PMS and PS is widely used due to its low cost and simplicity to operate. When PS is employed as the oxidant, the activation energy required for thermally cracking the oxygen-oxygen bond of persulfate ion was reported to be 8.1 kJ/mol. (164) From this consideration, the operating temperature has to be elevated to a high level to ensure the energy is higher than the activation energy of the O-O bond breaking. Liang et al. employed direct PS oxidation of trichloroethylene (TCE) and 1,1,1-trichloroethane (TCA) within the aqueous solution. (223) It was found when reaction temperature was 20 °C, degradation efficiency for both TCE and TCA was insignificant. However, when temperature was increased to the range of 40-60 °C, excellent degradation efficiency of TCE and TCA was observed due to the thermal cracking of PS to produce active sulfate radicals.

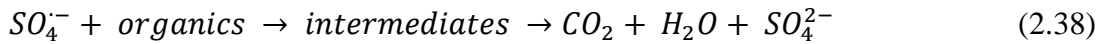
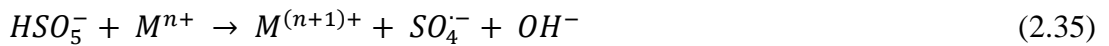
Apart from thermal activation, PMS and PS can be effectively activated under the light irradiation. In most cases, instead of visible light, UV or simulated solar light was utilized due to the higher energy which could successfully scissor the peroxy bond and oxygen-oxygen bond to produce active free radicals. (224-226) And due to the better absorbance of UV light, PS has been widely investigated as sulfate radicals precursor in the photochemical oxidation system. (227-229) Dionysiou et al. investigated the photo-oxidation efficiencies of PS, PMS and hydrogen peroxide under UV light for the degradation of 2,4-dichlorophenol (2,4-DCP). (220) It was found that the mineralization of the organic carbon of 2,4-DCP follows the order of UV/PS > UV/PMS > UV/H₂O₂.

In semiconductor mediated photocatalysis systems, PMS and PS can also act as the electron scavengers to increase the recombination time of electrons and holes and thus enhancing the quantum efficiency through scavenging electrons in conduction bands. Moreover, the generated highly active sulfate radicals can also participate in the degradation of the contaminants. (230, 231) Therefore, compared with normal photocatalysis, the participation of PMS or PS could enhance the decomposition efficiency of the contaminants by several folds.

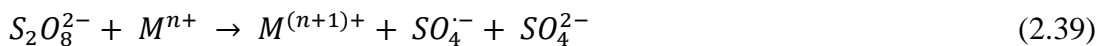
2.5.5.2 Homogeneous sulfate radical oxidation

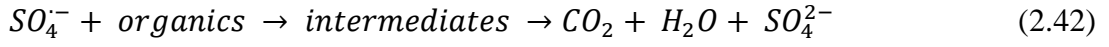
Although the energy induced sulfate radical-based oxidation processes demonstrate their superior efficiency for removal of aqueous organic contaminants, the requirement of large amount of energy results in complexity and high costs of these processes. Utilizing of homogeneous or heterogeneous catalysts can circumvent the requirement of energy and thus decreasing the complexity and the cost of the process.

Like Fenton reaction, transition metal ions are the mostly used homogeneous catalysts for activating PMS or PS to generate active free radicals. Dionysiou et al. studied the homogeneous activation of PMS for 2,4-dichlorophenol degradation by utilizing Co^{2+} , Ni^{2+} , Fe^{2+} , Fe^{3+} , Mn^{2+} , Ru^{3+} , Ag^+ and Ce^{3+} as catalysts. (219) According to their investigation, Co^{2+} showed the highest catalytic activity for homogeneous activation of peroxymonosulfate to generate free radicals. It was also found that, when reacting with PMS, Mn^{2+} , Ce^{3+} and Ni^{2+} could form caged or bounded metal sulfate radicals, while metal ions such as Co^{2+} , Ru^{3+} and Fe^{2+} can produce freely diffusible sulfate radicals. Reaction mechanisms for homogeneous catalytic activation of PMS can be proposed as shown below. (221)



And the generation routes of sulfate radicals by employing homogeneous activation of persulfate are shown below. (221)

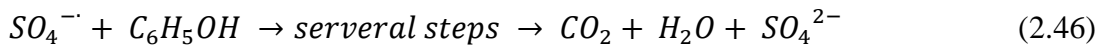
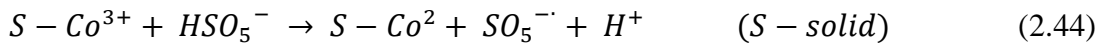
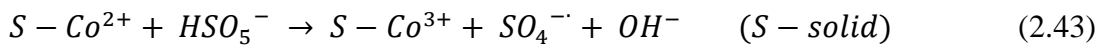




However, the employment of transition metal ions as homogeneous catalysts can result in metal leaching and increased cost for further treatment. In addition, as mentioned before, heavy metal ions such as cobalt ion is toxic and can lead to various lung-related health problem to human beings.

2.5.5.3 Heterogeneous sulfate radical oxidation

In order to minimize the metal leaching problem and the corresponding secondary pollution, heterogeneous catalysts have attracted intensive attention for activation of PMS or PS to produce sulfate radicals due to their high stability and durability, cost-effectiveness and recoverability. Recent years, fruitful researches have been performed on heterogeneous Co/PMS system for organic contaminants degradation in waste water treatment. Various cobalt-based materials such as Co oxides (232), supported Co (27, 233-236), Co-exchanged zeolites (237) and CoFe₂O₄ (238) have been synthesized and employed as heterogeneous catalysts for activation of PMS. The PMS activation mechanisms for cobalt based materials are shown as below. (41)



Nevertheless, neither homogeneous Co²⁺/PMS nor heterogeneous catalysis utilizing supported cobalt oxides can completely avoid the leaching or loss of toxic cobalt ions,

thus resulting in secondary metal pollution (26, 29) Therefore, searching for low toxic heterogeneous solid catalyst for efficient activating PMS is in highly demand.

Manganese oxides are abundant in soils and have various forms such as MnO, MnO₂, Mn₂O₃ and Mn₃O₄. Manganese ions have a low toxicity to the environment compared with cobalt ions. Based on these features, manganese oxides have been reported as promising alternatives to Co systems for PMS activation to produce reactive species. (105, 239, 240) In the recent researches, manganese oxides with various shapes, dimensions(113, 218) and oxidation states (28, 31, 105, 240) have been synthesized and applied for activation of PMS for aqueous phenolic pollutant degradation. The following figure shows the mechanism for PMS activation for phenol degradation on 1D MnO₂ nanowires.

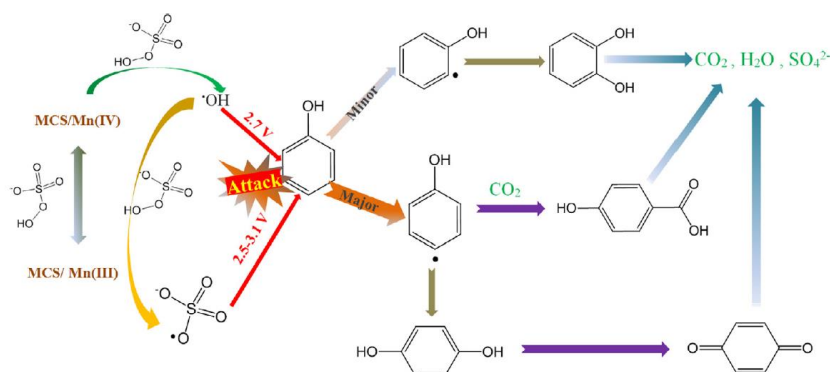


Figure 2.7. Mechanism for PMS activation for phenol degradation on 1D MnO₂ nanowires.(113)

It was found that, when PMS was activated, both hydroxyl radicals and sulfate radicals were generated for decomposition of organic contaminants. Moreover, when phenol was utilized as the target pollutant, its para- and meta- positions are more vulnerable to be attacked. (113, 218)

Apart from manganese catalysts, novel metal-free catalysts such as reduced graphene oxide (rGO) and carbon nanotubes (CNT) have been discovered to be catalytic active for activation of PMS or PS for degradation of aqueous organic pollutants. (29, 44,

69) And the sp^2 hybrid carbon, the surface functional groups as well as the defects are considered to be the active sites for PMS/PS activation.

To conclude, sulfate radicals which could be generated from PMS or PS by external energy sources or catalysis have been proven to be effective for degradation of various organic pollutants. Compared with Fenton reactions and catalytic ozonation process, utilizing sulfate radicals for decomposition of contaminants demonstrates a higher efficiency due to the higher redox potential of the sulfate radicals. Moreover, the employment of catalytic sulfate radical process is less complicated and cost-intensive due to the neutral pH requirement and less dependent on external power sources. Therefore, utilizing sulfate radicals for destruction of aqueous organic pollutants has become a promising remediation technology in terms of AOPs.

2.5.6 Other advanced oxidation processes

Apart from Fenton reactions, catalytic ozonation, photocatalysis and sulfate radicals oxidation, there are some other AOPs having demonstrated their efficiencies for degradation of aqueous organic pollutants. Electro-chemical treatment is the process utilizing direct or indirect anodic reaction to generate hydroxyl radicals and/or hydrogen peroxide from water molecules for the oxidation of aqueous organic pollutants.(241) For non-thermal plasma process, collision of charged particles and excitation-ionization of neutral molecules are initiated by the electric discharge in water.(242) And the generated non-thermal plasma containing reactive electrons and radicals is responsible for the destruction of organic pollutants in water. Another process is γ -ray and electron beam irradiation. In this process, water is radiolysis by ionizing radiation such as radioactive γ -source (^{60}Co) and particle accelerators to produce active radical species for decomposition of aqueous contaminants. (243)

2.6 Development of heterogeneous catalysts for peroxymonosulfate activation

Utilizing sulfate radicals for destruction of aqueous organic pollutants has become a promising remediation technology owing to the high degradation efficiency, complete mineralization and simple reaction conditions. Although homogeneous activation of sulfate radicals obtains excellent degradation efficiency, the leaching of the transition metal ions leads to the requirement of further treatment to avoid the secondary pollution of the toxic heavy metal ions. While heterogeneously activated sulfate radicals for oxidation reactions not only circumvent this problem but also achieve similar decomposition efficiency of the organic pollutants. Various types of heterogeneous catalysts have been developed for the activation of PMS or PS to produce these highly reactive sulfate radicals for organic pollutant decomposition. (41, 44, 105, 201, 218, 244) And these catalysts can be classified into two streams: metal-based catalysts by employing transition metal oxides and metal-free catalysts by utilizing some carbonaceous materials.

2.6.1 Metal-based heterogeneous catalysts

Although homogeneous Co^{2+} /PMS system was revealed to be the most efficient for the generation of sulfate radicals for mineralization of organic pollutants (219, 220), if the reaction solution is not well treated the dissolved cobalt ions can be harmful to both aquatic life and human beings. (29) In order to overcome this disadvantage, heterogeneous Co/PMS system was then developed. (245, 246) Anipsitakis et al. found that Co_3O_4 possessed excellent ability to activate PMS to produce sulfate radicals for 2,4-dichlorophenol decomposition. (246) And the catalytic activity of Co_3O_4 mainly arises from its large surface area and narrow particle size distribution. In another study, nano- Co_3O_4 particles were prepared and employed for activation PMS for Acid Orange 7 (AO7) degradation. (245) It was found that these nano- Co_3O_4 particles

possessed good catalytic activity at neutral pH value and AO7 was completely decomposed. Nevertheless, leaching of cobalt ions was still observed. In order to minimize the cobalt ion leaching, supported Co catalysts including Co/SBA-15 (201), Co/activated carbon (236), Co/TiO₂ (247), Co/SiO₂ (247), Co/zeolites (237) and Co/MgO (235) have been reported to be highly active for PMS activation. However, leaching of toxic cobalt ions cannot be completely avoided by using supported cobalt catalysts.

Manganese oxides abundantly exist in the environment and manganese ions have much lower toxicity than cobalt ions. Manganese-based materials are regarded as the promising alternatives to cobalt based catalysts due to the unique redox cycles between Mn²⁺ and Mn⁴⁺. These redox cycles enable manganese-based materials to obtain excellent oxygen mobility in the oxide lattice and thus could induce high efficiency in redox reactions.(240) Many types of manganese oxides have been synthesized and used for activation of PMS for removal of contaminants. It was found that the crystalline phase of the manganese oxides has a critical effect on the catalyst activity.(239) Saputra et al. prepared MnO₂ in α , β and γ phases in the morphologies of nanowires, nanorods and nanofibers, respectively, and their catalytic activities in PMS activation were examined for degradation of phenol.(248) It was suggested α -MnO₂ showed the highest activity. The effects of oxidation states of manganese on activation of PMS were also investigated by employing a series of MnO_x (MnO, MnO₂, Mn₂O₃ and Mn₃O₄). It was found that the activity follows an order of Mn₂O₃ > MnO > Mn₃O₄ > MnO₂.(31) Furthermore, the effect of the exposed facets were studied by the synthesis of various shape-controlled manganese oxide catalysts.(249) Mn₂O₃ in the shapes of cube, octahedra and truncated octahedra were synthesized and their catalytic activity for producing sulfate radicals were examined by activation of PMS for phenol decomposition. It was found that these Mn₂O₃ in various shapes showed different activities in phenol degradation and the cubic Mn₂O₃ demonstrated the highest catalytic activity in phenol oxidation.(240)

In recent years, dimensionally controlled catalysts have attracted numerous research interests due to their special structures and unique physical and chemical properties. Some manganese-based catalysts in various dimensions have also been developed. Wang et al. synthesized 1D α -MnO₂ nanorods, nanotubes and nanowires via a facile one-pot hydrothermal process without addition of any surfactant.(113) The synthesized materials were utilized for activation of PMS to generate sulfate radicals for phenol degradation. It was found that 1D α -MnO₂ nanowires obtained the highest catalytic activity due to the exposure of the crystal facet with a higher energy. Application of hierarchical materials in heterogeneous catalysis is promising due to the ease of separation of bulk materials and the high performance of the nanostructure. Recently, some hierarchical 3D structured manganese oxides have been successfully synthesized. Yu et al. employed a novel hydrothermal method using MnSO₄ and K₂S₂O₈ as precursors to synthesize 3D sea-urchin like and 3D clew-like MnO₂ and tested their performance as electrochemical supercapacitors.(250) Duan et al. synthesized 3D nanocube-like MnO₂ by using KMnO₄, Mn(AC)₂·4H₂O and glucose as precursors and polyvinylpyrrolidone (PVP) as a surfactant.(251) For sulfate radicals generation using 3D hierarchical structure MnO₂ as catalysts, Wang et al. prepared 3D hierarchical structure MnO₂ in corolla and sea-urchin shapes via a facile hydrothermal method.(218) The prepared catalysts showed outstanding catalytic activity in activation of PMS for degradation of phenol solutions and remarkable stability for repeating uses.

Apart from cobalt and manganese-based catalysts, zero valent iron (ZVI) has been widely utilized as an efficient catalyst to generate free radicals for the removal of a large variety of pollutants such as chlorinated hydrocarbons, nitrobenzenes, chlorinated phenols, polychlorinated biphenyls (PCBs), heavy metals, and various anions due to the low cost and strong redox potentials.(252, 253) Recently, because of its large specific surface area and high surface activity, nanoscale ZVI has received more research attention than conventional ZVI.(254) Ghanbari et al. utilized ZVI for activation PMS to produce sulfate radicals for the decolorization of various textile

wastewater and compared its degradation efficiency with ZVI/H₂O₂ system.(255) It was found that compared with ZVI/H₂O₂ system, ZVI/PMS possessed a higher efficiency for both dye degradation and COD removal. Moreover, ZVI presented the highest catalytic activity when the solution pH = 4. Xiong et al. employed Fe⁰ for activation of sodium persulfate for degradation of various aqueous organic pollutants under weak magnetic field.(256) It was found that sodium persulfate could be efficiently activated by Fe⁰ under neutral pH value to produce sulfate radicals and thus provided an ecofriendly route for degradation of aqueous organic pollutants.

However, despite of the high activity in reduction reactions, nano-Fe⁰ suffers from poor stability in air due to its high surface energy.(20, 257) Studies revealed that nano-Fe⁰ can be encapsulated into porous carbon spheres for enhancement of transportation and suspension and therefore to improve its stability.(258) Sun et al. synthesized carbon microsphere encapsulated nano-Fe⁰ catalyst for activation of PMS for phenol degradation.(259) Compared with bare Fe⁰ catalysts, the as-synthesized material showed much better catalytic stability without significantly sacrificing activity. Because of strong dipole-dipole attraction and high surface area to volume ratio, nano-Fe⁰ particles also favor strong inter-particle aggregation which leads to the reduction of their surface area and hiding their active sites.(260) In order to prevent the strong aggregation, different types of supporting materials have been employed including activated carbon (261), bentonite (262), alumina (263) and polystyrene resin (264) for the better distribution under aqueous solution. And a liquid-phase reduction method as most widely applied for preparation of supported nano-Fe⁰ composites.(261-263) Nevertheless, the preparation processes of supported nano-Fe⁰ composites are complex and cost-intensive due to the vacuum operation, production of massive volume of hydrogen and high cost of borohydride. Wang et al. recently found a novel and facile way for synthesizing supported nano-Fe⁰ composites by using g-C₃N₄ as the supporting materials.(244) The as-prepared material presented excellent distribution ability in aqueous solution and superior catalytic activity to activate PMS for degradation of phenol solution.

Another concern for metal-based catalysts is their recyclability. Though metal leaching problem can be minimized in heterogeneous forms, these heterogeneous catalysts would still result in secondary pollution if not well recycled. The development of magnetic catalysts can well circumvent this problem since the catalysts remained in the reaction solution can be easily separated under magnetic field. Moreover, compared with vacuum separation or sedimentation processes, magnetic separation process is more efficient, less complicated and requires less energy input. In the past decades, utilizing magnetite nanoparticles (Fe_3O_4 NPs) as magnetic separating materials has attracted great research interests because of their morphology-dependent physical and chemical properties, biocompatibility and excellent magnetic properties. (34, 36, 37, 265). However, similar as nano- Fe^0 , significant inter-particle agglomeration limits the wider application of pure Fe_3O_4 NPs.(266) In order to reduce the agglomeration, recently, Yao et al. had applied graphene as a supporting material to prepare magnetic Fe_3O_4 adsorbents or catalysts.(267, 268) Furthermore, core/shell structured Fe_3O_4 /carbon spheres have attracted research attention owing to their unique magnetic response, low cytotoxicity and highly functional surface.(39, 40) Wang et al. synthesized magnetic separable Fe_3O_4 /carbon spheres loaded with cobalt and manganese oxides for activation of PMS for phenol degradation.(41) The as-prepared materials were dispersed well in aqueous solution and showed remarkable catalytic activity for generation of sulfate radicals. Apart from Fe_3O_4 NPs and their composites, ZnFe_2O_4 nanoparticles have been proposed as a promising alternative owing to their superior dispersion and excellent stability in water and atmosphere. (269, 270) Compared with other magnetic materials, ZnFe_2O_4 possesses advantages of high stability under humid air, easy synthesis and low cost.(271, 272) ZnFe_2O_4 also shows better dispersion and less dipole-dipole attraction than iron based magnetic materials.(270) By utilizing these advantages, Wang et al. prepared MnO_2 / ZnFe_2O_4 hierarchical structured micro composites and tested their activity for PMS activation to produce sulfate radicals.(273) Moreover, ZnFe_2O_4 nanoparticles have successfully demonstrated their extensive applications in photocatalysis,(274) adsorption(275) and solar cells.(276, 277)

2.6.2 Metal-free heterogeneous catalysts

Although metal-ion leaching problem can be controlled by using various types of heterogeneous catalysts including low toxic metal-based catalysts, supported metal oxide catalysts and magnetic separable catalysts, leaching is still inevitable. In order to completely circumvent metal ion leaching, the development of novel metal-free catalysts with high catalytic activity is in highly demand. Recently, nanocarbon materials including graphene, graphene oxide/reduced graphene oxide and carbon nanotubes (CNTs) have attracted worldwide attention due to their large theoretical surface area, unique electronic property, outstanding thermal conductivity and sp^2 hybridized carbon configuration.(278-280) Various studies have revealed that these nanocarbon materials have promising catalytic activity for energy and environmental applications.(42, 43)

In a pioneering study, Sun et al. found that reduced graphene oxide could activate PMS to produce sulfate radicals for decomposition of various aqueous organic pollutants such as phenol, chlorophenol and dye.(30) Compared with conventional carbon materials such as activated carbon, this novel nanocarbon presented much better catalytic activity owing to the unique zigzag edges, structural defects and the oxygen containing groups on the graphene surface with rich electrons. From then on, the door to the nanocarbon catalysis for sulfate radical generation has been opened and various types of nanocarbon catalysts have been developed and utilized for activation of PMS for aqueous organic pollutants degradation. Fullerene, graphene oxide, graphene nanoplates, single-wall carbon nanotubes (SWCNTs) and multi-wall carbon nanotubes (MWCNTs) have been demonstrated to be catalytically active for PMS activation.(29, 30, 44-46) To enhance the catalytic activity, some structure modified reduced graphene oxides were prepared by chemical or physical activation to increase the specific surface area (SSA).(281, 282) These activated rGOs were utilized for adsorption and catalytic oxidation of methylene blue. It was found that the oxygen containing groups and the specific surface area have significant effects on both

adsorption and catalytic activity. Furthermore, heteroatoms such as boron, nitrogen, and phosphate were also introduced to rGO and SWCNTs structure to improve their catalytic activities.(29, 45, 69) Studies demonstrated that nitrogen doping can immensely improve the catalytic efficiency for PMS activation to produce free radicals for aqueous organic pollutants degradation. (29)

2.7 Conclusions

Due to the rapid development in industrialization and urbanization, increasing amount of aqueous organic contaminants have been discharged from refinery processes and households to the freshwater system and resulting in detrimental effects to both the environment and human beings. Among these organic pollutants, phenol and its derivatives, which are used as raw materials in chemical, petrochemical and pharmaceutical industries, have attracted intensive attention because of their toxicity and refractory to natural degradation. In order to degrade these pollutants, various wastewater treatment technologies such as adsorption, wet air oxidation and chemical oxidation have been developed. However, these processes suffer from low degradation efficiency and post-treatment is required. Advanced oxidation processes (AOPs) have been proven to be most effective among the available environmental remediation technologies. Compared with conventional technologies, AOPs have much better degradation efficiency and complete mineralization without producing toxic byproducts. Fenton reactions demonstrate their high efficiency in degradation of aqueous organic pollutants by utilizing hydroxyl radicals generated from hydrogen peroxide using homo/heterogeneous catalysts. Though homogeneous Fenton reactions may result in problems such as metal leaching, production of sludge, low pH

requirement, the development of Fenton-like reactions utilizing other activation sources circumvents these disadvantages. Photocatalytic process has demonstrated its efficiency as the promising alternatives to Fenton/Fenton-like processes due to its discharging of “zero” waste and cost-effectiveness. And various types of catalysts have been developed to further improve the degradation efficiency. Catalytic ozonation process has demonstrated to be an efficient strategy for aqueous organic pollutant removal. Compared with traditional ozonation process, the organic pollutants can be effectively and completely mineralized owing to the contribution of catalysts. Recently, advanced oxidation process by utilizing sulfate radicals has attracted research attentions. Sulfate radicals not only possesses a higher standard redox potential than hydroxyl radicals (3.1V vs. 2.7V), but also can be easily generated under neutral pH. Development of heterogeneous catalysts with a high catalytic activity for AOPs is quite promising. Various types of metal-based and metal-free catalysts have been synthesized and tested for their catalytic activities in different AOPs. It has been found that compared with cobalt-based catalysts, manganese-based catalysts show similar catalytic activity but much lower toxicity and obtain promising potentials in advanced oxidation processes. On the other hand, proper recycle of the used catalysts becomes another important concern for the consideration of the catalysts’ regeneration and the prevention of the secondary contaminant. Magnetic separable catalysts provide a feasible solution for the ease of the separation as well as minimizing the secondary pollution by integrating the catalytic active metal oxides with the magnetic materials such as Fe_3O_4 and ZnFe_2O_4 .

References

1. Bolong N, Ismail A, Salim MR, Matsuura T. A review of the effects of emerging contaminants in wastewater and options for their removal. *Desalination*. 2009;239(1):229-46.
2. Heng S, Yeung KL, Julbe A, Ayril A, Schrotter J-C. Preparation of composite zeolite membrane separator/contactor for ozone water treatment. *Microporous Mesoporous Mater*. 2008;115(1–2):137-46.
3. Matheswaran M, Moon IS. Influence parameters in the ozonation of phenol wastewater treatment using bubble column reactor under continuous circulation. *J. Ind. Eng. Chem*. 2009;15(3):287-92.
4. Bokare AD, Choi W. Review of iron-free Fenton-like systems for activating H₂O₂ in advanced oxidation processes. *J. Hazard. Mater*. 2014;275(0):121-35.
5. Chan YJ, Chong MF, Law CL, Hassell D. A review on anaerobic–aerobic treatment of industrial and municipal wastewater. *Chem. Eng. J*. 2009;155(1):1-18.
6. Arslan-Alaton I, Ferry JL. Application of polyoxotungstates as environmental catalysts: wet air oxidation of acid dye Orange II. *Dyes Pigm*. 2002;54(1):25-36.
7. Dietrich MJ, Randall TL, Canney PJ. Wet air oxidation of hazardous organics in wastewater. *Environ. Prog*. 1985;4(3):171–7.
8. Tyagi V, Lo S-L. Application of physico-chemical pretreatment methods to enhance the sludge disintegration and subsequent anaerobic digestion: an up to date review. *Rev Environ Sci Biotechnol*. 2011;10(3):215-42.
9. Tušar NN, Maučec D, Rangus M, Arčon I, Mazaj M, Cotman M, et al. Manganese Functionalized Silicate Nanoparticles as a Fenton-Type Catalyst for Water Purification by Advanced Oxidation Processes (AOP). *Adv. Funct. Mater*. 2012;22(4):820-6.
10. Wang S. A Comparative study of Fenton and Fenton-like reaction kinetics in decolourisation of wastewater. *Dyes Pigm*. 2008;76(3):714-20.
11. Watts R, Sarasa J, Loge F, Teel A. Oxidative and Reductive Pathways in Manganese-Catalyzed Fenton's Reactions. *J. Environ. Eng*. 2005;131(1):158-64.
12. Hartmann M, Kullmann S, Keller H. Wastewater treatment with heterogeneous Fenton-type catalysts based on porous materials. *J. Mater. Chem*. 2010;20(41):9002-17.
13. Kuo WG. Decolorizing dye wastewater with Fenton's reagent. *Water Res*.

1992;26(7):881-6.

14. Hu L, Yang X, Dang S. An easily recyclable Co/SBA-15 catalyst: Heterogeneous activation of peroxymonosulfate for the degradation of phenol in water. *Appl. Catal., B.* 2011;102(1–2):19-26.

15. Kasprzyk-Hordern B, Ziólek M, Nawrocki J. Catalytic ozonation and methods of enhancing molecular ozone reactions in water treatment. *Appl. Catal., B.* 2003;46(4):639-69.

16. Nawrocki J, Kasprzyk-Hordern B. The efficiency and mechanisms of catalytic ozonation. *Applied Catalysis B: Environmental.* 2010;99(1–2):27-42.

17. Cao H, Xing L, Wu G, Xie Y, Shi S, Zhang Y, et al. Promoting effect of nitration modification on activated carbon in the catalytic ozonation of oxalic acid. *Appl. Catal., B.* 2014;146(0):169-76.

18. Ma J, Sui M, Zhang T, Guan C. Effect of pH on MnO_x/GAC catalyzed ozonation for degradation of nitrobenzene. *Water Res.* 2005;39(5):779-86.

19. Anipsitakis GP, Dionysiou DD. Degradation of Organic Contaminants in Water with Sulfate Radicals Generated by the Conjunction of Peroxymonosulfate with Cobalt. *Environmental Science & Technology.* 2003;37(20):4790-7.

20. Rastogi A, Al-Abed SR, Dionysiou DD. Sulfate radical-based ferrous–peroxymonosulfate oxidative system for PCBs degradation in aqueous and sediment systems. *Appl. Catal., B.* 2009;85(3–4):171-9.

21. Anipsitakis GP, Dionysiou DD, Gonzalez MA. Cobalt-Mediated Activation of Peroxymonosulfate and Sulfate Radical Attack on Phenolic Compounds. Implications of Chloride Ions. *Environ. Sci. Technol.* 2005;40(3):1000-7.

22. Tsitonaki A, Petri B, Crimi M, Mosbæk H, Siegrist RL, Bjerg PL. In Situ Chemical Oxidation of Contaminated Soil and Groundwater Using Persulfate: A Review. *Crit. Rev. Env. Sci. Technol.* 2010;40(1):55-91.

23. Yao Y, Xu C, Yu S, Zhang D, Wang S. Facile Synthesis of Mn₃O₄–Reduced Graphene Oxide Hybrids for Catalytic Decomposition of Aqueous Organics. *Ind. Eng. Chem. Res.* 2013;52(10):3637-45.

24. Zhou G, Sun H, Wang S, Ming Ang H, Tade MO. Titanate supported cobalt catalysts for photochemical oxidation of phenol under visible light irradiations. *Sep. Purif. Technol.* 2011;80(3):626-34.

25. Tan C, Gao N, Deng Y, An N, Deng J. Heat-activated persulfate oxidation of diuron in water. *Chem. Eng. J.* 2012;203(0):294-300.

26. Liang H, Sun H, Patel A, Shukla P, Zhu ZH, Wang S. Excellent performance of mesoporous $\text{Co}_3\text{O}_4/\text{MnO}_2$ nanoparticles in heterogeneous activation of peroxymonosulfate for phenol degradation in aqueous solutions. *Appl. Catal., B.* 2012;127(0):330-5.
27. Shukla P, Sun H, Wang S, Ang HM, Tadé MO. Nanosized $\text{Co}_3\text{O}_4/\text{SiO}_2$ for heterogeneous oxidation of phenolic contaminants in waste water. *Sep. Purif. Technol.* 2011;77(2):230-6.
28. Saputra E, Muhammad S, Sun H, Ang H-M, Tadé MO, Wang S. A comparative study of spinel structured Mn_3O_4 , Co_3O_4 and Fe_3O_4 nanoparticles in catalytic oxidation of phenolic contaminants in aqueous solutions. *J. Colloid Interface Sci.* 2013;407(0):467-73.
29. Sun H, Wang Y, Liu S, Ge L, Wang L, Zhu Z, et al. Facile synthesis of nitrogen doped reduced graphene oxide as a superior metal-free catalyst for oxidation. *Chemical Communications.* 2013;49(85):9914-6.
30. Sun H, Liu S, Zhou G, Ang HM, Tadé MO, Wang S. Reduced Graphene Oxide for Catalytic Oxidation of Aqueous Organic Pollutants. *ACS Appl. Mater. Interfaces.* 2012;4(10):5466-71.
31. Saputra E, Muhammad S, Sun H, Ang H-M, Tadé MO, Wang S. Manganese oxides at different oxidation states for heterogeneous activation of peroxymonosulfate for phenol degradation in aqueous solutions. *Appl. Catal., B.* 2013;142–143(0):729-35.
32. Yao Y, Miao S, Yu S, Ma L, Sun H, Wang S. Fabrication of $\text{Fe}_3\text{O}_4/\text{SiO}_2$ core/shell nanoparticles attached to graphene oxide and its use as an adsorbent. *J. Colloid Interface Sci.* 2012;379:20-6.
33. Yao Y, Yang Z, Sun H, Wang S. Hydrothermal Synthesis of Co_3O_4 -Graphene for Heterogeneous Activation of Peroxymonosulfate for Decomposition of Phenol. *Ind. Eng. Chem. Res.* 2012;51(46):14958-65.
34. Gong JL, Wang B, Zeng GM, Yang CP, Niu CG, Niu QY, et al. Removal of cationic dyes from aqueous solution using magnetic multi-wall carbon nanotube nanocomposite as adsorbent. *J. Hazard. Mater.* 2009;164(2–3):1517-22.
35. Zhang P, Zhan Y, Cai B, Hao C, Wang J, Liu C, et al. Shape-controlled synthesis of Mn_3O_4 nanocrystals and their catalysis of the degradation of methylene blue. *Nano Res.* 2010;3(4):235-43.
36. Kaminski MD, Nuñez L. Extractant-coated magnetic particles for cobalt and nickel recovery from acidic solution. *J. Magn. Mater.* 1999;194(1–3):31-6.
37. Chen C, Hu J, Shao D, Li J, Wang X. Adsorption behavior of multiwall carbon

nanotube/iron oxide magnetic composites for Ni(II) and Sr(II). *Journal of Hazardous Materials*. 2009;164(2–3):923-8.

38. Yao Y, Miao S, Liu S, Ma L, Sun H, Wang S. Synthesis, characterization, and adsorption properties of magnetic Fe₃O₄@graphene nanocomposite. *Chem. Eng. J.* 2012;184:326-32.

39. Lu Z, Dai J, Song X, Wang G, Yang W. Facile synthesis of Fe₃O₄/SiO₂ composite nanoparticles from primary silica particles. *Colloids Surf., A.* 2008;317(1–3):450-6.

40. Cheng Y, Tan R, Wang W, Guo Y, Cui P, Song W. Controllable synthesis and magnetic properties of Fe₃O₄ and Fe₃O₄@SiO₂ microspheres. *J Mater Sci.* 2010;45(19):5347-52.

41. Wang Y, Sun H, Ang HM, Tadé MO, Wang S. Magnetic Fe₃O₄/carbon sphere/cobalt composites for catalytic oxidation of phenol solutions with sulfate radicals. *Chem. Eng. J.* 2014;245(0):1-9.

42. Su DS, Perathoner S, Centi G. Nanocarbons for the development of advanced catalysts. *Chem. Rev.* 2013;113(8):5782-816.

43. Lai L, Potts JR, Zhan D, Wang L, Poh CK, Tang C, et al. Exploration of the active center structure of nitrogen-doped graphene-based catalysts for oxygen reduction reaction. *Energy Environ. Sci.* 2012;5(7):7936-42.

44. Duan X, Ao Z, Sun H, Indrawirawan S, Wang Y, Jian K, et al. Nitrogen-Doped Graphene for Generation and Evolution of Reactive Radicals by Metal-Free Catalysis. *ACS Appl. Mater. Interfaces.* 2015;7(7):4169-78.

45. Duan X, Indrawirawan S, Sun H, Wang S. Effects of nitrogen-, boron-, and phosphorus-doping or codoping on metal-free graphene catalysis. *Catal. Today.* 2015;249(0):184-91.

46. Indrawirawan S, Sun H, Duan X, Wang S. Nanocarbons in different structural dimensions (0–3D) for phenol adsorption and metal-free catalytic oxidation. *Appl. Catal., B.* 2015;179(0):352-62.

47. Wang S, Peng Y. Natural zeolites as effective adsorbents in water and wastewater treatment. *Chem. Eng. J.* 2010;156(1):11–24.

48. Dias JM, Alvim-Ferraz MCM, Almeida MF, Rivera-Utrilla J, Sánchez-Polo M. Waste materials for activated carbon preparation and its use in aqueous-phase treatment: A review. *J. Environ. Manage.* 2007;85(4):833-46.

49. Pollard SJT, Fowler GD, Sollars CJ, Perry R. Low-cost adsorbents for waste and wastewater treatment: a review. *Sci. Total Environ.* 1992;116(1–2):31-52.

50. Aguiar Mrd, Novaes AC, Guarino AWS. Remoção de metais pesados de efluentes industriais por aluminossilicatos. *Quim. Nova.* 2002;25:1145-54.
51. Crini G. Non-conventional low-cost adsorbents for dye removal: a review. *Bioresour. Technol.* 2006;97(9):1061–85.
52. Babel S, Kurniawan TA. Low-cost adsorbents for heavy metals uptake from contaminated water: a review. *J. Hazard. Mater.* 2003;97(1):219-43.
53. Crini G. Recent developments in polysaccharide-based materials used as adsorbents in wastewater treatment. *Prog. Polym. Sci.* 2005;30(1):38-70.
54. Wang S, Ang H, Tadé M. Novel applications of red mud as coagulant, adsorbent and catalyst for environmentally benign processes. *Chemosphere.* 2008;72(11):1621-35.
55. Wang S, Sun H, Ang H-M, Tadé M. Adsorptive remediation of environmental pollutants using novel graphene-based nanomaterials. *Chem. Eng. J.* 2013;226:336-47.
56. Ren X, Chen C, Nagatsu M, Wang X. Carbon nanotubes as adsorbents in environmental pollution management: a review. *Chem. Eng. J.* 2011;170(2):395-410.
57. Moreno-Castilla C, Rivera-Utrilla J. Carbon materials as adsorbents for the removal of pollutants from the aqueous phase. *MRS Bull.* 2001;26(11):890-4.
58. Chen C, Hu J, Shao D, Li J, Wang X. Adsorption behavior of multiwall carbon nanotube/iron oxide magnetic composites for Ni(II) and Sr(II). *J. Hazard. Mater.* 2009;164(2-3):923–8.
59. Li Y-H, Wang S, Wei J, Zhang X, Xu C, Luan Z, et al. Lead adsorption on carbon nanotubes. *Chem. Phys. Lett.* 2002;357(3):263-6.
60. Li YH, Ding J, Luan Z, Di Z, Zhu Y, Xu C, et al. Competitive adsorption of Pb^{2+} , Cu^{2+} and Cd^{2+} ions from aqueous solutions by multiwalled carbon nanotubes. *Carbon.* 2003;41(14):2787-92.
61. Chen C, Wang X, Nagatsu M. Europium adsorption on multiwall carbon nanotube/iron oxide magnetic composite in the presence of polyacrylic acid. *Environ. Sci. Technol.* 2009;43(7):2362-7.
62. Chen C, Hu J, Xu D, Tan X, Meng Y, Wang X. Surface complexation modeling of Sr (II) and Eu (III) adsorption onto oxidized multiwall carbon nanotubes. *J. Colloid Interface Sci.* 2008;323(1):33-41.
63. Chen CH, Huang CC. Hydrogen adsorption in defective carbon nanotubes. *Sep. Purif. Technol.* 2009;65(3):305-10.

64. Gaur A, Shim M. Substrate-enhanced O₂ adsorption and complexity in the Raman G-band spectra of individual metallic carbon nanotubes. *Phys. Rev. B: Condens. Matter.* 2008;78(12):125422.
65. Goering J, Kadossov E, Burghaus U. Adsorption Kinetics of Alcohols on Single-Wall Carbon Nanotubes: An Ultrahigh Vacuum Surface Chemistry Study. *J. Phys. Chem. C.* 2008;112(27):10114-24.
66. Hyung H, Kim JH. Natural Organic Matter (NOM) Adsorption to Multi-Walled Carbon Nanotubes: Effect of NOM Characteristics and Water Quality Parameters. *Environ. Sci. Technol.* 2008;42(12):4416-21.
67. Gatica SM, Bojan MJ, Stan G, Cole MW. Quasi-one- and two-dimensional transitions of gases adsorbed on nanotube bundles. *J. Chem. Phys.* 2001;114(8):3765-9.
68. Agnihotri S, Mota JPB, Rostam-Abadi M, Rood MJ. Structural characterization of single-walled carbon nanotube bundles by experiment and molecular simulation. *Langmuir.* 2005;21.
69. Duan X, Ao Z, Sun H, Indrawirawan S, Wang Y, Kang J, et al. Nitrogen-Doped Graphene for Generation and Evolution of Reactive Radicals by Metal-Free Catalysis. *ACS Appl. Mater. Interfaces.* 2015;7(7):4169-78.
70. Hartono T, Wang S, Ma Q, Zhu Z. Layer structured graphite oxide as a novel adsorbent for humic acid removal from aqueous solution. *J. Colloid Interface Sci.* 2009;333(1):114-9.
71. Bradder P, Ling SK, Wang S, Liu S. Dye Adsorption on Layered Graphite Oxide. *J. Chem. Eng. Data.* 2011;56(1):138-41.
72. Zhang S, Shao Y, Liu J, Aksay IA, Lin Y. Graphene–Polypyrrole Nanocomposite as a Highly Efficient and Low Cost Electrically Switched Ion Exchanger for Removing ClO₄⁻ from Wastewater. *ACS Appl. Mater. Interfaces.* 2011;3(9):3633-7.
73. Gao W, Majumder M, Alemany LB, Narayanan TN, Ibarra MA, Pradhan BK, et al. Engineered Graphite Oxide Materials for Application in Water Purification. *ACS Appl. Mater. Interfaces.* 2011;3(6):1821-6.
74. Fan L, Luo C, Li X, Lu F, Qiu H, Sun M. Fabrication of novel magnetic chitosan grafted with graphene oxide to enhance adsorption properties for methyl blue. *J. Hazard. Mater.* 2012;215–216(0):272-9.
75. Ai L, Zhang C, Chen Z. Removal of methylene blue from aqueous solution by a solvothermal-synthesized graphene/magnetite composite. *J. Hazard. Mater.* 2011;192(3):1515–24.

76. Sui Z, Meng Q, Zhang X, Ma R, Cao B. Green synthesis of carbon nanotube-graphene hybrid aerogels and their use as versatile agents for water purification. *J. Mater. Chem.* 2012;22(18):8767-71.
77. Yang S-T, Chen S, Chang Y, Cao A, Liu Y, Wang H. Removal of methylene blue from aqueous solution by graphene oxide. *J. Colloid Interface Sci.* 2011;359(1):24-9.
78. Li N, Zheng M, Chang X, Ji G, Lu H, Xue L, et al. Preparation of magnetic CoFe₂O₄-functionalized graphene sheets via a facile hydrothermal method and their adsorption properties. *J. Solid State Chem.* 2011;184(4):953-8.
79. Wu T, Cai X, Tan S, Li H, Liu J, Yang W. Adsorption characteristics of acrylonitrile, p-toluenesulfonic acid, 1-naphthalenesulfonic acid and methyl blue on graphene in aqueous solutions. *Chem. Eng. J.* 2011;173(1):144-9.
80. Li Y, Du Q, Liu T, Sun J, Jiao Y, Xia Y, et al. Equilibrium, kinetic and thermodynamic studies on the adsorption of phenol onto graphene. *Mater. Res. Bull.* 2012;47(8):1898-904.
81. Gao Y, Li Y, Zhang L, Huang H, Hu J, Shah SM, et al. Adsorption and removal of tetracycline antibiotics from aqueous solution by graphene oxide. *J. Colloid Interface Sci.* 2012;368(1):540-6.
82. Wang S, Ng CW, Wang W, Li Q, Hao Z. Synergistic and competitive adsorption of organic dyes on multiwalled carbon nanotubes. *Chem. Eng. J.* 2012;197(0):34-40.
83. Luck F. Wet air oxidation: past, present and future. *Catal. Today.* 1999;53(1):81–91.
84. Miguélez JRP, Bernal JL, Sanz EN, Ossa EMDL, Miguélez JRP, Bernal JL. Kinetics of wet air oxidation of phenol. *Chem. Eng. J.* 1997;67:115–21.
85. Kolaczowski ST, Plucinski P, Beltran FJ, Rivas FJ, Mclurgh DB. Wet air oxidation: a review of process technologies and aspects in reactor design. *Chem. Eng. J.* 1999;73(2):143–60.
86. Luck F. A review of industrial catalytic wet air oxidation processes. *Catal. Today.* 1996;27(1):195–202.
87. Devlin HR, Harris IJ. Mechanism of the oxidation of aqueous phenol with dissolved oxygen. *Ind. Eng. Chem. Fundam.* 1984;23(4):387-92.
88. Nikolaou N, Abatzoglou N, Gasso S, Chornet E. The oxidation of valeric acid in aqueous solution. *Can. J. Chem. Eng.* 1994;72(3):522–33.
89. Tester JW, Holgate HR, Armellini FJ, Webley PA, Killilea WR, Hong GT, et al., editors. *Supercritical Water Oxidation Technology*. ACS Symposium Series; 1993.

90. Levec J, Pintar A. Catalytic wet-air oxidation processes: A review. *Catal. Today*. 2007;124(3–4):172-84.
91. Sadana A, Katzer JR. Catalytic Oxidation of Phenol in Aqueous Solution over Copper Oxide. *Ind. Eng. Chem. Fundam.* 2002;17(3):234-.
92. Mishra VS, Mahajani VV, Joshi JB. Wet Air Oxidation. *Ind. Eng. Chem. Res.* 1995;34(1):2-48.
93. Pintar A, Levec J. Catalytic liquid-phase oxidation of refractory organics in waste water. *Chem. Eng. Sci.* 1992;47(9–11):2395-400.
94. Imamura S, Nakamura M, Kawabata N, Yoshida J, Ishida S. Wet oxidation of poly(ethylene glycol) catalyzed by manganese-cerium composite oxide. *Ind. Eng. Chem. Prod. Res. Dev.* 1986;25(1):34-7.
95. Ito MM, Akita K, Inoue H. Wet oxidation of oxygen- and nitrogen-containing organic compounds catalyzed by cobalt(III) oxide. *Ind. Eng. Chem. Res.* 1989(7).
96. Imamura S, Hirano A, Kawabata N. Wet oxidation of acetic acid catalyzed by Co-Bi complex oxides. *Ind. Eng. Chem. Prod. Res. Dev.* 1982;21(4):570-5.
97. Imamura S, Doi A, Ishida S. Wet oxidation of ammonia catalyzed by cerium-based composite oxides. *Ind. Eng. Chem. Prod. Res. Dev.* 1985;24(1):75-80.
98. Imamura S, Fukuda I, Ishida S. Wet oxidation catalyzed by ruthenium supported on cerium(IV) oxides. *Ind. Eng. Chem. Res.* 2002(4):718-21.
99. Matatov-Meytal YI, Sheintuch M. Catalytic Abatement of Water Pollutants. *Ind. Eng. Chem. Res.* 1998;37(2):309-26.
100. Duprez D, Delanoe F, Barbier J, Isnard P, Blanchard G. Catalytic oxidation of organic compounds in aqueous media. *Catal. Today*. 1996;29(95):317–22.
101. Gallezot P, Laurain N, Isnard P. Catalytic wet-air oxidation of carboxylic acids on carbon-supported platinum catalysts. *Appl. Catal., B.* 1996;9(1):L11–L7.
102. Mantzavinos D, Hellenbrand R, Livingston AG, Metcalfe IS. Catalytic wet air oxidation of polyethylene glycol. *Appl. Catal., B.* 1996;11(1):99–119.
103. Barbier J, Jabouille F, Duprez D, Blanchard G, Isnard P, Delanoe F. Total oxidation of acetic acid in aqueous solutions over noble metal catalysts. *J. Catal.* 1998;177(2):378–85.
104. Zhang Q, Chuang KT. Alumina-Supported Noble Metal Catalysts for Destructive Oxidation of Organic Pollutants in Effluent from a Softwood Kraft Pulp Mill. *Ind. Eng. Chem. Res.* 1998;37(8):3343-9.

105. Saputra E, Muhammad S, Sun H, Ang HM, Tadé MO, Wang S. Different Crystallographic One-dimensional MnO₂ Nanomaterials and Their Superior Performance in Catalytic Phenol Degradation. *Environ. Sci. Technol.* 2013;47(11):5882-7.
106. Xu F, Deng S, Xu J, Zhang W, Wu M, Wang B, et al. Highly Active and Stable Ni-Fe Bimetal Prepared by Ball Milling for Catalytic Hydrodechlorination of 4-Chlorophenol. *Environ. Sci. Technol.* 2012;46(8):4576-82.
107. Lai B, Zhang Y, Chen Z, Yang P, Zhou Y, Wang J. Removal of p-nitrophenol (PNP) in aqueous solution by the micron-scale iron-copper (Fe/Cu) bimetallic particles. *Appl. Catal., B.* 2014;144(0):816-30.
108. Casero I, Sicilia D, Rubio S, Pérez-Bendito D. Chemical degradation of aromatic amines by Fenton's reagent. *Water Res.* 1997;31(8):1985-95.
109. Nam S, Renganathan V, Tratnyek PG. Substituent effects on azo dye oxidation by the Fe^{III}-EDTA-H₂O₂ system. *Chemosphere.* 2001;45(1):59-65.
110. Huston PL, Pignatello JJ. Degradation of selected pesticide active ingredients and commercial formulations in water by the photo-assisted Fenton reaction. *Water Res.* 1999;33(5):1238-46.
111. Park JW, Lee SE, Rhee IK, Kim JE. Transformation of the Fungicide Chlorothalonil by Fenton Reagent. *J. Agric. Food. Chem.* 2002;50(26):7570-5.
112. Dunford HB. Oxidations of iron(II)/(III) by hydrogen peroxide: from aquo to enzyme. *Coord. Chem. Rev.* 2002;233-234(0):311-8.
113. Wang Y, Indrawirawan S, Duan X, Sun H, Ang HM, Tadé MO, et al. New insights into heterogeneous generation and evolution processes of sulfate radicals for phenol degradation over one-dimensional α -MnO₂ nanostructures. *Chem. Eng. J.* 2015;266(0):12-20.
114. Gumy D, Fernández-Ibáñez P, Malato S, Pulgarin C, Enea O, Kiwi J. Supported Fe/C and Fe/Nafion/C catalysts for the photo-Fenton degradation of Orange II under solar irradiation. *Catal. Today.* 2005;101(3-4):375-82.
115. Liou R-M, Chen S-H, Hung M-Y, Hsu C-S, Lai J-Y. Fe (III) supported on resin as effective catalyst for the heterogeneous oxidation of phenol in aqueous solution. *Chemosphere.* 2005;59(1):117-25.
116. Navalon S, Alvaro M, Garcia H. Heterogeneous Fenton catalysts based on clays, silicas and zeolites. *Appl. Catal., B.* 2010;99(1-2):1-26.
117. Ramirez JH, Maldonado-Hódar FJ, Pérez-Cadenas AF, Moreno-Castilla C, Costa CA, Madeira LM. Azo-dye Orange II degradation by heterogeneous Fenton-like

- reaction using carbon-Fe catalysts. *Appl. Catal., B.* 2007;75(3–4):312-23.
118. Guo J, Wang R, Tjiu WW, Pan J, Liu T. Synthesis of Fe nanoparticles@graphene composites for environmental applications. *J. Hazard. Mater.* 2012;225–226(0):63-73.
119. Liao Q, Sun J, Gao L. Degradation of phenol by heterogeneous Fenton reaction using multi-walled carbon nanotube supported Fe₂O₃ catalysts. *Colloids Surf., A.* 2009;345(1–3):95-100.
120. Herney-Ramirez J, Vicente MA, Madeira LM. Heterogeneous photo-Fenton oxidation with pillared clay-based catalysts for wastewater treatment: A review. *Appl. Catal., B.* 2010;98(1 – 2):10-26.
121. Muthuvel I, Swaminathan M. Highly solar active Fe(III) immobilised alumina for the degradation of Acid Violet 7. *Sol. Energy Mater. Sol. Cells.* 2008;92(8):857-63.
122. Pereira MC, Oliveira LCA, Murad E. Iron oxide catalysts: Fenton and Fenton-like reactions - a review. *Clay Miner.* 2012;47(3):285-302.
123. Melero JA, Calleja G, Martínez F, Molina R. Nanocomposite of crystalline Fe₂O₃ and CuO particles and mesostructured SBA-15 silica as an active catalyst for wet peroxide oxidation processes. *Catal. Commun.* 2006;7(7):478-83.
124. Bradu C, Frunza L, Mihalche N, Avramescu S-M, Neață M, Udrea I. Removal of Reactive Black 5 azo dye from aqueous solutions by catalytic oxidation using CuO/Al₂O₃ and NiO/Al₂O₃. *Appl. Catal., B.* 2010;96(3–4):548-56.
125. Driehaus W, Seith R, Jekel M. Oxidation of arsenate(III) with manganese oxides in water treatment. *Water Res.* 1995;29(1):297-305.
126. Bokare AD, Choi W. Chromate-Induced Activation of Hydrogen Peroxide for Oxidative Degradation of Aqueous Organic Pollutants. *Environ. Sci. Technol.* 2010;44(19):7232-7.
127. Ji P, Wang L, Chen F, Zhang J. Ce³⁺-Centric Organic Pollutant Elimination by CeO₂ in the Presence of H₂O₂. *ChemCatChem.* 2010;2(12):1552-4.
128. Li XS, Xu LD, Shan YB, Yuan BF, Feng YQ. Preparation of magnetic poly(diethyl vinylphosphonate-co-ethylene glycol dimethacrylate) for the determination of chlorophenols in water samples. *J. Chromatogr. A.* 2012;1265(0):24-30.
129. Southworth BA, Voelker BM. Hydroxyl Radical Production via the Photo-Fenton Reaction in the Presence of Fulvic Acid. *Environ. Sci. Technol.* 2003;37(6):1130-6.

130. Zepp RG, Faust BC, Hoigne J. Hydroxyl radical formation in aqueous reactions (pH 3-8) of iron(II) with hydrogen peroxide: the photo-Fenton reaction. *Environ. Sci. Technol.* 1992;26(2):313-9.
131. Malato S, Blanco J, Alarcón DC, Maldonado MI, Fernández-Ibáñez P, Gernjak W. Photocatalytic decontamination and disinfection of water with solar collectors. *Catal. Today.* 2007;122(1-2):137-49.
132. Oller I, Malato S, Sánchez-Pérez JA, Gernjak W, Maldonado MI, Pérez-Estrada LA, et al. A combined solar photocatalytic-biological field system for the mineralization of an industrial pollutant at pilot scale. *Catal. Today.* 2007;122(1-2):150-9.
133. Cheng M, Song W, Ma W, Chen C, Zhao J, Lin J, et al. Catalytic activity of iron species in layered clays for photodegradation of organic dyes under visible irradiation. *Appl. Catal., B.* 2008;77(3-4):355-63.
134. Liu R, Xiao D, Guo Y, Wang Z, Liu J. A novel photosensitized Fenton reaction catalyzed by sandwiched iron in synthetic nontronite. *RSC Adv.* 2014;4(25):12958-63.
135. Adewuyi YG. Sonochemistry in Environmental Remediation. 1. Combinative and Hybrid Sonophotochemical Oxidation Processes for the Treatment of Pollutants in Water. *Environ. Sci. Technol.* 2005;39(10):3409-20.
136. Chen B, Wang X, Wang C, Jiang W, Li S. Degradation of azo dye direct sky blue 5B by sonication combined with zero-valent iron. *Ultrason. Sonochem.* 2011;18(5):1091-6.
137. Özdemir C, Öden MK, Şahinkaya S, Kalipçi E. Color Removal from Synthetic Textile Wastewater by Sono-Fenton Process. *Clean Air.* 2011;39(1):60-7.
138. Bremner DH, Carlo SD, Chakinala AG, Cravotto G. Mineralisation of 2,4-dichlorophenoxyacetic acid by acoustic or hydrodynamic cavitation in conjunction with the advanced Fenton process. *Ultrason. Sonochem.* 2008;15(4):416-9.
139. Brillas E, Sirés I, Oturan MA. Electro-Fenton Process and Related Electrochemical Technologies Based on Fenton's Reaction Chemistry. *Chem. Rev.* 2009;109(12):6570-631.
140. Umar M, Aziz HA, Yusoff MS. Trends in the use of Fenton, electro-Fenton and photo-Fenton for the treatment of landfill leachate. *Waste Manage.* 2010;30(11):2113-21.
141. Nidheesh P, Gandhimathi R, Ramesh S. Degradation of dyes from aqueous solution by Fenton processes: a review. *Environ Sci Pollut Res.*

2013;20(4):2099-132.

142. García-Ripoll A, Amat AM, Arques A, Vicente R, López MF, Oller I, et al. Increased biodegradability of UltracidTM in aqueous solutions with solar TiO₂ photocatalysis. *Chemosphere*. 2007;68(2):293-300.

143. Oller I, Gernjak W, Maldonado MI, Pérez-Estrada LA, Sánchez-Pérez JA, Malato S. Solar photocatalytic degradation of some hazardous water-soluble pesticides at pilot-plant scale. *J. Hazard. Mater.* 2006;138(3):507-17.

144. Ahmed S, Rasul MG, Martens WN, Brown R, Hashib MA. Heterogeneous photocatalytic degradation of phenols in wastewater: A review on current status and developments. *Desalination*. 2010;261(1-2):3-18.

145. Chong MN, Jin B, Chow CWK, Saint C. Recent developments in photocatalytic water treatment technology: A review. *Water Res.* 2010;44(10):2997-3027.

146. Fujishima A, Zhang X, Tryk DA. TiO₂ photocatalysis and related surface phenomena. *Surf. Sci. Rep.* 2008;63(12):515-82.

147. Gaya UI, Abdullah AH. Heterogeneous photocatalytic degradation of organic contaminants over titanium dioxide: A review of fundamentals, progress and problems. *J. Photochem. Photobiol., C*. 2008;9(1):1-12.

148. Siddiquey IA, Furusawa T, Sato M, Honda K, Suzuki N. Control of the photocatalytic activity of TiO₂ nanoparticles by silica coating with polydiethoxysiloxane. *Dyes Pigm.* 2008;76(3):754-9.

149. Li H, Li J, Huo Y. Highly Active TiO₂N Photocatalysts Prepared by Treating TiO₂ Precursors in NH₃/Ethanol Fluid under Supercritical Conditions. *J. Phys. Chem. B*. 2006;110(4):1559-65.

150. Huang M, Tso E, Datye AK, Prairie MR, Stange BM. Removal of Silver in Photographic Processing Waste by TiO₂-Based Photocatalysis. *Environ. Sci. Technol.* 1996;30(10):3084-8.

151. Sakthivel S, Neppolian B, Shankar MV, Arabindoo B, Palanichamy M, Murugesan V. Solar photocatalytic degradation of azo dye: comparison of photocatalytic efficiency of ZnO and TiO₂. *Sol. Energy Mater. Sol. Cells*. 2003;77(1):65-82.

152. Sun H, Liu S, Liu S, Wang S. A comparative study of reduced graphene oxide modified TiO₂, ZnO and Ta₂O₅ in visible light photocatalytic/photochemical oxidation of methylene blue. *Appl. Catal., B*. 2014;146(0):162-8.

153. Murase T, Irie H, Hashimoto K. Visible Light Sensitive Photocatalysts,

- Nitrogen-Doped Ta₂O₅ Powders. *J. Phys. Chem. B.* 2004;108(40):15803-7.
154. Khan Z, Chetia TR, Qureshi M. Rational design of hyperbranched 3D heteroarrays of SrS/CdS: synthesis, characterization and evaluation of photocatalytic properties for efficient hydrogen generation and organic dye degradation. *Nanoscale.* 2012;4(11):3543-50.
155. Gao P, Liu J, Sun DD, Ng W. Graphene oxide–CdS composite with high photocatalytic degradation and disinfection activities under visible light irradiation. *J. Hazard. Mater.* 2013;250–251(0):412-20.
156. Yao X, Liu T, Liu X, Lu L. Loading of CdS nanoparticles on the surface of elongated TiO₂ nanocrystals for efficient visible-light photocatalytic hydrogen evolution from water splitting. *Chem. Eng. J.* 2014;255(0):28-39.
157. Xiong Z, Zhang LL, Ma J, Zhao XS. Photocatalytic degradation of dyes over graphene-gold nanocomposites under visible light irradiation. *Chem. Commun.* 2010;46(33):6099-101.
158. Kozlova EA, Lyubina TP, Nasalevich MA, Vorontsov AV, Miller AV, Kaichev VV, et al. Influence of the method of platinum deposition on activity and stability of Pt/TiO₂ photocatalysts in the photocatalytic oxidation of dimethyl methylphosphonate. *Catal. Commun.* 2011;12(7):597-601.
159. Sun H, Bai Y, Liu H, Jin W, Xu N, Chen G, et al. Mechanism of Nitrogen-Concentration Dependence on pH Value: Experimental and Theoretical Studies on Nitrogen-Doped TiO₂. *J. Phys. Chem. C.* 2008;112(34):13304-9.
160. Sun H, Ullah R, Chong S, Ang HM, Tadé MO, Wang S. Room-light-induced indoor air purification using an efficient Pt/N-TiO₂ photocatalyst. *Appl. Catal., B.* 2011;108–109(0):127-33.
161. Ohno T, Sarukawa K, Tokieda K, Matsumura M. Morphology of a TiO₂ Photocatalyst (Degussa, P-25) Consisting of Anatase and Rutile Crystalline Phases. *J. Catal.* 2001;203(1):82-6.
162. Sun H, Zhou G, Wang Y, Suvorova A, Wang S. A New Metal-Free Carbon Hybrid for Enhanced Photocatalysis. *ACS Appl. Mater. Interfaces.* 2014;6(19):16745-54.
163. Zhang LL, Xiong Z, Zhao XS. Pillaring Chemically Exfoliated Graphene Oxide with Carbon Nanotubes for Photocatalytic Degradation of Dyes under Visible Light Irradiation. *ACS Nano.* 2010;4(11):7030-6.
164. Li H, Liu R, Lian S, Liu Y, Huang H, Kang Z. Near-infrared light controlled photocatalytic activity of carbon quantum dots for highly selective oxidation reaction. *Nanoscale.* 2013;5(8):3289-97.

165. Liu J, Wen S, Hou Y, Zuo F, Beran GJO, Feng P. Boron Carbides as Efficient, Metal-Free, Visible-Light-Responsive Photocatalysts. *Angew. Chem. Int. Ed.* 2013;125(11):3323-7.
166. Cui Y, Huang J, Fu X, Wang X. Metal-free photocatalytic degradation of 4-chlorophenol in water by mesoporous carbon nitride semiconductors. *Catal. Sci. Technol.* 2012;2(7):1396-402.
167. Zhang J, Sun J, Maeda K, Domen K, Liu P, Antonietti M, et al. Sulfur-mediated synthesis of carbon nitride: Band-gap engineering and improved functions for photocatalysis. *Energy Environ. Sci.* 2011;4(3):675-8.
168. Chang C, Zhu L, Wang S, Chu X, Yue L. Novel Mesoporous Graphite Carbon Nitride/BiOI Heterojunction for Enhancing Photocatalytic Performance Under Visible-Light Irradiation. *ACS Appl. Mater. Interfaces.* 2014;6(7):5083-93.
169. Singh HK, Saquib M, Haque MM, Muneer M, Bahnemann DW. Titanium dioxide mediated photocatalysed degradation of phenoxyacetic acid and 2,4,5-trichlorophenoxyacetic acid, in aqueous suspensions. *J. Mol. Catal. A: Chem.* 2007;264(1-2):66-72.
170. Haque MM, Muneer M, Bahnemann DW. Semiconductor-Mediated Photocatalyzed Degradation of a Herbicide Derivative, Chlorotoluron, in Aqueous Suspensions. *Environ. Sci. Technol.* 2006;40(15):4765-70.
171. Parida KM, Dash SS, Das DP. Physico-chemical characterization and photocatalytic activity of zinc oxide prepared by various methods. *J. Colloid Interface Sci.* 2006;298(2):787-93.
172. Pardeshi SK, Patil AB. A simple route for photocatalytic degradation of phenol in aqueous zinc oxide suspension using solar energy. *Sol. Energy.* 2008;82(8):700-5.
173. Venkatachalam N, Palanichamy M, Murugesan V. Sol-gel preparation and characterization of alkaline earth metal doped nano TiO₂: Efficient photocatalytic degradation of 4-chlorophenol. *J. Mol. Catal. A: Chem.* 2007;273(1-2):177-85.
174. Khodja AA, Sehili T, Pilichowski J-F, Boule P. Photocatalytic degradation of 2-phenylphenol on TiO₂ and ZnO in aqueous suspensions. *J. Photochem. Photobiol., A.* 2001;141(2-3):231-9.
175. Barakat MA, Schaeffer H, Hayes G, Ismat-Shah S. Photocatalytic degradation of 2-chlorophenol by Co-doped TiO₂ nanoparticles. *Appl. Catal., B.* 2005;57(1):23-30.
176. Selvam K, Muruganandham M, Muthuvel I, Swaminathan M. The influence of inorganic oxidants and metal ions on semiconductor sensitized photodegradation

of 4-fluorophenol. *Chem. Eng. J.* 2007;128(1):51-7.

177. Akbal F, Nur Onar A. Photocatalytic Degradation of Phenol. *Environ. Monit. Assess.* 2003;83(3):295-302.

178. Chiou CH, Wu CY, Juang RS. Photocatalytic degradation of phenol and m-nitrophenol using irradiated TiO₂ in aqueous solutions. *Sep. Purif. Technol.* 2008;62(3):559-64.

179. Gogate PR, Pandit AB. A review of imperative technologies for wastewater treatment I: oxidation technologies at ambient conditions. *Adv. Environ. Res.* 2004;8(3):501-51.

180. Camel V, Bermond A. The use of ozone and associated oxidation processes in drinking water treatment. *Water Res.* 1998;32(11):3208-22.

181. Kreetachat T, Damrongsri M, Punsuwon V, Vaithanomsat P, Chiemchaisri C, Chomsurin C. Effects of ozonation process on lignin-derived compounds in pulp and paper mill effluents. *J. Hazard. Mater.* 2007;142(1):250-7.

182. Hsu YC, Chen JT, Yang HC, Chen JH, Fang CF. Ozone decolorization of mixed-dye solutions in a gas-induced reactor. *Water Environ. Res.* 2001:494-503.

183. Kulik N, Trapido M, Veressinina Y, Munter R, editors. Oil Shale Semicoke Leachate Pre-treatment by means of Advanced Oxidation. International Conference Ozone and UV; 2006.

184. Ormad M, Miguel N, Claver A, Matesanz J, Ovelleiro J. Pesticides removal in the process of drinking water production. *Chemosphere.* 2008;71(1):97-106.

185. Perkowski J, Kos L, Ledakowicz S. Application of ozone in textile wastewater treatment. 1996.

186. Am Water Works Res F, Langlais B, Reckhow DA, Brink DR. Ozone in water treatment: application and engineering: CRC press; 1991.

187. Legube B, Karpel Vel Leitner N. Catalytic ozonation: a promising advanced oxidation technology for water treatment. *Catal. Today.* 1999;53(1):61-72.

188. Gracia R, Aragües JL, Ovelleiro JL. Study of the Catalytic Ozonation of Humic Substances in Water and Their Ozonation Byproducts. *Ozone Sci. Eng.* 1996;18(3):195-208.

189. Cortés S, Sarasa J, Ormad P, Gracia R, Ovelleiro JL. Comparative Efficiency of the Systems O₃/High pH And O₃/catalyst for the Oxidation of Chlorobenzenes in Water. *Ozone Sci. Eng.* 2000;22(4):415-26.

190. Wu CH, Kuo CY, Chang CL. Decolorization of C.I. Reactive Red 2 by

- catalytic ozonation processes. *J. Hazard. Mater.* 2008;153(3):1052-8.
191. Tong S, Liu W, Leng W, Zhang Q. Characteristics of MnO₂ catalytic ozonation of sulfosalicylic acid and propionic acid in water. *Chemosphere.* 2003;50(10):1359-64.
192. Andreozzi R, Lo Casale MS, Marotta R, Pinto G, Pollio A. N-methyl-p-aminophenol (metol) ozonation in aqueous solution: kinetics, mechanism and toxicological characterization of ozonized samples. *Water Res.* 2000;34(18):4419-29.
193. Rivas J, Rodríguez E, Beltrán FJ, García-Araya JF, Alvarez P. Homogeneous catalyzed ozonation of simazine. Effect of Mn(II) and Fe(II). *J. Environ. Sci. Health., Part B.* 2001;36(3):317-30.
194. Pines DS, Reckhow DA. Effect of Dissolved Cobalt(II) on the Ozonation of Oxalic Acid. *Environ. Sci. Technol.* 2002;36(19):4046-51.
195. Pi Y, Ernst M, Schrotter J-C. Effect of Phosphate Buffer upon CuO/Al₂O₃ and Cu (II) Catalyzed Ozonation of Oxalic Acid Solution. *Ozone Sci. Eng.* 2003;25(5):393-7.
196. Matheswaran M, Balaji S, Chung SJ, Moon IS. Studies on cerium oxidation in catalytic ozonation process: A novel approach for organic mineralization. *Catal. Commun.* 2007;8(10):1497-501.
197. Trapido M, Veressinina Y, Munter R, Kallas J. Catalytic Ozonation of m-Dinitrobenzene. *Ozone Sci. Eng.* 2005;27(5):359-63.
198. Rice RG. Applications of ozone for industrial wastewater treatment — A review. *Ozone Sci. Eng.* 1996;18(6):477-515.
199. Sauleda R, Brillas E. Mineralization of aniline and 4-chlorophenol in acidic solution by ozonation catalyzed with Fe²⁺ and UVA light. *Appl. Catal., B.* 2001;29(2):135-45.
200. Beltrán FJ, Rivas FJ, Montero-de-Espinosa R. Ozone-enhanced oxidation of oxalic acid in water with cobalt catalysts. 1. Homogeneous catalytic ozonation. *Ind. Eng. Chem. Res.* 2003;42(14):3210-7.
201. Shukla P, Sun H, Wang S, Ang HM, Tadó MO. Co-SBA-15 for heterogeneous oxidation of phenol with sulfate radical for wastewater treatment. *Catal. Today.* 2011;175(1):380-5.
202. Dong Y, Yang H, He K, Song S, Zhang A. β-MnO₂ nanowires: a novel ozonation catalyst for water treatment. *Appl. Catal., B.* 2009;85(3):155-61.

203. Alsheyab MA, Muñoz AH. Comparative study of ozone and MnO_2/O_3 effects on the elimination of TOC and COD of raw water at the Valmayor station. *Desalination*. 2007;207(1):179-83.
204. Faria P, Monteiro D, Órfão J, Pereira M. Cerium, manganese and cobalt oxides as catalysts for the ozonation of selected organic compounds. *Chemosphere*. 2009;74(6):818-24.
205. Cooper C, Burch R. An investigation of catalytic ozonation for the oxidation of halocarbons in drinking water preparation. *Water Res*. 1999;33(18):3695-700.
206. Rosal R, Rodríguez A, Gonzalo M, García-Calvo E. Catalytic ozonation of naproxen and carbamazepine on titanium dioxide. *Appl. Catal., B*. 2008;84(1):48-57.
207. Beltran FJ, Rivas FJ, Montero-de-Espinosa R. Catalytic ozonation of oxalic acid in an aqueous TiO_2 slurry reactor. *Appl. Catal., B*. 2002;39(3):221-31.
208. Sui M, Sheng L, Lu K, Tian F. FeOOH catalytic ozonation of oxalic acid and the effect of phosphate binding on its catalytic activity. *Appl. Catal., B*. 2010;96(1-2):94-100.
209. Alvarez P, Beltrán F, Pocostales J, Masa F. Preparation and structural characterization of $\text{Co}/\text{Al}_2\text{O}_3$ catalysts for the ozonation of pyruvic acid. *Appl. Catal., B*. 2007;72(3):322-30.
210. Avramescu SM, Bradu C, Udrea I, Mihalache N, Ruta F. Degradation of oxalic acid from aqueous solutions by ozonation in presence of $\text{Ni}/\text{Al}_2\text{O}_3$ catalysts. *Catal. Commun*. 2008;9(14):2386-91.
211. Yang L, Hu C, Nie Y, Qu J. Catalytic ozonation of selected pharmaceuticals over mesoporous alumina-supported manganese oxide. *Environ. Sci. Technol*. 2009;43(7):2525-9.
212. Martins RC, Quinta-Ferreira RM. Catalytic ozonation of phenolic acids over a Mn-Ce-O catalyst. *Appl. Catal., B*. 2009;90(1-2):268-77.
213. Oyama ST. Chemical and Catalytic Properties of Ozone. *Catal. Rev. Sci. Eng*. 2000;42(3):279-322.
214. Andreozzi R, Caprio V, Insola A, Marotta R, Tufano V. The ozonation of pyruvic acid in aqueous solutions catalyzed by suspended and dissolved manganese. *Water Res*. 1998;32(5):1492-6.
215. Liu ZQ, Ma J, Cui YH, Zhao L, Zhang BP. Factors affecting the catalytic activity of multi-walled carbon nanotube for ozonation of oxalic acid. *Sep. Purif. Technol*. 2011;78(2):147-53.

216. Roscoe JM, Abbatt JPD. Diffuse Reflectance FTIR Study of the Interaction of Alumina Surfaces with Ozone and Water Vapor. *J. Phys. Chem. A.* 2005;109(40):9028-34.
217. Zhang T, Li C, Ma J, Tian H, Qiang Z. Surface hydroxyl groups of synthetic α -FeOOH in promoting OH generation from aqueous ozone: Property and activity relationship. *Appl. Catal., B.* 2008;82(1-2):131-7.
218. Wang Y, Sun H, Ang HM, Tadé MO, Wang S. 3D-hierarchically structured MnO₂ for catalytic oxidation of phenol solutions by activation of peroxymonosulfate: Structure dependence and mechanism. *Appl. Catal., B.* 2015;164(0):159-67.
219. Dionysiou DD, Anipsitakis GP. Radical Generation by the Interaction of Transition Metals with Common Oxidants. *Environ. Sci. Technol.* 2004;38(13):págs. 3705-12.
220. Anipsitakis GP, Dionysiou DD. Degradation of Organic Contaminants in Water with Sulfate Radicals Generated by the Conjunction of Peroxymonosulfate with Cobalt. *Environ. Sci. Technol.* 2003;37(20):págs. 4790-7.
221. Zhang BT, Zhang Y, Teng Y, Fan M. Sulfate Radical and its Application in Decontamination Technologies. *Crit. Rev. Env. Sci. Technol.* 2014.
222. Meunier B. Metalloporphyrins as versatile catalysts for oxidation reactions and oxidative DNA cleavage. *Cheminform.* 1992;92(6):1411-56.
223. Liang CJ, Bruell CJ. Thermally Activated Persulfate Oxidation of Trichloroethylene (TCE) and 1,1,1Trichloroethane (TCA) in Aqueous Systems and Soil Slurries. *Soil Sediment Contam.* 2003;12(2):207-28.
224. Hori H, Yamamoto A, Hayakawa E, Taniyasu S, Yamashita N, Kutsuna S, et al. Efficient Decomposition of Environmentally Persistent Perfluorocarboxylic Acids by Use of Persulfate as a Photochemical Oxidant. *Environ. Sci. Technol.* 2005;39(7):2383-8.
225. Anipsitakis GP, Dionysiou DD. Transition metal/UV-based advanced oxidation technologies for water decontamination. *Appl. Catal., B.* 2004;54(3):155-63.
226. He X, Cruz AADL, Dionysiou DD. Destruction of cyanobacterial toxin cylindrospermopsin by hydroxyl radicals and sulfate radicals using UV-254nm activation of hydrogen peroxide, persulfate and peroxymonosulfate. *J. Photochem. Photobiol., A.* 2013;251(48):19758-71.
227. Chan TW. Degradation of iopromide by combined UV irradiation and peroxydisulfate. *J. Hazard. Mater.* 2010;181(1-3):508-13.

228. Shih YJ. Mineralization and defluorization of 2,2,3,3-tetrafluoro-1-propanol (TFP) by UV/persulfate oxidation and sequential adsorption. *Chemosphere*. 2012;89(10):1262–6.
229. Lin CC, Wu MS, Lin CC, Wu MS. UV/S₂O₈²⁻ process for degrading polyvinyl alcohol in aqueous solutions. *Chem. Eng. Prog.* 2014.
230. Shukla P, Fatimah I, Wang S, Ang HM, Tade M. Photocatalytic generation of sulphate and hydroxyl radicals using zinc oxide under low-power UV to oxidise phenolic contaminants in wastewater. *Catal. Today*. 2010;157(1-4):410–4.
231. Shukla PR, Wang S, Ang HM, Tade MO. Photocatalytic oxidation of phenolic compounds using zinc oxide and sulphate radicals under artificial solar light. *Sep. Purif. Technol.* 2010;70(3):338–44.
232. Yang Q, Choi H, Al-Abed SR, Dionysiou DD. Iron–cobalt mixed oxide nanocatalysts: Heterogeneous peroxymonosulfate activation, cobalt leaching, and ferromagnetic properties for environmental applications. *Appl. Catal., B*. 2009;88(3–4):462–9.
233. Yang Q, Choi H, Chen Y, Dionysiou DD. Heterogeneous activation of peroxymonosulfate by supported cobalt catalysts for the degradation of 2,4-dichlorophenol in water: The effect of support, cobalt precursor, and UV radiation. *Appl. Catal., B*. 2008;77(3–4):300–7.
234. Yang Q, Choi H, Dionysiou DD. Nanocrystalline cobalt oxide immobilized on titanium dioxide nanoparticles for the heterogeneous activation of peroxymonosulfate. *Appl. Catal., B*. 2007;74(1–2):170–8.
235. Zhang W, Tay HL, Lim SS, Wang Y, Zhong Z, Xu R. Supported cobalt oxide on MgO: Highly efficient catalysts for degradation of organic dyes in dilute solutions. *Appl. Catal., B*. 2010;95(1–2):93–9.
236. Shukla PR, Wang S, Sun H, Ang HM, Tade M. Activated carbon supported cobalt catalysts for advanced oxidation of organic contaminants in aqueous solution. *Appl. Catal., B*. 2010;100(3–4):529–34.
237. Shukla P, Wang S, Singh K, Ang HM, Tade MO. Cobalt exchanged zeolites for heterogeneous catalytic oxidation of phenol in the presence of peroxymonosulphate. *Appl. Catal., B*. 2010;99(1–2):163–9.
238. Yao Y, Yang Z, Zhang D, Peng W, Sun H, Wang S. Magnetic CoFe₂O₄ – Graphene Hybrids: Facile Synthesis, Characterization, and Catalytic Properties. *Ind. Eng. Chem. Res.* 2012;51(17):6044–51.
239. Saputra E, Muhammad S, Sun H, Patel A, Shukla P, Zhu ZH, et al. α -MnO₂ activation of peroxymonosulfate for catalytic phenol degradation in aqueous

solutions. *Catal. Commun.* 2012;26(0):144-8.

240. Saputra E, Muhammad S, Sun H, Ang HM, Tade MO, Wang S. Shape-controlled activation of peroxymonosulfate by single crystal α - Mn_2O_3 for catalytic phenol degradation in aqueous solution. *Appl. Catal., B.* 2014;154–155(0):246-51.

241. Chae KJ, Yim SK, Choi KH, Kim SK, Wk. P. Integrated biological and electro-chemical treatment of swine manure. *Water Sci. Technol.* 2004;49:427-34.

242. Locke BR, Sato M, Sunka P, Hoffmann MR, Chang JS. Electrohydraulic Discharge and Nonthermal Plasma for Water Treatment. *Ind. Eng. Chem. Res.* 2006;45(3):págs. 882-905.

243. Cooper WJ, Nickelsen MG, Meacham DE, Cadavid E, Waite TD, Kurucz CN. High energy electron beam irradiation: An innovative process for the treatment of aqueous based organic hazardous wastes. *J. Environ. Sci. Health., Part A.* 1992;27(1):219-44.

244. Wang Y, Sun H, Duan X, Ang HM, Tade MO, Wang S. A new magnetic nano zero-valent iron encapsulated in carbon spheres for oxidative degradation of phenol. *Appl. Catal., B.* 2015;172–173(0):73-81.

245. Chen X, Chen J, Qiao X, Wang D, Cai X. Performance of nano- Co_3O_4 /peroxymonosulfate system: Kinetics and mechanism study using Acid Orange 7 as a model compound. *Appl. Catal., B.* 2008;80(1–2):116-21.

246. Anipsitakis GP, Stathatos E, Dionysiou DD. Heterogeneous Activation of Oxone Using Co_3O_4 . *J. Phys. Chem. B.* 2005;109(27):13052-5.

247. Sun H, Liang H, Zhou G, Wang S. Supported cobalt catalysts by one-pot aqueous combustion synthesis for catalytic phenol degradation. *J. Colloid Interface Sci.* 2013;394(0):394-400.

248. Saputra E, Muhammad S, Sun H, Ang HM, Tade MO, Wang S. A comparative study of spinel structured Mn_3O_4 , Co_3O_4 and Fe_3O_4 nanoparticles in catalytic oxidation of phenolic contaminants in aqueous solutions. *J. Colloid Interface Sci.* 2013;407:467-73.

249. Sun H, Ang HM, Tade MO, Wang S. Co_3O_4 nanocrystals with predominantly exposed facets: synthesis, environmental and energy applications. *J. Mater. Chem. A.* 2013;1(46):14427-42.

250. Yu P, Zhang X, Wang D, Wang L, Ma Y. Shape-Controlled Synthesis of 3D Hierarchical MnO_2 Nanostructures for Electrochemical Supercapacitors. *Cryst. Growth Des.* 2008;9(1):528-33.

251. Duan X, Yang J, Gao H, Ma J, Jiao L, Zheng W. Controllable hydrothermal synthesis of manganese dioxide nanostructures: shape evolution, growth mechanism and electrochemical properties. *CrystEngComm*. 2012;14(12):4196-204.
252. O'Carroll D, Sleep B, Krol M, Boparai H, Kocur C. Nanoscale zero valent iron and bimetallic particles for contaminated site remediation. *Adv. Water Resour.* 2013;51(0):104-22.
253. Crane RA, Scott TB. Nanoscale zero-valent iron: Future prospects for an emerging water treatment technology. *J. Hazard. Mater.* 2012;211–212(0):112-25.
254. Ryu A, Jeong SW, Jang A, Choi H. Reduction of highly concentrated nitrate using nanoscale zero-valent iron: Effects of aggregation and catalyst on reactivity. *Appl. Catal., B*. 2011;105(1–2):128-35.
255. Ghanbari F, Moradi M, Manshouri M. Textile wastewater decolorization by zero valent iron activated peroxydisulfate: Compared with zero valent copper. *J. Environ. Chem. Eng.* 2014;2(3):1846-51.
256. Xiong X, Sun B, Zhang J, Gao N, Shen J, Li J, et al. Activating persulfate by Fe⁰ coupling with weak magnetic field: Performance and mechanism. *Water Res.* 2014;62(0):53-62.
257. Song H, Carraway ER. Reduction of Chlorinated Ethanes by Nanosized Zero-Valent Iron: Kinetics, Pathways, and Effects of Reaction Conditions. *Environ. Sci. Technol.* 2005;39(16):6237-45.
258. Liu H, Xu J, Li Y, Li Y. Aggregate Nanostructures of Organic Molecular Materials. *Acc. Chem. Res.* 2010;43(12):1496-508.
259. Sun H, Zhou G, Liu S, Ang HM, Tadé MO, Wang S. Nano-Fe⁰ Encapsulated in Microcarbon Spheres: Synthesis, Characterization, and Environmental Applications. *ACS Appl. Mater. Interfaces*. 2012;4(11):6235-41.
260. Li Y, Zhang Y, Li J, Zheng X. Enhanced removal of pentachlorophenol by a novel composite: Nanoscale zero valent iron immobilized on organobentonite. *Environ. Pollut.* 2011;159(12):3744-9.
261. Zhu H, Jia Y, Wu X, Wang H. Removal of arsenic from water by supported nano zero-valent iron on activated carbon. *J. Hazard. Mater.* 2009;172(2–3):1591-6.
262. Chen Z, Jin X, Chen Z, Megharaj M, Naidu R. Removal of methyl orange from aqueous solution using bentonite-supported nanoscale zero-valent iron. *J. Colloid Interface Sci.* 2011;363(2):601-7.
263. Karabelli D, Ünal S, Shahwan T, Eroğlu AE. Preparation and characterization of alumina-supported iron nanoparticles and its application for the

removal of aqueous Cu^{2+} ions. *Chem. Eng. J.* 2011;168(2):979-84.

264. Jiang Z, Lv L, Zhang W, Du Q, Pan B, Yang L, et al. Nitrate reduction using nanosized zero-valent iron supported by polystyrene resins: Role of surface functional groups. *Water Res.* 2011;45(6):2191-8.

265. Chen L, Xu Z, Dai H, Zhang S. Facile synthesis and magnetic properties of monodisperse Fe_3O_4 /silica nanocomposite microspheres with embedded structures via a direct solution-based route. *J. Alloys Compd.* 2010;497(1-2):221-7.

266. Lai GS, Zhang HL, Han DY. A novel hydrogen peroxide biosensor based on hemoglobin immobilized on magnetic chitosan microspheres modified electrode. *Sens. Actuators, B.* 2008;129(2):497-503.

267. Yao Y, Xu C, Qin JC, Wei FY, Rao MN, Wang S. Synthesis of Magnetic Cobalt Nanoparticles Anchored on Graphene Nanosheets and Catalytic Decomposition of Orange II. *Ind. Eng. Chem. Res.* 2013;52(49):17341-50.

268. Yao Y, Miao S, Liu S, Ma LP, Sun H, Wang S. Synthesis, characterization, and adsorption properties of magnetic Fe_3O_4 @graphene nanocomposite. *Chem. Eng. J.* 2012;184(0):326-32.

269. Guo P, Cui L, Wang Y, Lv M, Wang B, Zhao XS. Facile Synthesis of ZnFe_2O_4 Nanoparticles with Tunable Magnetic and Sensing Properties. *Langmuir.* 2013;29(28):8997-9003.

270. Zhang S, Li J, Zeng M, Zhao G, Xu J, Hu W, et al. In Situ Synthesis of Water-Soluble Magnetic Graphitic Carbon Nitride Photocatalyst and Its Synergistic Catalytic Performance. *ACS Appl. Mater. Interfaces.* 2013;5(23):12735-43.

271. McDonald KJ, Choi K-S. Synthesis and Photoelectrochemical Properties of $\text{Fe}_2\text{O}_3/\text{ZnFe}_2\text{O}_4$ Composite Photoanodes for Use in Solar Water Oxidation. *Chem. Mater.* 2011;23(21):4863-9.

272. Aranishi K, Jiang HL, Akita T, Haruta M, Xu Q. One-step synthesis of magnetically recyclable Au/Co/Fe triple-layered core-shell nanoparticles as highly efficient catalysts for the hydrolytic dehydrogenation of ammonia borane. *Nano Res.* 2011;4(12):1233-41.

273. Wang Y, Sun H, Ang HM, Tadé MO, Wang S. Facile Synthesis of Hierarchically Structured Magnetic $\text{MnO}_2/\text{ZnFe}_2\text{O}_4$ Hybrid Materials and Their Performance in Heterogeneous Activation of Peroxymonosulfate. *ACS Appl. Mater. Interfaces.* 2014;6(22):19914-23.

274. Jia Z, Ren D, Liang Y, Zhu R. A new strategy for the preparation of porous zinc ferrite nanorods with subsequently light-driven photocatalytic activity. *Mater. Lett.* 2011;65(19-20):3116-9.

275. Wang M, Ai Z, Zhang L. Generalized Preparation of Porous Nanocrystalline ZnFe₂O₄ Superstructures from Zinc Ferrioxalate Precursor and Its Superparamagnetic Property. *J. Phys. Chem. C*. 2008;112(34):13163-70.
276. Habibi MH, Habibi AH, Zendehtdel M, Habibi M. Dye-sensitized solar cell characteristics of nanocomposite zinc ferrite working electrode: Effect of composite precursors and titania as a blocking layer on photovoltaic performance. *Spectrochim. Acta, Part A*. 2013;110(0):226-32.
277. Tahir AA, Wijayantha KGU. Photoelectrochemical water splitting at nanostructured ZnFe₂O₄ electrodes. *J. Photochem. Photobiol., A*. 2010;216(2-3):119-25.
278. Geim AK, Novoselov KS. The rise of graphene. *Nat. Mater*. 2007;6(3):183-91.
279. Zhu Y, Murali S, Cai W, Li X, Suk JW, Potts JR, et al. Graphene and graphene oxide: synthesis, properties, and applications. *Adv. Mater*. 2010;22(35):3906-24.
280. Loh KP, Bao Q, Ang PK, Yang J. The chemistry of graphene. *J. Mater. Chem*. 2010;20(12):2277-89.
281. Liu S, Peng W, Sun H, Wang S. Physical and chemical activation of reduced graphene oxide for enhanced adsorption and catalytic oxidation. *Nanoscale*. 2014;6(2):766-71.
282. Peng W, Liu S, Sun H, Yao Y, Zhi L, Wang S. Synthesis of porous reduced graphene oxide as metal-free carbon for adsorption and catalytic oxidation of organics in water. *J. Mater. Chem. A*. 2013;1(19):5854-9.

Chapter 3: 3 D-hierarchically Structured MnO₂ for Catalytic Oxidation of Phenol Solutions by Activation of Peroxymonosulfate: Structure Dependence and Mechanism

ABSTRACT

Hierarchical materials have facilitated fascinating applications in heterogeneous catalysis due to that micro-sized bulk is easily separable and nano-sized sub-blocks can significantly enhance catalytic performance. In this chapter, corolla-like δ -MnO₂ with sub-blocks of nanosheets, and urchin-shaped α -MnO₂ with sub-blocks of nanorods were synthesized by a simple hydrothermal route. The hydrothermal temperature significantly influenced the crystal structure, morphology and textural structure of the obtained three-dimensional (3D) MnO₂ catalysts. The catalytic activities of three samples prepared at 60, 100 and 110 °C (denoted as Mn-60, -100 and -110, respectively) were thoroughly evaluated by activation of peroxydisulfate (PDS) for catalytic oxidation of phenol solutions. Based on first-order kinetics, the rate constants of Mn-60, -100 and -110 catalysts were determined to be 0.062, 0.132, and 0.075 min⁻¹, respectively. The activation energy of Mn-100 in catalytic oxidation of phenol solutions was estimated to be 25.3 kJ/mol. The catalytic stability of Mn-100 was also tested and discussed by monitoring Mn leaching. Electron paramagnetic resonance (EPR), quenching tests, total organic carbon (TOC) analysis and identification of intermediates were applied to illustrate the activation processes of PDS and the mechanism of phenol degradation.

3.1. Introduction

Aqueous organic pollutants, discharged from natural processes, industrial activities, and households, are detrimental to human health and the eco-environment. As one of the important organic pollutants in wastewater, phenol is widely used in many industrial processes, such as chemical, petrochemical and pharmaceutical industries.(1) Moreover, phenol and phenolic compounds are not only resistant to natural degradation, but toxic even at a low concentration, therefore development of effective strategies for removal of phenolics from water are highly in demand.(2, 3) In the past a few years, advanced oxidation processes (AOPs) have been widely applied owing to the promising capability of complete decomposition of the organics. As one of typical AOPs, Fenton reaction has demonstrated to be highly effective in complete removal of pollutants by producing hydroxyl radicals ($\cdot\text{OH}$).(4) To overcome the limitations of Fenton reaction, such as low pH 3-4, large amount of sludge produced, and metal leaching, sulfate radicals were introduced as an alternative to hydroxyl radicals.(5-7) Sulfate radicals can be effectively activated in both homogeneous (8, 9) and heterogeneous cobalt catalysis,(10, 11) metal leaching problem leading to secondary contamination can thus be minimized. However, for cobalt catalysis, neither homogeneous nor heterogeneous reactions can completely prevent the cobalt leaching, which might lead to severe health problems.(12-14) Therefore, sourcing novel catalysts for activation of PMS is critical in employment of sulfate radicals for environmental remediation.

Manganese oxides are common metal oxides present in soils and have a low toxicity to the environment. As promising catalysts alternative to Fe-based materials, a variety of Mn oxides were applied in Fenton or Fenton-like reactions for producing hydroxyl radicals.(15, 16) In a recent study on supported cobalt catalysts, we for the first time discovered that $\alpha\text{-MnO}_2$ has a moderate activity in activation of PMS.(17) Thereafter, several $\alpha\text{-MnO}_2$ catalysts in forms of nanospheres, nanorods and nan-

owires were developed and used in activation of PMS. Crystalline phase of the materials was found to play a critical role in the catalytic oxidation of phenol. (18) The effects of oxidation states of manganese on activation of PMS were also investigated by employing a series of MnO_x (MnO , MnO_2 , Mn_2O_3 and Mn_3O_4). It was suggested that the activity follows an order of $Mn_2O_3 > MnO > Mn_3O_4 > MnO_2$.(19) Shape-controlled synthesis can significantly improve the catalytic activity of the oxides, owing to the intrinsic atomic arrangements of the exposed facets.(20) Mn_2O_3 shaped in cube, octahedra and truncated octahedra showed different activities in phenol degradation, with the highest phenol oxidation achieved on cubic Mn_2O_3 .(21) α -, β - and γ - MnO_2 materials presented in morphologies of nanowires, nanorods and nanofibers respectively were examined in catalytic oxidation of phenol, and α - MnO_2 showed the highest activity.(22) So far, hierarchically structured Mn oxides have not been employed for activation of PMS in environmental applications. Moreover, the PMS activation processes have not been well illustrated.

Three-dimensional (3D) structures are of much importance because of their attractive physical and chemical properties. (23-25) It would be very interesting to apply hierarchical materials in heterogeneous catalysis because they can both remain easy separation of bulk materials and provide a high performance due to the nanostructure. The successful synthesis of 3D manganese oxides has been reported recently. Li et al. (26) reported a homogeneous catalytic route to prepare urchin-like sphere network and nanowire network of α - MnO_2 hierarchical nanostructures. Yu et al. (27) reported 3D sea-urchin like and 3D clew-like MnO_2 by a hydrothermal method using $MnSO_4$ and $K_2S_2O_8$ as precursors and tested their performance as electrochemical supercapacitors. Duan et al. (28) synthesized 3D nanocube-like MnO_2 by using $KMnO_4$, $Mn(AC)_2 \cdot 4H_2O$ and glucose as precursors and poly(vinylpyrrolidone) as a surfactant.

In this chapter, we demonstrated a facile one-pot hydrothermal method to synthesize corolla and sea-urchin shaped MnO_2 nanostructures by reduction of potassium permanganate solution under hydrochloric acid condition without any surfactant. MnO_2

in 3D hierarchical structures were selectively obtained by simply varying the reaction temperature in the hydrothermal process and showed microscale in diameter and nanoscale in sub-blocks of nanosheets or nanorods. The prepared catalysts showed outstanding catalytic activity in activation of PMS for degradation of phenol solutions and remarkable stability for repeating uses. The PMS activation processes and the mechanism of catalytic oxidation of phenol on MnO_2 were further investigated by means of EPR studies.

3.2. Experimental Section

3.2.1. Materials

Potassium permanganate (99.8%), hydrochloric acid (37%), and phenol (99%), ethanol (99.9%) and tert-butyl alcohol (99.9%) were purchased from Sigma-Aldrich. Oxone[®] ($2\text{KHSO}_5 \cdot \text{KHSO}_4 \cdot \text{K}_2\text{SO}_4$, PMS) was obtained from Aldrich. 5,5-Dimethyl-1-pyrroline (DMPO, >99.0%) and commercial activated Mn (IV) dioxide (99.9%) were obtained from Fluka. All chemicals were used as received without further purification.

3.2.2. Synthesis of hierarchically structured MnO_2

3 D-hierarchically structured MnO_2 was prepared by a modified hydrothermal process with reduction of KMnO_4 reported by Xiao et al. (29) The concentration of precursors and hydrothermal temperatures were modified to obtain desired nanostructured MnO_2 materials. Scheme 3.1 shows the preparation procedure of MnO_2 catalysts. In a typical synthesis, 2.8 mmol (0.45 g) of KMnO_4 was first dissolved in 80 mL of deionized water. Then 0.027 mol of HCl (37 wt%) was added to the solution drop wisely under magnetic stirring to form the precursor solution. After stirring for about 20 min, the solution was transferred into a Teflon-lined stainless steel auto-

clave with the capacity of 120 mL. The autoclave was then heated in an electric oven at 60, 100 and 110 °C for 12 h, respectively. After the autoclave was naturally cooled down to room temperature, each of the black precipitate was harvested by vacuum filtration and washed with deionized water for 3 times before being dried at 60 °C overnight. Referring to the hydrothermal temperature, the obtained samples were labelled as Mn-60, -100 and -110, respectively.



Scheme 3.1. Synthesis procedure of MnO₂ nanostructures.

3.2.3. Characterization

The structure and morphology of the materials were observed on a ZEISS NEON 40EsB scanning electron microscope (SEM). XRD (X-ray diffraction) patterns were obtained on a Bruker D8 diffractometer (Bruker-AXS, Karlsruhe, Germany) using filtered Cu K α radiation ($\lambda = 1.5418 \text{ \AA}$) with an accelerating voltage of 40 kV and a current of 30 mA. The Brunauer–Emmett–Teller (BET) specific surface area and the pore size distribution of the samples were evaluated by N₂ adsorption/desorption using a Micromeritics Tristar 3000. Prior to measurement the samples were degassed at 100 °C overnight under vacuum condition.

3.2.4. PMS activation and catalytic oxidation

The catalytic oxidation of phenol was carried out in a 500 mL reactor containing 20

mg/L of phenol solution with a constant stirring at 400 rpm. The reactor was attached to a stand and dipped into a water bath with a temperature controller. Unless specifically stated, the reaction temperature was 25 °C. In a typical test, firstly, 0.1 g catalyst was added into the phenol solution for 30 min to achieve adsorption-desorption equilibrium, then Oxone[®] was added into the solution at 2 g/L. At certain intervals, 1 mL aqueous sample was withdrawn by a syringe and filtered into a HPLC vial, which was priorly injected by 0.5 mL of methanol to quench the reaction. For catalytic phenol degradation, each experiment was repeated in order to obtain error bars on the plots. The concentration of phenol was analyzed using a Varian HPLC with a UV detector at wavelength of 270 nm. A C-18 column was used to separate the organics while the mobile phase with a flow rate of 1 mL/min was made of 30% CH₃CN and 70% water.

Total organic carbon (TOC) was determined using a Shimadzu TOC-5000 CE analyzer for selected samples. For the measurement of TOC, 10 mL sample was extracted at a fixed interval and quenched with 10 mL of 0.3 M sodium nitrite solution and then analyzed.⁽⁷⁾ The intermediates of phenol degradation were investigated by the HPLC. Classical quenching tests were performed on corolla-like MnO₂ (Mn-100) using ethanol (EtOH) and tert-butyl alcohol (TBA) as quenching agents to distinguish the dominant reactive species for phenol degradation.

For the recycle tests of the catalyst, the material was obtained by vacuum filtration and washed with ultrapure water for several times after each run. Then the washed catalyst was dried in an oven at 60 °C for 12 h. For radical detection, various electron paramagnetic resonance (EPR) experiments were performed on a Bruker EMX-E spectrometer (Germany) with DMPO as a spin-trapping agent.

3.3. Results and discussion

3.3.1. Characterization of the hierarchical materials

Fig. 3.1 shows XRD patterns of three MnO₂ nanostructures. Mn-60 and Mn-100 display similar XRD patterns. Diffraction peaks at 12.3, 25.5, 36.7 and 66.2° were observed, corresponding to the crystal planes of (0 0 1), (0 0 2), (1 1 1) and (3 1 1), respectively. The XRD patterns of Mn-60 and Mn-100 were identified to pure layered birnessite-type MnO₂ (JCPDS No. 80-1098, monoclinic, *C2/m*, $a=5.15$ Å, $b=2.84$ Å, $c=7.17$ Å), denoted as δ -MnO₂.(29) While the pattern of Mn-110 confirmed the formation of α -MnO₂ (JCPDS No. 44-0141, tetragonal, *I4/m*, $a=b=9.78$ Å, $c=2.86$ Å).(27) The characteristic peaks in Mn-60 pattern were much broader than those of Mn-100, indicating that the crystallinity of Mn-60 sample was not as high as Mn-100. As seen, at hydrothermal temperature below 100 °C, the crystal structures of the synthesized samples were similar, while crystalline structure would be changed at the temperature above 100 °C. Moreover, since no other characteristic peaks were observed, the obtained samples were confirmed to be of high purity.

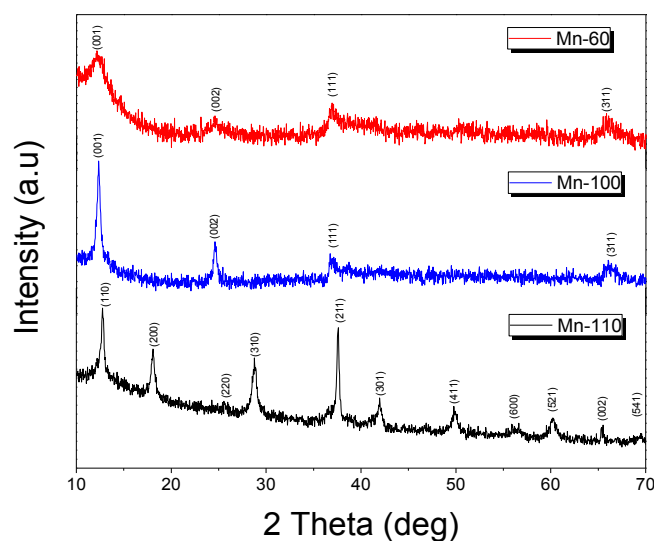


Figure 3.1. XRD patterns of Mn-60, -100 (δ -MnO₂) and -110 (α -MnO₂).

The reactions involved in the hydrothermal process for MnO₂ formation can be briefly described as follows. (26)

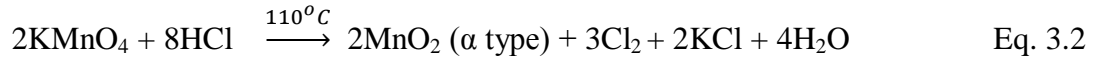
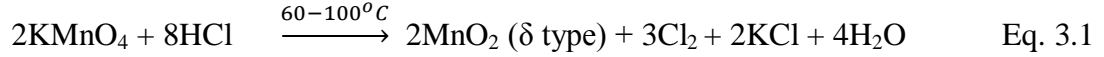


Fig. 3.2 shows SEM images of the synthesized samples for displaying their structure and morphology. Fig. 3.2 (a) and (b) illustrate SEM images of Mn-60. It can be observed that this product is presented as uniform δ -MnO₂ nanosphere with an average diameter of 200 nm, which is consisted of developing nanosheets on the surface. The SEM images of Mn-100 are shown in Fig. 3.2 (c) and (d). The microsphere/nanosheet hierarchical nanostructures with a diameter of 2-3 μm were observed. Compared with Mn-60, the nanosheets on Mn-100 surface grew more compact and deeper, and thus providing a larger diameter with more corolla-like morphology. The growth of the nanosheets is significantly affected by the hydrothermal temperature (60–100 °C), and the nanosheets on the MnO₂ nuclei gradually develop and grow up perpendicular to the MnO₂ nuclei. The growth mechanism from MnO₂ nuclei to corolla-like microspheres can be ascribed as follows. In the first phase, preliminary crystallization process occurred. A large number of nuclei were formed within a rather short time period. With the aid of pressure and temperature, the nuclei would develop larger. Meanwhile, the heterogeneous growth of 2D nanosheets on these nuclei happened and the diameter of the nanoparticles as well as the compactness of the 2D nanosheets within the corolla were strongly dependent on the precursors' concentrations.(30)

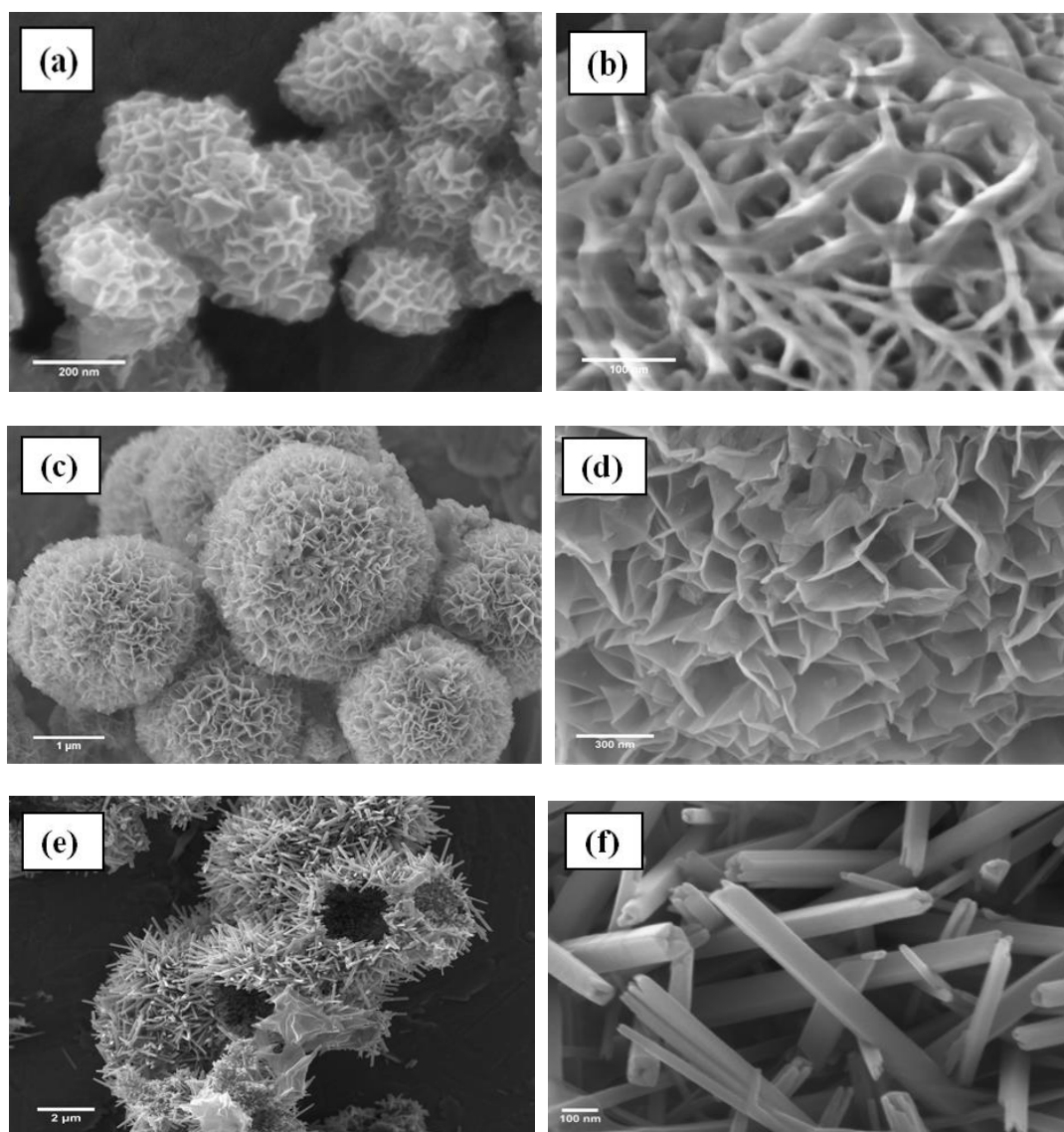
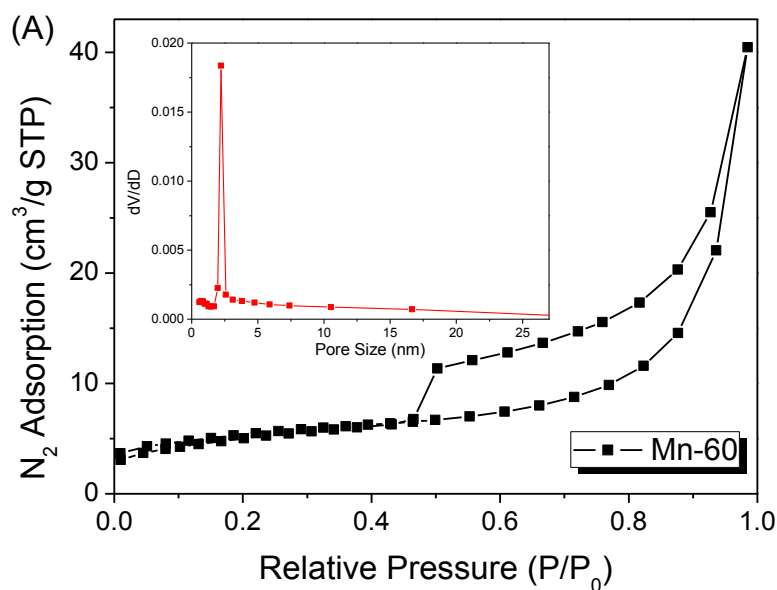


Figure 3.2. SEM images of Mn-60 (a and b), -100 (c and d) and -110 (e and f).

When hydrothermal temperature was further increased to 110 °C, corolla-like microspheres consisting of 2D nanosheets converted to hollow sea-urchin shaped MnO_2 with a diameter of 3-4 μm (Fig. 3.2 (e) and (f)). The hollow sea-urchin shaped MnO_2 particles are made of straight hollow tetragonal nanorods with a uniform diameter of 30-40 nm. Comparison of the three samples suggested that MnO_2 experienced a phase change at around 100 - 110 °C in current synthesis route, as also confirmed by XRD patterns.

Fig. 3.3 shows N_2 adsorption/desorption isotherms and the associated pore size dis-

tribution of three MnO₂ samples. It can be seen that all the three samples possess the type IV isotherm with a type H3 hysteresis loop indicating a mesoporous structure. (31) Comparison of the specific surface area and pore size distribution was shown in Table 3.1. It was found that Mn-100 presents the highest surface area of 41.7 m²/g and a large pore volume of 0.149 cm³/g. While Mn-60 and Mn-110 show the similar surface area (19.4 and 17.5 m²/g, respectively). The difference in surface areas of the samples was also reflected by SEM images shown previously. The highest surface area and pore volume of Mn-100 were attributed to the compact and deep 2D nanosheets. While the scattered and shallow layer of Mn-60 sample and urchin-like structure of Mn-110 would not contribute much to either surface area or pore volume.



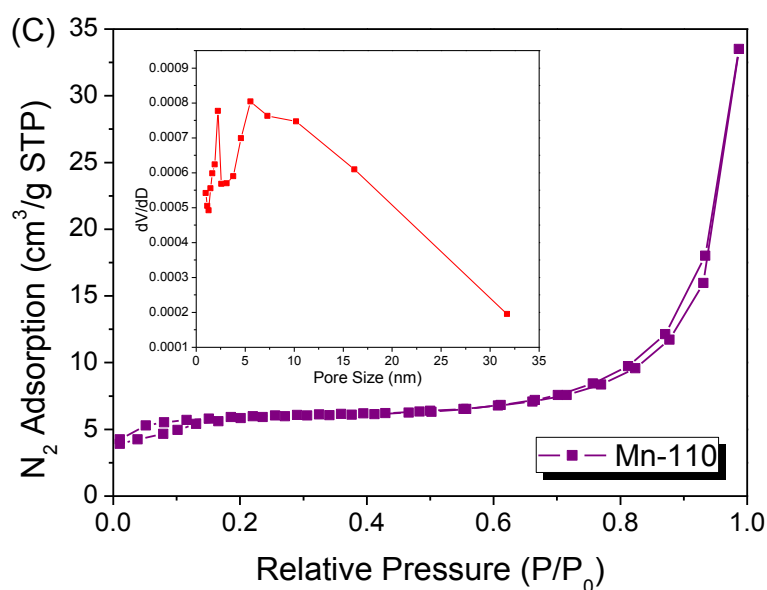
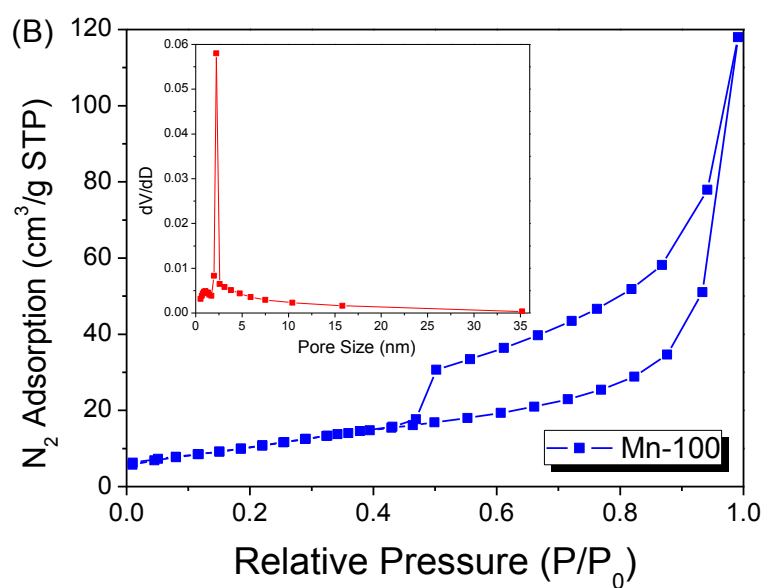


Figure 3.3. Nitrogen sorption isotherms and pore size distribution of Mn-60, -100 and -110.

The hysteresis loops of Mn-60 and Mn-100 samples are similar, and are broad in a lower relative pressure range ($0.45 < P/P_0 < 0.9$). Moreover, both samples have a rather narrow pore size distribution concentrating at a similar position around 2.5 nm and thus resulting in a similar average pore size (6.7 nm for Mn-60 and 6.3 nm for Mn-100).

Table 3.1. Textural property of MnO₂ catalysts and their activities in phenol degradation.

Catalyst	Surface area (S _{BET} m ² /g)	Pore volume (cm ³ /g)	Average pore diameter (nm)	First-order rate constant (min ⁻¹)	R ²
Mn-60	19.4	0.0493	6.7	0.059	0.992
Mn-100	41.7	0.149	6.3	0.19	0.993
Mn-110	17.5	0.0412	11.6	0.069	0.999

Comparatively, sea-urchin-like sample (Mn-110) demonstrated a narrow hysteresis loop at a relative pressure (P/P_0) range of 0.6 to 0.95 and a bimodal pore size distribution concentrating at 2.2 and 6.3 nm, respectively (Fig. 3.3(C)). Based on the SEM image shown in Fig. 3.2 (f), the occurrence of the bimodal pore distribution can be ascribed to the hollow structure of the tetragonal nanorods and the void space enclosed by the tetragonal nanorods. Moreover, due to the hollow structure and the void space, the average pore size of Mn-110 was almost double as compared to that of Mn-60 and Mn-100.

3.3.2. Catalytic oxidation of phenol

Fig. 3.4 presents phenol removal profiles under various reaction conditions. In order to provide benchmark for the catalytic performance of MnO₂, control experiments were carried out to investigate PMS self-oxidation and catalyst self-adsorption. It was found that without MnO₂ as the catalyst, PMS could not induce significant phenol degradation. Less than 4% of phenol was degraded after 120 min, indicating that, at current experimental conditions, thermal activation of PMS for production of reactive sulfate radicals is negligible. For adsorption on various MnO₂ nanostructures without PMS, similar trend was observed and less than 5% of phenol was adsorbed in 120 min. Corolla-like MnO₂ (Mn-100) presented a higher adsorption than others due to the higher BET surface area and larger pore volume. The fluctuation of phenol removal profiles in the first 30 min can be ascribed to achieving adsorp-

tion/desorption equilibrium. For catalytic reactions with the presence of PMS, all the three MnO₂ nanostructures demonstrated superior catalytic activity to the commercial activated MnO₂ which provided a less than 20% phenol degradation after 120 min. Corolla-like Mn-100 showed the highest activity for activation of PMS to produce sulfate radicals and 100% phenol removal was achieved within 30 min. Sea-urchin like MnO₂ (Mn-110) possessed a lower activity and provided 100% phenol removal in 45 min. While Mn-60 presented the least phenol degradation rate and 100% phenol removal was achieved after 60 min.

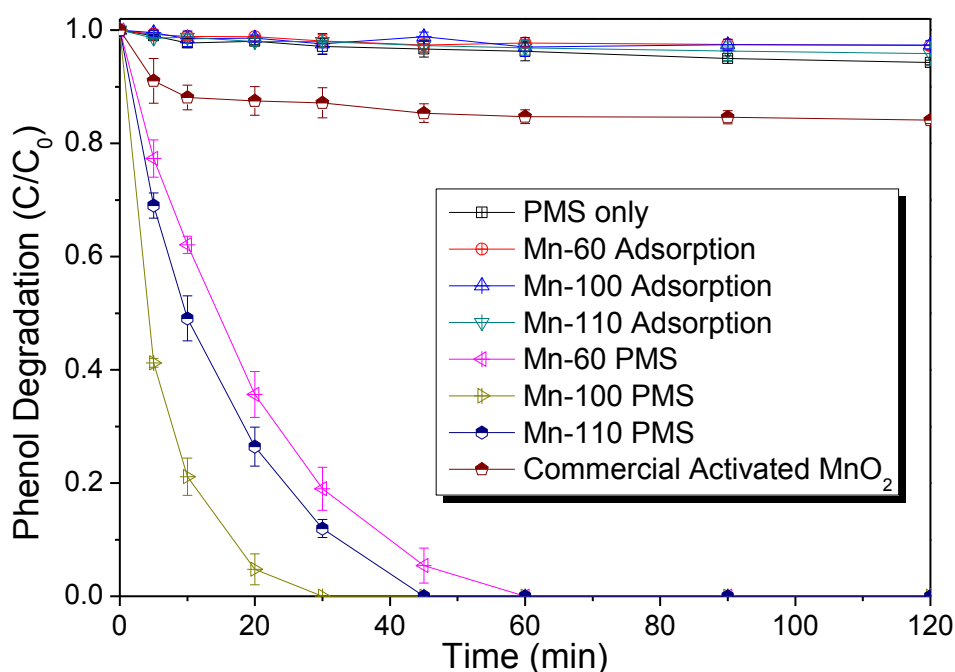


Figure 3.4. Phenol removal on different materials in adsorption and reaction. Reaction conditions: [phenol]₀ = 20 mg/L; catalyst loading = 0.2 g/L; Oxone[®] loading = 2.0 g/L; Temperature: 25 °C.

Previous researches have shown that Co and Mn based catalytic reactions for phenol degradation using PMS as an oxidant followed a first-order kinetic model. (17, 21, 32-34) In this study, a first-order kinetic model (Eq. 3.3) was applied for evaluation of the kinetics of phenol degradation.

$$\ln\left(\frac{C}{C_0}\right) = -kt \quad \text{Eq. 3.3}$$

Where C and C_0 are the phenol concentrations at time (t) and $t = 0$, respectively and k is the reaction rate constant. Fig. 3.5 shows that phenol degradation curves of three MnO_2 nanostructures can be fitted well by the first-order kinetics with high values of regressions coefficients ($R^2 > 0.992$). The reaction rate constants for the three catalysts are provided in Table 1. As seen, the reaction rate constant of corolla-like MnO_2 (Mn-100) was about 3 times higher than Mn-60.

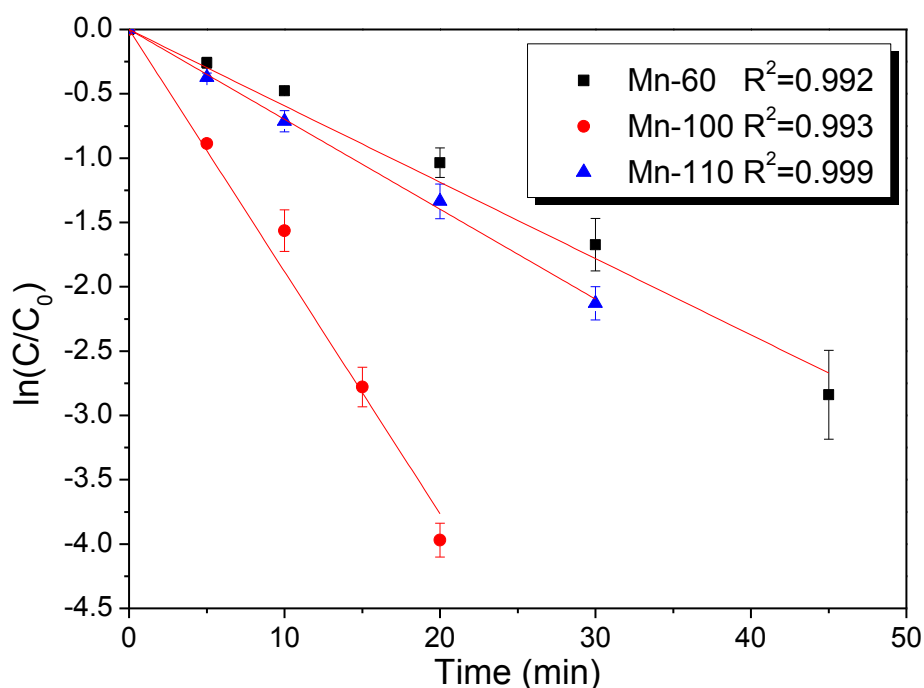


Figure 3.5. First order kinetic model of catalytic phenol reactions.

It was evidenced that MnO_2 nanostructures in various shapes showed different catalytic performances in phenol degradation, and the catalytic activity of corolla-like $\delta\text{-MnO}_2$ is higher than sea-urchin like $\alpha\text{-MnO}_2$. It was also deduced that the high catalytic activity of corolla-like $\delta\text{-MnO}_2$ can be ascribed to the higher surface area and the highly active surface facet with the arrangement of inherent distinction of surface atoms. (20, 21) The shape-dependent catalytic performances of manganese oxides were also reported in other catalyst systems. Fang et al. (35) prepared K_xMnO_2

nanostructures with two different morphologies (honeycomb and hollow needle), and evaluated their catalytic activity in oxidative decomposition of formaldehyde and found that honeycomb K_xMnO_2 showed a superior catalytic activity to hollow needle K_xMnO_2 . Zhang et al. (31) investigated shape-controlled Mn_3O_4 nanocrystals and their catalysis for degradation of methylene blue, and found that octahedral shaped Mn_3O_4 exposing the facet of (111) possessed an excellent catalytic activity for H_2O_2 activation.

Fig. 3.6 reveals the effect of reaction temperature on phenol degradation using corolla-like MnO_2 (Mn-100) as the catalyst. A general trend can be observed that higher temperature will result in an increase in reaction rate. As seen, phenol degradation could reach 100% at 20 min when temperature was elevated to 35 °C. While at 25 °C, phenol was able to be fully removed in 30 min. The relationship between reaction rate and temperature reveals that the PMS activation process is an endothermic reaction: higher temperature would drive the reaction to produce more reactive sulfate and hydroxyl radicals and thus enhance the phenol degradation efficiency. To evaluate the activation energy, reaction rate constants at varying temperature were determined on the basis of the first-order kinetics and the correlation between the rate constants and reaction temperature was fitted by the Arrhenius equation. The relationship was shown in the inset of Fig. 3.6. The activation energy of Mn-100 catalytic reaction was then obtained to be 25.3 kJ/mol.

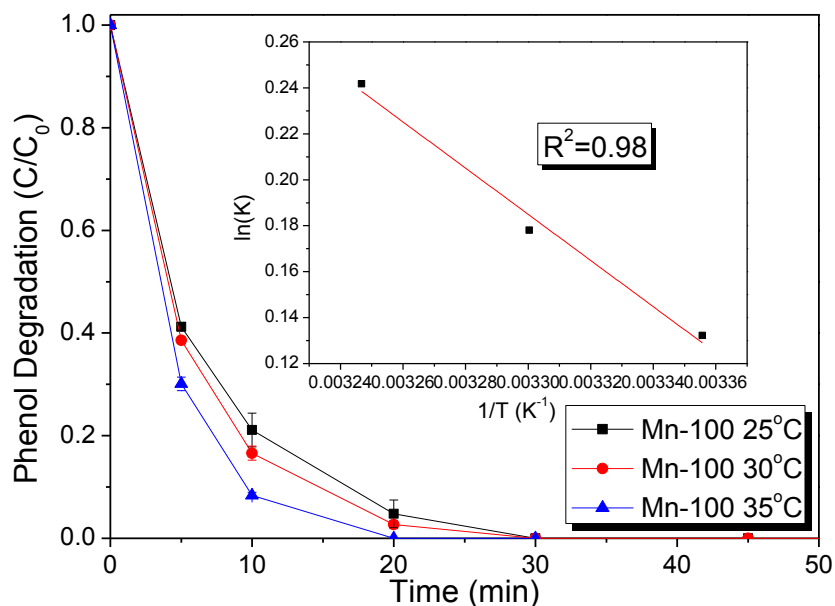


Figure 3.6. Effect of reaction temperature on phenol degradation and estimation of activation energy. Reaction conditions: $[\text{phenol}]_0 = 20 \text{ mg/L}$; Catalyst loading = 0.2 g/L ; Oxone loading = 2.0 g/L .

Table 3.2. Comparison of activation energy in Mn-based catalysis.

Catalyst	Organics	Activation energy (kJ/mol)	Reference
Mn_2O_3 sphere	Phenol	11.4	(19)
Mn_2O_3 cube	Phenol	61.2	(21)
$\alpha\text{-MnO}_2$ nanowire	Phenol	21.9	(22)
$\text{Mn}_3\text{O}_4\text{-rGO}$	Orange II	49.5	(36)
corolla-like MnO_2	Phenol	25.3	This work

For Mn activation of PMS for organics degradation, a few of investigations have reported the kinetics and activation energies. For comparison, Table 3.2 summarizes the activation energies obtained from previous researches on PMS activation using Mn-based materials. As seen, corolla-like $\delta\text{-MnO}_2$ presented lower activation energy than most of manganese oxide catalysts.

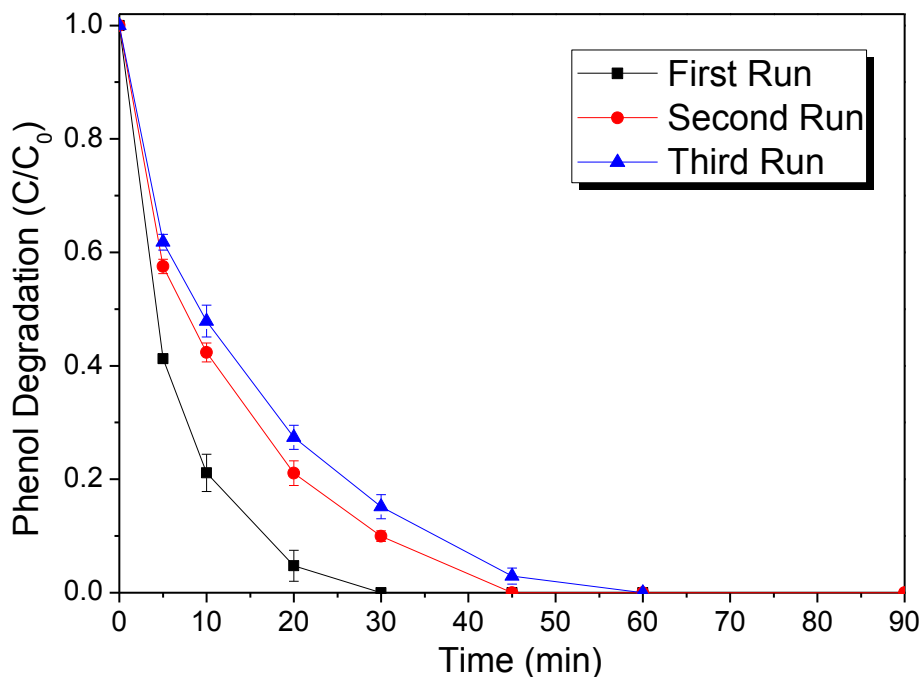


Figure 3.7. Phenol degradation on Mn-100 at different runs after repeated uses. Reaction conditions: $[\text{phenol}]_0 = 20 \text{ mg/L}$; Catalyst loading = 0.2 g/L ; Oxone[®] loading = 2.0 g/L ; and $T = 25 \text{ }^\circ\text{C}$.

Fig. 3.7 shows the activity of recycled corolla-like $\delta\text{-MnO}_2$ (Mn-100) by simple water washing in phenol degradation. As can be seen, corolla-like $\delta\text{-MnO}_2$ shows a slight decrease in the second run but 100% phenol removal was still obtained within 45 min. While in the third run, the catalyst presented a similar activity as the second run, suggesting the high stability of corolla-like $\delta\text{-MnO}_2$. After 3 h reaction, the reaction solutions were collected and the concentrations of leached Mn ions were analyzed by atomic absorption spectroscopy (AAS SpectrAA 110, Varian). The concentration of Mn remained in the solution was detected to be around 3 ppm, which suggests the loss of catalyst activity caused by Mn leaching is negligible. The activity decrease for the second run could be attributed to the adsorption of reaction intermediates on the catalyst surface. By comparison of the reaction rates of the second and third run, one can be seen that these reaction intermediates attached on catalyst surface cannot be removed by the simple water washing process. In a recent study of phenol degradation on Mn_2O_3 , phenol degradation decreased from 100% to 27%, but

could be recovered to be almost 100% after a heat treatment of Mn_2O_3 at 500°C for 1 h.(19) The study strongly suggested that these intermediates can be completely removed by calcination either in air or N_2 atmosphere. (32, 37)

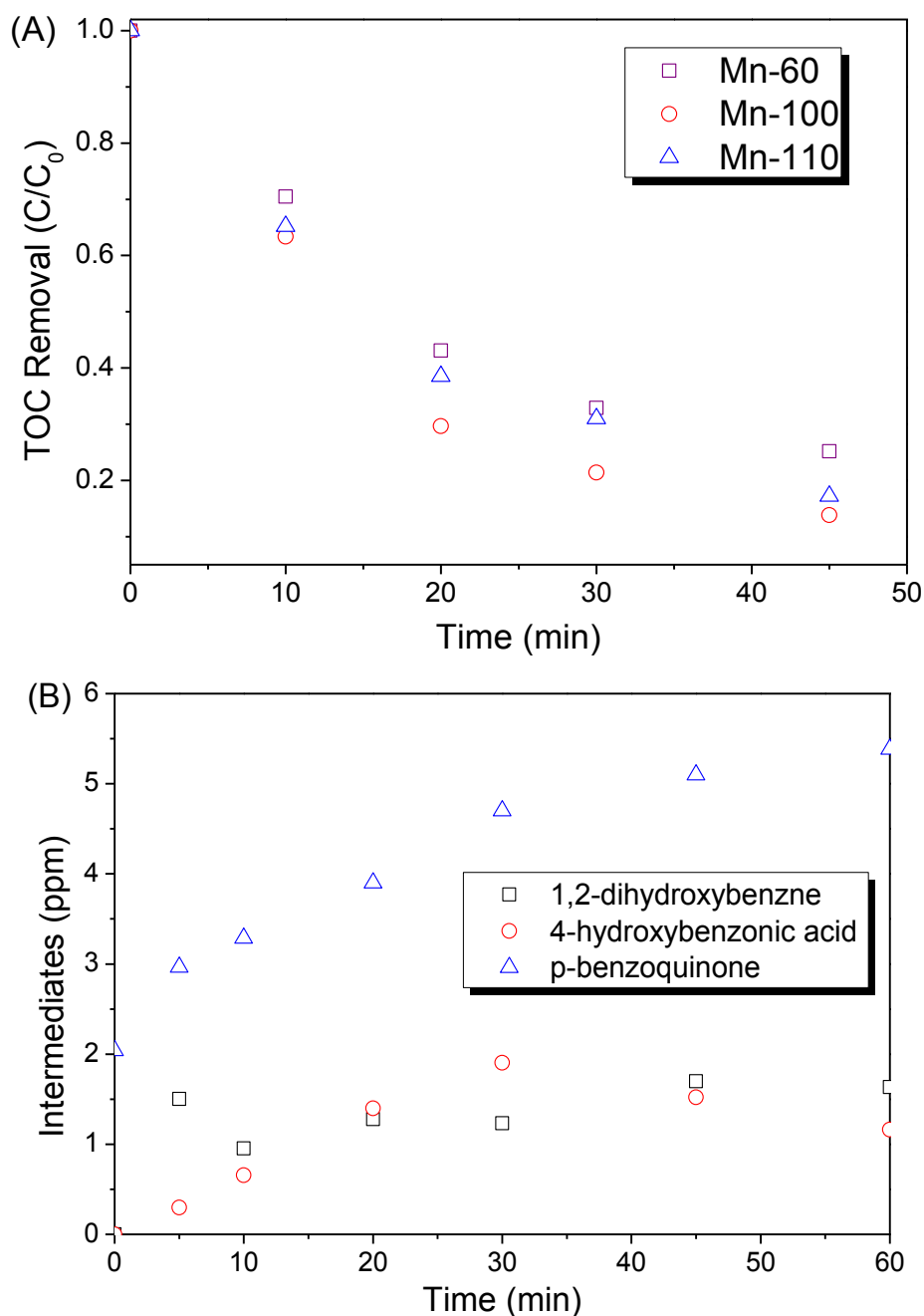


Figure 3.8. TOC removal profiles and variation of intermediate concentrations during phenol degradation. (A) TOC removal efficiencies during phenol degradation on various 3D MnO_2 catalysts. (B) Variation of intermediate concentrations during phenol degradation on Mn-100.

Fig. 3.8(A) presents the TOC removal profiles of phenol decomposition on various 3D MnO₂ catalysts. All three catalysts were able to provide efficient TOC reduction in a short time. Mn-100 provided the best TOC reduction and more than 80% of TOC was removed and transferred into inorganic carbon forms within 45 min. While for Mn-60, around 70% of TOC was reduced after 45 min. The order of the TOC removal rates were in accordance with the order of phenol degradation rates on the various catalysts.

In order to investigate the reaction intermediates, the reaction solutions at certain intervals were analyzed using HPLC with a UV detector set at wavelength of 270 nm and the mobile phase flow rate of 0.2 mL/min. It was found that *p*-benzoquinone, 4-hydroxybenzoic acid and 1,2-dihydroxybenzene were the major intermediates during the catalytic phenol degradation reaction. The concentration variations of the intermediates with time on Mn-100 are shown in Fig. 3.8(B). As seen, compared with the concentration variation of 1,2-dihydroxybenzene, *p*-benzoquinone and 4-hydroxybenzoic acid were the more abundant aromatic intermediates, suggesting that hydroxylation took place predominantly in the para position.(17)

3.3.3. PMS activation processes on MnO₂

In activation of PMS using metal-based catalysts, it is well accepted that sulfate radicals (SO₄^{•-}) are the key active species for degradation of organic pollutants.(32, 34, 37, 38) In order to investigate the catalytic oxidation mechanism and identify whether other radicals have been involved in the reactions, EPR tests were carried out using corolla-like δ-MnO₂ as the catalyst and DMPO as the spin trapping agent.

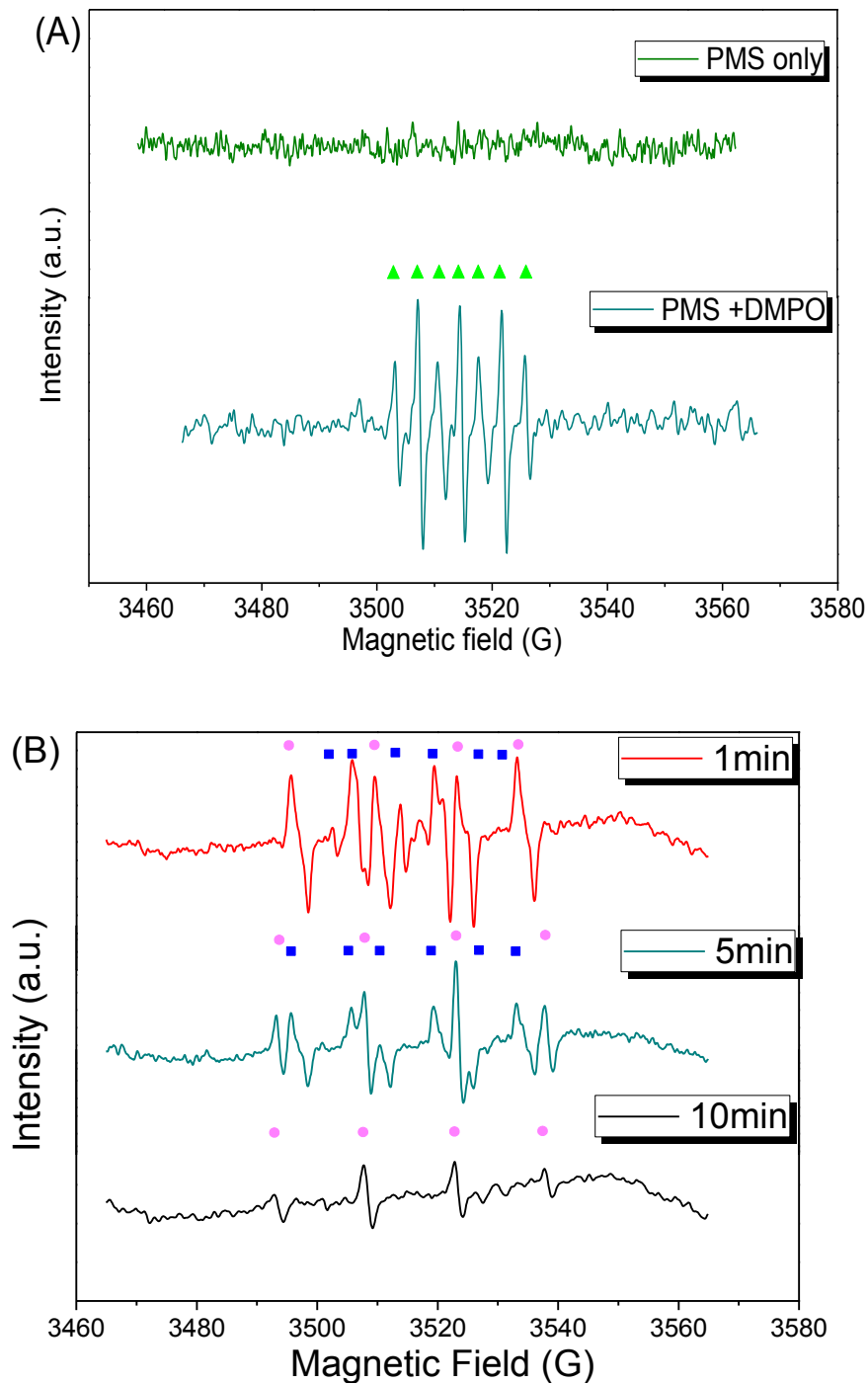


Figure 3.9. EPR spectra in various conditions. Centerfield: 3510 G; Sweep width: 100 G; Microwave frequency: 9.87 GHz; Modulation frequency: 100 GHz; and Power: 18.11 mW. Reaction condition: Phenol = 20 mg/L; Catalyst loading= 0.2 g/L; Oxone[®] loading = 2.0 g/L, pH = 7.0; DMPO = 0.08 M. ▲ : DMPOX; ● : DMPO-[•]OH; ■ : DMPO-SO₄⁻

As shown in Fig. 3.9(A), no peaks were identified in the EPR spectra when 2 g/L PMS solution was tested without adding the spin trapping agent (DMPO) or phenol solution, indicating that no spins had been trapped without DMPO. When DMPO was added in the as-mentioned PMS solution, characteristic signals with an intensity ratio of 1: 2: 1: 2: 1: 2: 1 were captured, which were assigned to nitroxide radicals of DMPO (5,5-dimethylpyrroline-(2)-oxyl-(1); DMPOX).(39) The appearance of a nitroxide radical peak such as DMPOX was not derived from spin-trapping of DMPO- \cdot OH, but from direct oxidation by single electron sources. (40) In this case, immense amount of \cdot OH generated by H₂O₂, which was the hydrolysis product of HSO₅⁻ and would oxidize most of the spin trapping agent to DMPOX in the absence of degradation target, phenol. And the correspondent hydrolysis reaction of HSO₅⁻ is shown in Eq. 3.4.



When corolla-like δ -MnO₂ was added together with PMS (2 g/L) and phenol solution (20 mg/L), sulfate radicals and hydroxyl radicals were identified, as shown in Fig. 3.8(B). At 1 min, characteristic signals of DMPO- \cdot OH adducts (with hyperfine splitting constants of $a_N = a_H = 14.9$ G) and DMPO-SO₄⁻ adducts (with hyperfine splitting constants of $a_N = 13.2$ G, $a_H = 9.6$ G, $a_H = 1.48$ G and $a_H = 0.78$ G) were observed. [32] The appearance of DMPO- \cdot OH and DMPO-SO₄⁻ adducts revealed that both \cdot OH and SO₄⁻ radicals were generated at the initial phase of the reaction. In addition, no characteristic peaks of DMPOX were observed in this EPR spectrum, suggesting that with the participation of phenol, \cdot OH preferred reacting with phenol other than DMPO.

When reaction time was prolonged to 5 min, the peak intensities of DMPO-SO₄⁻ adducts decreased dramatically. Furthermore, little or no intensities of DMPO-SO₄⁻ signals could be observed when reaction time was extended to 10 min. While within the same reaction time period (5-10 min), the peak intensities of DMPO- \cdot OH adducts

also experienced a decrease though not as sharp as $\text{DMPO-SO}_4^{\bullet-}$ adducts. And in the EPR spectra at 10 min, only signals of $\text{DMPO-}\cdot\text{OH}$ adducts were identified. The sharper intensity decrease of $\text{DMPO-SO}_4^{\bullet-}$ adducts indicates that sulfate radicals were more active than hydroxyl radicals in phenol degradation process. The rapid intensity decrease of the radicals is also in agreement with the fast reaction rate of corolla-like $\delta\text{-MnO}_2$ shown in Table 3.1.

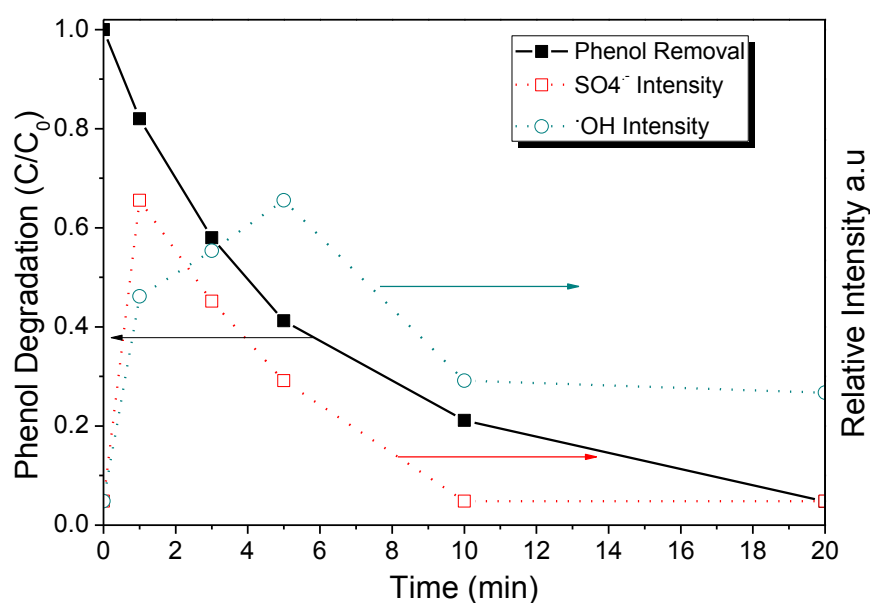


Figure 3.10. Phenol removal profile and intensity variations of $\text{DMPO-}\cdot\text{OH}$ and $\text{DMPO-SO}_4^{\bullet-}$ during reaction on Mn-100.

Fig. 3.10 shows the relationship between phenol removal and the peak intensities of the $\text{DMPO-}\cdot\text{OH}$ / $\text{DMPO-SO}_4^{\bullet-}$ dependent on reaction time over Mn-100 catalyst. As shown clearly, at 1 min after addition of PMS, the $\text{DMPO-SO}_4^{\bullet-}$ reached the highest peak intensity. After that the intensity of $\text{DMPO-SO}_4^{\bullet-}$ gradually decreased, and reached zero at 10 min, indicating the complete consumption. However, the evolution of $\text{DMPO-}\cdot\text{OH}$ intensity had a different trend. It reached peak at 5 min and almost half of the intensity remained during the phenol degradation process. Combined the intensity variation of $\text{DMPO-}\cdot\text{OH}$ / $\text{DMPO-SO}_4^{\bullet-}$ with the phenol degradation profile, it could be induced that 80% of phenol degradation at the first 10 min might be ascribed to the dominant role of sulfate radicals.

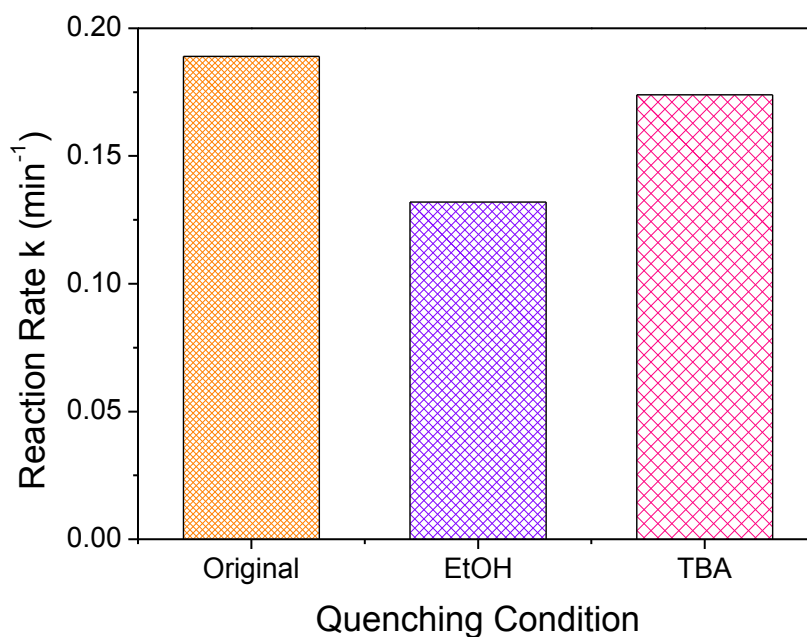


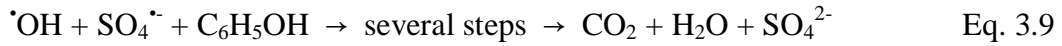
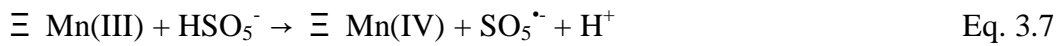
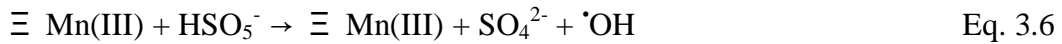
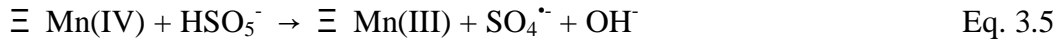
Figure 3.11. Changes of reaction rate (k) of catalysts with and without quenching agents of EtOH (0.2 M) and TBA (0.2 M). Reaction conditions: $[\text{phenol}]_0 = 20 \text{ mg/L}$, catalyst loading = 0.2 g/L, Oxone[®] loading = 2.0 g/L, and $T = 25 \text{ }^\circ\text{C}$.

To further investigate the major reactive species responsible for phenol degradation, classical quenching tests using ethanol (EtOH) and tert-butyl alcohol (TBA) as quenching agents were carried out. It was suggested that both EtOH and TBA could sufficiently quench $\bullet\text{OH}$ and the reaction rates are $1.2 \times 10^9 - 2.8 \times 10^9 \text{ M}^{-1}\text{s}^{-1}$ and $3.8 \times 10^8 - 7.6 \times 10^8 \text{ M}^{-1}\text{s}^{-1}$, respectively. (41) $\text{SO}_4^{\bullet-}$ can be quenched more rapidly by the quenching agents with α -hydrogen. It was reported that the reaction rates of EtOH (with α -hydrogen) and TBA (without α -hydrogen) with $\text{SO}_4^{\bullet-}$ are $1.6 \times 10^7 - 7.7 \times 10^7$ and $4.0 \times 10^5 - 9.1 \times 10^5 \text{ M}^{-1}\text{s}^{-1}$, respectively. (41, 42) Therefore, by adding EtOH or TBA into the reaction solutions, the reactive radicals responsible for phenol degradation can be well differentiated.

Fig. 3.11 shows the results of the quenching tests in form of changes in reaction rate constant k . When 0.2 M EtOH was added in the original reaction solution, more than 20% of decrease in reaction rate was observed, compared with the original one, sug-

gesting that part of the hydroxyl and sulfate radicals were quenched. However, by addition of 0.2 M TBA, less than 5% decrease occurred to reaction rate. Therefore, since the addition of EtOH could incur more remarkable decrease in reaction rate than TBA, the dominant reactive species for phenol degradation were suggested to be sulfate radicals.

Based on EPR investigations as well as the results of the quenching tests, the mechanism of activation of PMS by δ -MnO₂ nanostructures for phenol degradation could be proposed as follows.



First, δ -MnO₂ activated PMS to generate $\text{SO}_4^{\bullet-}$ and $\bullet\text{OH}$ at the same time and thus Eqs. 3.5 and 3.6 happened simultaneously. Then most of the produced $\text{SO}_4^{\bullet-}$ radicals were depleted quickly by reacting with phenol. During the reaction between $\text{SO}_4^{\bullet-}$ radicals and phenol, some of the generated $\bullet\text{OH}$ also participated, though at an inferior reaction rate (Eq. 3.9). After the depletion of $\text{SO}_4^{\bullet-}$, $\bullet\text{OH}$ became the only reactive species to react with phenol. Meanwhile, the reduced δ -MnO₂ catalyst ($\Xi\text{Mn(III)}$) reacted with PMS resulting in the recovery of the original δ -MnO₂ ($\Xi\text{Mn(IV)}$) and the

generation of $\cdot\text{OH}$ (Eqs 3.7 and 3.8). Moreover, some of the competitive reactions also happened which might negatively influence the generation of the reactive radicals (Eqs. 3.10-3.12).

3.4 Conclusions

Shape-controlled 3D MnO_2 hierarchical nanostructures were fabricated via a facile one-step hydrothermal method and their catalytic activities in activation of PMS for phenol degradation were evaluated. Corolla-like $\delta\text{-MnO}_2$, prepared at a hydrothermal temperature of 100 °C, showed 2D compact layers of nanosheets on the surface. It also had a higher catalytic activity than 3D sea-urchin like $\alpha\text{-MnO}_2$, which was prepared at 110 °C and made of 1D tetragonal nanorods. Catalytic degradation of phenol was influenced by reaction temperature, higher temperature would accelerate PMS activation to produce more radicals and thus enhance the reaction rates. The kinetic studies suggested that the heterogeneous catalytic system followed first-order kinetics and the activation energy was 25.3 kJ/mol. The catalyst stability tests revealed that corolla-like $\delta\text{-MnO}_2$ possessed a high stability with little deactivation after several tests. The mechanism of catalytic reaction for PMS activation was investigated by EPR spectra and showed that both of $\cdot\text{OH}$ and $\text{SO}_4^{\cdot-}$ are produced in the activation processes, and $\text{SO}_4^{\cdot-}$ plays a more critical role in phenol oxidation.

References

1. Fortuny A, Font J, Fabregat A. Wet air oxidation of phenol using active carbon as catalyst. *Appl. Catal., B.* 1998;19(3–4):165-73.
2. Esplugas S, Gimenez J, Contreras S, Pascual E, Rodriguez M. Comparison of different advanced oxidation processes for phenol degradation. *Water Res.* 2002;36(4):1034-42.
3. Pera-Titus M, Garcia-Molina V, Banos MA, Gimenez J, Esplugas S. Degradation of chlorophenols by means of advanced oxidation processes: a general review. *Appl. Catal., B.* 2004;47(4):219-56.
4. Wang S. A Comparative study of Fenton and Fenton-like reaction kinetics in decolourisation of wastewater. *Dyes Pigm.* 2008;76(3):714-20.
5. Hu L, Yang X, Dang S. An easily recyclable Co/SBA-15 catalyst: Heterogeneous activation of peroxymonosulfate for the degradation of phenol in water. *Appl. Catal., B.* 2011;102(1–2):19-26.
6. Shukla P, Sun H, Wang S, Ang HM, Tade MO. Co-SBA-15 for heterogeneous oxidation of phenol with sulfate radical for wastewater treatment. *Catal. Today.* 2011;175(1):380-5.
7. Shukla P, Wang S, Singh K, Ang HM, Tade MO. Cobalt exchanged zeolites for heterogeneous catalytic oxidation of phenol in the presence of peroxymonosulphate. *Appl. Catal., B.* 2010;99(1-2):163-9.
8. Anipsitakis GP, Dionysiou DD. Degradation of Organic Contaminants in Water with Sulfate Radicals Generated by the Conjunction of Peroxymonosulfate with Cobalt. *Environmental Science & Technology.* 2003;37(20):4790-7.
9. Anipsitakis GP, Dionysiou DD. Radical Generation by the Interaction of Transition Metals with Common Oxidants. *Environ. Sci. Technol.* 2004;38(13):3705-12.
10. Anipsitakis GP, Stathatos E, Dionysiou DD. Heterogeneous Activation of Oxone Using Co_3O_4 . *J. Phys. Chem. B.* 2005;109(27):13052-5.
11. Chen X, Chen J, Qiao X, Wang D, Cai X. Performance of nano- Co_3O_4 /peroxymonosulfate system: Kinetics and mechanism study using Acid Orange 7 as a model compound. *Appl. Catal., B.* 2008;80(1–2):116-21.
12. Sun H, Liu S, Zhou G, Ang HM, Tade MO, Wang S. Reduced Graphene Oxide for Catalytic Oxidation of Aqueous Organic Pollutants. *ACS Appl. Mater. Interfaces.*

2012;4(10):5466-71.

13. Sun H, Zhou G, Liu S, Ang HM, Tade MO, Wang S. Nano-Fe⁰ Encapsulated in Microcarbon Spheres: Synthesis, Characterization, and Environmental Applications. *ACS Appl. Mater. Interfaces*. 2012;4(11):6235-41.

14. Sun HQ, Liang HW, Zhou GL, Wang SB. Supported cobalt catalysts by one-pot aqueous combustion synthesis for catalytic phenol degradation. *J. Colloid Interface Sci*. 2013;394:394-400.

15. Watts R, Sarasa J, Loge F, Teel A. Oxidative and Reductive Pathways in Manganese-Catalyzed Fenton's Reactions. *J. Environ. Eng*. 2005;131(1):158-64.

16. Xu L, Xu C, Zhao M, Qiu Y, Sheng GD. Oxidative removal of aqueous steroid estrogens by manganese oxides. *Water Res*. 2008;42(20):5038-44.

17. Liang H, Sun H, Patel A, Shukla P, Zhu ZH, Wang S. Excellent performance of mesoporous Co₃O₄/MnO₂ nanoparticles in heterogeneous activation of peroxymonosulfate for phenol degradation in aqueous solutions. *Appl. Catal., B*. 2012;127(0):330-5.

18. Saputra E, Muhammad S, Sun H, Patel A, Shukla P, Zhu ZH, et al. α -MnO₂ activation of peroxymonosulfate for catalytic phenol degradation in aqueous solutions. *Catal. Commun*. 2012;26(0):144-8.

19. Saputra E, Muhammad S, Sun H, Ang H-M, Tadé MO, Wang S. Manganese oxides at different oxidation states for heterogeneous activation of peroxymonosulfate for phenol degradation in aqueous solutions. *Appl. Catal., B*. 2013;142-143(0):729-35.

20. Sun HQ, Ang HM, Tade MO, Wang SB. Co₃O₄ nanocrystals with predominantly exposed facets: synthesis, environmental and energy applications. *J. Mater. Chem. A*. 2013;1(46):14427-42.

21. Saputra E, Muhammad S, Sun H, Ang H-M, Tadé MO, Wang S. Shape-controlled activation of peroxymonosulfate by single crystal α -Mn₂O₃ for catalytic phenol degradation in aqueous solution. *Appl. Catal., B*. 2014;154-155(0):246-51.

22. Saputra E, Muhammad S, Sun H, Ang HM, Tade MO, Wang S. A comparative study of spinel structured Mn₃O₄, Co₃O₄ and Fe₃O₄ nanoparticles in catalytic oxidation of phenolic contaminants in aqueous solutions. *J. Colloid Interface Sci*. 2013;407:467-73.

23. Long JW, Rhodes CP, Young AL, Rolison DR. Ultrathin, Protective Coatings of Poly(o-phenylenediamine) as Electrochemical Proton Gates: Making Mesoporous MnO₂ Nanoarchitectures Stable in Acid Electrolytes. *Nano Lett*. 2003;3(8):1155-61.

24. Sides CR, Martin CR. Nanostructured Electrodes and the Low-Temperature Performance of Li-Ion Batteries. *Adv. Mater.* 2005;17(1):125-8.
25. Chang K-H, Hu CC. Coalescence inhibition of hydrous RuO₂ crystallites prepared by a hydrothermal method. *Appl. Phys. Lett.* 2006;88(19):-.
26. Li Z, Ding Y, Xiong Y, Xie Y. Rational Growth of Various α -MnO₂ Hierarchical Structures and β -MnO₂ Nanorods via a Homogeneous Catalytic Route. *Cryst. Growth Des.* 2005;5(5):1953-8.
27. Yu P, Zhang X, Wang D, Wang L, Ma Y. Shape-Controlled Synthesis of 3D Hierarchical MnO₂ Nanostructures for Electrochemical Supercapacitors. *Cryst. Growth Des.* 2008;9(1):528-33.
28. Duan X, Yang J, Gao H, Ma J, Jiao L, Zheng W. Controllable hydrothermal synthesis of manganese dioxide nanostructures: shape evolution, growth mechanism and electrochemical properties. *CrystEngComm.* 2012;14(12):4196-204.
29. Xiao W, Wang D, Lou XW. Shape-Controlled Synthesis of MnO₂ Nanostructures with Enhanced Electrocatalytic Activity for Oxygen Reduction. *J. Phys. Chem. C.* 2009;114(3):1694-700.
30. Hill JP, Alam S, Ariga K, Anson CE, Powell AK. Nanostructured microspheres of MnO₂ formed by room temperature solution processing. *Chem. Commun.* 2008(3):383-5.
31. Zhang P, Zhan Y, Cai B, Hao C, Wang J, Liu C, et al. Shape-controlled synthesis of Mn₃O₄ nanocrystals and their catalysis of the degradation of methylene blue. *Nano Res.* 2010;3(4):235-43.
32. Wang Y, Sun H, Ang HM, Tadé MO, Wang S. Magnetic Fe₃O₄/carbon sphere/cobalt composites for catalytic oxidation of phenol solutions with sulfate radicals. *Chem. Eng. J.* 2014;245(0):1-9.
33. Saputra E, Muhammad S, Sun H, Ang H-M, Tadé MO, Wang S. A comparative study of spinel structured Mn₃O₄, Co₃O₄ and Fe₃O₄ nanoparticles in catalytic oxidation of phenolic contaminants in aqueous solutions. *J. Colloid Interface Sci.* 2013;407(0):467-73.
34. Yao Y, Yang Z, Sun H, Wang S. Hydrothermal Synthesis of Co₃O₄-Graphene for Heterogeneous Activation of Peroxymonosulfate for Decomposition of Phenol. *Ind. Eng. Chem. Res.* 2012;51(46):14958-65.
35. Fang GD, Dionysiou DD, Al-Abed SR, Zhou DM. Superoxide radical driving the activation of persulfate by magnetite nanoparticles: Implications for the degradation of PCBs. *Appl. Catal., B.* 2013;129(0):325-32.

36. Yao Y, Xu C, Yu S, Zhang D, Wang S. Facile Synthesis of Mn_3O_4 -Reduced Graphene Oxide Hybrids for Catalytic Decomposition of Aqueous Organics. *Ind. Eng. Chem. Res.* 2013;52(10):3637-45.
37. Sun H, Wang Y, Liu S, Ge L, Wang L, Zhu Z, et al. Facile synthesis of nitrogen doped reduced graphene oxide as a superior metal-free catalyst for oxidation. *Chemical Communications.* 2013;49(85):9914-6.
38. Hu L, Yang F, Lu W, Hao Y, Yuan H. Heterogeneous activation of oxone with CoMg/SBA-15 for the degradation of dye Rhodamine B in aqueous solution. *Appl. Catal., B.* 2013;134-135(0):7-18.
39. Rosen GM, Raukman EJ. Spin Trapping of the Primary Radical Involved in the Activation of the Carcinogen N-Hydroxy-2-acetylaminofluorene by Cumene Hydroperoxide-Hematin. *Mol. Pharmacol.* 1980;17(2):233-8.
40. Floyd RA, Soong LM. Spin trapping in biological systems. Oxidation of the spin trap 5,5-dimethyl-1-pyrroline-1-oxide by a hydroperoxide-hematin-system. *Biochemical and biophysical research communications.* 1977;74(1):79-84.
41. Buxton GV, Greenstock CL, Helman WP, Ross AB. Critical Review of rate constants for reactions of hydrated electrons, hydrogen atoms and hydroxyl radicals ($\cdot OH/\cdot O^-$ in Aqueous Solution. *J. Phys. Chem. Ref. Data.* 1988;17(2):513-886.
42. Neta P, Huie RE, Ross AB. Rate Constants for Reactions of Inorganic Radicals in Aqueous Solution. *J. Phys. Chem. Ref. Data.* 1988;17(3):1027-284.

Chapter 4: New Insights into Heterogeneous Generation and Evolution Processes of Sulfate radicals for Phenol Degradation over One-dimensional α -MnO₂ Nanostructures

ABSTRACT

In the last chapter, we discussed three-dimensional (3D) MnO₂ catalysts for efficient activation of PMS for phenol oxidation. In order to probe the structural effect of manganese oxide on PMS activation, in this chapter, we fabricated three one-dimensional (1D) α -MnO₂ nanostructures, nanorods, nanotubes and nanowires by a one-pot hydrothermal method without addition of any surfactants. Shape-dependent performance of 1D α -MnO₂ was observed in catalytic degradation of phenol solutions. The phenol oxidation can be described by a first-order kinetic model and the activation energies of phenol oxidation on the three α -MnO₂ materials were estimated to be 20.3, 39.3 and 87.1 kJ/mol for nanowires, nanorods, and nanotubes, respectively. Both electron paramagnetic resonance (EPR) spectra and competitive radical tests were applied to investigate the PMS activation processes and to differentiate the major reactive species dominating the catalytic oxidation. The processes of PMS activation, evolution of sulfate radicals, and phenol degradation pathways were clearly illustrated.

4.1 Introduction

Manganese oxides are abundant in soils and have various forms such as MnO, MnO₂, Mn₂O₃ and Mn₃O₄. Due to variation of the oxidation states between 2+ and 4+ redox cycles, manganese oxides have excellent oxygen mobility in the oxide lattices and thus induce superior redox reactions (1). Therefore, they have been widely used as catalysts, electrodes for energy storage and supercapacitors (2-5). Moreover, manganese ions have a low toxicity to the environment compared with cobalt ions. Based on these features, manganese oxides have been reported as promising alternatives to Co systems for PMS activation to produce reactive species (1, 2, 6). However, PMS activation mechanism by MnO_x has not been explored.

In the past few years, 1D nanomaterials in nanotube, nanofibre, nanowire or nanorod have attracted intensive attention due to their unique physical and chemical properties (7-9). The performances of 1D nanomaterials depend on shape and structure. Wang and Li (10) reported a low temperature liquid-phase comproportionation method for synthesis of single crystalline α -MnO₂ nanorods with diameters 20-80 nm. Luo et al.(11) synthesized single crystals of tetragonal α -MnO₂ nanotubes by a facile hydrothermal treatment of KMnO₄ in hydrochloric acid solution. Su et al.(12) used a hydrothermal method to prepare α -MnO₂ and β -MnO₂ nanorods and tested their performances as the cathode materials for sodium ion batteries. They found that β -MnO₂ could be a promising cathode material with high capacity due to the more compact tunnel-structure.

Herein, a facile one-pot hydrothermal method was applied to synthesize α -MnO₂ nanorods, nanotubes and nanowires using KMnO₄ with hydrochloric acid or MnSO₄. The as-prepared α -MnO₂ 1D structures demonstrated superior catalytic activities in activation of PMS for phenol degradation. The physicochemical properties of crystalline structure, morphology, and reusability of the as-prepared shape-controlled

catalysts were investigated. Moreover, the PMS activation and sulfate radical evolution were thoroughly studied by means of EPR and competitive radical tests.

4.2 Materials and Methods

Chemicals were same as that in Chapter 3.

4.2.1 Synthesis of 1 D structured MnO₂

MnO₂ nanorods and nanotubes were prepared by a hydrothermal route using KMnO₄ and HCl at 120 and 140 °C, respectively (3). In the synthesis, 2.8 mmol of potassium permanganate was first dissolved in 80 mL of ultrapure water. After 10 min stirring, 0.027 mol of HCl (37 wt%) was added dropwisely under stirring to form a precursor solution. After stirring for another 20 min, the solution was transferred into a Teflon-lined stainless steel autoclave with the volume of 120 mL. Two autoclave reactors were then sealed and put in an oven at temperature of 120 and 140 °C for 12 h, respectively, and were then cooled down to room temperature naturally. The products were harvested by vacuum filtration and washed with ultrapure water for 3 times before dried at 60 °C overnight. The obtained samples were labelled as Mn-nanorods and Mn-nanotubes, respectively.

MnO₂ nanowires were synthesized by a similar hydrothermal method reported before (4). Firstly, 1.2 mmol of manganese sulfate hydrate and 3.2 mmol of potassium permanganate were dissolved in 80 mL of ultrapure water at room temperature and magnetically stirred for 20 min to form a homogeneous solution. The solution was then transferred into a Teflon-lined stainless steel autoclave with the capacity of 120 mL. The autoclave was sealed and maintained at 140 °C for 12 h. The resulted product was filtered and washed by ultrapure water for 3 times and dried at 60 °C overnight. The product was referred as Mn-nanowires.

4.2.2 Characterization of materials and catalytic oxidation

Characterization details and phenol oxidation as well as mechanistic studies can be found in Chapter 3.

4.3 Results and Discussion

4.3.1 Characterization of 1D MnO₂ materials

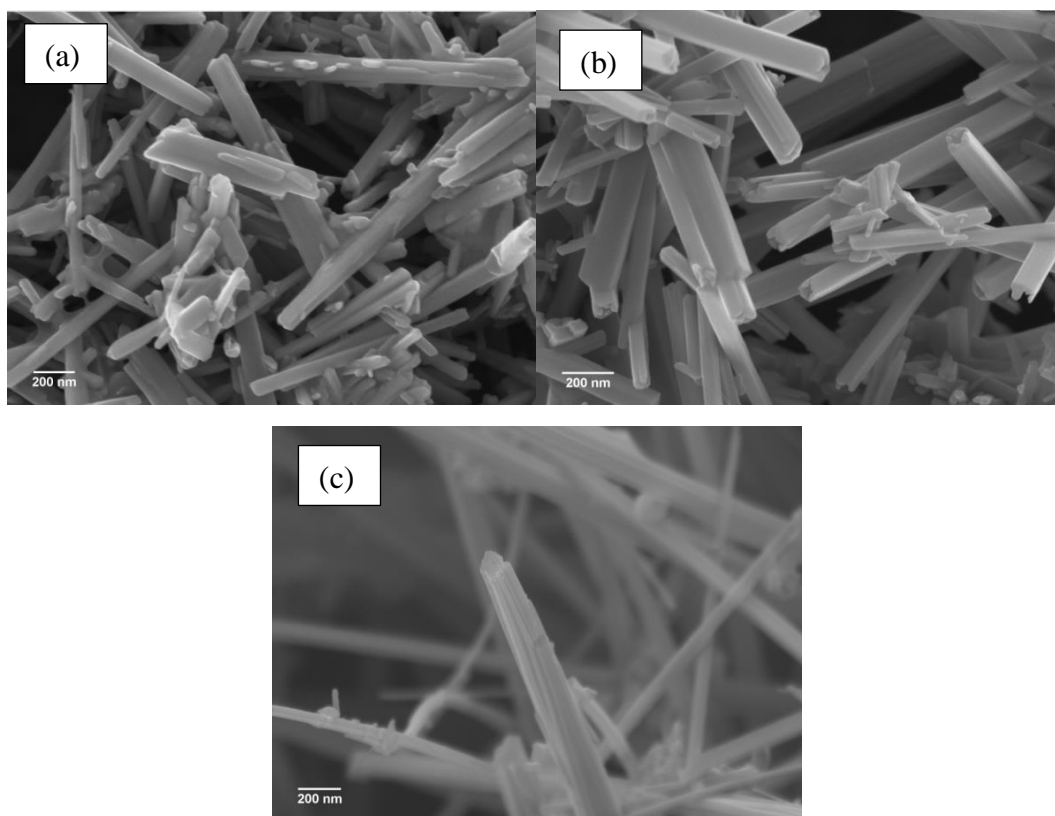


Figure 4.1 SEM images of α -MnO₂ (a) nanorods, (b) nanotubes, and (c) nanowires.

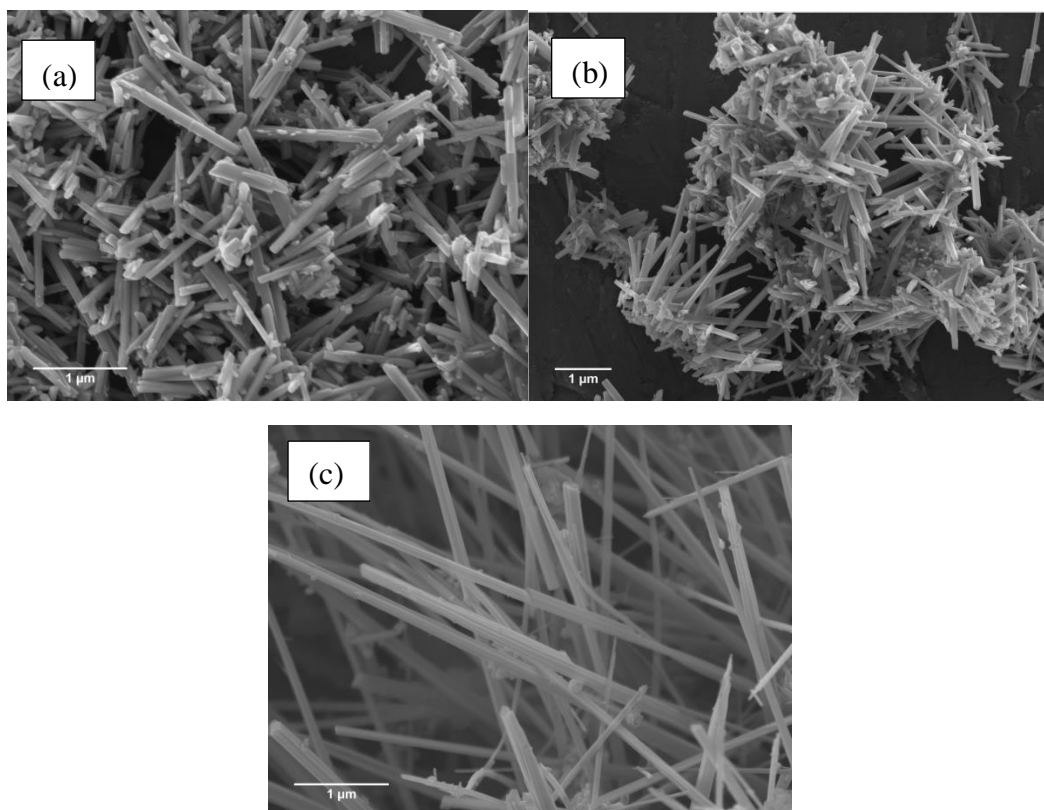


Figure 4.2 SEM images of α - MnO_2 nanostructures. (a) nanorods, (b) nanotubes, and (c) nanowires.

Fig. 4.1 shows SEM images of the samples prepared in different hydrothermal conditions. The morphologies of the products at low magnification can be found in Fig. 4.2. Using potassium permanganate and hydrochloric acid as the precursors, the sample prepared at 120 °C showed a uniform morphology of nanorods. The 1 D tetragonal nanorods had a size of 1-2 μm in length and possessed a square cross section with the edge length ranging in 30-50 nm. At 140 °C, the particle morphology changed to 1 D tetragonal nanotubes with a length of around 2 μm and a similar square-cross section to nanorods. The evolution of the morphology from nanorods to nanotubes was ascribed to the “etching mechanism” (11), which was more favored at a higher temperature (13, 14). Due to the anisotropic growth driven by chemical potential, MnO_2 nanorods were firstly formed. When hydrothermal temperature was elevated, etching process occurred in each nanorod from both ends towards the center along the long axis (001) to form hollow nanotubes, which have the most stable

low-index nonpolar surface (3, 11). Maintaining the temperature at 140 °C and using potassium permanganate and manganese sulfate as the precursors, nanowires with sharp ends were obtained, as shown in Fig. 4.1(c). They had sizes of 5-6 μm in length and around 40 nm in diameter. The nanowires had a much larger aspect ratio than the tetragonal nanorods/nanotubes prepared using potassium permanganate and hydrochloric acid as precursors.

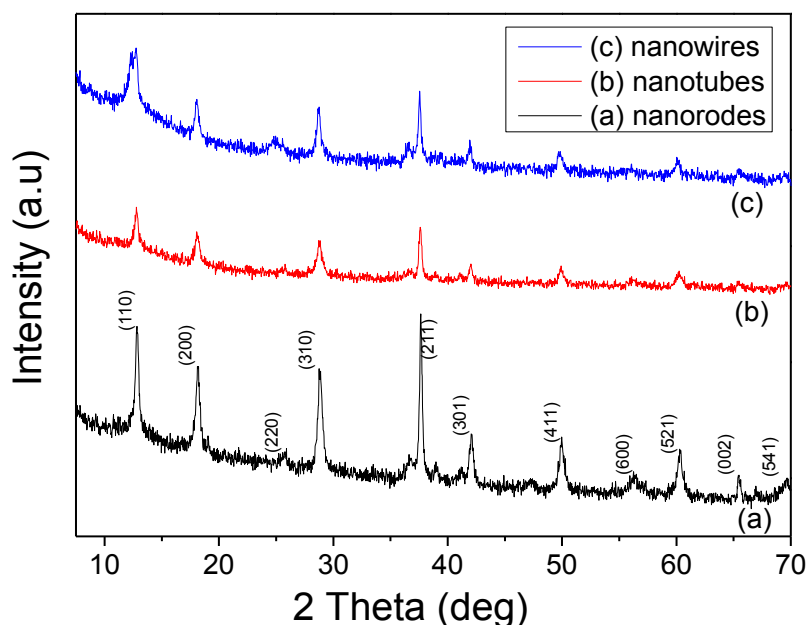


Figure 4.3 XRD patterns of various α -MnO₂ nanostructures.

Fig. 4.3 shows XRD patterns of three MnO₂ nanomaterials. Same characteristic peaks were observed on MnO₂ nanorods, nanotubes and nanowires, which are well agreement with a pure α -MnO₂ phase (JCPDS No. 44-0141, tetragonal, I4/m, $a=b=9.78$ Å, $c=2.86$ Å). The sharp characteristic peaks and the strong intensities indicate that the obtained α -MnO₂ products were of good crystallinities. Moreover, the intensities of the three samples followed an order of nanorods > nanowires > nanotubes, indicating the crystallinity is controlled by both precursors and temperature. α -MnO₂ is constructed by the double chains of edge-sharing MnO₆ octahedra that are linked at the corners to form (2 × 2) + (1 × 1) tunnel structure, and these tunnels ex-

tend in the direction parallel to the c axis of the tetragonal unit cell (12). Some cations could be involved within the (2×2) tunnel structures during the synthesis processes (the 1×1 tunnels are generally too small for cations) and thus direct the growth pattern (3). In both methods, potassium ions from KMnO_4 serve as the crucial cations to direct the MnO_6 octahedral units to form the (2×2) dominating tunnel structure of $\alpha\text{-MnO}_2$ (15).

The reactions involved during the hydrothermal processes can be briefly described as follows (4, 16).

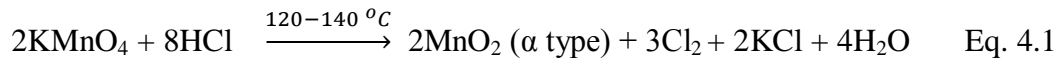


Fig. 4.4 displays N_2 adsorption/desorption isotherms and the correspondent pore size distributions of three $\alpha\text{-MnO}_2$ nanomaterials. Generally, all the three $\alpha\text{-MnO}_2$ nanostructures had a IV isotherm with a type of H3 hysteresis loop, suggesting a mesoporous structure (17). Compared with other two nanostructures, $\alpha\text{-MnO}_2$ nanowires possessed a higher surface area ($66.0 \text{ m}^2/\text{g}$) and pore volume ($0.149 \text{ cm}^3/\text{g}$), indicating that, though three 1 D nanostructures showed the same crystal structure, the surface area and pore volume varied with the synthesis precursors. The BET specific surface area and pore volumes are shown in Table 4.1. Both nanorods and nanotubes demonstrated a narrow hysteresis loop at a relative pressure (P/P_0) range of 0.5 to 0.95 and a bimodal pore size distribution centered at 1.0 and 2.2 nm, respectively (Fig. 4.4(A) and (B)). Despite of the similarities, the proportion of the micropores in nanotubes ranging between 0.5-1.5 nm was enhanced when compared to nanorods, which is in accordance with the evolution of the morphology. Comparatively, nanowires showed a broad hysteresis loop, appearing at lower relative pressure ($0.45 < P/P_0 < 0.9$). Moreover, the as-synthesized sample had a rather narrow pore size distribution concentrating at 2.5 nm.

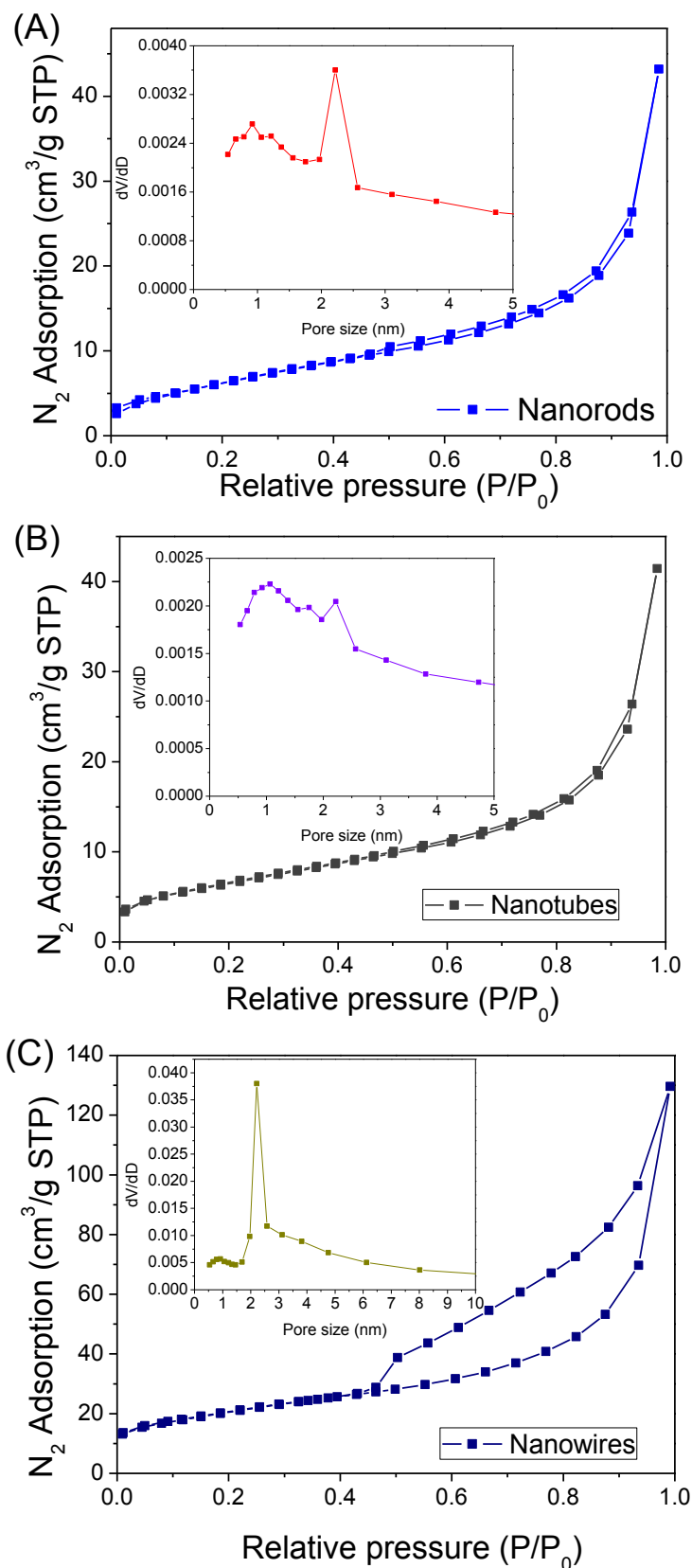


Figure 4.4 Nitrogen sorption isotherms and pore size distribution (insets) of three α - MnO_2 nanostructures.

Table 4.1 Textural properties of MnO₂ nanomaterials and their activities in phenol degradation.

Catalyst	Surface area (S _{BET} , m ² /g)	Pore volume (cm ³ /g)	First-order constant (min ⁻¹)	rate R ²
Nanorods	19.6	0.0524	0.147	0.996
Nanotubes	23.9	0.0495	0.112	0.997
Nanowires	66.0	0.149	0.179	0.999

4.3.2 Catalytic oxidation of phenol

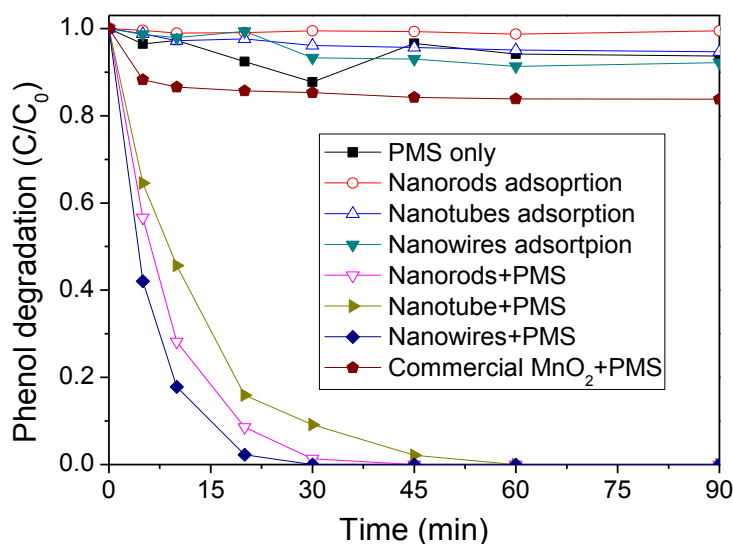


Figure 4.5 Phenol removal profiles in various conditions. Reaction conditions: [phenol]₀ = 20 mg/L, catalyst loading = 0.2 g/L, Oxone[®] loading = 2.0 g/L, Temperature: 25 °C.

Fig. 4.5 shows the adsorption and degradation profiles of phenol over three α -MnO₂ nanomaterials. Control experiments were first carried out to reveal phenol removals induced by adsorption and PMS self-oxidation. Negligible phenol degradation occurred when PMS alone was used. A decline of less than 5% in phenol concentration was found after 90 min without a catalyst. For the adsorption tests, similar phenol removal profiles were observed for the three catalysts in which phenol removal fluctuated

tuated in the first 30 min to achieve adsorption/desorption equilibrium. For catalytic reactions with PMS, it was shown that commercial activated MnO₂ could not effectively activate PMS for phenol degradation and 80% of phenol was still remained after 90 min. It was interesting to find that all the 1 D α-MnO₂ can effectively activate PMS to achieve fast phenol degradation. As seen, α-MnO₂ nanowires demonstrated the highest phenol degradation rate and thus indicated the best catalytic activity. It removed 100% phenol within 30 min. α-MnO₂ nanotubes possessed the lowest catalytic activity but phenol was fully degraded in 60 min.

On the basis of the phenol degradation profiles, a first-order kinetic model (Eq. (3)) was applied to evaluate the catalytic reaction kinetics.

$$\ln\left(\frac{C}{C_0}\right) = -kt \quad \text{Eq. 4.3}$$

Where C is phenol concentration at time (t) and C₀ is the phenol concentration at initial time (t₀). k is the first order reaction rate constant. Fig. 4.6 shows that phenol degradation curves were fitted well to the first-order kinetics with high values of regression coefficients.

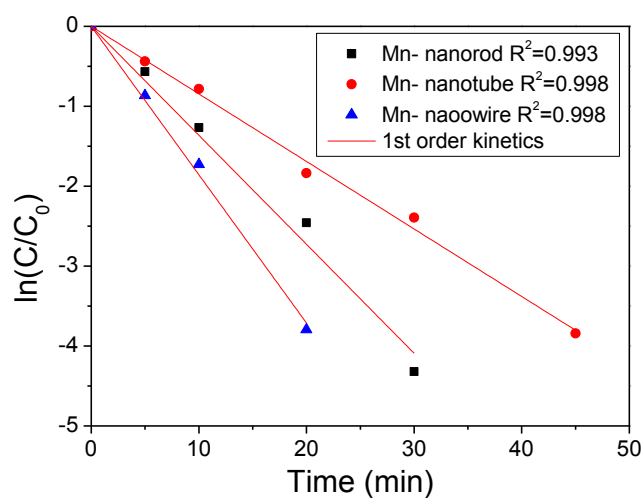


Figure 4.6 First order kinetic model of phenol oxidation reactions on various MnO₂ materials.

The shape-dependent performances of α - MnO_2 1D nanostructures in phenol oxidation can be related to their physicochemical properties. Recently, three Mn_2O_3 nanostructures were synthesized and their catalytic activities were tested in phenol oxidation (1). It was found the order of catalytic activity was Mn_2O_3 cube > Mn_2O_3 cuboctahedra > Mn_2O_3 octahedra, suggesting that facet (001) possess the highest catalytic potential. 1D MnO_2 with different crystallographic structures, α -, β - and λ -phases were also prepared and examined in catalytic oxidation of phenol solutions. α - MnO_2 demonstrated a higher activity than β - and λ - MnO_2 (2). In the present study, α - MnO_2 nanowires have the largest BET surface area ($66.0 \text{ m}^2/\text{g}$) and thus obtain the highest catalytic activity. However, the catalytic activity of α - MnO_2 nanorods is higher than that of α - MnO_2 nanotubes, which did not follow the same order as the BET surface areas. The difference in catalytic activity can be related to the activity of different facets of MnO_2 . The evolution of nanorods to nanotubes could be explained by the gradual disappearance of the metastable (001) facet, and thus suggesting that the metastable facet (001) possesses the higher activity potential than facet (200) (3, 11).

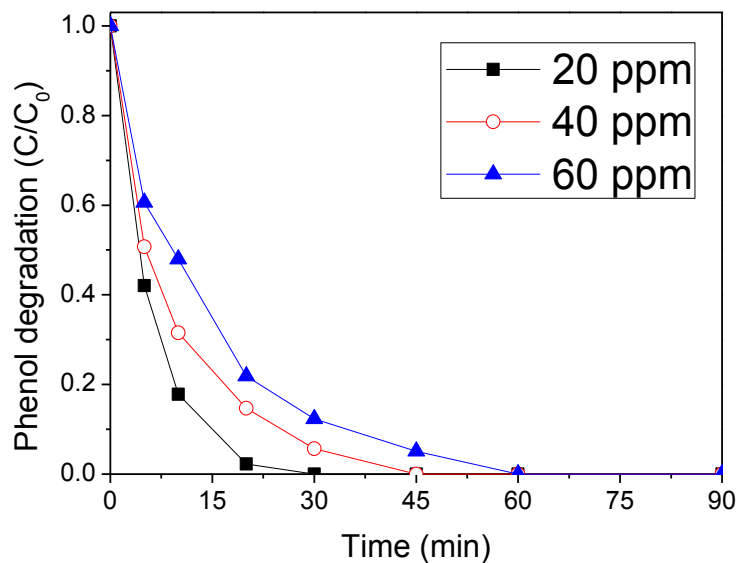


Figure 4.7 Effect of initial phenol concentration on phenol degradation on α -MnO₂ nanowires. Reaction conditions: catalyst loading = 0.2 g/L, Oxone[®] loading = 2.0 g/L, T=25 °C.

To investigate the effects of reaction conditions on catalytic phenol degradation, further kinetic studies were carried out on the most effective catalyst, α -MnO₂ nanowires. Fig. 4.7 shows the effect of initial phenol concentration on phenol degradation efficiency. A general trend can be observed that, with increasing initial phenol concentration, the time for 100% phenol degradation became longer, indicating the decrease in degradation efficiency. As shown, when initial phenol concentration was increased to 40 and 60 ppm, 100% degradation of phenol would take 45 and 60 min, respectively.

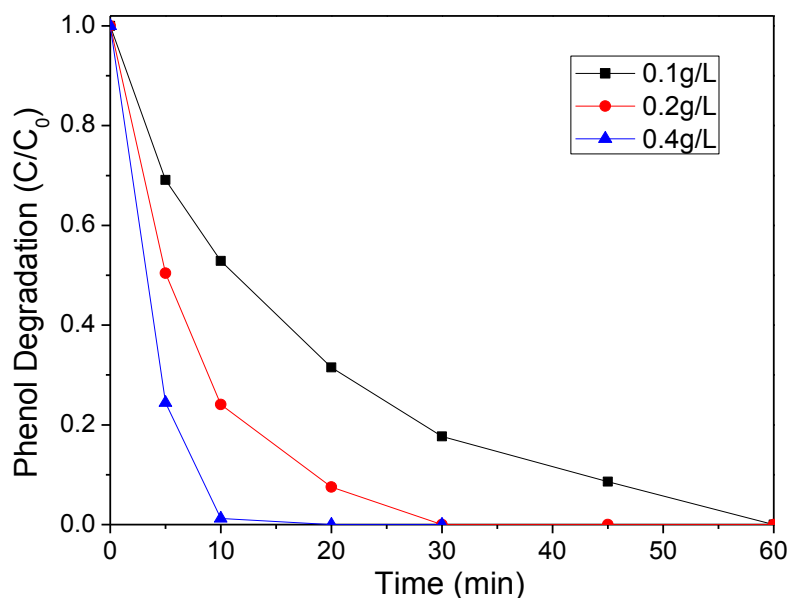


Figure 4.8 Effect of catalyst loading on phenol degradation on α -MnO₂ nanowires. Reaction conditions: = [phenol]₀ = 20 mg/L, Oxone[®] loading = 2.0 g/L, T=25 °C.

The effect of catalyst loading on phenol degradation is shown in Fig. 4.8. As shown, catalyst amount could dramatically influence phenol degradation. Increasing catalyst loading resulted in significant enhancement of phenol degradation efficiency. When catalyst loading was 0.1 g/L, phenol was completely degraded within 60 min, whereas 0.4 g/L catalyst loading resulted in 100% phenol degradation within 20 min. The increased efficiency can be ascribed to the increased active sites in the solution for reaction with PMS thereby generating more reactive species.

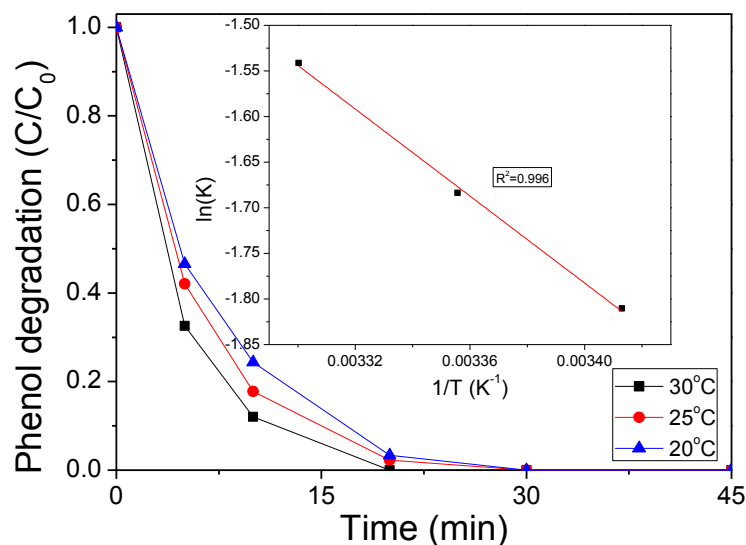


Figure 4.9 Effect of reaction temperature on phenol degradation on α -MnO₂ nanowires. Reaction conditions: [phenol]₀ = 20 mg/L, catalyst loading = 0.2 g/L, Ox-one[®] loading = 2.0 g/L.

Fig. 4.9 shows phenol degradation profiles on α -MnO₂ nanowires at varying temperatures. A general trend can also be observed that, at elevated temperature, phenol degradation rates are enhanced, revealing the endothermic nature of the PMS activation process. As seen, phenol degradation could reach 100% within 20 min when reaction temperature was increased to 30 °C. Based on the first-order kinetics, reaction rate constants at varying temperatures were determined and the correlation between the rate constant and reaction temperature was fitted well by the Arrhenius equation with a high regression coefficient (inset figure). The activation energy was then obtained to be 20.3 kJ/mol. Fig. 4.10 further illustrated the phenol degradation profiles on α -MnO₂ nanorods/nanotubes at varying temperatures. Similar trends were observed for α -MnO₂ nanorods and nanotubes as for α -MnO₂ nanowires. Moreover, the activation energies for α -MnO₂ nanorods and nanotubes were 39.3 and 87.1 kJ/mol, respectively. The lowest activation energy of α -MnO₂ nanowires was in agreement with its best phenol degradation efficiency.

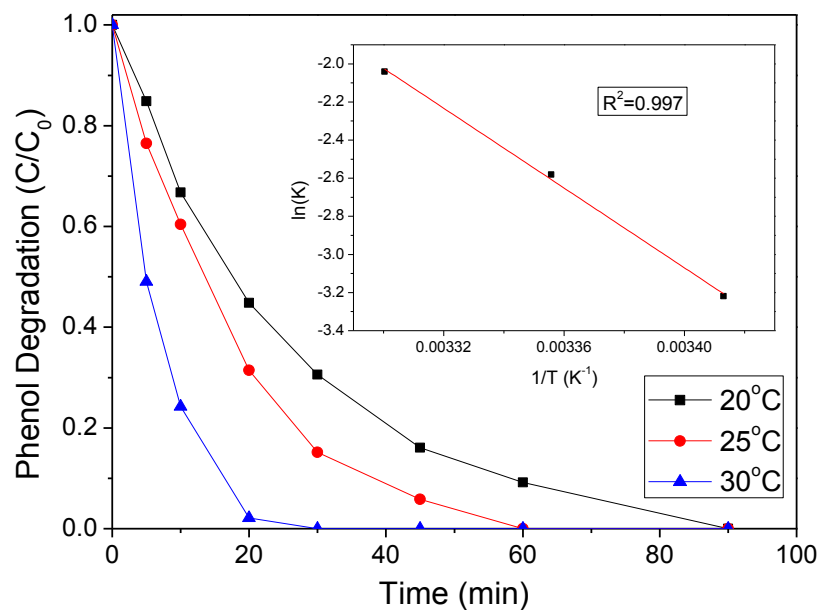


Figure 4.10 Effect of reaction temperature on phenol degradation on various catalysts. (A) α -MnO₂ nanorods (B) α -MnO₂ nanotubes. Reaction conditions: [phenol]₀ = 20 mg/L, catalyst loading = 0.2 g/L, Oxone[®] loading = 2.0 g/L.

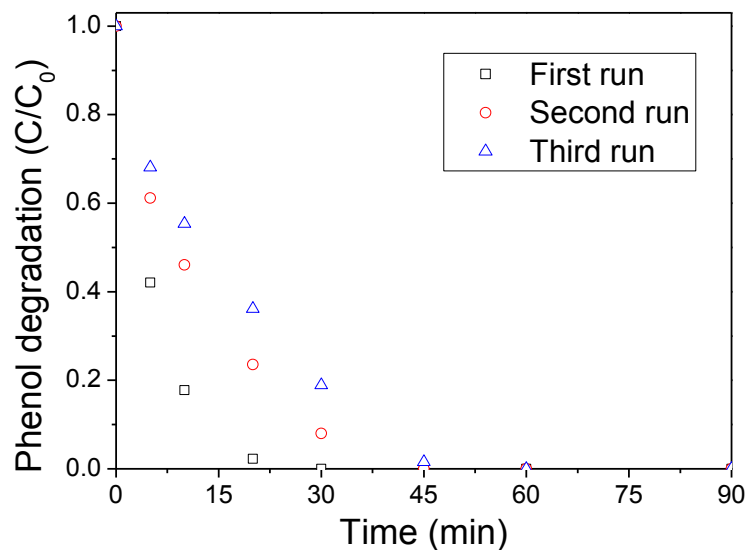


Figure 4.11 Phenol degradation on α -MnO₂ nanowire at different runs after repeated uses. Reaction conditions: [phenol]₀ = 20 mg/L, catalyst loading = 0.2 g/L, Oxone[®] loading = 2.0 g/L, and T = 25 °C.

The stability of nanowires was further investigated by a three-run reusability test, as

shown in Fig. 4.11. For recycle, the catalyst was simply regenerated by water washing. As shown, the phenol degradation rates were similar for the second and third runs and phenol removals were achieved at 100% in 45 min. The decrease of catalytic activity can be attributed to the degradation intermediates which block the active sites on the surface of catalyst and could not be fully removed by water washing. However, these intermediates can be completely removed by calcination either in air or N₂ atmosphere and the catalytic activity will be fully recovered (18, 19).

4.3.3 Activation of PMS and evolution processes of sulfate radicals

In order to investigate the activation and oxidation mechanism, EPR spectra were acquired to identify the hydroxyl and sulfate radicals produced in activation of PMS, using α -MnO₂ as a catalyst and DMPO as the spin trapping agent.

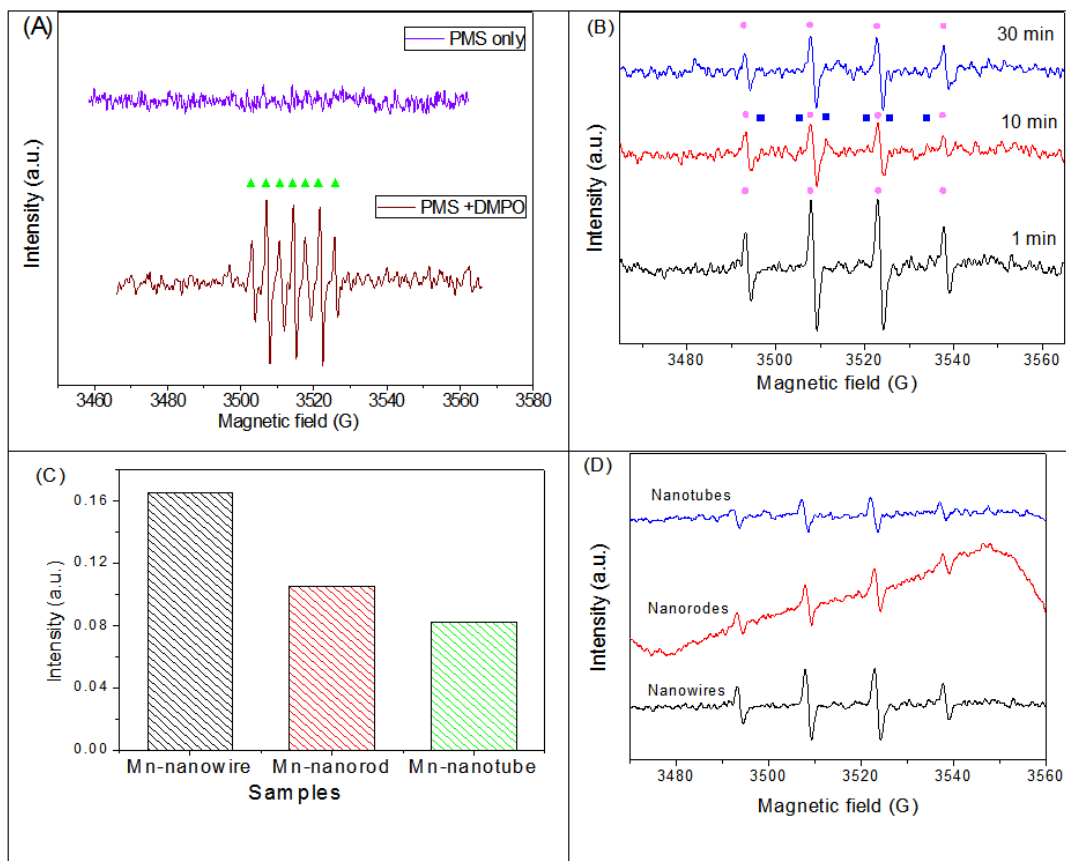


Figure 4.12 EPR spectra in various conditions. (A) Signal of DMPOX, (B) Free radicals in catalytic oxidation of phenol on MnO₂ nanowires, (C) Hydroxyl radical intensities on different catalysts at 1 min activation, and (D) EPR spectra at 1 min activation on different MnO₂ nanomaterials. Centerfield: 3510 G; sweep width: 100 G; microwave frequency: 9.87 GHz; modulation frequency: 100 GHz; and power: 18.11 mW. Reaction conditions: [phenol]₀ = 20 mg/L, catalyst loading= 0.2 g/L, Oxone loading = 2.0 g/L, pH = 7.0, DMPO = 0.08 M. ▲ : DMPOX; ● : DMPO-HO•; ■ : DMPO-SO₄•⁻

To identify the reactive species generated during the catalytic reaction, control experiments were first carried out to study the influence of PMS and PMS with addition of DMPO on EPR spectra. As seen in Fig. 4.12 (A), when 2 g/L PMS solution was tested without addition of DMPO or phenol, no characteristic peaks were identified, suggesting that without the spin-trapping agent, no signals of reactive species were captured. With the addition of 0.08 M DMPO solution to the PMS solution,

strong EPR signals with an intensity ratio of 1:2:1:2:1:2:1 appeared, which can be assigned to the characteristic signals of 5,5-dimethylpyrroline-(2)-oxyl-(1) (DMPOX), the nitroxide radical of DMPO (20). The DMPOX signals can be related to the hydrolysis process of HSO_5^- (Eq. 4.4) (21). The hydrolysis product, H_2O_2 , can then generate hydroxyl radicals (Eq. 4.5) that would directly oxidize DMPO to DMPOX in the absence of phenol.



Fig. 4.12 (B) shows EPR spectra of reactive radicals during the catalytic oxidation on $\alpha\text{-MnO}_2$ nanowires with PMS (2 g/L) in phenol (20 mg/L) solution. As seen, within the overall activation and oxidation processes, both hydroxyl and sulfate radicals were identified through the signals of DMPO- $\text{HO}\cdot$ and DMPO- $\text{SO}_4^{\cdot-}$ adducts, respectively. At 1 min, DMPO- $\text{HO}\cdot$ adducts (with hyperfine splitting constants of $a_{\text{N}} = a_{\text{H}} = 14.9$ G) were observed, suggesting that only hydroxyl radicals were generated at the initial stage of the catalytic reaction (22). Moreover, the absence of DMPOX characteristic peaks in the EPR spectra indicates the selective oxidation behavior of hydroxyl radicals, which preferred to react with phenol rather than DMPO (23). When reaction time was prolonged to 10 min, signals of DMPO- $\text{SO}_4^{\cdot-}$ adducts (with hyperfine splitting constants of $a_{\text{N}} = 13.2$ G, $a_{\text{H}} = 9.6$ G, $a_{\text{H}} = 1.48$ G and $a_{\text{H}} = 0.78$ G) (22) were detected together with the signals of DMPO- $\text{HO}\cdot$ adducts, suggesting that both sulfate and hydroxyl radicals were generated at this reaction stage. It is noted that, the intensity of the DMPO- $\text{HO}\cdot$ peaks decreased within this period, which can be attributed to the reaction of hydroxyl radicals for the generation of sulfate radicals. However, when reaction time was further extended to 30 min, little or no intensities of DMPO- $\text{SO}_4^{\cdot-}$ adducts could be detected, revealing the fact that the generated sulfate radicals were consumed rapidly in the catalytic reaction. The fast disappearance of the DMPO- $\text{SO}_4^{\cdot-}$ not only confirms that sulfate radicals are more active than hy-

droxyl radicals in phenol degradation process, but also indicates that sulfate radicals are the major reactive species for phenol degradation.

Fig. 4.12(C) shows the peak intensities of hydroxyl radicals activated by α -MnO₂ nanostructures (nanowire, nanorod and nanotube) at 1 min and their corresponding EPR spectra are shown in Fig. 4.12 (D). As seen, α -MnO₂ nanowires obtained the highest peak intensity which was almost double of that on α -MnO₂ nanotubes. While α -MnO₂ nanorods presented the peak intensity in between. Given that the intensities are proportional to the concentrations of reactive species at 1 min, the amounts of the hydroxyl radicals generated by the three α -MnO₂ 1D nanostructures follow the order of α -MnO₂ nanowires > α -MnO₂ nanorods > α -MnO₂ nanotubes. Since sulfate radicals were later induced by hydroxyl radicals, it was deduced that the amounts of sulfate radicals in the oxidation also followed the same order.

To further differentiate the major reactive radical species dominating phenol oxidation processes on α -MnO₂ nanowires, competitive radical tests using ethanol (EtOH) and tert-butyl alcohol (TBA) as quenching agents were also carried out. Previous researches have shown that EtOH (with α -hydrogen) can rapidly react with both hydroxyl and sulfate radicals, with the reaction rate constants of $1.2 \times 10^9 - 2.8 \times 10^9$ and $1.6 \times 10^7 - 7.7 \times 10^7 \text{ M}^{-1}\text{s}^{-1}$, respectively (24, 25). TBA (without α -hydrogen) can effectively quench hydroxyl radicals and it reacts approximately 1000-fold faster than sulfate radicals; the reaction rates with hydroxyl radicals and sulfate radicals are $3.8 \times 10^8 - 7.6 \times 10^8$ and $4.0 \times 10^5 - 9.1 \times 10^5 \text{ M}^{-1}\text{s}^{-1}$, respectively (24, 25). Fig. 4.13 shows the results in terms of reaction rate constant of phenol degradation. As seen, by addition of 0.2 M of EtOH, the rate constant experienced a notable decrease, from 0.19 min^{-1} to 0.14 min^{-1} under the same reaction condition, indicating that some of hydroxyl and sulfate radicals were quenched by EtOH and thus the reaction rate decreased significantly. However, when 0.2 M of TBA was added, minor decrease in reaction rate constant was observed, suggesting that, though some of the hydroxyl radicals were quickly quenched, sulfate radicals can still provide the similar phenol

reaction rate to that without quenching agents. Therefore, these results reveal that the major reactive species for phenol degradation were sulfate radicals.

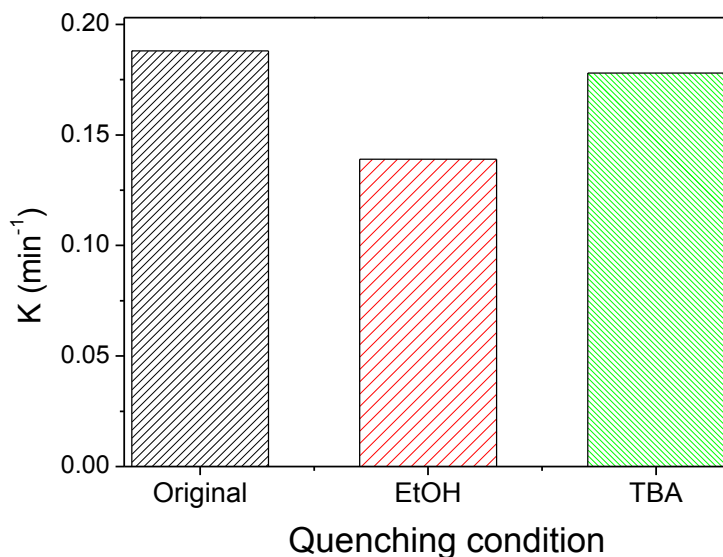


Figure 4.13 Changes of reaction rate (K) on α -MnO₂ nanowire/PMS with and without quenching agents of EtOH (0.2 M) and TBA (0.2 M). Reaction conditions: [phenol]₀ = 20 mg/L, catalyst loading = 0.2 g/L, Oxone[®] loading = 2.0 g/L, and T = 25 °C.

To investigate the intermediates produced from catalytic phenol degradation, reaction solutions taken out at certain time intervals were analyzed using HPLC with a UV detector set at wavelength of 220 nm and a mobile phase flow rate of 0.1 mL/min. Detection results indicated that *p*-benzoquinone, 1,2-dihydroxybenzene and 4-hydroxybenzoic acid were the major intermediates during the catalytic phenol degradation reaction. The concentration variations of the intermediates with time on Mn nanowire are shown in Fig. 4.14. As seen, *p*-benzoquinone and 4-hydroxybenzoic acid were the more abundant aromatic intermediates than 1,2-dihydroxybenzene, revealing that hydroxylation took place in the para position predominantly rather than ortho position (26).

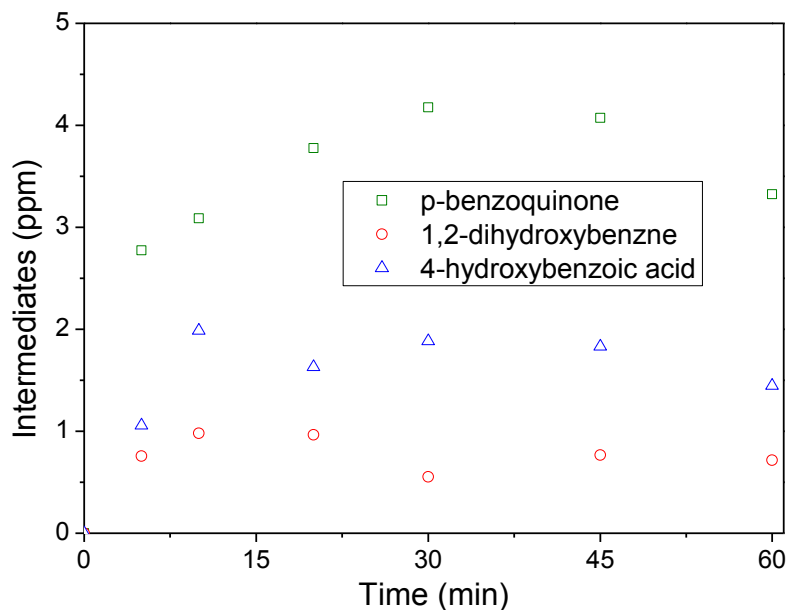
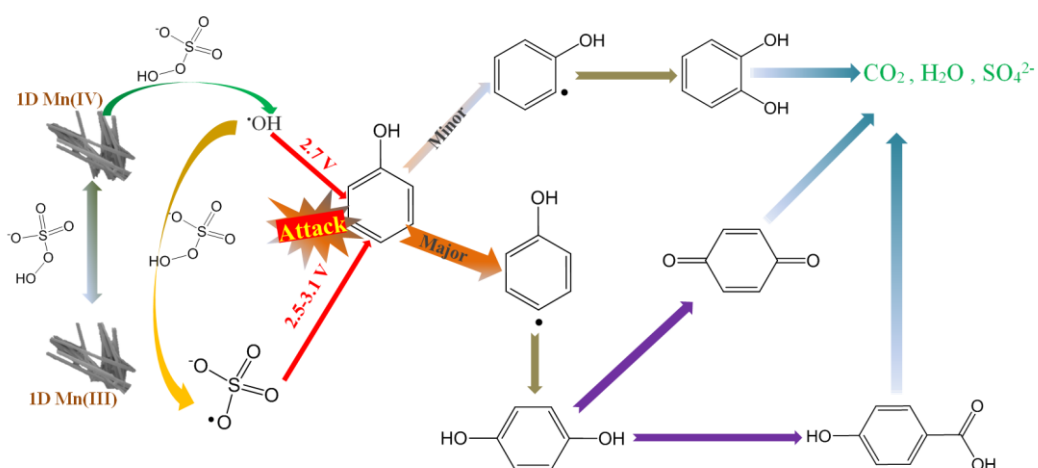
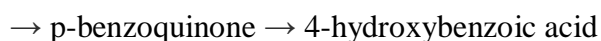


Figure 4.14 Variation of intermediate concentrations during phenol degradation on Mn-100.

On the basis of competitive radical tests, EPR spectra as well as the intermediate identification, the mechanisms of PMS activation on α -MnO₂ nanowires for phenol degradation can be proposed as follows. And Scheme 4.1 describes the mechanism of PMS activation and phenol degradation processes.



Scheme 4.1 Mechanism for PMS activation for phenol degradation on MnO₂ nanowires.



In the first stage, $\alpha\text{-MnO}_2$ nanowires activated PMS to generate hydroxyl radicals (Eq. 4.6). Then some of the hydroxyl radicals further induced PMS to produce sulfate radicals (Eq. 4.7). However, the sulfate radicals were depleted in a short time by rapid reaction with phenol. During the phenol oxidation by sulfate radicals, hydroxyl radicals also participated, though at an inferior reaction rate (Eq. 4.10). After the depletion of sulfate radicals, hydroxyl radicals became the only reactive species reacting with phenol. Meanwhile, the recovery reactions on the reduced $\alpha\text{-MnO}_2$ nanowires resulted in the production of original state of the catalyst as well as the further generation of hydroxyl radicals (Eqs. 4.8 and 4.9). At the same time, competitive reactions may also happen which might negatively affect the generation of reactive species (Eqs. 4.11-13)). On the basis of the comprehensive investigations, it was suggested that the hydroxyl radicals generated by $\alpha\text{-MnO}_2$ initially determines the order of phenol degradation on the three $\alpha\text{-MnO}_2$ 1D nanostructures.

4.4 Conclusions

Several 1D α -MnO₂ catalysts with shapes of nanorods, nanotubes and nanowires were prepared by a one-step hydrothermal method. Their catalytic activities in PMS activation for phenol degradation were investigated. α -MnO₂ nanowires showed the highest BET surface area and largest amount of hydroxyl radical generation thus presenting the best catalytic activity. Although α -MnO₂ nanotubes possess a slightly larger surface area than α -MnO₂ nanorods, the catalytic activity was lower due to less active facet exposure. Catalytic degradation of phenol was influenced by initial phenol concentration, catalyst loading and reaction temperature. Kinetic studies revealed that the phenol degradation using 1D α -MnO₂ catalysts followed a first-order kinetic model, and the activation energies of α -MnO₂ nanorods, nanotubes and nanowires were 39.3, 87.1 and 20.3 kJ/mol, respectively. The mechanism of PMS activation and the roles of reactive radicals were investigated by EPR spectra and competitive radical tests. It was found that the generation of sulfate radicals was initiated by hydroxyl radicals produced at the initial stage and the sulfate radicals were the major reactive species responsible for the catalytic phenol oxidation.

References

1. Saputra E, Muhammad S, Sun H, Ang H-M, Tadé MO, Wang S. Shape-controlled activation of peroxydisulfate by single crystal α - Mn_2O_3 for catalytic phenol degradation in aqueous solution. *Appl. Catal., B.* 2014;154–155(0):246-51.
2. Saputra E, Muhammad S, Sun H, Ang HM, Tadé MO, Wang S. Different Crystallographic One-dimensional MnO_2 Nanomaterials and Their Superior Performance in Catalytic Phenol Degradation. *Environ. Sci. Technol.* 2013;47(11):5882-7.
3. Xiao W, Wang D, Lou XW. Shape-Controlled Synthesis of MnO_2 Nanostructures with Enhanced Electrocatalytic Activity for Oxygen Reduction. *J. Phys. Chem. C.* 2009;114(3):1694-700.
4. Cheng F, Zhao J, Song W, Li C, Ma H, Chen J, et al. Facile Controlled Synthesis of MnO_2 Nanostructures of Novel Shapes and Their Application in Batteries. *Inorg. Chem.* 2006;45(5):2038-44.
5. Yu P, Zhang X, Wang D, Wang L, Ma Y. Shape-Controlled Synthesis of 3D Hierarchical MnO_2 Nanostructures for Electrochemical Supercapacitors. *Cryst. Growth Des.* 2008;9(1):528-33.
6. Saputra E, Muhammad S, Sun H, Patel A, Shukla P, Zhu ZH, et al. α - MnO_2 activation of peroxydisulfate for catalytic phenol degradation in aqueous solutions. *Catal. Commun.* 2012;26(0):144-8.
7. Long JW, Rhodes CP, Young AL, Rolison DR. Ultrathin, Protective Coatings of Poly(o-phenylenediamine) as Electrochemical Proton Gates: Making Mesoporous MnO_2 Nanoarchitectures Stable in Acid Electrolytes. *Nano Lett.* 2003;3(8):1155-61.
8. Sides CR, Martin CR. Nanostructured Electrodes and the Low-Temperature Performance of Li-Ion Batteries. *Adv. Mater.* 2005;17(1):125-8.
9. Chang K-H, Hu C-C. Coalescence inhibition of hydrous RuO_2 crystallites prepared by a hydrothermal method. *Appl. Phys. Lett.* 2006;88(19):-.
10. Wang X, Li Y. Rational synthesis of [small alpha]- MnO_2 single-crystal nanorods. *Chem. Commun.* 2002(7):764-5.
11. Luo J, Zhu HT, Fan HM, Liang JK, Shi HL, Rao GH, et al. Synthesis of Single-Crystal Tetragonal α - MnO_2 Nanotubes. *J. Phys. Chem. C.* 2008;112(33):12594-8.

12. Su D, Ahn H-J, Wang G. Hydrothermal synthesis of [small alpha]-MnO₂ and [small beta]-MnO₂ nanorods as high capacity cathode materials for sodium ion batteries. *J. Mater. Chem. A*. 2013;1(15):4845-50.
13. Li F, Ding Y, Gao P, Xin X, Wang ZL. Single-Crystal Hexagonal Disks and Rings of ZnO: Low-Temperature, Large-Scale Synthesis and Growth Mechanism. *Angew. Chem. Int. Ed.* 2004;43(39):5238-42.
14. Jia C-J, Sun L-D, Yan Z-G, You L-P, Luo F, Han X-D, et al. Single-Crystalline Iron Oxide Nanotubes. *Angew. Chem. Int. Ed.* 2005;44(28):4328-33.
15. Shen XF, Ding YS, Liu J, Cai J, Laubernds K, Zerger RP, et al. Control of Nanometer-Scale Tunnel Sizes of Porous Manganese Oxide Octahedral Molecular Sieve Nanomaterials. *Adv. Mater.* 2005;17(7):805-9.
16. Li Z, Ding Y, Xiong Y, Xie Y. Rational Growth of Various α -MnO₂ Hierarchical Structures and β -MnO₂ Nanorods via a Homogeneous Catalytic Route. *Cryst. Growth Des.* 2005;5(5):1953-8.
17. Zhang P, Zhan Y, Cai B, Hao C, Wang J, Liu C, et al. Shape-controlled synthesis of Mn₃O₄ nanocrystals and their catalysis of the degradation of methylene blue. *Nano Res.* 2010;3(4):235-43.
18. Sun H, Wang Y, Liu S, Ge L, Wang L, Zhu Z, et al. Facile synthesis of nitrogen doped reduced graphene oxide as a superior metal-free catalyst for oxidation. *Chemical Communications*. 2013;49(85):9914-6.
19. Zhao H, Dong Y, Jiang P, Wang G, Zhang J, Li K, et al. An [small alpha]-MnO₂ nanotube used as a novel catalyst in ozonation: performance and the mechanism. *New J. Chem.* 2014;38(4):1743-50.
20. Rosen GM, Raukman EJ. Spin Trapping of the Primary Radical Involved in the Activation of the Carcinogen N-Hydroxy-2-acetylaminofluorene by Cumene Hydroperoxide-Hematin. *Mol. Pharmacol.* 1980;17(2):233-8.
21. Floyd RA, Soong LM. Spin trapping in biological systems. Oxidation of the spin trap 5,5-dimethyl-1-pyrroline-1-oxide by a hydroperoxide-hematin-system. *Biochemical and biophysical research communications*. 1977;74(1):79-84.
22. Fang G-D, Dionysiou DD, Al-Abed SR, Zhou D-M. Superoxide radical driving the activation of persulfate by magnetite nanoparticles: Implications for the degradation of PCBs. *Appl. Catal., B*. 2013;129(0):325-32.
23. Huang YF, Huang YH. Behavioral evidence of the dominant radicals and intermediates involved in Bisphenol A degradation using an efficient Co²⁺/PMS oxidation process. *J. Hazard. Mater.* 2009;167(1-3):418-26.

24. Buxton GV, Greenstock CL, Helman WP, Ross AB. Critical Review of rate constants for reactions of hydrated electrons, hydrogen atoms and hydroxyl radicals ($\cdot\text{OH}/\cdot\text{O}^-$ in Aqueous Solution. *J. Phys. Chem. Ref. Data.* 1988;17(2):513-886.
25. Neta P, Huie RE, Ross AB. Rate Constants for Reactions of Inorganic Radicals in Aqueous Solution. *J. Phys. Chem. Ref. Data.* 1988;17(3):1027-284.
26. Sun H, Liu S, Zhou G, Ang HM, Tadé MO, Wang S. Reduced Graphene Oxide for Catalytic Oxidation of Aqueous Organic Pollutants. *ACS Appl. Mater. Interfaces.* 2012;4(10):5466-71.

Chapter 5: Facile Synthesis of Hierarchically Structured Magnetic MnO₂/ZnFe₂O₄ Hybrid Materials and Their Performance in Heterogeneous Activation of Peroxymonosulfate

ABSTRACT

The effect of morphology of manganese oxide on PMS activation was examined in Chapters 3 and 4. In heterogeneous catalysis for water treatment, feasible recovery of nanocatalysts is also crucial to make the process cost-effective and environmentally benign. In this chapter, we applied two strategies, e.g. magnetic separation and hierarchical structure of solid catalysts, to ensure manganese catalysts are readily separable, meanwhile their catalytic performance was retained by the nanosized structure of MnO₂ nanosheets or nanorods. ZnFe₂O₄ was used as the magnetic core while MnO₂ corolla-like sphere consisting of nanosheets and sea-urchin shaped structure made of nanorods were fabricated by a hydrothermal method at 100 and 140 °C, respectively. Crystalline structure, morphology and textural property of the materials were investigated. The prepared catalysts were able to effectively activate peroxydisulfate (PMS) to generate sulfate radicals for catalytic oxidation of a typical organic pollutant of phenol. After the heterogeneous catalysis, the catalysts were easily recovered by applying an external magnetic field. The effects of temperature and repeated use on the degradation efficiencies were evaluated. The generation and evolution of sulfate radicals and phenol oxidation were studied using both competitive radical tests and electron paramagnetic resonance (EPR).

5.1 Introduction

For catalyst recycling, magnetic separation technology using external magnetic fields provides a convenient and cost-effective way.(1, 2) Over the past decades, magnetite (Fe_3O_4) nanoparticles have been widely used in drug delivery (3-5) and catalyst separation. (6, 7) The magnetic nanoparticles suffer from the drawbacks such as strong dipole–dipole attraction between particles and susceptible to oxidation when exposing to the atmosphere.(8) ZnFe_2O_4 nanoparticles have been proposed as an alternative owing to their better dispersion and outstanding stability in water and atmosphere. (9, 10) Apart from being a magnetic material,(11) ZnFe_2O_4 nanoparticles have successfully demonstrated their extensive applications in photocatalysis,(12) adsorption(13) and solar cells.(14, 15) Compared with other magnetic materials, ZnFe_2O_4 possesses advantages of high stability under humid air, easy synthesis and low cost.(16, 17) ZnFe_2O_4 also shows better dispersion and less dipole-dipole attraction than iron based magnetic materials.(10)

To the best our knowledge, no studies have been reported on synthesis of magnetic 3D-hierarchically structured $\text{ZnFe}_2\text{O}_4/\text{MnO}_2$ hybrid structures. In this chapter, we first demonstrated a facile hydrothermal method to synthesize magnetically separable MnO_2 by hydrothermal treatment of KMnO_4 with HCl , in which ZnFe_2O_4 was used as the magnetic dots integrated on the MnO_2 sub-structure. 3D hierarchical structures were able to be selectively obtained by simply varying the hydrothermal reaction temperature. The prepared catalysts showed outstanding catalytic activity in activation of PMS for degradation of phenol solutions and the activation mechanism was also studied using competitive radical tests and electron paramagnetic resonance (EPR) analysis.

5.2 Experimental Section

5.2.1 Materials.

Iron (III) chloride hexahydrate (99.8%) and zinc chloride (99.5%) were purchased

from Sigma-Aldrich. Sodium acetate (99.5%), ethylene glycol (99.0%) and commercial activated Mn (IV) dioxide (99.9%) were obtained from Fluka. All other chemicals used can be found in previous chapters. All chemicals were used as received without any further purification.

5.2.2 Synthesis of ZnFe₂O₄/MnO₂ hybrid structures.

ZnFe₂O₄ nanoparticles were synthesized via a modified hydrothermal method. In typical synthesis, 0.54 g FeCl₃·6H₂O and 0.14 g ZnCl₂ were dissolved in 30 mL of 1:1 glycerol and water solution by magnetic stirring for 30 min. Then 0.8 g CH₃COONa was added into the mixed solution under vigorous stirring. After stirring for about 20 min, the solution was transferred into a 40 mL Teflon-lined stainless steel autoclave. The autoclave was then sealed and maintained at 200 °C for 12 h and was then cooled down to room temperature naturally. The products were harvested by vacuum filtration and washed with deionized water 3 times before being dried at 60 °C overnight.

For synthesis of ZnFe₂O₄/MnO₂ hybrid structures, 0.25 g of ZnFe₂O₄ was dispersed in 80 mL ultrapure water by sonication for 10 min. Then 0.45 g KMnO₄ and 1 mL of 37% HCl were added to the suspension under vigorous stirring. After stirring for about 30 min, the homogeneous solution was transferred into a Teflon-lined stainless steel autoclave with the capacity of 120 mL. The autoclave was tightly sealed and heated in an electric oven at 100 and 140 °C for 12 h, respectively. After the autoclave was naturally cooled down to room temperature, each of the black precipitate was harvested by vacuum filtration and washed with deionized water 3 times before being dried at 60 °C overnight. According to the hydrothermal temperature, the obtained samples were labelled as mMn-100 and mMn-140, respectively. According to the recovery, the weight loading of MnO₂ was calculated to be 50.5% and 59.2% for mMn-100 and mMn-140, respectively.

5.2.3 Characterization and catalytic oxidation

Characterization details and phenol oxidation as well as mechanistic studies can be found in previous chapters.

5.3 Results and Discussion

5.3.1 Characterization of the hierarchical materials.

The crystalline structures of samples were investigated by XRD. The XRD pattern of the as-prepared ZnFe_2O_4 is shown in Fig. 1(A). As seen, the diffraction peaks found at 2θ of 30.2, 35.5, 42.9, 53.3, 56.8 and 62.3° confirm the formation of cubic ZnFe_2O_4 with a spinel structure (JCPDS No. 77-0011).(9) And these peaks can be indexed to (220), (311), (400), (422), (511) and (440) planes of spinel ZnFe_2O_4 , respectively. The average crystallite size of ZnFe_2O_4 was estimated to be 19.4 nm by the Debye–Scherrer formula. Fig. 1(B) presents the XRD patterns of $\text{ZnFe}_2\text{O}_4/\text{MnO}_2$ hybrid structures synthesized at 100 °C and 140 °C, respectively. Characteristic diffraction peaks of ZnFe_2O_4 were observed on both $\text{ZnFe}_2\text{O}_4/\text{MnO}_2$ samples, indicating the presence of ZnFe_2O_4 in these samples. For $\text{ZnFe}_2\text{O}_4/\text{MnO}_2$ synthesized at 100 °C, peaks at 12.3, 25.5, 36.7 and 66.2° were also observed, corresponding to a pure layered birnessite-type MnO_2 (JCPDS No. 80-1098, monoclinic, $C2/m$, $a=5.15$ Å, $b=2.84$ Å, $c=7.17$ Å), denoted as $\delta\text{-MnO}_2$.(18) And the diffraction peaks identified correspond to the crystal planes of (0 0 1), (0 0 2), (1 1 1) and (3 1 1), respectively. When hydrothermal temperature was elevated to 140 °C, according to the corresponding diffraction peaks, the manganese oxide was found to be pure $\alpha\text{-MnO}_2$ (JCPDS No. 44-0141, tetragonal, $I4/m$, $a=b=9.78$ Å, $c=2.86$ Å).(19) In this temperature-elevation process, the crystalline structure of MnO_2 experienced a transformation from δ -type to α -type, revealing temperature-dependent property of MnO_2 structure. Since no other characteristic peaks from impurities were observed, the obtained samples were confirmed to be of high purity.

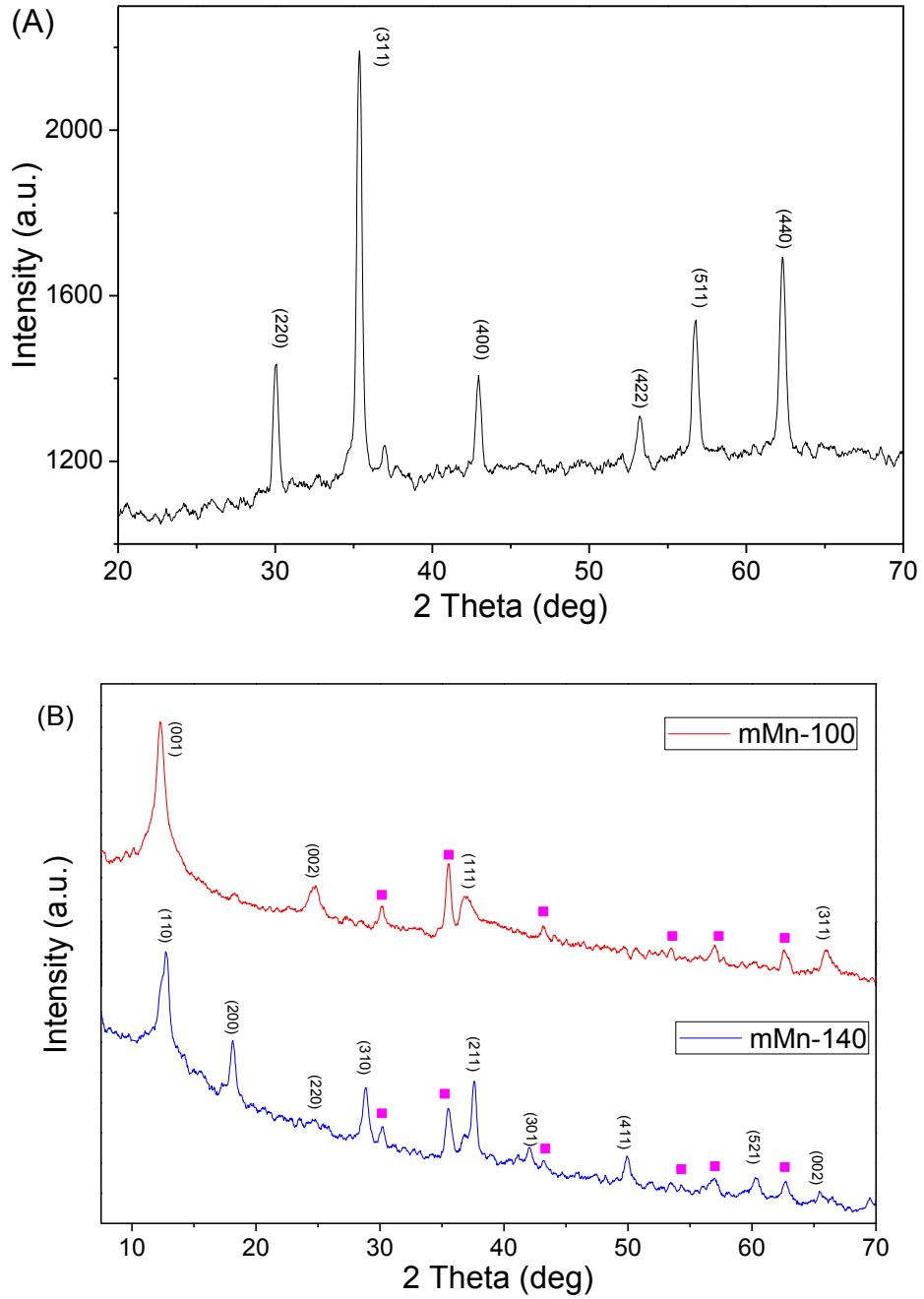


Fig. 5.1 XRD patterns of ZnFe₂O₄ (A) and mMn-100 and mMn-140 (B). ■: ZnFe₂O₄ peaks.

The reactions involved during the hydrothermal processes can be briefly described as follows. (20)



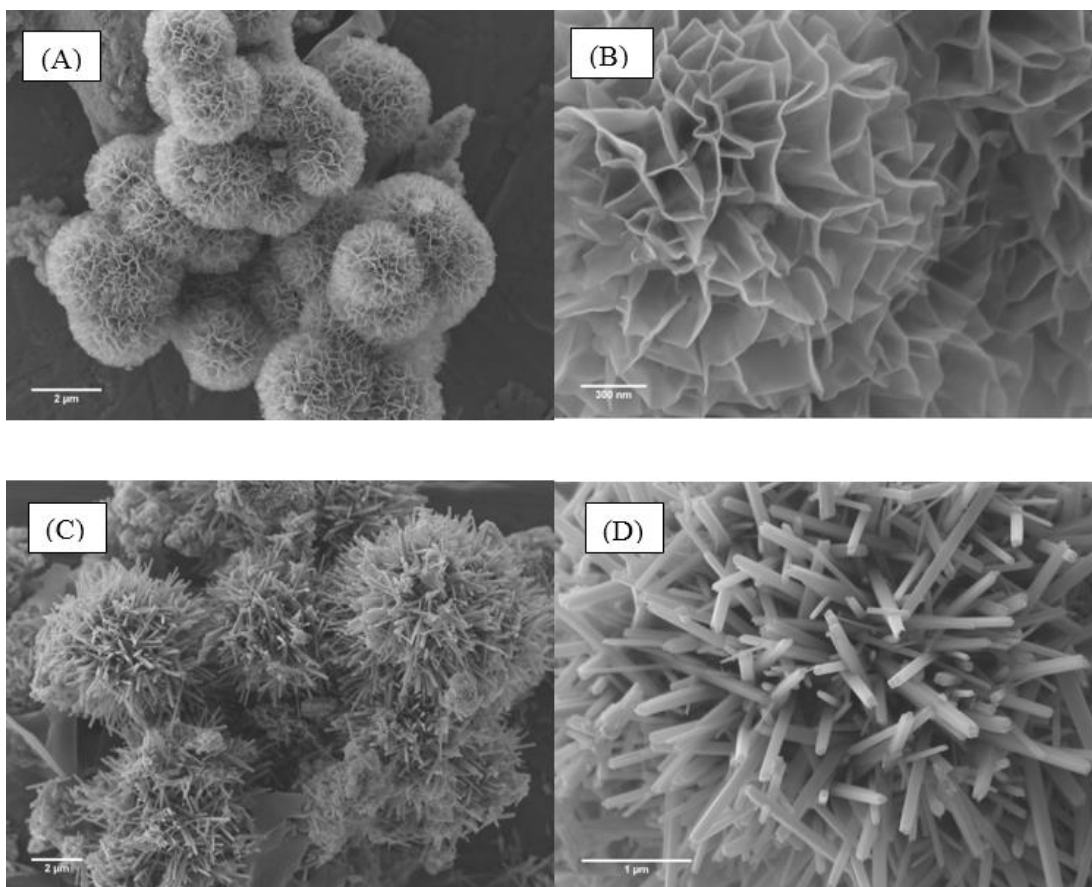
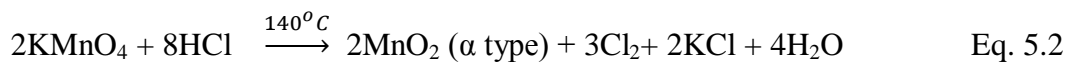


Figure. 5.2 SEM images of $\text{ZnFe}_2\text{O}_4/\text{MnO}_2$ samples. (a) and (b) mMn-100, (c) and (d) mMn-140.

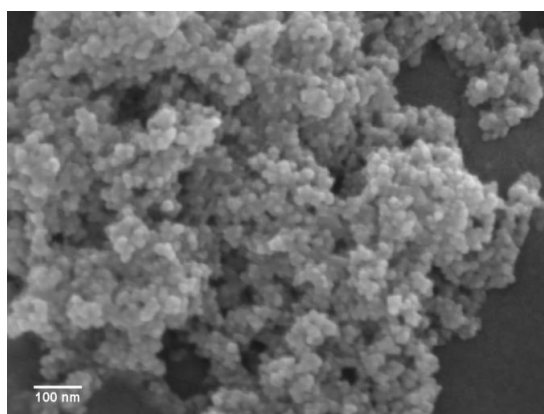


Figure 5.3 SEM image of ZnFe_2O_4 nanoparticles.

Structure and morphology of the magnetic catalysts are displayed by SEM images. Fig. 5.3 illustrates SEM image of ZnFe_2O_4 nanoparticles. It was found that these na-

nanoparticles agglomerated and presented a sphere-like morphology with the average size of 10-20 nm, which is well in agreement with XRD result. The agglomeration of these nanoparticles can be ascribed to the magnetic dipole interaction between them and the high surface energy due to their nano-scaled size.(21) Fig. 5.2 (a) and (b) show SEM images of mMn-100, the sample prepared at 100 °C. It can be observed that this sample shows a uniform corolla-like structure consisting of micro-sphere/nanosheet hierarchical nanostructures with an average diameter around 2 μm . The crystal growth processes of this hierarchical structure include several stages. In the initial stage, a large number of nuclei were formed by the reactions of KMnO_4 and HCl solution.(18) Due to the high surface energy, these nuclei were captured by the well dispersed ZnFe_2O_4 nanoparticles and then grew on their surfaces to encapsulate the ZnFe_2O_4 and form sphere-like structure. At last, the heterogeneous growth of 2D nanosheets on these nuclei happened following a general Ostwald ripening process. (22, 23)

When the hydrothermal temperature was increased to 140 °C, tetragonal $\alpha\text{-MnO}_2$ was produced. As a result, the morphology of mMn-140 transformed to hierarchical sea-urchin shaped microstructure with a diameter of 3-4 μm , made of straight tetragonal nanorods with a uniform diameter of 30-40 nm (Fig. 5.2 (c) and (d)). The transformation of MnO_2 crystalline structure from layered δ -phase to tetragonal α -phase can be assigned to anisotropic growth of crystal favored at elevated temperature to provide higher aspect ratios. (24)

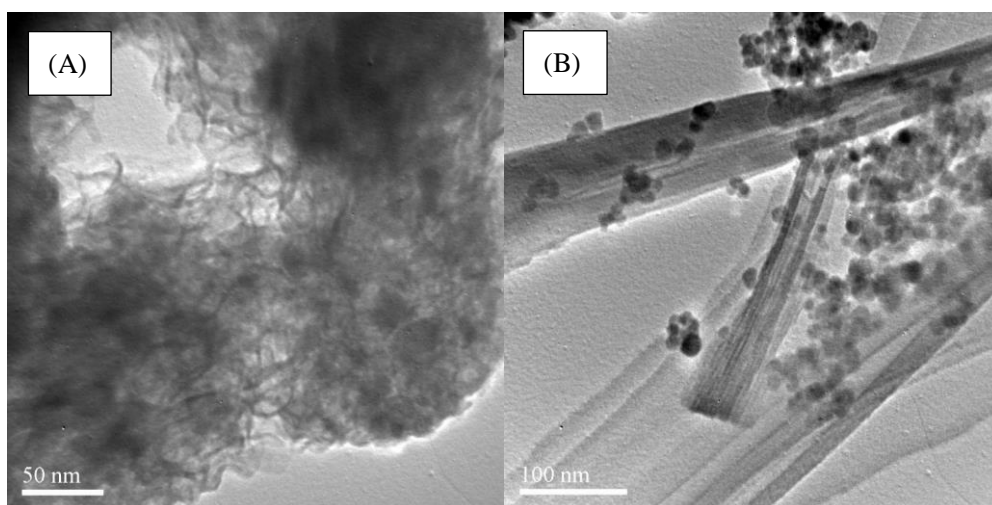


Fig. 5.4 TEM images of (A) mMn-100 and (B) mMn-140.

Fig. 5.4 shows TEM images for mMn-100 and mMn-140. On mMn-100, a two-dimensional sheet-like structure consisting of wrinkles was observed, suggesting a sub-block of 2D layer from the 3D corona-like spheres. Magnetic ZnFe_2O_4 nanoparticles were attached on the layers. For mMn-14, ZnFe_2O_4 nanoparticles were found to be distributed on the surface of the 1D nanorods of the 3D urchin-like structure. The ZnFe_2O_4 nanoparticles in both samples were dispersed well on the MnO_2 . Moreover, the ZnFe_2O_4 nanoparticles had an average size around 10-20 nm, which was in agreement with the average particle size calculated using the Scherrer's formula based on XRD patterns.

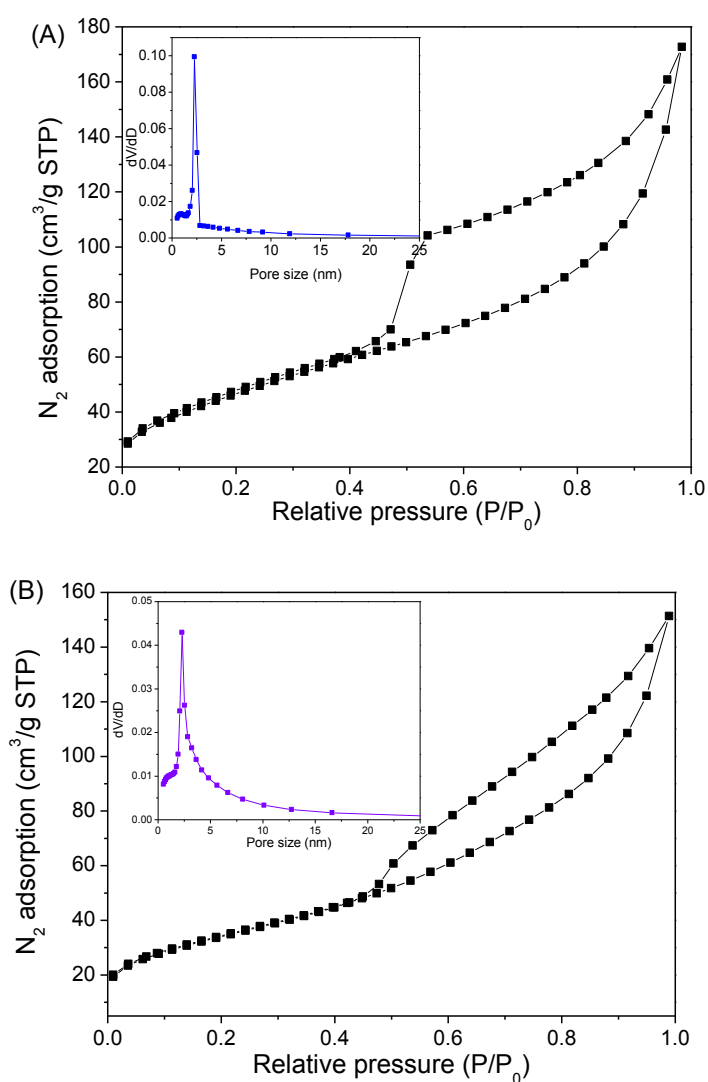


Fig. 5.5 Nitrogen sorption isotherms and pore size distributions of (A) mMn-100 and (B) mMn-140.

N_2 sorption isotherms and pore size distributions of $\text{ZnFe}_2\text{O}_4/\text{MnO}_2$ samples were

evaluated through N₂ adsorption/desorption measurements (Fig. 5.5). According to the IUPAC classification, both of the samples presented a type IV isotherm with a type H3 hysteresis loop, indicating a typical mesoporous structure.(25) As seen, the samples displayed a broad hysteresis loop at a relative pressure range (P/P₀) of 0.4 to 0.95. However, the hysteresis loop on mMn-100 was broader than that of mMn-140, suggesting a more porous structure and thus larger surface area and pore volume, which were confirmed by the results shown in Table 5.1. The BET specific surface area of mMn-100 is about 50% greater than that of mMn-140 (166.5 m²/g vs. 113.1 m²/g) which might be owing to the vast spaces between 2D layered hierarchical structures grown on the surfaces. While the pore size distributions for both samples are quite similar: a single modal pore diameter distribution centred at around 2.5 nm was observed for each sample.

Table 5.1 Textural properties of supported MnO₂ and their activities in phenol degradation

Catalyst	Surface area (S _{BET} , m ² /g)	Pore volume (cm ³ /g)	First-order rate constant (min ⁻¹)	R ²
mMn-100	166.5	0.161	0.032	0.998
mMn-140	113.1	0.154	0.022	0.997

5.3.2 Catalytic oxidation of phenol

Fig. 5.6 shows the adsorption and phenol degradation profiles on various samples. In order to compare the catalytic activity of the samples, control experiments were carried out to evaluate phenol removal caused by catalyst adsorption and PMS self-activation at ambient environment. As seen, less than 10% phenol was degraded when PMS was alone involved in the reaction without a catalyst, indicating that PMS could not be effectively activated under ambient thermal condition. For adsorption tests, both ZnFe₂O₄/MnO₂ samples exerted insignificant phenol removal, suggesting that phenol removal by adsorption was negligible during the heterogeneous catalytic reaction. The fluctuation of phenol removal profiles in adsorption tests might be ascribed to that samples were achieving adsorption/desorption equilibrium.

For catalytic reactions, ZnFe_2O_4 was tested with PMS first and it showed a non-competitive catalytic activity. Around 20% phenol was degraded within 180 min. A commercial MnO_2 sample provided a similar efficiency, less than 20% of phenol was degraded after 180 min. However, mMn-100 demonstrated a much better catalytic activity, and 100% removal of phenol was achieved within 120 min whilst the catalytic activity of mMn-140 was slightly lower providing 100% phenol degradation within 150 min. It was found that the activities followed the order of their BET specific surface area, indicating that higher surface area would provide more active sites for catalytic reaction.

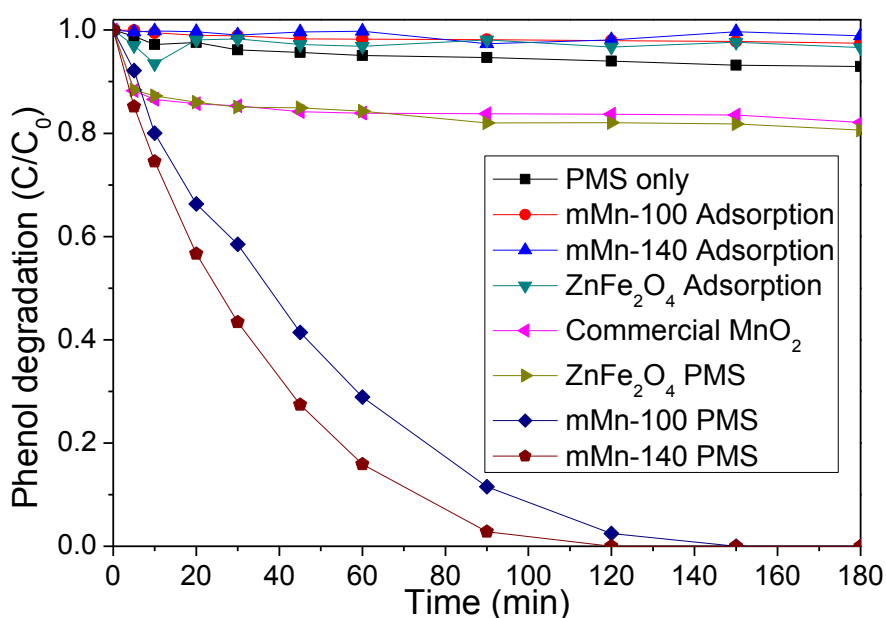


Fig. 5.6 Phenol removal in various conditions. Reaction conditions: $[\text{phenol}]_0 = 20$ mg/L, catalyst loading = 0.2 g/L, Oxone loading = 2.0 g/L, Temperature: 25 °C.

For reaction kinetic studies, a first order mode (Eq.5.3) was employed to evaluate the catalytic reaction kinetics.

$$\ln\left(\frac{C}{C_0}\right) = -kt \quad \text{Eq. 5.3}$$

Where C is the concentration of phenol at time (t) and C_0 is initial phenol concentration. K is the first order reaction rate constant. Fig. 5.7 shows that phenol degradation curve was well fitted with the first-order kinetics with high values of regressions co-

efficients. The reaction rate constants for the two catalysts are provided in Table 5.1.

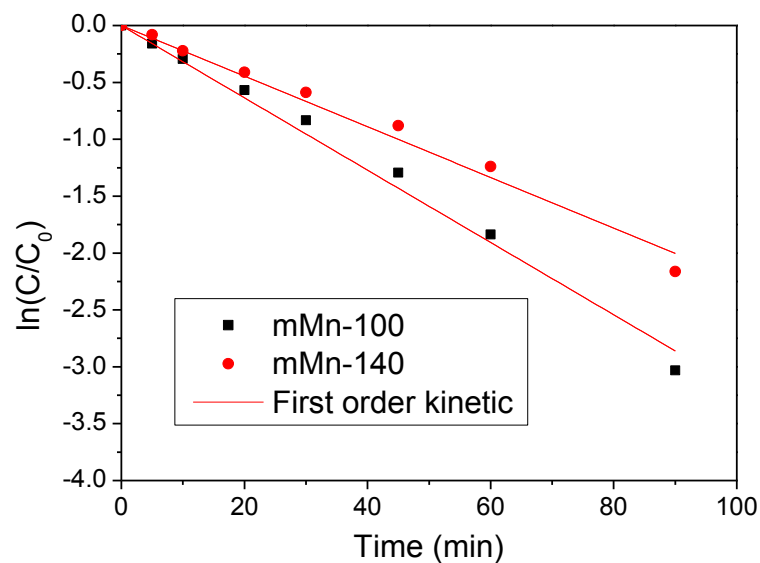


Figure 5.7 First order kinetic model of reactions.

The as-synthesized $\text{ZnFe}_2\text{O}_4/\text{MnO}_2$ catalysts can be easily recycled from reaction solution by simply applying an external magnetic field. As shown in Fig. 5.8, both of the $\text{ZnFe}_2\text{O}_4/\text{MnO}_2$ catalysts can be well dispersed in deionized water and form a stable suspension before magnetic separation (Fig. 5.8(A)). When a magnet was approached to the glass vial, both of the samples rapidly accumulated to the magnet side, and nearly transparent solution was obtained within 3 min (Fig. 5.8(B)). Removing the external magnetic field and sonicating the solution, the solid samples can be dispersed again in solution. Since attraction and dispersion processes can be readily altered by simply approaching or removing an external magnetic field, the as-synthesized $\text{ZnFe}_2\text{O}_4/\text{MnO}_2$ catalysts demonstrated excellent water dispersion and magnetic attraction for effective separation.(26)

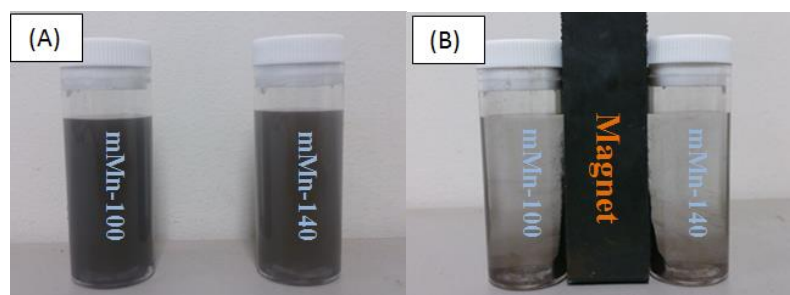


Figure 5.8 Photographs of the separation and dispersion processes. (A) Without an external magnetic field, and (B) with an external magnetic field.

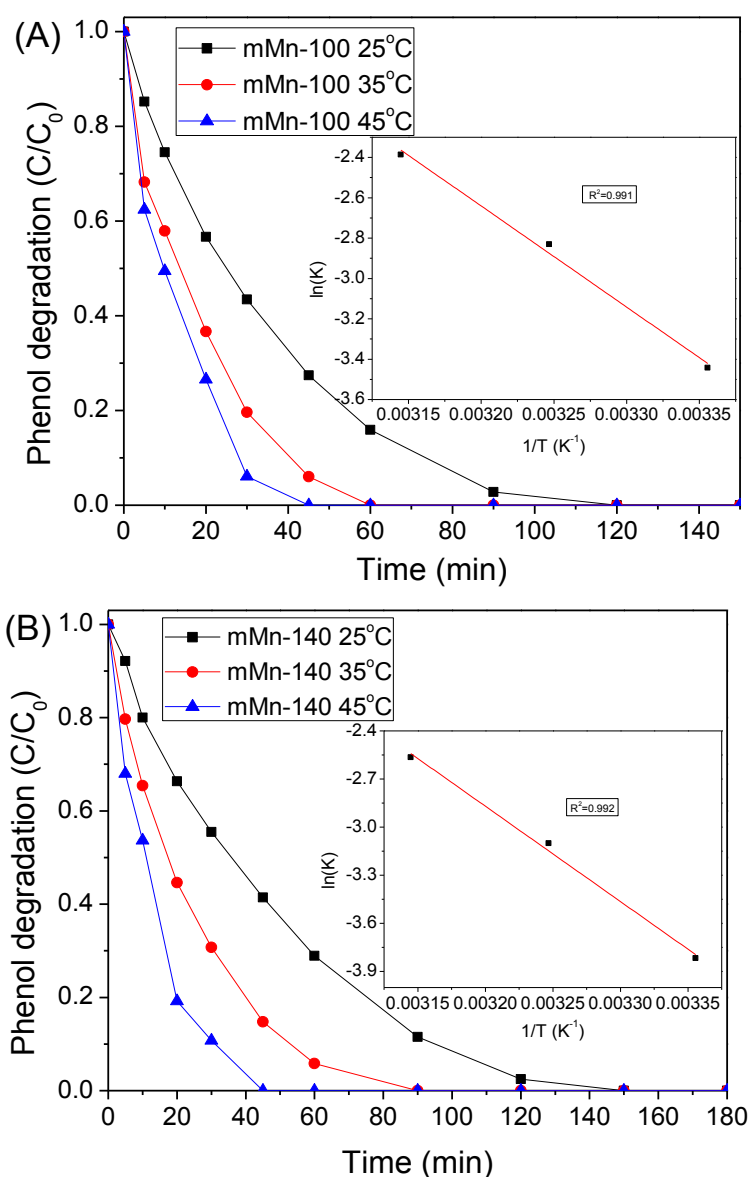


Fig. 5.9 Effect of reaction temperature on phenol degradation and estimation of activation energy for (A) mMn-100 and (B) mMn-140. Reaction conditions: [phenol]₀ = 20 mg/L, catalyst loading = 0.2 g/L, Oxone loading = 2.0 g/L.

Table 5.2 Kinetic results of ZnFe₂O₄/MnO₂ catalysts in activation of PMS for phenol degradation at different temperatures.

Catalyst	T (°C)	K (min ⁻¹)	R ² of K	E _a (kJ/mol)	R ² of E _a
mMn-100	25	0.032	0.991	41.7	0.991
	35	0.059	0.989		
	45	0.092	0.999		
mMn-140	25	0.022	0.994	49.4	0.992
	35	0.045	0.994		
	45	0.077	0.989		

Reaction temperature is a key operating factor in AOPs. Phenol degradation was examined within a temperature range of 25 to 45 °C for both ZnFe₂O₄/MnO₂ catalysts by heterogeneous activation of PMS, and the results are shown in Fig. 5.9. A general trend observed for both catalysts is that temperature will remarkably influence the reaction rate, higher temperature resulting in higher reaction rate. As seen, for mMn-100, when temperature was enhanced from 25 to 45 °C, the time for 100% phenol degradation decreased dramatically from 120 to 45 min. Meanwhile similar phenol degradation profiles were also observed for mMn-140. On the basis of this trend, it might be deduced that PMS activation process is endothermic: higher temperature would shift the equilibrium to produce more reactive species and thus improve the phenol degradation efficiency.

All of these reaction profiles were then fitted with the first order kinetics, and the kinetic rate constants are presented in Table 5.2. The rate constants (K) at varying temperatures for mMn-100 were higher than those of mMn-140, which was in accordance with the degradation profiles in Fig. 5.9. By plotting the lnK against 1/T (inset of Fig. 5.9(A) and (B)) based on the Arrhenius equation, activation energies (E_a) of the catalytic reaction for mMn-100 and mMn-140 can be calculated as 41.7 and 49.4 kJ/mol, respectively. And the lower activation energy of mMn-100 validated its higher catalytic activity than mMn-140. The lower activation energy of mMn-100 might be due to the different crystal structure and preferential facet. When comparing with standard XRD patterns, it was found that mMn-100 had δ-phase with a main exposure of (001), while mMn-140 had α-phase with (110) as main facet. The dif-

ferent crystal phase and facet will contribute to the lower activation energy and higher catalytic performance of mMn-100.

Table 5.3 Comparison of activation energies of Mn-based catalysts.

Catalyst	Organics	E_a (kJ/mol)	Reference
Mn ₃ O ₄ -rGO	Orange II	49.5	(27)
MnFe ₂ O ₄	Orange II	31.7	(28)
MnFe ₂ O ₄ -rGO	Orange II	25.7	(28)
Co ₃ O ₄ /MnO ₂	Phenol	20.3	(29)
α -MnO ₂ nanowire	Phenol	21.9	(30)
ZnFe ₂ O ₄ /MnO ₂ -100	Phenol	41.7	This study
ZnFe ₂ O ₄ /MnO ₂ -140	Phenol	49.4	This study

To our best knowledge, no investigation has been reported on supported MnO₂ or magnetic MnO₂ hybrid structure for activation of PMS for phenol degradation. However, a few studies have been carried out using Mn-based catalysts for heterogeneous activation of PMS for organic removal. Table 5.3 presents the activation energies obtained from these investigations on PMS activation using the as-mentioned catalysts. It was found that magnetic MnO₂ catalysts in this study had higher activation energies in phenol oxidation.

The stability and recyclability of ZnFe₂O₄/MnO₂ catalysts were also evaluated by successive three-run reusability tests (Fig. 5.10). The catalysts were treated by simple water washing without any further regeneration. A general trend for both catalysts is that catalytic activities decreased in recycled tests. As seen in the third run, for both catalysts, 20% of phenol still remained in solution at the end of each reaction, indicating the deactivation of the catalysts. The decrease in catalytic activity might be attributed to the attachment of reaction intermediates on the catalyst surface, which thus deactivated the correspondent active sites. Due to the strong Van de Waals force, these intermediates cannot be fully removed by simple water washing. Recently, we have reported that deactivation induced by attachment of intermediates can be eliminated by calcination at high temperature either in air or N₂ atmosphere.(6, 31)

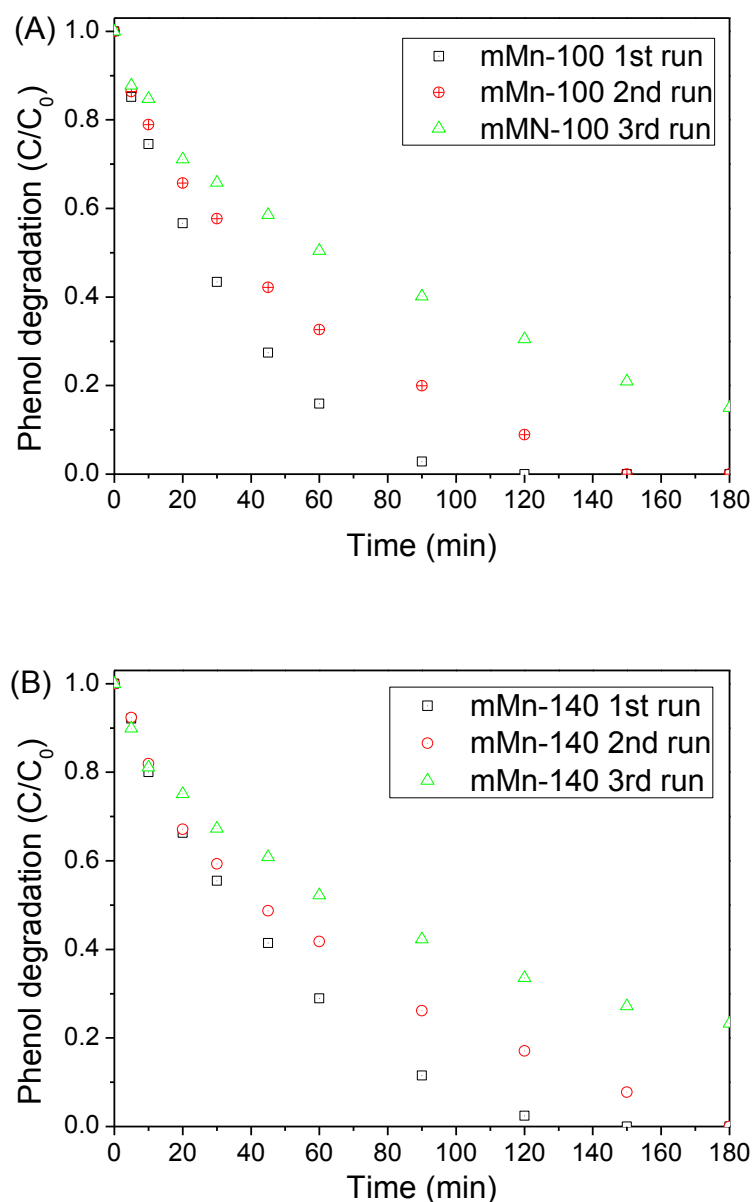
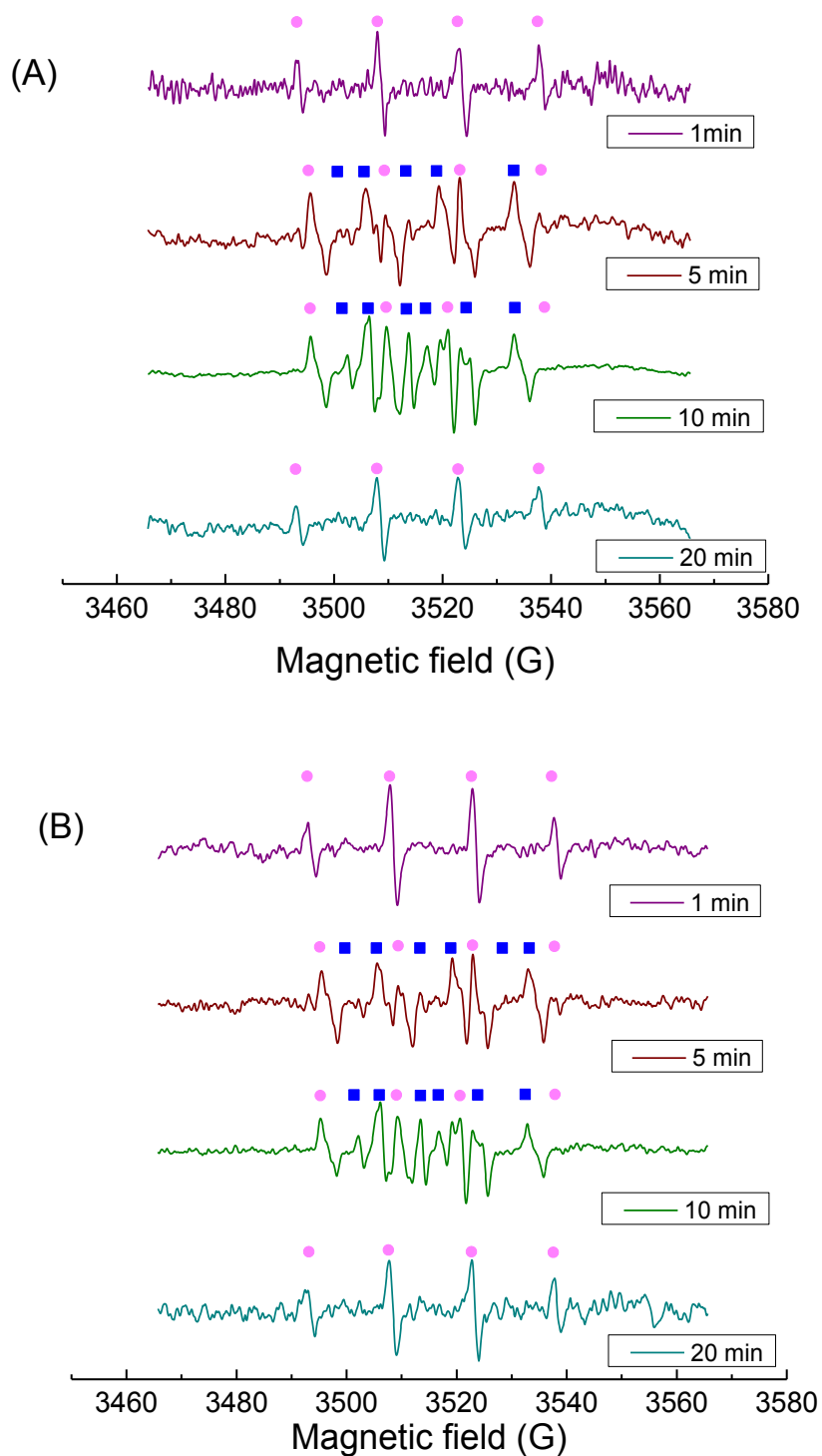


Fig. 5.10 Phenol degradation on mMn-100 and mMn-140 at different runs after repeated uses. (A) Phenol degradation on mMn-100 at different runs after repeated uses; (B) Phenol degradation on mMn-140 at different runs after repeated uses; Reaction conditions: $[\text{phenol}]_0 = 20 \text{ mg/L}$, catalyst loading = 0.2 g/L , Oxone loading = 2.0 g/L , and $T = 25 \text{ }^\circ\text{C}$.

5.3.3 Activation processes of PMS and mechanism of phenol degradation.

Previous studies have reported that PMS can generate hydroxyl radicals ($\cdot\text{OH}$) and sulfate radicals ($\text{SO}_4^{\cdot-}$) by either homogeneous or heterogeneous activation for phe-

nol degradation. (32, 33) Peroxymonosulfate radicals ($\text{SO}_5^{\cdot-}$) might be also formed, but would not contribute to phenol degradation due to the low redox potential. (34) In order to detect the reactive species generated during the PMS activation process, electron paramagnetic resonance (EPR) tests with DMPO as the spin trapping agent were conducted.



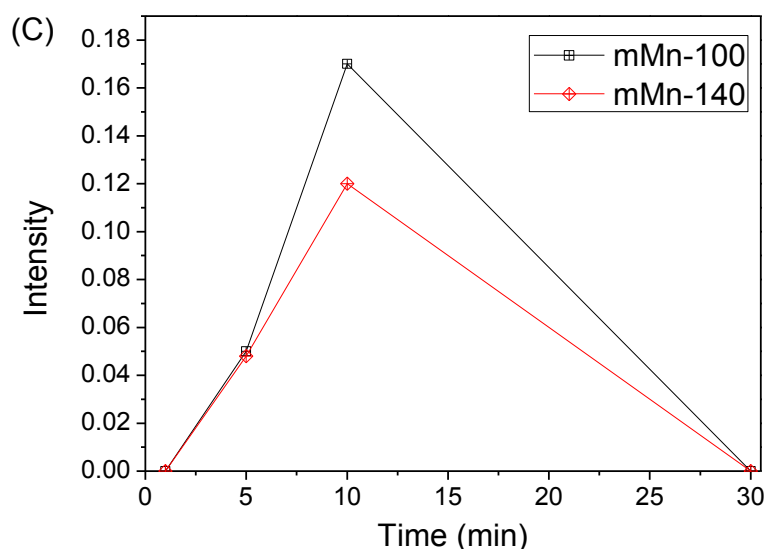


Fig. 5.11 EPR spectra in various conditions. (A) Reactive radicals dependent on activation time over mMn-100, (B) Reactive radicals dependent on activation time over mMn-140, (C) Comparison of sulfate radicals on mMn-100 and mMn-140. Center-field: 3517 G; sweep width: 100 G; microwave frequency: 9.87 GHz; modulation frequency: 100 GHz; and power: 18.11 mW. Reaction conditions: [phenol]₀ = 20 mg/L, catalyst loading = 0.2 g/L, Oxone loading = 2.0 g/L, pH = 7.0, DMPO = 0.08 M. ● : DMPO-HO•; ■ : DMPO-SO₄^{•-}

Control experiments were conducted to investigate PMS self-activation without the presence of catalysts. As seen in Fig. 5.12, when 2 g/L PMS solution was tested without addition of phenol, characteristic signals of 5,5-dimethylpyrroline-(2)-oxyl-(1) (DMPOX), the nitroxide radical of DMPO, were observed. (35) The occurrence of DMPOX signals can be ascribed to the immense amount of hydroxyl radicals produced by strong hydrolysis process of HSO₅⁻, which directly oxidized DMPO to DMPOX without the presence of phenol.(36) The relevant hydrolysis reactions of HSO₅⁻ are shown in Eqs. 5.4 and 5.5.



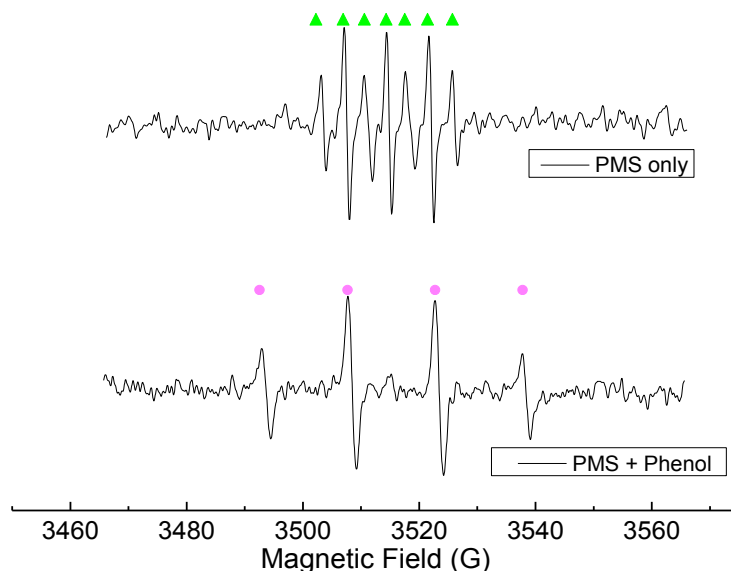


Figure 5.12 EPR spectra at various conditions. Centerfield: 3517 G; sweep width: 100 G; microwave frequency: 9.87 GHz; modulation frequency: 100 GHz; and power: 18.11 mW. Reaction conditions: $[\text{phenol}]_0 = 20 \text{ mg/L}$, catalyst loading = 0.2 g/L, Oxone loading = 2.0 g/L, pH = 7.0, DMPO = 0.08 M. ▲: DMPOX; ●: DMPO-HO \cdot .

When 20 ppm of phenol was added in solution without any catalyst, it could be observed that characteristic peaks of DMPO-HO \cdot adducts having the intensity ratio of 1:2:2:1 (with hyperfine splitting constants of $a_N = a_H = 14.9 \text{ G}$) were presented, indicating that hydroxyl radicals were produced with the presence of phenol. (37) The absence of DMPOX peaks revealed that hydroxyl radicals prefer to react with phenol rather than DMPO. (38)

Fig. 5.11 (A) and (B) display EPR spectra of reactive radicals generated during the catalytic oxidation on $\text{ZnFe}_2\text{O}_4/\text{MnO}_2$ with PMS (2 g/L) for phenol (20 mg/L) degradation. As seen, EPR spectra for both catalysts show the identical trend. Within the overall activation and oxidation processes, both $\cdot\text{OH}$ and $\text{SO}_4^{\cdot-}$ were produced through the identification of signals of DMPO-HO \cdot and DMPO- $\text{SO}_4^{\cdot-}$ adducts, respectively. At the beginning of the reaction (1 min), only hydroxyl radicals were produced by identification of DMPO-HO \cdot adducts, which was similar to that of PMS reacting with phenol solution without the presence of catalysts. This similarity indicates that at the very initial stage of the reaction, the peroxydisulfate anions

(HSO₅⁻) were not fully bonded with the active sites on the catalyst surface to be activated to generate sulfate radicals.

When reaction time was prolonged to 5 min, besides the presence of signals of DMPO-HO[•] adducts, signals of DMPO-SO₄^{•-} adducts (with hyperfine splitting constants of $a_N = 13.2$ G, $a_H = 9.6$ G, $a_H = 1.48$ G and $a_H = 0.78$ G) (37) were also detected, suggesting that HSO₅⁻ had been activated to produce sulfate radicals at this reaction stage. In addition, the appearance of SO₄^{•-} led to the decrease of DMPO-HO[•] signal intensity, which indicates that, in the presence of catalysts, hydroxyl radicals could induce the generation of sulfate radicals. When reaction time was further extended to 10 min, the signal intensity of DMPO-SO₄^{•-} adducts increased, indicating more sulfate radicals had been produced compared with the reaction at 5 min. However, at 30 min, little or no intensities of DMPO-SO₄^{•-} adducts could be detected, suggesting the depletion of sulfate radicals by the rapid reaction, and only signals of DMPO-HO[•] adducts remained, which was again similar to the initial condition. On the basis of this appearance/disappearance cycle of sulfate radicals and the phenol degradation profiles shown in Fig. 5, it can be deduced that sulfate radicals are more active than hydroxyl radicals in phenol degradation process and are responsible for phenol degradation.

Fig. 5.11 (C) shows the evolution of the peak intensities of DMPO-SO₄^{•-} adducts dependence on time over both ZnFe₂O₄/MnO₂ catalysts. As shown clearly, the peak intensities for DMPO-SO₄^{•-} adducts displayed a cycle-like trend. Moreover, the DMPO-SO₄^{•-} peak intensities for mMn-100 were generally higher than those of mMn-140, suggesting that amount of sulfate radicals produced by mMn-100 were greater than those of mMn-140 and thus mMn-100 showed a higher catalytic activity. This observation was not only in accordance with the phenol degradation (shown in Fig. 5.5), but also further confirmed the importance of sulfate radicals in phenol degradation.

To further investigate the major reactive radical species responsible for phenol degradation, competitive radical tests using ethanol (EtOH) and tert-butyl alcohol (TBA) as quenching agents were also carried out. Researches have shown that both EtOH

and TBA could sufficiently quench $\cdot\text{OH}$ and the reaction rates are nearly diffusion controlled at $1.2 \times 10^9 - 2.8 \times 10^9$ and $3.8 \times 10^8 - 7.6 \times 10^8 \text{ M}^{-1} \text{ s}^{-1}$, respectively. (39) While $\text{SO}_4^{\cdot-}$ is selective to be quenched more rapidly by EtOH with α -hydrogen than TBA without α -hydrogen ($1.6 \times 10^7 - 7.7 \times 10^7 \text{ M}^{-1} \text{ s}^{-1}$ vs. $4.0 \times 10^5 - 9.1 \times 10^5 \text{ M}^{-1} \text{ s}^{-1}$). (34, 39) Therefore, by addition of EtOH or TBA into reaction solution, the responsible radical species for phenol degradation could be well differentiated.

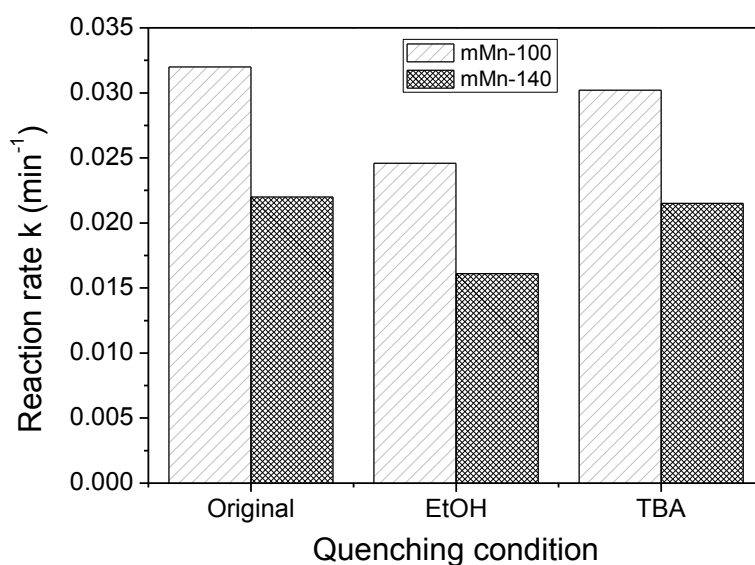
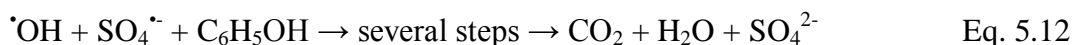
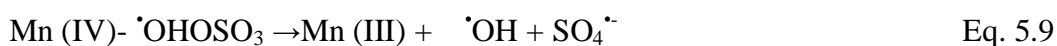


Figure. 5.13 Changes of reaction rate (k) of $\text{ZnFe}_2\text{O}_4/\text{MnO}_2$ catalysts with and without quenching agents of EtOH (0.2M) and TBA (0.2M). Reaction conditions: $[\text{phenol}]_0 = 20 \text{ mg/L}$, catalyst loading = 0.2 g/L , Oxone loading = 2.0 g/L , and $T = 25 \text{ }^\circ\text{C}$.

Fig. 5.13 shows the changes of phenol degradation in form of reaction rate constant k . Both $\text{ZnFe}_2\text{O}_4/\text{MnO}_2$ catalysts shared a similar trend; when 0.2 M EtOH was added in the original reaction solution, remarkable decrease in reaction rate was observed, suggesting that part of the hydroxyl and sulfate radicals were quenched. However, by addition of 0.2 M TBA, negligible decrease occurred to the reaction rate, indicating that, with the quenching of hydroxyl radicals, sulfate radicals could still provide the similar reaction rate. Therefore, the more remarkable decrease of reaction rate caused by EtOH than TBA suggested that the major reactive species dominating phenol degradation were sulfate radicals.

Based on the results of both competitive radical tests and EPR investigations, the mechanism of PMS activation on ZnFe₂O₄/MnO₂ for phenol degradation can be proposed as follows.



In the first stage, hydrolysis of HSO₅⁻ happened to produce hydroxyl radicals (Eq. 5.6). Then some of the hydroxyl radicals attached on the active sites of MnO₂ based catalysts (Eq. 5.7). The Mn(IV) sites with hydroxyl radicals would induce HSO₅⁻ to produce Mn(IV)-·OHOSO₃ and then subsequently to generate sulfate radicals which are dominant for phenol degradation. Meanwhile, some of the attached hydroxyl radicals would also detach (Eqs. 5.8 and 5.9). The produced sulfate radicals and the detached hydroxyl radicals would react with phenol at different reaction rates (Eq. 5.12). After the depletion of sulfate radicals, hydroxyl radicals would become the only reactive species for phenol degradation though at an inferior reaction rate. In the meantime, the recovery reaction for the catalyst resulted in the production of the original catalyst as well as further generation of hydroxyl radicals (Eqs. 5.10) and 5.11). On the basis of the comprehensive investigations, it was suggested that the order of sulfate radicals' generation reflects the order of the reaction rates in phenol degradation on the ZnFe₂O₄/MnO₂ catalysts.

5.4 Conclusions

3-D magnetic $\text{ZnFe}_2\text{O}_4/\text{MnO}_2$ hybrid catalysts with two hierarchical nanostructures were synthesized by a hydrothermal method at varying temperatures. Their catalytic activities were investigated in terms of PMS activation for phenol degradation. It was found that $\text{ZnFe}_2\text{O}_4/\text{MnO}_2$ with microsphere/nanosheet hierarchical structure possessed the higher BET surface area and thus the better catalytic activity than urchin-like catalysts. A first order kinetic model was used to evaluate the kinetic parameters, and the activation energies for microsphere/nanosheet hierarchical structure and urchin-like structure were calculated to be 41.7 and 49.4 kJ/mol, respectively. Catalyst stability tests suggested that deactivation of the catalysts occurred due to the blockage of active sites by the reaction intermediates. The mechanism of catalytic reaction for activation of PMS was illustrated by competitive radical tests and EPR spectra. Sulfate radicals were the major reactive species taking effect in this catalytic reaction and the generation of sulfate radicals could be induced by hydroxyl radicals produced at the initial stage.

References

1. Balu AM, Baruwati B, Serrano E, Cot J, Garcia-Martinez J, Varma RS, et al. Magnetically separable nanocomposites with photocatalytic activity under visible light for the selective transformation of biomass-derived platform molecules. *Green Chem.* 2011;13(10):2750-8.
2. Cano M, Sbagoud K, Allard E, Larpent C. Magnetic separation of fatty acids with iron oxide nanoparticles and application to extractive deacidification of vegetable oils. *Green Chem.* 2012;14(6):1786-95.
3. Zhang L, Qiao SZ, Jin YG, Chen ZG, Gu HC, Lu GQ. Magnetic Hollow Spheres of Periodic Mesoporous Organosilica and Fe₃O₄ Nanocrystals: Fabrication and Structure Control. *Adv. Mater.* 2008;20(4):805-9.
4. Liu J, Wang B, Budi Hartono S, Liu T, Kantharidis P, Middelberg APJ, et al. Magnetic silica spheres with large nanopores for nucleic acid adsorption and cellular uptake. *Biomaterials.* 2012;33(3):970-8.
5. Yonghua S, Shizhang Q, Huagui Y, Chen Y, Yonggang J, Frances S, et al. Titanate-silica mesostructured nanocables: synthesis, structural analysis and biomedical applications. *Nanotechnology.* 2010;21(6):065604.
6. Wang Y, Sun H, Ang HM, Tadé MO, Wang S. Magnetic Fe₃O₄/carbon sphere/cobalt composites for catalytic oxidation of phenol solutions with sulfate radicals. *Chem. Eng. J.* 2014;245(0):1-9.
7. Wang Y, Sun H, Ang HM, Tadé MO, Wang S. Synthesis of magnetic core/shell carbon nanosphere supported manganese catalysts for oxidation of organics in water by peroxydisulfate. *J. Colloid Interface Sci.* 2014;433(0):68-75.
8. Chandra V, Park J, Chun Y, Lee JW, Hwang I-C, Kim KS. Water-Dispersible Magnetite-Reduced Graphene Oxide Composites for Arsenic Removal. *ACS Nano.* 2010;4(7):3979-86.
9. Guo P, Cui L, Wang Y, Lv M, Wang B, Zhao XS. Facile Synthesis of ZnFe₂O₄ Nanoparticles with Tunable Magnetic and Sensing Properties. *Langmuir.* 2013;29(28):8997-9003.
10. Zhang S, Li J, Zeng M, Zhao G, Xu J, Hu W, et al. In Situ Synthesis of Water-Soluble Magnetic Graphitic Carbon Nitride Photocatalyst and Its Synergistic Catalytic Performance. *ACS Appl. Mater. Interfaces.* 2013;5(23):12735-43.
11. Deng H, Li X, Peng Q, Wang X, Chen J, Li Y. Monodisperse Magnetic Single-Crystal Ferrite Microspheres. *Angew. Chem. Int. Ed.* 2005;44(18):2782-5.

12. Jia Z, Ren D, Liang Y, Zhu R. A new strategy for the preparation of porous zinc ferrite nanorods with subsequently light-driven photocatalytic activity. *Mater. Lett.* 2011;65(19–20):3116-9.
13. Wang M, Ai Z, Zhang L. Generalized Preparation of Porous Nanocrystalline ZnFe_2O_4 Superstructures from Zinc Ferrioxalate Precursor and Its Superparamagnetic Property. *J. Phys. Chem. C.* 2008;112(34):13163-70.
14. Habibi MH, Habibi AH, Zendehtdel M, Habibi M. Dye-sensitized solar cell characteristics of nanocomposite zinc ferrite working electrode: Effect of composite precursors and titania as a blocking layer on photovoltaic performance. *Spectrochim. Acta, Part A.* 2013;110(0):226-32.
15. Tahir AA, Wijayantha KGU. Photoelectrochemical water splitting at nanostructured ZnFe_2O_4 electrodes. *J. Photochem. Photobiol., A.* 2010;216(2–3):119-25.
16. McDonald KJ, Choi K-S. Synthesis and Photoelectrochemical Properties of $\text{Fe}_2\text{O}_3/\text{ZnFe}_2\text{O}_4$ Composite Photoanodes for Use in Solar Water Oxidation. *Chem. Mater.* 2011;23(21):4863-9.
17. Aranishi K, Jiang H-L, Akita T, Haruta M, Xu Q. One-step synthesis of magnetically recyclable Au/Co/Fe triple-layered core-shell nanoparticles as highly efficient catalysts for the hydrolytic dehydrogenation of ammonia borane. *Nano Res.* 2011;4(12):1233-41.
18. Xiao W, Wang D, Lou XW. Shape-Controlled Synthesis of MnO_2 Nanostructures with Enhanced Electrocatalytic Activity for Oxygen Reduction. *J. Phys. Chem. C.* 2009;114(3):1694-700.
19. Yu P, Zhang X, Wang D, Wang L, Ma Y. Shape-Controlled Synthesis of 3D Hierarchical MnO_2 Nanostructures for Electrochemical Supercapacitors. *Cryst. Growth Des.* 2008;9(1):528-33.
20. Li Z, Ding Y, Xiong Y, Xie Y. Rational Growth of Various $\alpha\text{-MnO}_2$ Hierarchical Structures and $\beta\text{-MnO}_2$ Nanorods via a Homogeneous Catalytic Route. *Cryst. Growth Des.* 2005;5(5):1953-8.
21. Li Y, Yi R, Yan A, Deng L, Zhou K, Liu X. Facile synthesis and properties of ZnFe_2O_4 and $\text{ZnFe}_2\text{O}_4/\text{polypyrrole}$ core-shell nanoparticles. *Solid State Sci.* 2009;11(8):1319-24.
22. Oaki Y, Imai H. One-Pot Synthesis of Manganese Oxide Nanosheets in Aqueous Solution: Chelation-Mediated Parallel Control of Reaction and Morphology. *Angew. Chem. Int. Ed.* 2007;46(26):4951-5.
23. Portehault D, Cassaignon S, Nassif N, Baudrin E, Jolivet J-P. A Core–Corona

Hierarchical Manganese Oxide and its Formation by an Aqueous Soft Chemistry Mechanism. *Angew. Chem. Int. Ed.* 2008;47(34):6441-4.

24. Wang X, Li Y. Rational synthesis of [small alpha]-MnO₂ single-crystal nanorods. *Chem. Commun.* 2002(7):764-5.

25. Zhang P, Zhan Y, Cai B, Hao C, Wang J, Liu C, et al. Shape-controlled synthesis of Mn₃O₄ nanocrystals and their catalysis of the degradation of methylene blue. *Nano Res.* 2010;3(4):235-43.

26. Hui C, Shen C, Tian J, Bao L, Ding H, Li C, et al. Core-shell Fe₃O₄@SiO₂ nanoparticles synthesized with well-dispersed hydrophilic Fe₃O₄ seeds. *Nanoscale.* 2011;3(2):701-5.

27. Yao Y, Xu C, Yu S, Zhang D, Wang S. Facile Synthesis of Mn₃O₄-Reduced Graphene Oxide Hybrids for Catalytic Decomposition of Aqueous Organics. *Ind. Eng. Chem. Res.* 2013;52(10):3637-45.

28. Yao Y, Cai Y, Lu F, Wei F, Wang X, Wang S. Magnetic recoverable MnFe₂O₄ and MnFe₂O₄-graphene hybrid as heterogeneous catalysts of peroxymonosulfate activation for efficient degradation of aqueous organic pollutants. *J. Hazard. Mater.* 2014;270(0):61-70.

29. Liang H, Sun H, Patel A, Shukla P, Zhu ZH, Wang S. Excellent performance of mesoporous Co₃O₄/MnO₂ nanoparticles in heterogeneous activation of peroxymonosulfate for phenol degradation in aqueous solutions. *Appl. Catal., B.* 2012;127(0):330-5.

30. Saputra E, Muhammad S, Sun H, Ang HM, Tadé MO, Wang S. Different Crystallographic One-dimensional MnO₂ Nanomaterials and Their Superior Performance in Catalytic Phenol Degradation. *Environ. Sci. Technol.* 2013;47(11):5882-7.

31. Sun H, Wang Y, Liu S, Ge L, Wang L, Zhu Z, et al. Facile synthesis of nitrogen doped reduced graphene oxide as a superior metal-free catalyst for oxidation. *Chemical Communications.* 2013;49(85):9914-6.

32. Saputra E, Muhammad S, Sun H, Ang H-M, Tadé MO, Wang S. Manganese oxides at different oxidation states for heterogeneous activation of peroxymonosulfate for phenol degradation in aqueous solutions. *Appl. Catal., B.* 2013;142-143(0):729-35.

33. Anipsitakis GP, Dionysiou DD. Degradation of Organic Contaminants in Water with Sulfate Radicals Generated by the Conjunction of Peroxymonosulfate with Cobalt. *Environmental Science & Technology.* 2003;37(20):4790-7.

34. Neta P, Huie RE, Ross AB. Rate Constants for Reactions of Inorganic Radicals

in Aqueous Solution. *J. Phys. Chem. Ref. Data.* 1988;17(3):1027-284.

35. Rosen GM, Raukman EJ. Spin Trapping of the Primary Radical Involved in the Activation of the Carcinogen N-Hydroxy-2-acetylaminofluorene by Cumene Hydroperoxide-Hematin. *Mol. Pharmacol.* 1980;17(2):233-8.

36. Floyd RA, Soong LM. Spin trapping in biological systems. Oxidation of the spin trap 5,5-dimethyl-1-pyrroline-1-oxide by a hydroperoxide-hematin-system. *Biochemical and biophysical research communications.* 1977;74(1):79-84.

37. Fang GD, Dionysiou DD, Al-Abed SR, Zhou DM. Superoxide radical driving the activation of persulfate by magnetite nanoparticles: Implications for the degradation of PCBs. *Appl. Catal., B.* 2013;129(0):325-32.

38. Huang YF, Huang YH. Behavioral evidence of the dominant radicals and intermediates involved in Bisphenol A degradation using an efficient Co^{2+} /PMS oxidation process. *J. Hazard. Mater.* 2009;167(1-3):418-26.

39. Buxton GV, Greenstock CL, Helman WP, Ross AB. Critical Review of rate constants for reactions of hydrated electrons, hydrogen atoms and hydroxyl radicals ($\cdot\text{OH}/\cdot\text{O}^-$ in Aqueous Solution. *J. Phys. Chem. Ref. Data.* 1988;17(2):513-886.

Chapter 6: A New Magnetic Nano Zero-valent Iron Encapsulated in Carbon Spheres for Oxidative Degradation of Phenol

ABSTRACT

Other than ZnFe_2O_4 as the magnetic core in the last chapter for feasible separation, in this chapter, a magnetic carbon encapsulated nano iron hybrid (nano $\text{Fe}^0/\text{Fe}_3\text{C}@CS$) was synthesized via a novel one-pot hydrothermal method followed by self-reduction in N_2 atmosphere. The structural, morphological, and physicochemical properties of the samples were thoroughly investigated by X-ray diffraction (XRD), field emission scanning electron microscopy (FE-SEM), N_2 sorption isotherms and thermogravimetric analysis–differential scanning calorimetry (TGA-DSC). Catalytic performance of the as-synthesized nanoparticles was tested in activation of Oxone[®] for phenol degradation in aqueous solutions. Superior catalytic performance was observed by complete removal of 20 ppm phenol within 10 min. The formation of Fe_3C was found to contribute to a better stability and magnetic separation of $\text{Fe}^0/\text{Fe}_3\text{C}@CS$ in its repeated uses. Both electron paramagnetic resonance (EPR) and classic quenching tests were carried out to investigate the mechanism of radical generation and evolution in phenol oxidation. Different from Co- and Mn-based catalysts in generation of sulfate radicals, $\text{Fe}^0/\text{Fe}_3\text{C}@CS$ selectively induced hydroxyl radicals for phenol degradation.

6.1 Introduction

Due to low cost and strong redox potential, zero-valent iron (ZVI) has been widely applied for removal of a variety of pollutants such as chlorinated hydrocarbons, nitrobenzenes, chlorinated phenols, polychlorinated biphenyls (PCBs), heavy metals, and various anions.(1, 2) Compared with bulk ZVI, nanoscaled ZVI (nano-Fe⁰) shows a higher activity in reduction reactions due to its high specific surface area and surface reactivity.(3) However, nano-Fe⁰ suffers from poor air stability due to its high surface energy.(4, 5) To improve the stability, it was suggested that nano-Fe⁰ can be encapsulated into porous carbon spheres for enhancement of transportation and suspension, without significantly sacrificing activity.(6) Another concern to nano-Fe⁰ particles is that they favor strong aggregation due to their strong inter-particle dipole-dipole attraction and the high surface area to volume ratio.(7) Therefore, for a better distribution, various types of support materials have been employed, such as bentonite(8), activated carbon(9), alumina(10) and polystyrene resin(11), etc. In general, borohydride salt was used in liquid-phase reduction methods for preparation of most of the supported nano-Fe⁰ composites.(8-10) Nevertheless, vacuum operation, N₂ atmosphere, massive production of hydrogen and high cost of borohydride in the synthesis make such processes complex and cost-intensive.

Recently, we discovered that nano-Fe⁰ encapsulated in microscaled carbon spheres (Fe⁰@CS) can activate PMS to produce sulfate radicals for phenol degradation.(12) However, catalytic stability of the nanocomposites was below anticipation due to the rapid consumption of nano-Fe⁰ in acid condition. In this chapter, a novel magnetic carbon encapsulated nano Fe⁰/Fe₃C was fabricated by an *in situ* hydrothermal carbonization of glucose with addition of melamine, followed by a self-reduction in N₂ atmosphere. Owing to the emerging phase of Fe₃C, the as-synthesized Fe⁰/Fe₃C@CS catalyst showed a much higher stability than reported Fe⁰@CS.(12) Electron paramagnetic resonance (EPR) spectra suggested that hydroxyl radicals were selectively

produced during the heterogeneous PMS activation, indicating an alternative to homogeneous Fenton reaction. Moreover, the prepared catalysts showed both high activity and magnetic separation efficiency in catalytic oxidation of phenol solutions.

6.2 Experimental Sections

6.2.1 Chemicals and materials

Iron (II) chloride tetrahydrate (99.9%), iron (III) hexahydrate (99.9%) and melamine (99.8%) were purchased from Sigma Aldrich. D-glucose (99.9%) was obtained from Fluka. Ammonia solution (28%) was obtained from Ajax Finechem. High purity nitrogen gas (99.999%) was received from BOC. All other chemicals can be found in the previous chapters. And all chemicals were used as received without further purification.

6.2.2 Synthesis of magnetic carbon encapsulated Fe⁰

Magnetic Fe⁰/Fe₃C@CS was synthesized via a modified hydrothermal method. In a typical synthesis, 2.52 g (0.02 mol) melamine and 7.24 g (0.02 mol) D-glucose were dissolved in 50 mL of ultrapure water. Then 5.41 g (0.02 mol) of FeCl₃·6H₂O and 2.01 g (0.01 mol) of FeCl₂·4H₂O were dissolved in the D-glucose/melamine solution, followed by 1 h stirring. Under vigorous stirring, 28% ammonia solution was added dropwisely at a rate of 0.5 mL/min under nitrogen flow (40 mL/min) to make solution pH reach 10. The mixed solution was then transferred into a Teflon-lined autoclave (120 mL) and treated in an oven at 180 °C for 18 h. After naturally cooling to room temperature, the obtained black suspension was filtered and washed by ethanol/water for three cycles. The precipitate was dried in an oven at 80 °C and labelled as Fe^x@CS. The dried samples were further annealed in N₂ atmosphere in a tubular furnace at 350 °C, 550 °C and 750 °C for 4 h, respectively and then were accordingly

denoted as Fe^x@CS-350, Fe⁰/Fe₃C@CS and Fe^x@CS-750. Nano-Fe⁰@CS was prepared as a reference material according to our previous study(12).

6.2.3 Characterization and catalytic oxidation tests

The iron content and thermal stability of Fe^x@CS were investigated using thermogravimetric analysis-differential scanning calorimetry (TGA-DSC) in argon or air on a Mettler-Toledo Stare system. Argon/air flow rate was set to be 100 mL/min and the heating rate was 10 °C/min. X-ray photoelectron spectroscopy (XPS) was conducted on a Thermo Escalab 250 with Al-K α X-ray to investigate the chemical states of elements. A Shirley background was first subtracted followed by component fitting using Voigt functions with a 30% Lorentzian component.

Other characterization details and phenol oxidation as well as mechanistic studies can be found in previous chapters.

6.3 Results and Discussion

6.3.1 Physicochemical properties of the materials

Fig. 6.1 illustrates XRD patterns of the as-prepared nanocomposites. For Fe^x@CS, cubic structured γ -Fe₂O₃ (JCPDS no. 39-1346) with lattice constants of 8.3248 Å was discerned by the observation of diffraction peaks at 31.1, 35.6, 43.1, 57.9 and 62.5°. (13) These peaks are corresponding to the crystal planes of (2 2 0), (3 1 1), (4 0 0), (4 2 2) and (4 4 0), respectively. Besides, the diffraction peak located at 27.3° indicated the formation of g-C₃N₄. (14) Since no obvious peak from graphite (ca. 2 θ = 26 °) was present, the produced carbon was suggested to be amorphous. For Fe⁰/Fe₃C@CS, after thermal treatments under nitrogen, the diffraction peaks of γ -Fe₂O₃ became very weak, and the peak of g-C₃N₄ disappeared. Diffraction peaks

formed at around 45.1° confirmed the formation of zero-valent iron and Fe_3C .(15) According to the Scherrer's formula, the average grain size of the zero-valent iron particles was calculated to be 26 nm. The changes observed in XRD patterns before and after calcination indicated that a solid-state pyrolysis process occurred and Fe_2O_3 , carbon and $\text{g-C}_3\text{N}_4$ reacted with each other to form zero-valent iron and Fe_3C compound.(15)

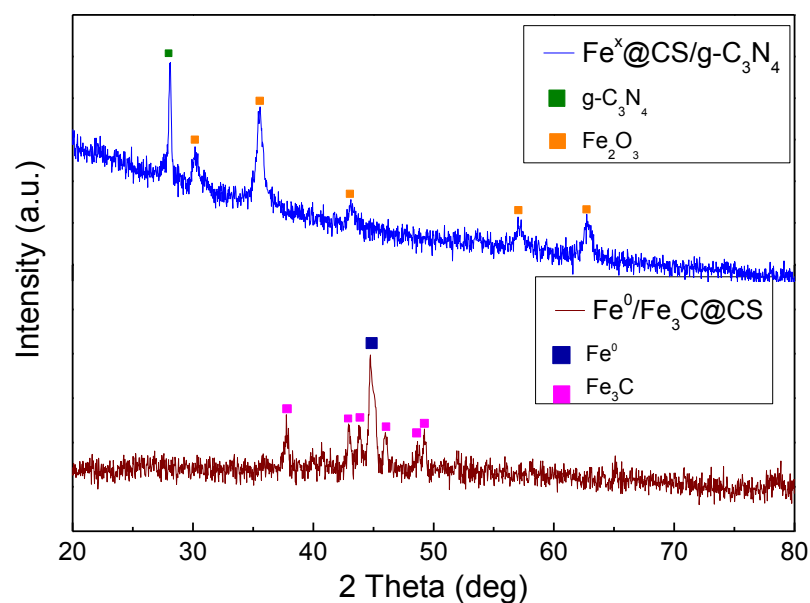


Figure 6.1 XRD patterns of $\text{Fe}^x@CS$ and $\text{Fe}^0/\text{Fe}_3\text{C}@CS$ composites.

Structure and morphology of the as-prepared samples were investigated by SEM images, as shown in Fig. 6.2. Before calcination (Fig. 6.2(A)), these nanoparticles were highly agglomerated due to the magnetic dipole interaction of $\gamma\text{-Fe}_2\text{O}_3$ nanoparticles and the high surface energy caused by the nano-scaled size.(16) From the magnification image (Fig. 6.2(B)), plate-like morphology with the average size of 50-100 nm was observed, which could be assigned to the 2D structure of the graphitic carbon nitride ($\text{g-C}_3\text{N}_4$). (14) While the irregular protrusions attached on the 2D plates could be ascribed to the carbonized glucose and the $\gamma\text{-Fe}_2\text{O}_3$ nanoparticles. After calcination in nitrogen atmosphere (Fig. 6.2(C) and (D)), the 2D plate-like morphology disappeared and regular nanospheres were formed with a diameter around 20-30 nm,

which was in agreement with the result obtained from XRD pattern using the Scherrer's formula. The transformation of the morphology suggested that most of the carbonized glucose and g-C₃N₄ had reacted with Fe₂O₃ to form zero-valent iron, showing good accordance with the changes discovered in XRD patterns.

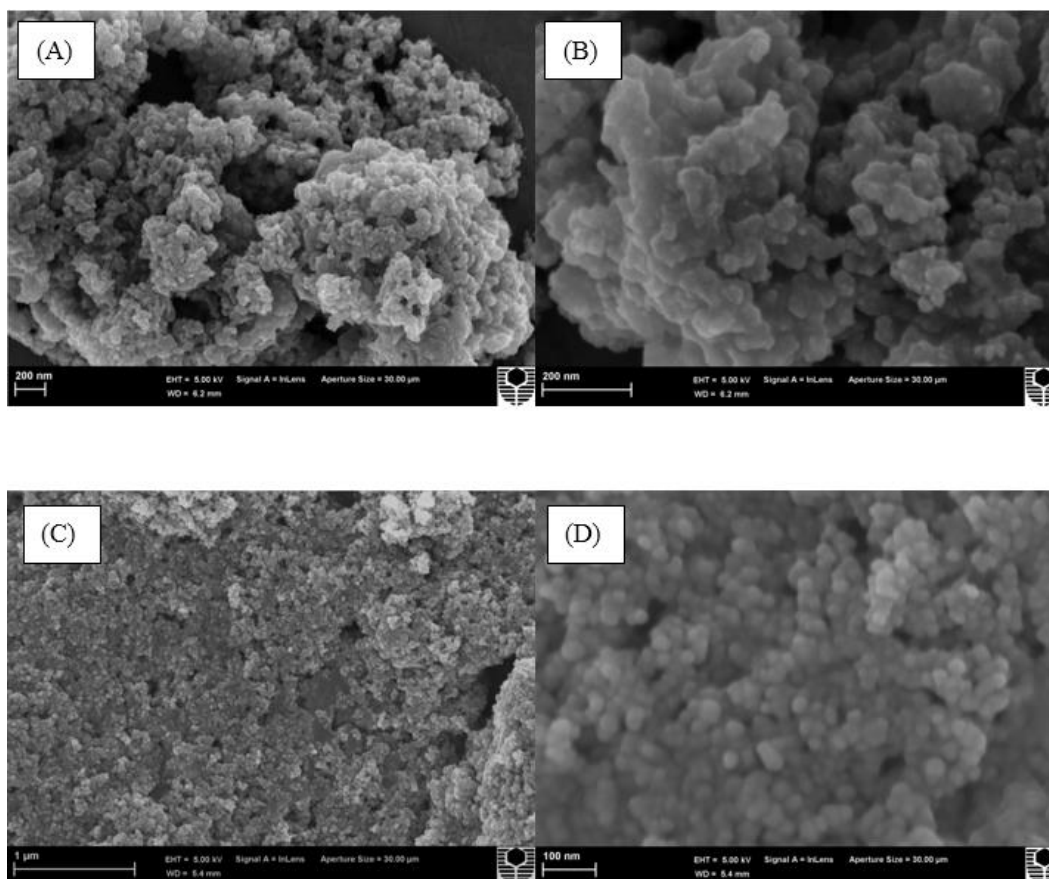


Figure 6.2 SEM images of Fe^x@CS (A) and (B), and Fe⁰/Fe₃C@CS (C) and (D).

N₂ sorption isotherms and pore size distributions of the samples were evaluated through N₂ adsorption/desorption (Fig. 6.3). Both samples presented a type IV isotherm with a type H3 hysteresis loop, suggesting a typical mesoporous structure in accordance with the classification of IUPAC.⁽¹⁷⁾ As seen in Fig. 6.3 (A), Fe^x@CS displayed a narrow hysteresis loop at a relative pressure P/P₀ range of 0.85 to 0.99. However, the hysteresis loop on Fe⁰/Fe₃C@CS was much broader, ranging from 0.45 to 0.99, as shown in Fig. 6.3(B), indicating a more porous structure and thus a larger surface area and pore volume. The BET surface area of Fe⁰/Fe₃C@CS was twice

greater than that of $\text{Fe}^x\text{@CS}$ ($42.3 \text{ m}^2/\text{g}$ vs. $18.0 \text{ m}^2/\text{g}$) and the pore volumes of the sample with/without calcination were 0.19 and $0.043 \text{ cm}^3/\text{g}$, respectively. The vast difference in surface area or pore volume between the two samples might be owed to the calcination process which could produce porous structures. In terms of pore size distributions, $\text{Fe}^x\text{@CS}$ (Fig. 6.3(A)) displayed a bimodal pore size distribution, centered at 0.5 and 26 nm , respectively. While $\text{Fe}^0/\text{Fe}_3\text{C@CS}$ showed a single modal pore size distribution concentrated at around 2.5 nm .

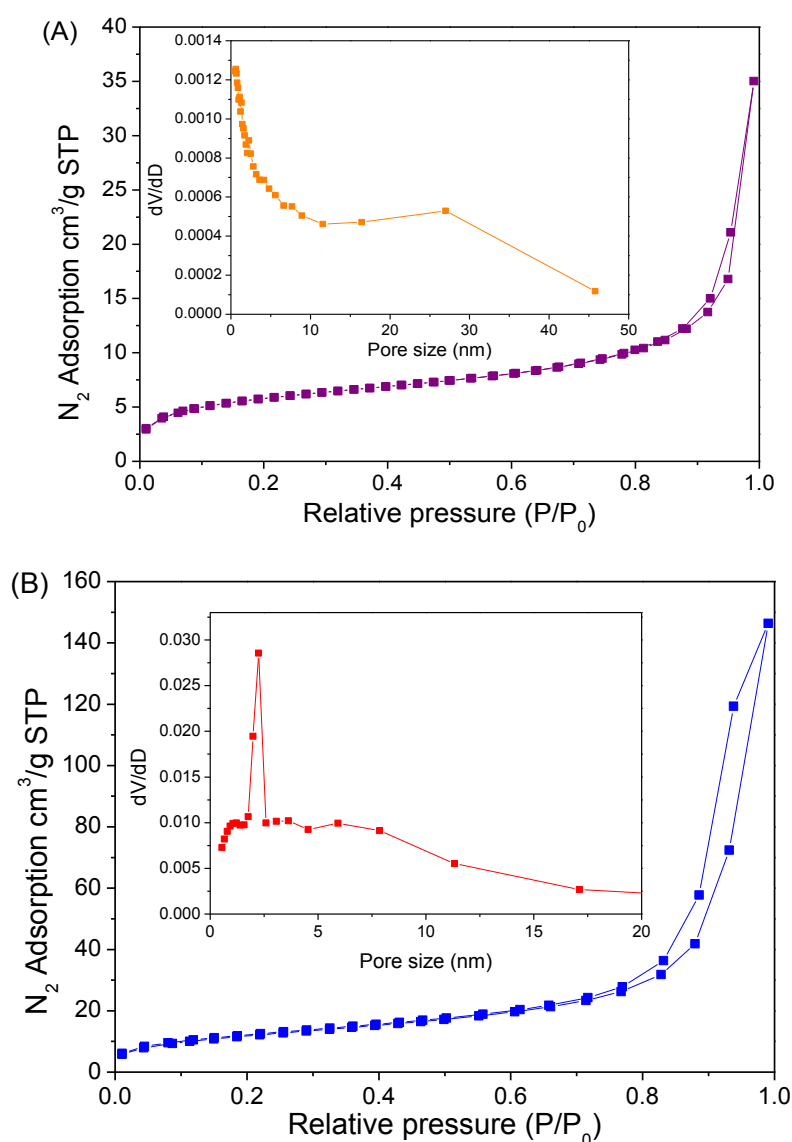
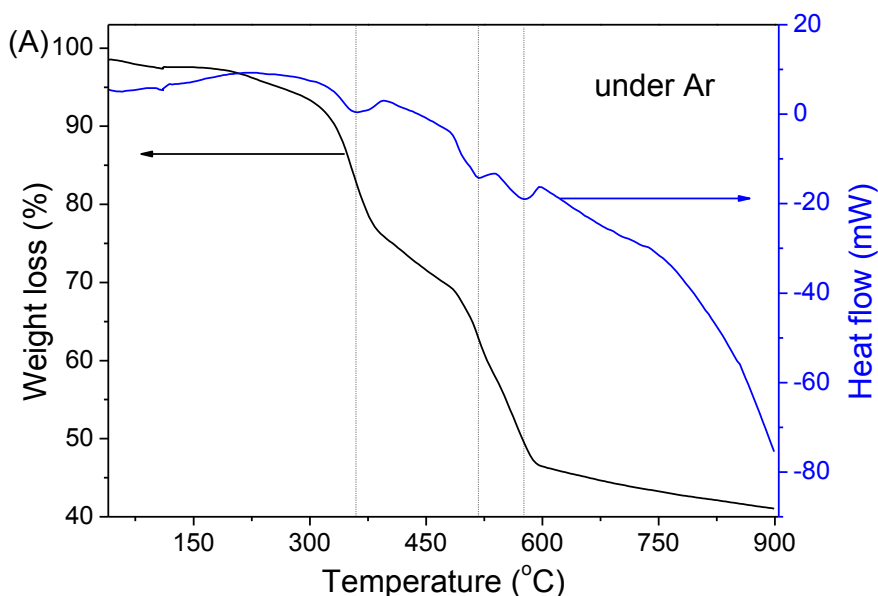


Figure 6.3 Nitrogen sorption isotherms and pore size distributions of the samples. (A) $\text{Fe}^x\text{@CS}$ and (B) $\text{Fe}^0/\text{Fe}_3\text{C@CS}$.

Fig. 6.4 displays TG-DSC profiles of $\text{Fe}^x\text{@CS}$ in argon and air. Fig. 6.4(A) shows the phase transformation of iron species under an argon atmosphere. As seen, three endothermic peaks were observed at 387, 514 and 573 °C, respectively. The first endothermic peak at 387 °C was attributed to the transformation of $\gamma\text{-Fe}_2\text{O}_3$ to Fe_3O_4 , while the peak at 514 °C could be assigned to the reduction of Fe_3O_4 to Fe^0 . (18) The third endothermic peak centering at 573 °C could be ascribed to the formation of Fe_3C , which was also shown in the XRD result. Fig. 6.4(B) shows the combustion performance of $\text{Fe}^x\text{@CS}$ under air. Two exothermic peaks were found at 200 to 380 °C which could be attributed to the decomposition and combustion of organic and amorphous carbons, respectively. (19) When temperature was elevated above 450 °C, weight loss was stabilized and was determined to be 43.0%, suggesting the complete combustion of amorphous carbon and oxidation of iron.



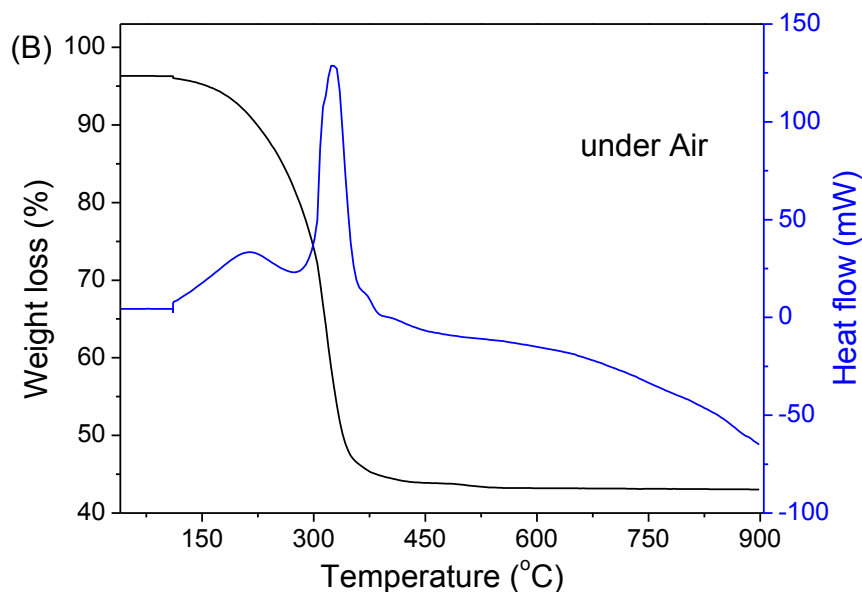


Figure 6.4 TG-DSC profiles of $\text{Fe}^x\text{@CS}$ under (A) argon and (B) air.

6.3.2 Catalytic oxidation of phenol

To investigate the catalytic activities of the samples, control experiments were firstly carried out in terms of catalyst adsorption and PMS self-oxidation. Fig. 6.5 displays the adsorption and phenol degradation profiles on various samples. When PMS alone was added to the phenol solution, less than 10% phenol was degraded, revealing that PMS could not be effectively activated by ambient temperature. For adsorption tests, when the $\text{Fe}^x\text{@CS}$ and $\text{Fe}^0/\text{Fe}_3\text{C@CS}$ samples were added to the phenol without the presence of PMS, insignificant phenol removal was observed on both samples, indicating that phenol removal by adsorption was negligible. For catalytic reactions, $\text{Fe}^x\text{@CS}$ was tested first for activation of PMS to produce reactive species to degrade phenol. As seen, around 20% phenol was degraded within 180 min. Our previous studies have showed that neither Fe_3O_4 nor Fe_2O_3 has notable catalytic activity in PMS activation.⁽¹²⁾ While $\text{Fe}^0/\text{Fe}_3\text{C@CS}$ provided a much fast catalytic activity, and 100% removal of phenol was achieved within 10 min. In the meantime, nano- $\text{Fe}^0\text{@CS}$ prepared according to a previous study (12) was also tested for activation of PMS for phenol degradation. It was found that in the same condition, com-

plete phenol removal was achieved within 30 min, revealing an inferior catalytic activity than $\text{Fe}^0/\text{Fe}_3\text{C}@CS$ synthesized in this study. These results strongly suggested that the nanoscaled ZVI had a superior catalytic activity and could activate PMS efficiently to produce reactive species for phenol degradation.

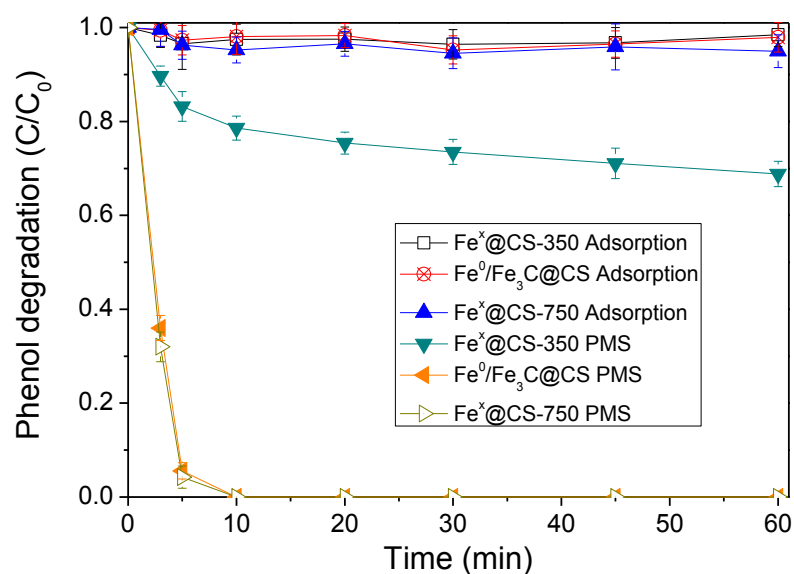
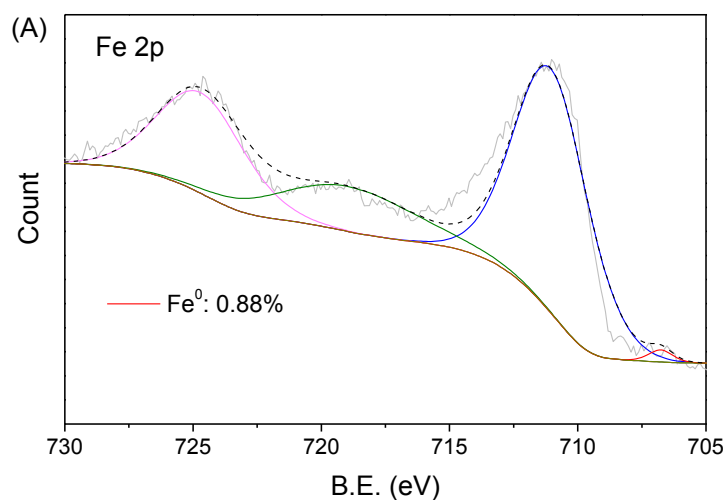


Figure 6.5 Phenol removals by adsorption and catalysis on $\text{Fe}^x@CS-350$, $\text{Fe}^0/\text{Fe}_3\text{C}@CS$ and $\text{Fe}^x@CS-750$. Reaction conditions: $[\text{phenol}]_0 = 20 \text{ mg/L}$, catalyst loading = 0.1 g/L , Oxone[®] loading = 2.0 g/L , and $T = 25 \text{ }^\circ\text{C}$.



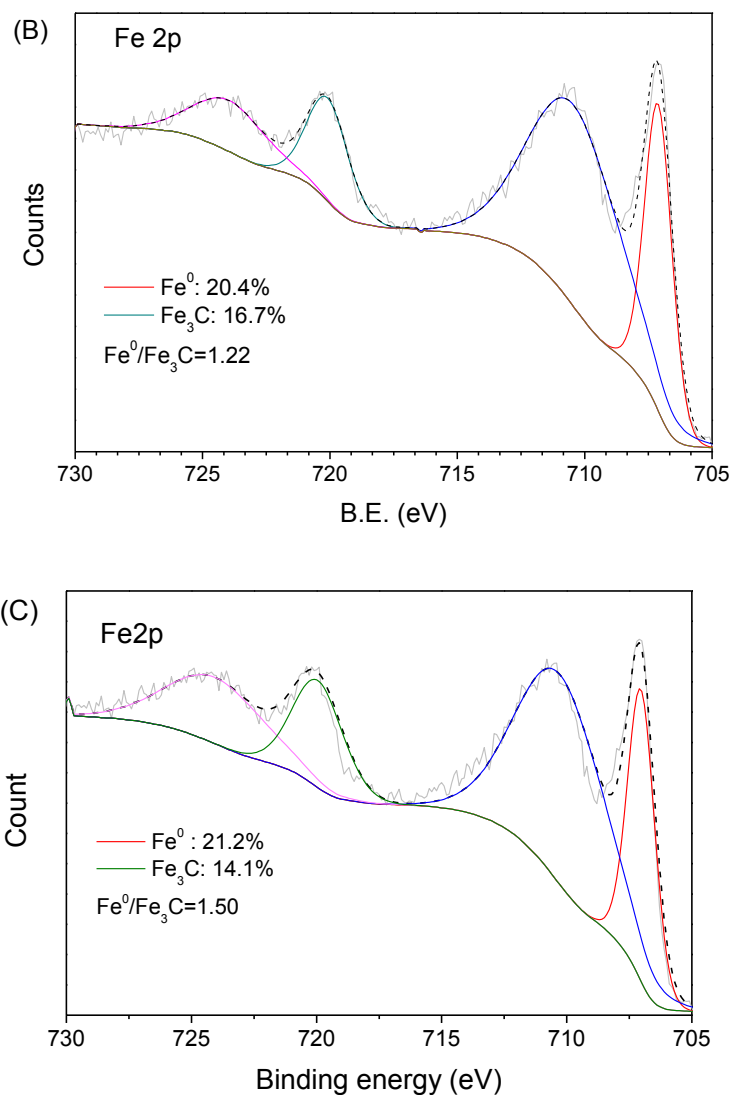


Figure 6.6 XPS Fe 2p spectra of (A) $\text{Fe}^x\text{@CS-350}$, (B) $\text{Fe}^0/\text{Fe}_3\text{C@CS}$, and (C) $\text{Fe}^x\text{@CS-750}$.

Fig. 6.5 displays the phenol removal induced by the prepared $\text{Fe}^0/\text{Fe}_3\text{C}$ catalysts. As shown, these catalysts showed insignificant adsorption of only less than 5% removal within 60 min. For catalytic oxidation, $\text{Fe}^x\text{@CS-350}$ was able to degrade around 30% phenol in 60 min. However, for both $\text{Fe}^0/\text{Fe}_3\text{C@CS}$ and $\text{Fe}^x\text{@CS-750}$, complete phenol degradation was achieved within 10 min. XPS Fe2p spectra of the three catalysts were shown in Fig. 6.6. For $\text{Fe}^x\text{@CS-350}$ (Fig. 6.6(A)), besides the characteristic peaks of oxidized iron(III) (711 eV and 724 eV) (20, 21), a weak peak (707 eV) from elemental Fe was observed with the composition of 0.9 at.%. (22, 23) No Fe_3C characteristic peak (720 eV) was observed. (23) Annealing at 350 °C might convert

iron(III) to FeOOH or Fe₂O₃ with trace of Fe⁰, phenol degradation might arise from the low catalytic activity of Fe₂O₃.(12) TG-DSC analysis suggested that when calcination temperature was above 514 °C, iron oxides would be transformed to Fe⁰ by the reduction of carbon. Moreover, at this temperature Fe₃C would gradually form. Fig. 6.6(B) shows the Fe 2p of XPS Fe⁰/Fe₃C@CS. As seen, notable peaks at 707 eV and 720 eV for Fe⁰ and Fe₃C respectively were presented, consistent with TG-DSC analysis. Fe⁰ and Fe₃C were determined to be 20.4 at.% and 14.7 at.%, respectively. When annealing temperature was further elevated to 750 °C (Fig. 6.6(C)), the corresponding XPS Fe 2p spectrum was similar to that of Fe⁰/Fe₃C@CS, so were Fe⁰ and Fe₃C levels. The increase of Fe⁰/Fe₃C ratio from 1.22 to 1.50 might be ascribed to the reduction of Fe₂O₃ to Fe⁰ at a higher annealing temperature. Due to the high Fe⁰ composition, efficient phenol degradation was shown for both of these catalysts.

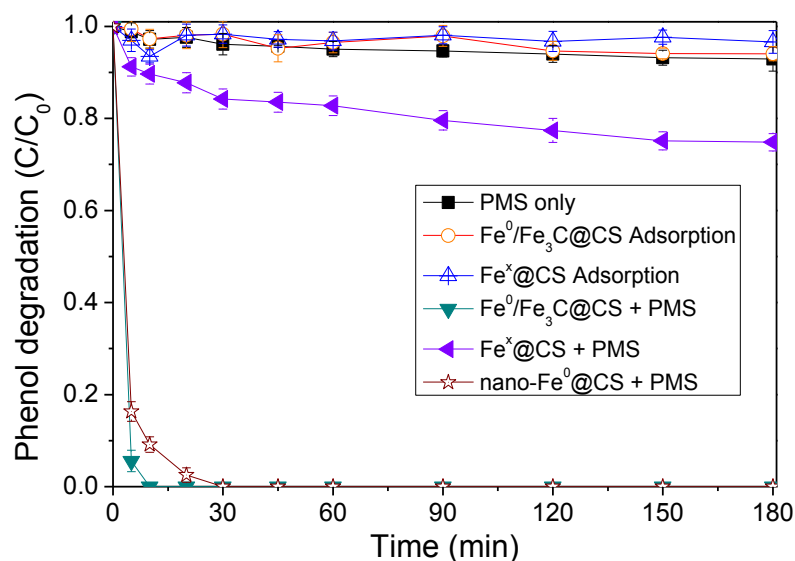


Figure 6.7 Phenol removals in various conditions. Reaction conditions: [phenol]₀ = 20 mg/L, catalyst loading = 0.2 g/L, Oxone loading = 2.0 g/L, Temperature: 25 °C.

To evaluate the effect of reaction conditions on catalytic phenol degradation, further studies were carried out by varying initial phenol concentration using Fe⁰/Fe₃C@CS. Fig. 6.7 shows the effect of the initial phenol concentration on its catalytic degradation efficiency. A general trend can be observed that with increased initial phenol

concentration, the time for 100% phenol degradation became longer. When the initial phenol concentration was increased from 20 to 40 and 60 ppm, 100% phenol degradation would require reaction duration at 10, 15 and 20 min, respectively.

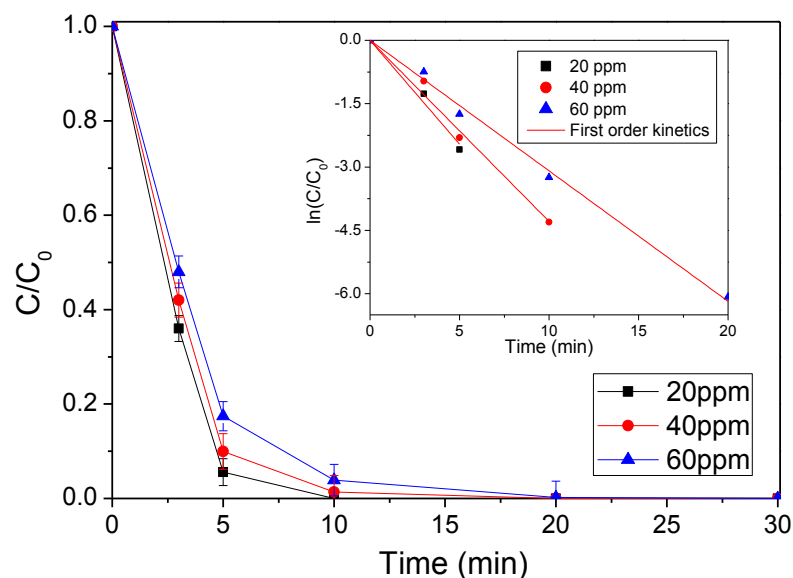


Figure 6.8 Effect of phenol concentration on phenol degradation using Fe⁰/Fe₃C@CS. Reaction conditions: catalyst loading = 0.1 g/L, Oxone loading = 2.0 g/L, temperature: 25 °C.

For reaction kinetic studies, a first order kinetic model (Eq.6.1) was employed to evaluate the catalytic reaction kinetics.

$$\ln\left(\frac{C}{C_0}\right) = -kt \quad \text{Eq. 6.1}$$

Where, C is the concentration of phenol at time (t) and C₀ is the initial phenol concentration. K is the first-order reaction rate constant. The inset of Fig. 6.8 shows that phenol degradation curves were well fitted by the first-order kinetics with high values of regressions coefficients. The reaction rate constants for the catalyst at three phenol concentrations were provided in Table 6.1. As seen, with the increase of the phenol concentration, the apparent rate constant (K) slightly decreased, indicating the

decrease of the phenol degradation efficiency.

Table 6.1 Kinetic parameters of Fe⁰/Fe₃C@CS in phenol degradation.

Catalyst	Phenol concentration (ppm)	K (min ⁻¹)	R ² of K
Fe ⁰ /Fe ₃ C@CS	20	0.58	0.989
	40	0.44	0.992
	60	0.31	0.997

In the past few years, investigations have been carried out using ZVI for degradation of organic pollutants and most of the investigations have been using H₂O₂(24-26), dissolved oxygen(27) and persulfate(24, 28, 29) to initiate the reactivity of ZVI. Lee et al. studied the effects of nano-ZVI/H₂O₂ systems on conversion of methanol to HCHO using H₂O₂ as the oxidant.(30) They found that with the addition of 1 mM polyoxometalate (POM), 100 mM of methanol could be fully converted to HCHO within 180 min. Liang and Guo investigated oxidative and reductive pathways of ZVI catalysts in activating persulfate to degrade naphthalene.(28) They found that 10 ppm of naphthalene could be rapidly degraded by the ZVI activated persulfate within 120 min and sequential doses of small quantities of ZVI enhanced the naphthalene degradation efficiency. Recently, Sun et al. investigated ZVI activated peroxymonosulfate (PMS) for phenol degradation and a superior catalytic activity of nanoscaled ZVI was observed compared with commercial ZVI and other metal catalysts.(12) This study presented similar reaction kinetics as the above.

Fig. 6.9 displays phenol degradation profiles on Fe⁰/Fe₃C@CS at varying temperatures. At elevated temperature, the phenol degradation rate was enhanced. The time for complete phenol degradation at 15, 25, and 35 °C was 60, 30 and 10 min, respectively. This trend implied the endothermic nature of the PMS activation process: higher temperature would stimulate PMS to generate reactive species more quickly for phenol degradation. Based on the first-order kinetics, reaction rate constants at

varying temperatures were determined and the correlation between the rate constants and reaction temperature was fitted well by the Arrhenius equation with a high regression coefficient, which is shown in the inset figure. The activation energy was then obtained to be 16.3 kJ/mol.

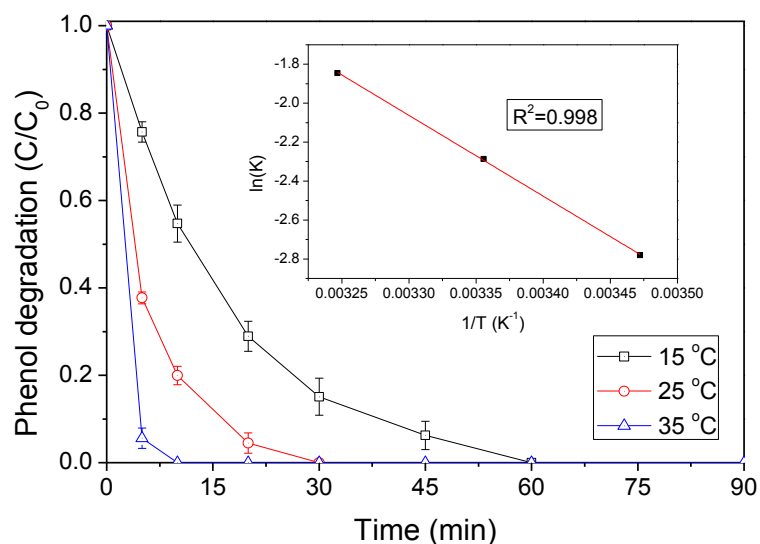


Figure 6.9 Effect of reaction temperature on phenol degradation and estimation of activation energy. Reaction conditions: $[\text{phenol}]_0 = 20 \text{ mg/L}$, catalyst loading = 0.1 g/L , Oxone[®] loading = 2.0 g/L .

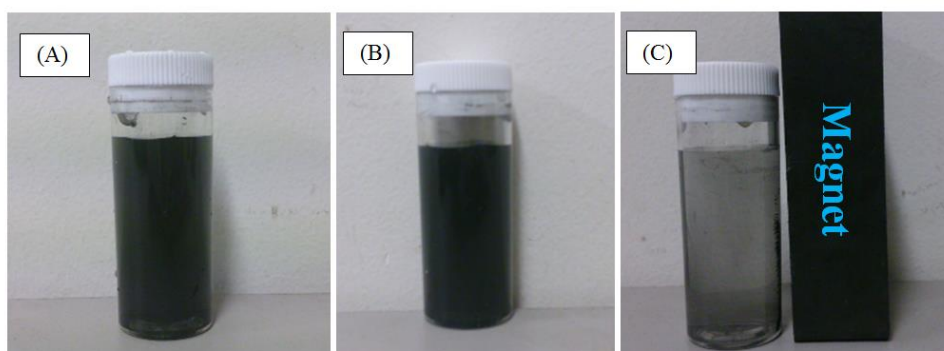


Figure 6.10 Photographs of the separation and dispersion processes for fresh $\text{Fe}^0/\text{Fe}_3\text{C}@CS$. (A) without external magnetic field, (B) without external magnetic field 10 min (C) with external magnetic field.

Fig. 6.10 shows photographs of $\text{Fe}^0/\text{Fe}_3\text{C}@\text{CS}$ dispersion in water and its response under an external magnetic field. It was found that $\text{Fe}^0/\text{Fe}_3\text{C}@\text{CS}$ could be well dispersed in water to form a stable black suspension after sonication for 1 min (Fig. 6.10(A)) and that the black suspension remained stable after 10 min (Fig. 6.10(B)). When a magnet approached, the catalyst accumulated quickly to the side wall near the magnet. And the solution became clear within 1 min (Fig. 6.10(C)). After the magnet was removed and as-mentioned sonication procedure was repeated, the $\text{Fe}^0/\text{Fe}_3\text{C}@\text{CS}$ sample was re-dispersed in water and formed the stable suspension again. Therefore, attraction and dispersion processes could be altered by an external magnetic field, and the as-synthesized $\text{Fe}^0/\text{Fe}_3\text{C}@\text{CS}$ demonstrated excellent water dispersion and magnetic separation for effective solid-solution separation.

6.3.3 Mechanism of enhanced reusability

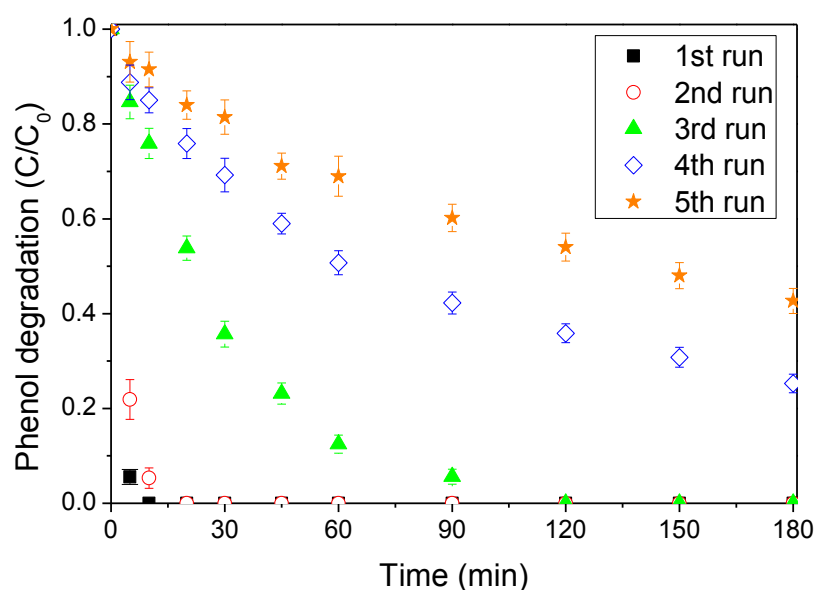


Figure 6.11 Phenol degradation on $\text{Fe}^0/\text{Fe}_3\text{C}@CS$ at different runs for repeated uses. Reaction conditions: $[\text{phenol}]_0 = 20 \text{ mg/L}$, catalyst loading = 0.2 g/L , Oxone[®] loading = 2.0 g/L , and $T = 25 \text{ }^\circ\text{C}$.

The stability and recyclability of $\text{Fe}^0/\text{Fe}_3\text{C}@CS$ were investigated by successive reusability tests (Fig. 6.11). The catalysts were regenerated by filtration followed by

water washing without any further treatment. In the reusability tests, the phenol degradation profile in the second run almost overlapped the first run indicating an excellent reusability. However, in the subsequent runs, the as-synthesized $\text{Fe}^0/\text{Fe}_3\text{C}@CS$ catalyst seemed to deactivate. For the third run, complete phenol removal occurred at 120 min which was much longer than the first and second runs. And for the 4th and 5th runs, around 30% and 50% phenol residue remained in solutions in 180 min. Although deactivation occurred, the as-prepared catalyst still displayed notable catalytic activity even in the 5th run. The stability was much higher than nano- Fe^0 encapsulated in microcarbon spheres in the recent study, (12) where the nano- $\text{Fe}^0@CS$ catalyst showed an inferior stability and deactivated dramatically from the second run. Compared with the nano- $\text{Fe}^0@CS$ in our previous study (12), the $\text{Fe}^0/\text{Fe}_3\text{C}@CS$ in this study presented significantly improved catalytic stability and reusability.

In order to probe the causes of deactivation, the catalyst from each test was collected and XRD analysis was then carried out. XRD patterns of $\text{Fe}^0/\text{Fe}_3\text{C}@CS$ after each run are shown in Fig. 6.12. As seen, compared with the fresh sample, diffraction peaks of $\gamma\text{-Fe}_2\text{O}_3$ (JCPDS card 39–1346) appeared, suggesting that some of the Fe^0 has been oxidized to Fe(III). Moreover, the peak intensity of Fe_3C also decreased on recycled catalyst from the 1st run, suggesting that besides Fe^0 was oxidized, some Fe_3C was also consumed during the catalytic reaction. However, unlike the Fe^0 after reaction with PMS,(12) Fe_3C appeared to exist even after the fourth run. The stable Fe_3C phase might enable to maintain catalytic activity in the 5th run, as indicated in Fig. 6.12.

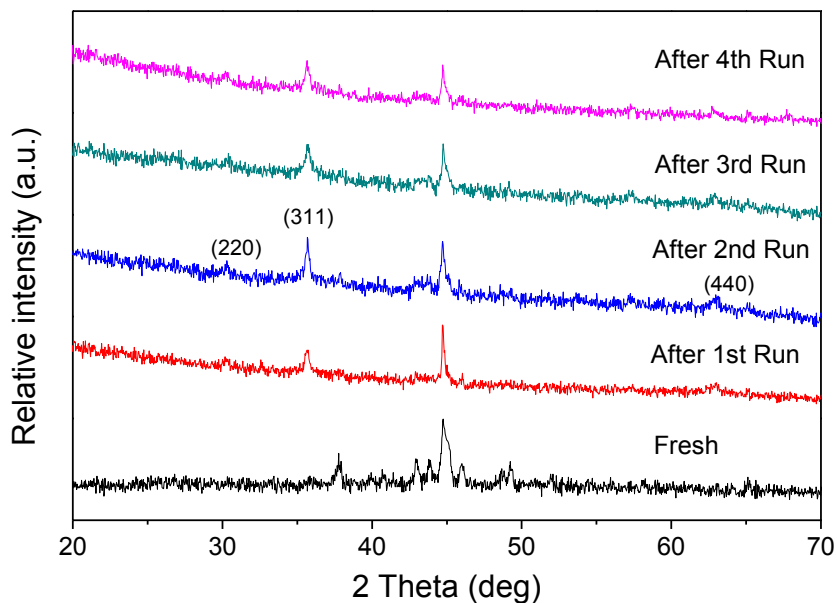


Figure 6.12 XRD patterns of $\text{Fe}^0/\text{Fe}_3\text{C}@CS$ after each run.

In order to further evaluate the changes on catalyst surface after uses and the deactivation mechanism, XPS study was carried out. XPS data of the fresh and the catalyst after the 4th use are provided in Fig.6.13. For XPS spectra of the fresh catalyst in the Fe 2p region (Fig. 6.13(A)), four characteristic peaks were identified. Binding energies of Fe 2p_{1/2} (ca. 724 eV) and Fe 2p_{3/2} (ca. 711 eV) were identified, referring to oxidized iron [Fe(III)].(20, 21) The peaks at ca. 720 and 707 eV indicated the presence of the iron carbide (Fe_3C) and elemental iron (Fe^0) on the catalyst surface, respectively (22, 23), which is in accordance with XRD analysis in Fig. 6.12.

The XPS O 1s (Fig. 6.13(B)) can be fitted into three components. The peak at ca. 529.9 eV was in agreement with the binding energy of O^{2-} , while the other peaks at ca. 531.2 and 534.5 eV could be indexed to OH^- and chemically/physically adsorbed water, respectively. The oxygen species were similar to those on the surface of iron oxides in water.(23) The presence of the oxidized iron suggests that nano ZVI (Fe^0) is extremely prone to being oxidized to Fe(III) even on the fresh catalyst.

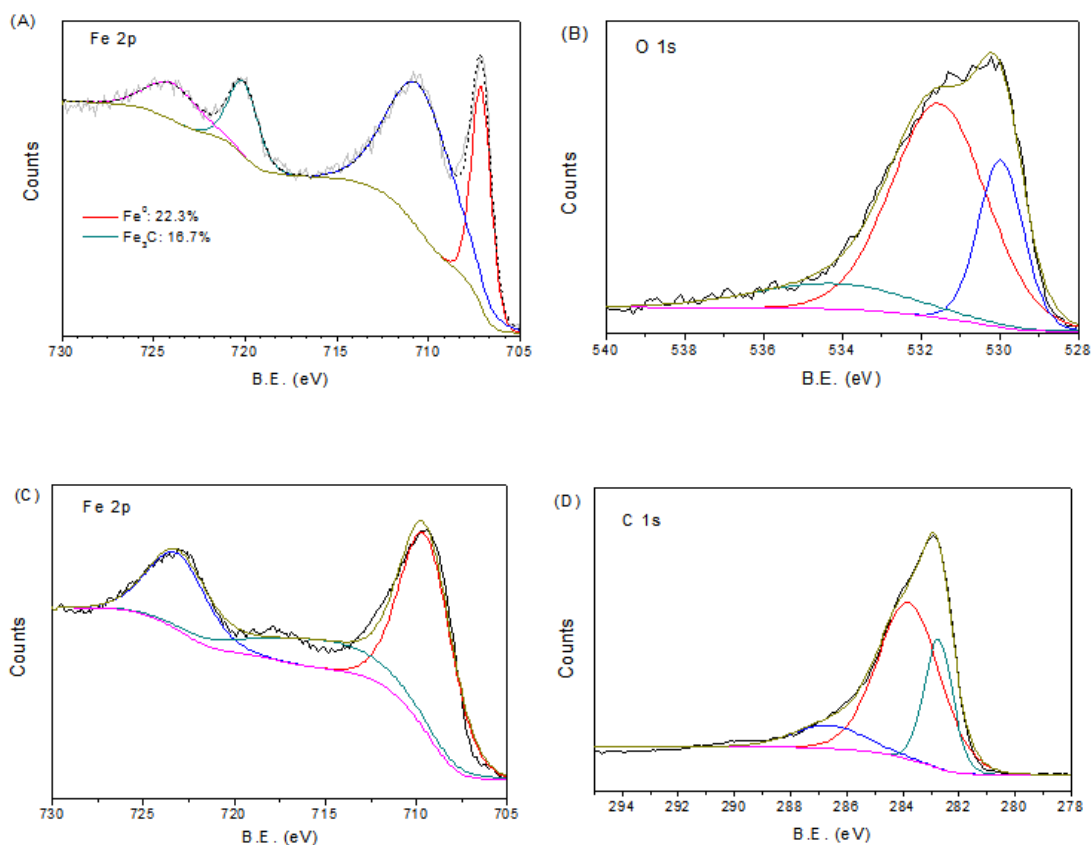


Figure 6.13 XPS spectra of fresh/used catalysts. (A) XPS spectrum of Fe 2p region for fresh catalyst; (B) XPS spectrum of O 1s region for fresh catalyst; (C) XPS spectrum of Fe 2p region for the 4th used catalyst; (D) XPS spectrum of C 1s region for the 4th used catalyst.

For the catalyst obtained after the 4th use, XPS spectra were quite different. For XPS in Fe 2p region (Fig. 6.13(C)), the photoelectron peak of metal iron (ca. 707 eV) disappeared. Only two main photoelectron peaks were identified at ca. 724 and 711 eV, which can be ascribed to the oxidized Fe(III). While the peaks at 719 eV represents the binding energies of shake-up satellite Fe 2p_{3/2}(20). The disappearance of metal iron suggests that most of the Fe⁰ on surface of the catalyst has been oxidized to Fe(III) during the catalytic reaction with PMS. The C1s spectrum of the used catalyst was also fitted with three components (Fig. 6.13(D)). The peak centered at ca. 283.6 eV confirmed the presence of Fe₃C, (31) while the other two peaks centered at 282.8 and 285.4 eV corresponded to the SiC and sp³-bonded carbon. The appearance of SiC might be resulted from the contamination brought by the calcination process.

The integrated areas of these three peaks correspond to Fe_3C , SiC , and $\text{sp}^3\text{-C}$ contents were 65.6%, 24.4% and 11.5%, respectively, suggested that most of the carbon was in the form of iron carbide.

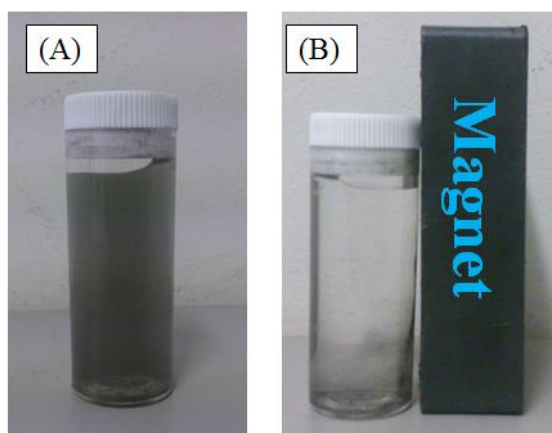


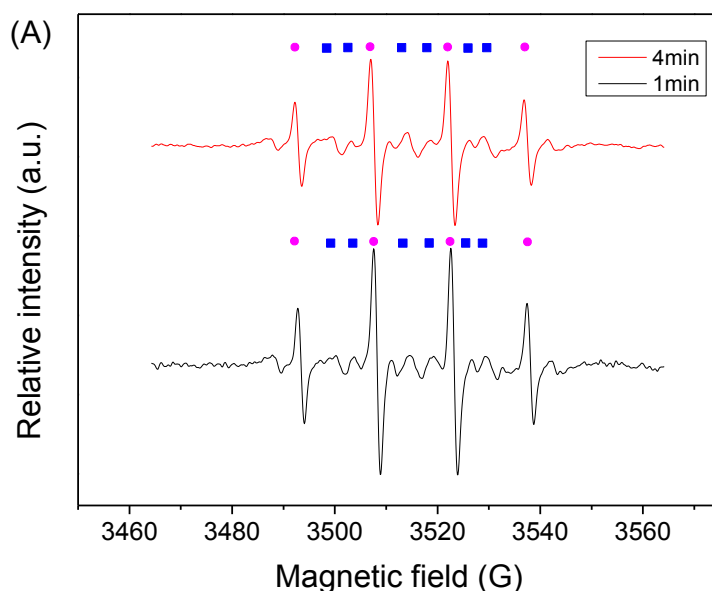
Figure 6.14 Photographs of the separation and dispersion processes for $\text{Fe}^0/\text{Fe}_3\text{C}@CS$ after the 4th use. (A) without external magnetic field, (B) with external magnetic field.

Based on XPS studies as well as XRD analysis, it can be concluded that, after catalytic reaction with PMS, most of surface elemental iron (Fe^0) was consumed and converted into $\gamma\text{-Fe}_2\text{O}_3$. However, iron carbide (Fe_3C) still remained, suggesting that the Fe_3C has a better stability than Fe^0 in catalytic reaction. Moreover, as shown in Fig. 6.14, the recycled catalyst after the 4th use still displayed similar magnetic behavior to the fresh sample, and the solution became clear within 1 min when approaching an external magnet. For the stability, in the first two runs, both Fe^0 and Fe_3C took part in catalytic reaction and the high reaction rate could be ascribed to the high catalytic activity of Fe^0 . With the repeating times increase and depletion of the surface Fe^0 , reaction rates of phenol degradation decreased. At the 4th and 5th runs, the main component contributing to catalytic reaction was iron carbide, because of the corrosion of Fe^0 (from XPS spectra) and the low catalytic activity for Fe_2O_3 in PMS activation.(12) In the catalysis processes, at first corrosion will simultaneously occur with Fe^0 activation of PMS, while Fe_3C might act like metal

oxide as a stable catalyst for a better stability. This is the first observation of Fe_3C catalysis catalytic oxidation of organic pollutants. Though the insightful mechanism has been still not very clear yet, it can be still concluded that with introduction of melamine to the synthesis, Fe_3C was formed together with Fe^0 to improve both activity and stability in phenol oxidation.

6.3.4 Mechanism of PMS activation and phenol degradation

Previous investigations have shown that homogeneous or heterogeneous activation of PMS could produce both hydroxyl radicals ($\cdot\text{OH}$) and sulfate radicals ($\text{SO}_4^{\cdot-}$).^(32, 33) In order to investigate the generation processes of reactive species on $\text{Fe}^0/\text{Fe}_3\text{C}@CS$ activating PMS and the dominant species for phenol degradation, both EPR tests with DMPO as the spin trapping agent and the classical quenching tests were performed.



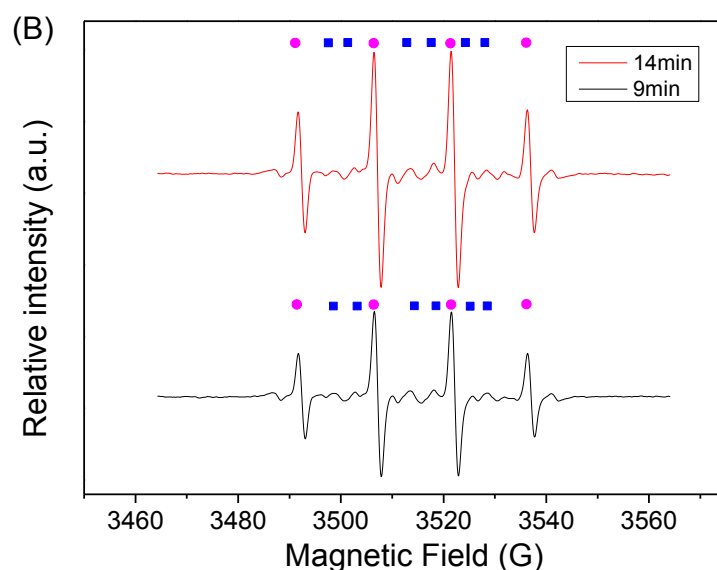


Figure 6.15 EPR spectra in various conditions. Centerfield: 3512 G; Sweep width: 100 G; Microwave frequency: 9.87 GHz; Modulation frequency: 100 GHz; and Power: 18.11 mW. Reaction condition: Phenol = 20 ppm; Catalyst loading= 0.1 g/L; PMS loading = 6.5 mM, pH = 7.0; DMPO = 0.08 M. ● : DMPO-•OH; ■ : DMPO-SO₄•⁻

Our previous study showed that no peaks were identified when 6.5 mM PMS solution was tested without addition of DMPO or phenol solution, revealing that no electron spins could be captured without addition of spin-trapping agent.(34) With the addition of 20 ppm of phenol and 0.08 M of DMPO to PMS solution, characteristic signals of 5,5-dimethylpyrroline-(2) -oxyl-(1) (DMPOX) were identified, indicating that due to strong hydrolysis process of PMS, DMPO was directly oxidized to DMPOX.(34, 35) When Fe⁰/Fe₃C@CS was added together with PMS (6.5 mM), DMPO (0.08 M) and phenol (20 ppm), both hydroxyl and sulfate radicals appeared by identification of the characteristic signals of DMPO-HO• and DMPO-SO₄•⁻ adducts, respectively.

Fig. 6.15 shows EPR spectra of reaction solution are dependent on reaction time. Within the first minute of the catalytic reaction, characteristic peaks of DMPO-HO•

adducts (with hyperfine splitting constants of $a_N = a_H = 14.9$ G) and DMPO-SO₄^{•-} adducts (with hyperfine splitting constants of $a_N = 13.2$ G, $a_H = 9.6$ G, $a_H = 1.48$ G and $a_H = 0.78$ G) were observed, revealing both hydroxyl and sulfate radicals were generated at the very initial stage of the catalytic reaction.(36) However, the peak intensity of DMPO-SO₄^{•-} adducts was much weaker compared with that of DMPO-HO• adducts, indicating that concentration of sulfate radicals was much lower than that of hydroxyl radicals. When reaction time was prolonged to 4 min, the intensity of the DMPO-SO₄^{•-} adducts signal peak decreased. The decrease of the peak intensity indicated that the radicals generated by PMS activation have been quickly consumed by reacting with phenol. However, when reaction time was extended to 9 min or longer (Fig. 6.15(B)), the peak intensity for DMPO-HO• increased to higher values, suggesting that excessive hydroxyl radicals have been generated. While the peak intensity of DMPO-SO₄^{•-} remained roughly the same as the initial.

Fig. 6.16 shows relationship between phenol removal profile and evolution of the DMPO-•OH /DMPO-SO₄^{•-} adduct peak intensities with time for Fe⁰/Fe₃C@CS catalyst. As seen, the relative intensity of hydroxyl radicals was much higher than that of sulfate radicals, while the unremarkable fluctuation in peak intensity of sulfate radicals happened during the catalytic reaction. These facts revealed that hydroxyl radicals were selectively produced during the PMS activation process. For variation of hydroxyl radicals, it reached the lowest point at 5 min, suggesting the fast consumption of the radicals since they have been generated. After that, their concentration increased significantly. Combined the DMPO-•OH intensity variation with the phenol degradation profile, 80% of phenol degradation at the first 5 min could be accounted for the decreased hydroxyl radicals.

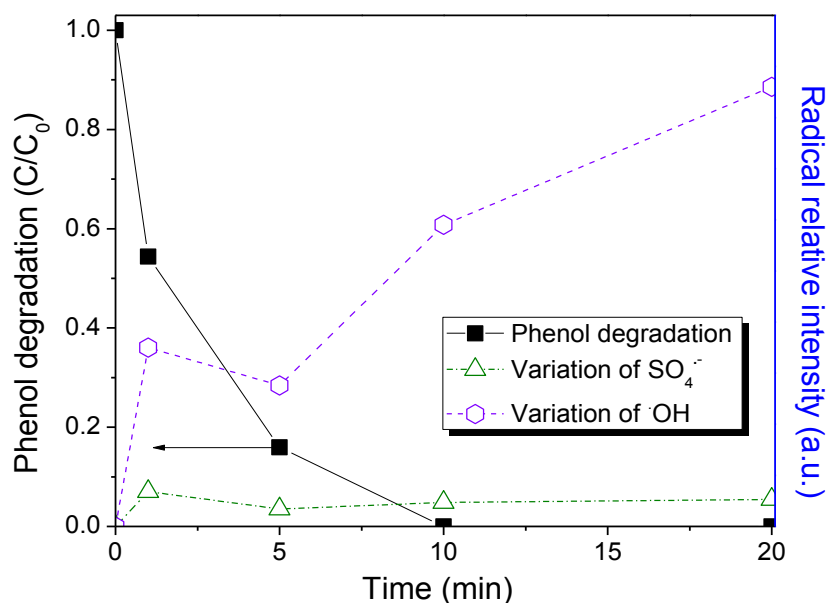


Figure 6.16 Phenol removal profile and intensity variations of DMPO-•OH and DMPO-SO₄^{•-} during reaction on Fe⁰/Fe₃C@CS. Reaction conditions: Phenol = 20 mg/L; Catalyst loading= 0.1 g/L; PMS loading = 6.5 mM, pH = 7.0.

Our previous study showed that, when 3D MnO₂ was employed as the catalyst, both sulfate and hydroxyl radicals were generated during the PMS activation and the sulfate radicals dominated phenol oxidation process.(34) However, this study suggested that Fe metal-based catalysts could generate different radicals during PMS activation process for phenol oxidation. To further investigate the dominant radical species responsible for phenol degradation, classical quenching tests employing ethanol (EtOH) and tert-butyl alcohol (TBA) as quenching agents were carried out. It is well accepted that SO₄^{•-} is selective to be quenched more rapidly by a quenching agent with α -hydrogen and the reaction rates of SO₄^{•-} with EtOH (with α -hydrogen) and TBA (without α -hydrogen) are $1.6 \times 10^7 - 7.7 \times 10^7$ and $4.0 \times 10^5 - 9.1 \times 10^5 \text{ M}^{-1} \text{ s}^{-1}$, respectively.(37, 38) While both EtOH and TBA could sufficiently quench •OH with the rates of $1.2 \times 10^9 - 2.8 \times 10^9$ and $3.8 \times 10^8 - 7.6 \times 10^8 \text{ M}^{-1} \text{ s}^{-1}$, respectively. (37)

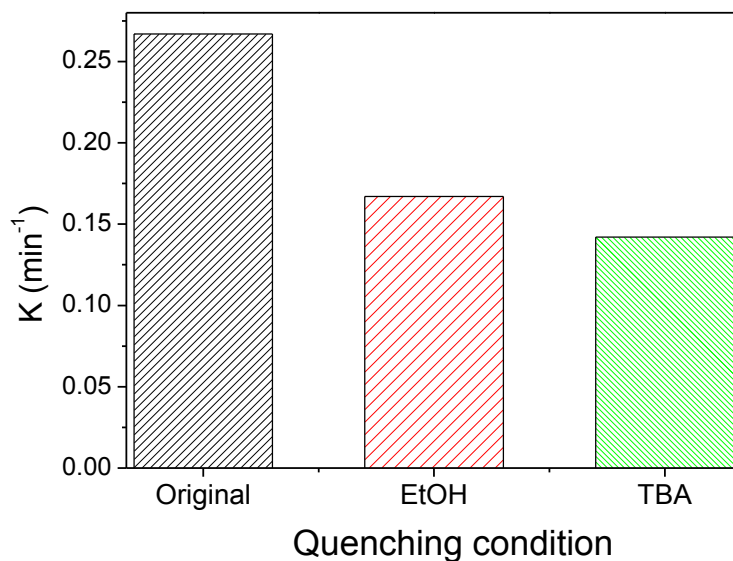
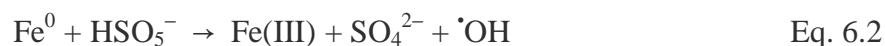
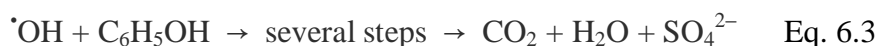


Figure 6.17 Changes of reaction rate (K) of catalysts with and without quenching agents of EtOH (0.2 M) and TBA (0.2 M). Reaction conditions: Phenol = 20 mg/L, catalyst loading = 0.1 g/L, Oxone loading = 6.5 mM, and T = 25 °C.

Fig. 6.17 shows the change of reaction rate constant (K) in quenching tests. When 0.2 M EtOH was added, the reaction rate reduced from 0.27 to 0.17 min⁻¹, indicating that some portions of hydroxyl and sulfate radicals were quenched during the catalytic reaction. When 0.2 M TBA was added to the original reaction solution, reaction rate decreased to around 0.15 min⁻¹, which was roughly the same as that by addition of EtOH. By combination of the EPR spectra variation and the results of the classical quenching tests, it was concluded that hydroxyl radicals were selectively generated against sulfate radicals during the heterogeneous PMS activation process. Because solid PMS is facile for transportation and storage, then it could be used as an alternate to hydrogen peroxide employed in homogenous Fenton reaction. Moreover, it was also deduced that hydroxyl radicals are dominating phenol degradation. And the mechanisms of PMS activation on Fe⁰/Fe₃C@CS for phenol degradation can be proposed as follows.





In this study, Fe⁰/Fe₃C based nano hybrids demonstrated efficient catalytic activation of PMS for organic pollutants degradation, in which Fe₃C catalysis was discovered for the very first time. Besides decomposition of aqueous organic pollutants, Fe⁰/Fe₃C based nanomaterials have been widely employed in reduction and adsorption of heavy metals. López et al., (39) prepared Fe/Fe₃C ultra small particles and compared their capability for adsorption of Se(IV) with Fe₃O₄ nanoparticles. They found that Fe/Fe₃C NPs were superior to Fe₃O₄ NPs because of their ability in immobilization of Se(IV) rapidly and irreversibly via reductive mechanism. Wang et al. (40) prepared Fe/Fe₃C@porous carbon sheets via biomass and used them for simultaneous reduction and adsorption of uranium (VI) for aqueous solution. It can be expected that such Fe⁰/Fe₃C hybrids in this study can be employed to removal of both organic pollutants and toxic heavy metals in water.

6.4 Conclusions

Fe⁰/Fe₃C@CS nanocomposites were synthesized via a modified hydrothermal method followed by self-reduction under heated nitrogen atmosphere. The addition of melamine appeared to enable the formation of an additional phase of Fe₃C along with Fe⁰. The novel ZVI-based nanocomposites showed a superior catalytic activity in activation of PMS for phenol degradation. The kinetic studies suggested that, in the heterogeneous systems, catalytic oxidation of phenol followed first order kinetics and the apparent activation energy was 16.3 kJ/mol. Moreover, Fe₃C catalysis for PMS activation was observed for the first time though detailed catalysis mechanism is still not very clear at current stage. The catalyst deactivation mechanism was also investigated and it was found that Fe₃C has a better catalytic stability than Fe⁰ in catalytic reaction. Magnetic separation was also remained even after five runs. The combina-

tion of EPR analysis and quenching tests showed that hydroxyl radicals were generated selectively against sulfate radicals within the PMS activation process and thus responsible for phenol oxidation. This study provided a feasible approach for removal of organic pollutants by magnetically separable catalysts via advanced material design.

References

1. O'Carroll D, Sleep B, Krol M, Boparai H, Kocur C. Nanoscale zero valent iron and bimetallic particles for contaminated site remediation. *Adv. Water Resour.* 2013;51(0):104-22.
2. Crane RA, Scott TB. Nanoscale zero-valent iron: Future prospects for an emerging water treatment technology. *J. Hazard. Mater.* 2012;211–212(0):112-25.
3. Ryu A, Jeong S-W, Jang A, Choi H. Reduction of highly concentrated nitrate using nanoscale zero-valent iron: Effects of aggregation and catalyst on reactivity. *Appl. Catal., B.* 2011;105(1–2):128-35.
4. Song H, Carraway ER. Reduction of Chlorinated Ethanes by Nanosized Zero-Valent Iron: Kinetics, Pathways, and Effects of Reaction Conditions. *Environ. Sci. Technol.* 2005;39(16):6237-45.
5. Rastogi A, Al-Abed SR, Dionysiou DD. Sulfate radical-based ferrous–peroxymonosulfate oxidative system for PCBs degradation in aqueous and sediment systems. *Appl. Catal., B.* 2009;85(3–4):171-9.
6. Liu H, Xu J, Li Y, Li Y. Aggregate Nanostructures of Organic Molecular Materials. *Acc. Chem. Res.* 2010;43(12):1496-508.
7. Li Y, Zhang Y, Li J, Zheng X. Enhanced removal of pentachlorophenol by a novel composite: Nanoscale zero valent iron immobilized on organobentonite. *Environ. Pollut.* 2011;159(12):3744-9.
8. Chen ZX, Jin XY, Chen Z, Megharaj M, Naidu R. Removal of methyl orange from aqueous solution using bentonite-supported nanoscale zero-valent iron. *J. Colloid Interface Sci.* 2011;363(2):601-7.

9. Zhu H, Jia Y, Wu X, Wang H. Removal of arsenic from water by supported nano zero-valent iron on activated carbon. *J. Hazard. Mater.* 2009;172(2–3):1591-6.
10. Karabelli D, Ünal S, Shahwan T, Eroğlu AE. Preparation and characterization of alumina-supported iron nanoparticles and its application for the removal of aqueous Cu²⁺ ions. *Chem. Eng. J.* 2011;168(2):979-84.
11. Jiang Z, Lv L, Zhang W, Du Q, Pan B, Yang L, et al. Nitrate reduction using nanosized zero-valent iron supported by polystyrene resins: Role of surface functional groups. *Water Res.* 2011;45(6):2191-8.
12. Sun H, Zhou G, Liu S, Ang HM, Tade MO, Wang SB. Nano-Fe⁰ Encapsulated in Microcarbon Spheres: Synthesis, Characterization, and Environmental Applications. *ACS Appl. Mater. Interfaces.* 2012;4(11):6235-41.
13. Fardis M, Douvalis AP, Tsi trouli D, Rabias I, Stamopoulos D, Th K, et al. Structural, static and dynamic magnetic properties of dextran coated γ -Fe₂O₃ nanoparticles studied by 57 Fe NMR, Mössbauer, TEM and magnetization measurements. *J. Phys.: Condens. Matter.* 2012;24(15):156001.
14. Dong G, Zhao K, Zhang L. Carbon self-doping induced high electronic conductivity and photoreactivity of g-C₃N₄. *Chem. Commun.* 2012;48(49):6178-80.
15. Wang L, Tian C, Wang B, Wang R, Zhou W, Fu H. Controllable synthesis of graphitic carbon nanostructures from ion-exchange resin-iron complex via solid-state pyrolysis process. *Chem. Commun.* 2008(42):5411-3.
16. Li Y, Yi R, Yan A, Deng L, Zhou K, Liu X. Facile synthesis and properties of ZnFe₂O₄ and ZnFe₂O₄/polypyrrole core-shell nanoparticles. *Solid State Sci.* 2009;11(8):1319-24.
17. Zhang P, Zhan Y, Cai B, Hao C, Wang J, Liu C, et al. Shape-controlled synthesis of Mn₃O₄ nanocrystals and their catalysis of the degradation of methylene blue. *Nano Res.* 2010;3(4):235-43.
18. Feyzi M, Irandoust M, Mirzaei AA. Effects of promoters and calcination conditions on the catalytic performance of iron–manganese catalysts for Fischer–Tropsch synthesis. *Fuel Process. Technol.* 2011;92(5):1136-43.
19. Sun H, Tian H, Hardjono Y, Buckley CE, Wang S. Preparation of cobalt/carbon-xerogel for heterogeneous oxidation of phenol. *Catal. Today.* 2012;186(1):63-8.
20. Sun YP, Li Xq, Cao J, Zhang Wx, Wang HP. Characterization of zero-valent iron nanoparticles. *Adv. Colloid Interface Sci.* 2006;120(1–3):47-56.
21. Mondal P, Bhowmick S, Jullok N, Ye W, Van Renterghem W, Van den Berghe S,

- et al. Behavior of As(V) with ZVI–H₂O System and the Reduction to As(0). *J. Phys. Chem. C*. 2014;118(37):21614-21.
22. Liang Y, Liu P, Xiao J, Li H, Wang C, Yang G. A microfibre assembly of an iron-carbon composite with giant magnetisation. *Sci. Rep.* 2013;3.
23. Li XQ, Elliott DW, Zhang WX. Zero-Valent Iron Nanoparticles for Abatement of Environmental Pollutants: Materials and Engineering Aspects. *Crit. Rev. Solid State Mater. Sci.* 2006;31(4):111-22.
24. Zhou T, Li Y, Ji J, Wong F-S, Lu X. Oxidation of 4-chlorophenol in a heterogeneous zero valent iron/H₂O₂ Fenton-like system: Kinetic, pathway and effect factors. *Sep. Purif. Technol.* 2008;62(3):551-8.
25. Kallel M, Belaid C, Boussahel R, Ksibi M, Montiel A, Elleuch B. Olive mill wastewater degradation by Fenton oxidation with zero-valent iron and hydrogen peroxide. *J. Hazard. Mater.* 2009;163(2–3):550-4.
26. Boussahel R, Harik D, Mammam M, Lamara-Mohamed S. Degradation of obsolete DDT by Fenton oxidation with zero-valent iron. *Desalination.* 2007;206(1–3):369-72.
27. Kim D-h, Kim J, Choi W. Effect of magnetic field on the zero valent iron induced oxidation reaction. *J. Hazard. Mater.* 2011;192(2):928-31.
28. Liang C, Guo Y-y. Mass Transfer and Chemical Oxidation of Naphthalene Particles with Zerovalent Iron Activated Persulfate. *Environ. Sci. Technol.* 2010;44(21):8203-8.
29. Kusic H, Peternel I, Ukic S, Koprivanac N, Bolanca T, Papic S, et al. Modeling of iron activated persulfate oxidation treating reactive azo dye in water matrix. *Chem. Eng. J.* 2011;172(1):109-21.
30. Jiang J, Pang SY, Ma J. Comment on “Polyoxometalate-Enhanced Oxidation of Organic Compounds by Nanoparticulate Zero-Valent Iron and Ferrous Ion in the Presence of Oxygen”. *Environ. Sci. Technol.* 2008;42(21):8167-8.
31. Goretzki H, Rosenstiel Pv, Mandziej S. Small area MXPS- and TEM-measurements on temper-embrittled 12% Cr steel. *Z. Anal. Chem.* 1989;333(4-5):451-2.
32. Saputra E, Muhammad S, Sun H, Ang H-M, Tadé MO, Wang S. Manganese oxides at different oxidation states for heterogeneous activation of peroxymonosulfate for phenol degradation in aqueous solutions. *Appl. Catal., B.* 2013;142–143(0):729-35.
33. Anipsitakis GP, Dionysiou DD. Degradation of Organic Contaminants in Water

with Sulfate Radicals Generated by the Conjunction of Peroxymonosulfate with Cobalt. *Environmental Science & Technology*. 2003;37(20):4790-7.

34. Xiao J, Xie Y, Cao H, Wang Y, Zhao Z. g-C₃N₄-triggered super synergy between photocatalysis and ozonation attributed to promoted OH generation. *Catal. Commun.* 2015;66(0):10-4.

35. Floyd RA, Soong LM. Spin trapping in biological systems. Oxidation of the spin trap 5,5-dimethyl-1-pyrroline-1-oxide by a hydroperoxide-hematin-system. *Biochemical and biophysical research communications*. 1977;74(1):79-84.

36. Fang GD, Dionysiou DD, Al-Abed SR, Zhou DM. Superoxide radical driving the activation of persulfate by magnetite nanoparticles: Implications for the degradation of PCBs. *Appl. Catal., B*. 2013;129(0):325-32.

37. Buxton GV, Greenstock CL, Helman WP, Ross AB. Critical Review of rate constants for reactions of hydrated electrons, hydrogen atoms and hydroxyl radicals ($\cdot\text{OH}/\cdot\text{O}^-$ in Aqueous Solution. *J. Phys. Chem. Ref. Data*. 1988;17(2):513-886.

38. Neta P, Huie RE, Ross AB. Rate Constants for Reactions of Inorganic Radicals in Aqueous Solution. *J. Phys. Chem. Ref. Data*. 1988;17(3):1027-284.

39. López de Arroyabe Loyo R, Nikitenko SI, Scheinost AC, Simonoff M. Immobilization of Selenite on Fe₃O₄ and Fe/Fe₃C Ultrasmall Particles. *Environ. Sci. Technol.* 2008;42(7):2451-6.

40. Wang X, Zhang S, Li J, Xu J, Wang X. Fabrication of Fe/Fe₃C@porous carbon sheets from biomass and their application for simultaneous reduction and adsorption of uranium(vi) from solution. *Inorg. Chem. Front.* 2014;1(8):641-8.

Chapter 7: Magnetic Fe₃O₄/carbon sphere/cobalt composites for catalytic oxidation of phenol solutions with sulfate radicals

ABSTRACT

In the last two chapters, magnetic cores of ZnFe₂O₄ and ZVI were discussed. In this chapter, magnetic carbon nanospheres (Fe₃O₄/CS core/shell) and their supported Co₃O₄ nanoparticles were synthesized using a novel one-step hydrothermal method followed by heat treatment. The nanocomposites were characterized by powder X-ray diffraction (XRD), field emission scanning electron microscopy (FESEM), energy-dispersive X-ray spectroscopy (EDS), Fourier transform infrared spectroscopy (FT-IR), thermogravimetric analysis (TGA), and N₂ sorption isotherms. The catalytic properties of the nanocomposites in activating Oxone[®] for oxidation of phenol solution were investigated. Fe₃O₄/CS supported Co₃O₄ nanoparticles exhibited high activity in Oxone[®] activation for phenol degradation with 100% conversion within 30 min. Phenol degradation was found to follow the first order kinetics. The nanoparticles also displayed good water dispersion and magnetic separation under the magnetic field. The deactivation of catalysts was investigated and their regeneration was also proposed.

7.1 Introduction

Cobalt/PMS is very efficient for catalytic degradation of organic pollutants. Although cobalt ion leaching can be minimized in heterogeneous forms, if not well recovered, the nanosized catalysts would still bring up secondary contamination to the environment. A promising strategy for resolving the problem is recovery of nanosized catalysts by magnetic separation. Over the past decades, magnetite (Fe_3O_4) nanoparticles (NPs) as separating magnetic materials have attracted great attention due to their biocompatibility and remarkable magnetic properties as well as unique size- and morphology-dependent physical and chemical properties (1-4). However, due to the significant aggregation from their strong inter-particle dipole-dipole attraction and high surface area to volume ratio, pure Fe_3O_4 NPs may not be very useful in technological applications (5). Yao et al. (6, 7) had applied graphene as a barrier material to prepare magnetic adsorbents or catalysts. Recently, core/shell magnetic carbon nanospheres have attracted intense attention owing to their unique magnetic response, low cytotoxicity and highly functional surface (8, 9).

In this chapter, we present a novel synthesis of core/shell magnetic carbon nanospheres (MCS), $\text{Fe}_3\text{O}_4/\text{CS}$, by a one-pot hydrothermal method. After that cobalt oxide is supported onto these MCS by an impregnation method followed by heat treatment. The prepared catalysts showed both high activity and magnetic separation performance in oxidation of phenol solutions.

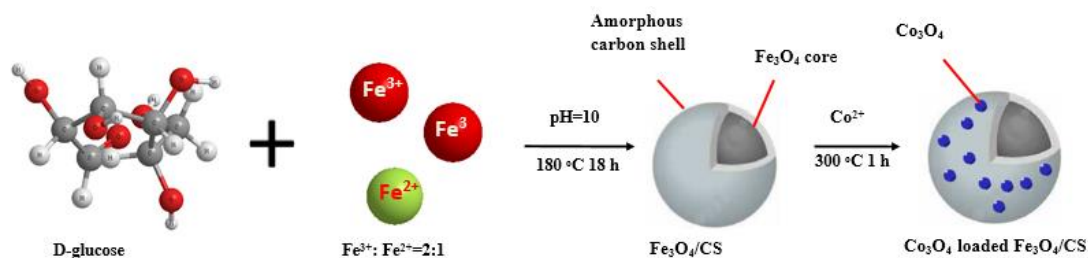
7.2 Experimental Sections

7.2.1 Materials

All chemicals used can be found in the previous chapters

7.2.2 Synthesis of magnetic carbon nanospheres (MCS)

Magnetic carbon nanospheres were synthesized via a modified hydrothermal method. Scheme 1 shows the procedure of MCS formation and the following cobalt impregnation. In a typical synthesis, 0.04 mol D-glucose was dissolved in 50 mL of ultrapure water. Then 0.02 mol $\text{FeCl}_3 \cdot 6\text{H}_2\text{O}$ and 0.01 mol $\text{FeCl}_2 \cdot 4\text{H}_2\text{O}$ were dissolved in the D-glucose solution, followed by 1 h stirring. With stirring, 28% ammonia solution was added dropwisely at a rate of 0.5 mL/min with nitrogen bubbling (40 mL/min) to make solution pH 10 for synthesis of magnetite Fe_3O_4 nanoparticles. The mixed solution was then transferred into a Teflon-lined autoclave (120 mL) and treated in an oven at 180 °C for 18 h. After naturally cooling down to room temperature, the obtained black suspension was filtered and washed by ethanol/water for three cycles. The precipitate was dried in an oven at 80 °C, and the obtained sample was labelled as MCS.



Scheme 7.1 Preparation procedure of Co/MCS.

7.2.3 Synthesis of Co/MCS catalysts.

Magnetic carbon nanospheres supported cobalt oxides (Co/MCS) were synthesized by an impregnation method followed by heat treatment. First, 1.0 g of MCS and 0.39 g of cobalt (II) nitrate hexahydrate (99%) were mixed in 50 mL of ethanol (99.8%) and the mixed solution was stirred for 30 min. Then solution temperature was increased to 50 °C to evaporate ethanol whilst stirring. The dried mixture was then put into a muffle furnace for calcination at 300 °C for 1 h in air at a heating rate of 5

°C/min. The sample was then washed by ethanol once and by ultrapure water for three times. After drying in an oven at 80 °C overnight, the samples were denoted as Co/MCS-300.

7.2.4 Characterization of materials

Characterization details and phenol oxidation as well as mechanistic studies can be found in previous chapters.

7.2.6 Regeneration methods

The spent catalysts of Co/MCS were regenerated by three different methods and their effects were tested respectively. (a) Ultrapure water wash: the collected spent catalyst was washed with ultrapure water three times and collected with magnetic field for each time. Then the washed catalyst was dried in oven with 80 °C overnight before next use. (b) Sonication: the collected spent catalyst was first dispersed in 50 mL of ultrapure water followed by ultrasonication for 30min. The sonicated spent catalyst was washed by ultrapure water for three times and collected with magnetic field. Then the washed catalyst was dried in oven with 80 °C overnight before next use. (c) Annealing in air: the dried spent catalyst was placed in into a muffle furnace for annealing at 300 °C for 1 h in air at a heating rate of 5 °C/min. The annealed catalyst was then washed by ultrapure water for three times and collected with magnetic field. Before next use, the washed catalyst was dried in oven with 80 °C overnight.

7.3 Results and Discussion

7.3.1 Characterization of the composites

The crystalline structures of the prepared materials were evaluated by XRD, as

shown in Fig. 7.1. For MCS, diffraction peaks at 30.1° , 35.4° , 43.05° , 56.92° and 62.51° were observed, corresponding to the crystal planes of Fe_3O_4 (2 2 0), (3 1 1), (4 0 0), (4 2 2) and (4 4 0), respectively. The signals were consistent with the standard XRD data for the inverse spinel structure Fe_3O_4 with lattice constants of $a = 8.397 \text{ \AA}$ (JCPDS no.65-3107)(10). The average grain size (D) of the Fe_3O_4 particles was calculated as 20 nm using the Scherrer's formula (11). Moreover, no obvious peak from graphite (ca. $2\theta = 26^\circ$) is present, indicating that the produced carbon was amorphous. The same characteristic peaks for inverse spinel structure Fe_3O_4 were also observed on Co/MCS-300, confirming the stability of the crystalline phase of Fe_3O_4 NPs in the material maintaining as the crystalline structure of Fe_3O_4 . Besides, a peak at $2\theta = 37.6^\circ$ was identified, which indicates the presence of Co_3O_4 (12).

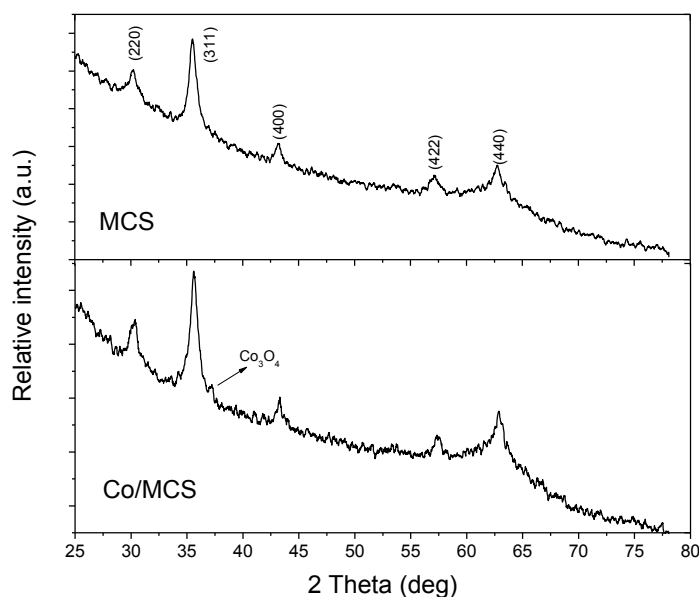


Figure 7.1 XRD patterns of MCS and Co/MCS.

Fig.7.2 displays N_2 adsorption-desorption isotherms and the pore size distributions of MCS and the annealed Co/MCS catalyst. The isotherms in Fig. 7.2 (A) show that N_2 adsorption of Co/MCS is higher than MCS, due to the higher surface area and pore volume from annealing in air at 300°C . The specific surface areas of MCS and Co/MCS were determined to be 37.4 and $95.4 \text{ m}^2/\text{g}$, respectively. The surface area of

Co/MCS-300 is almost double of that of MCS and the pore volume is also higher, which confirmed the effect of annealing. The hysteresis loops in $P/P_0 = 0.4-0.9$ indicated the mesoporous structure of the MCS and Co/MCS samples.

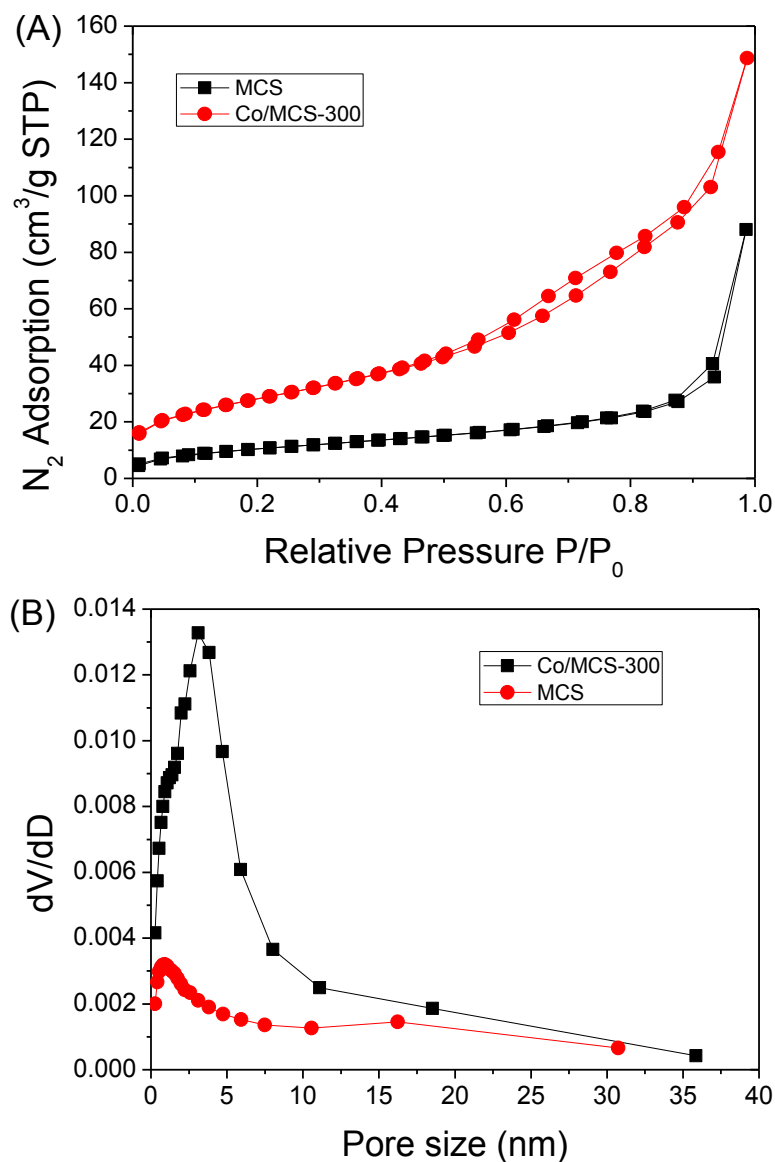


Figure 7.2 N_2 sorption isotherms (A) and pore size distributions (B) of MCS and Co/MCS-300.

Fig.7.2 (B) displays that both MCS and Co/MCS-300 present a single mode of pore size. The pore size of MCS is centered at 1.2 nm whereas the pore size of Co/MCS-300 is centered at 3.2 nm, which indicates that, after Co_3O_4 loading and calcination, the pore size became larger than original sample. Co/MCS-300 has a

narrower pore size distribution than the fresh MCS due to that calcination can also regulate the pore size by evaporation of organic substances from the carbonization of glucose.

Morphology and structure of the synthesized materials were then investigated by FESEM images. Fig.7.3 (A)-(D) show FESEM images of MCS and Co/MCS nanoparticles. Fig.7.3 (A) and (B) show that the $\text{Fe}_3\text{O}_4/\text{CS}$ core/shell nanoparticles had sphere-like morphology and the particle size varied between 20 and 30 nm. It was also shown that the nanoparticles aggregate due to the inter-molecular magnetic dipolar interaction. Fig. 7.3(C) and (D) show the morphology of Co/MCS-300 nanoparticles. As seen, compared with fresh MCS, these particles are more porous and finer, which is also confirmed by BET and pore size distribution results. For Co particles, they are homogeneously distributed on MCS. Fig. 7.3 (E) displays the EDS plot for Co/MCS nanoparticles and the area that EDS was taken from. As illustrated, the composition of the Co/MCS composite was confirmed by the presence of only O, C, Co and Fe elements. The atomic contents of the Co/MCS were evaluated to 16.81, 62.80, 17.19 and 3.20% for Fe, O, C and Co, respectively. The inset of Fig. 7.3 (E) also shows the Co mapping in the selected area of Co/MCS, confirming the homogeneous distribution of Co on the sample.

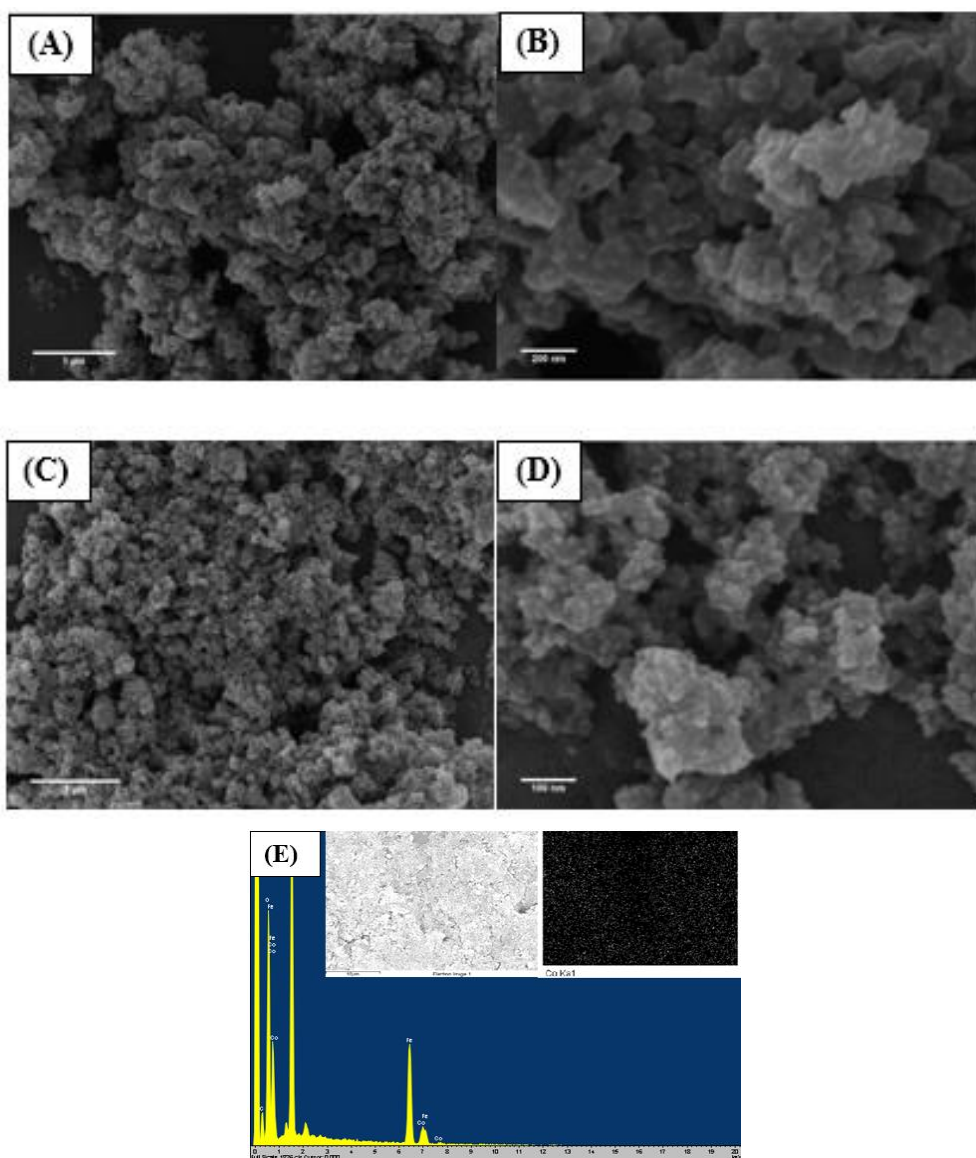


Figure 7.3 SEM images of MCS (A, B) and Co/MCS (C, D), and EDS and Co elemental mapping of Co/MCS (E).

Fig.7.4 (A) shows the representative TGA and DTA curves of Co/MCS, which were performed in air atmosphere with a heating rate of 10 °C/min. There are three weight loss processes. A slight weight loss below 110 °C can be assigned to the evaporation of adsorbed water molecules. Then the mild weight loss occurs from 110 to 350 °C, which can be ascribed to the removal of the labile oxygen-containing functional groups on the carbon surface such as –OH and C=O, etc. The organic compounds would be removed in the form of H₂O, CO and CO₂ from the sample due to the destruction of the oxygenated functional groups (13). The TG/DSC curves of the

nanocomposites present a characteristic step/peak in the range from 350 to 450 °C. It can be assigned to the decomposition of carbon skeleton for the carbon coated on the Fe₃O₄ (14). When temperature reached 450 °C, the weight of the sample remained and almost no weight loss occurred beyond this temperature. Fig. 7.4(B) shows the TGA curve of the fresh MCS and Co/MCS before annealing in the air. According to mass loss in Co/MCS, about 4.95 wt.% of Co deposited on the surface of the MCS. For the MCS, the fresh one has about 42.90 wt.% carbon content, whereas only 12.50 wt.% carbon left for the Co/MCS annealed in the air at 300 °C for 1 h.

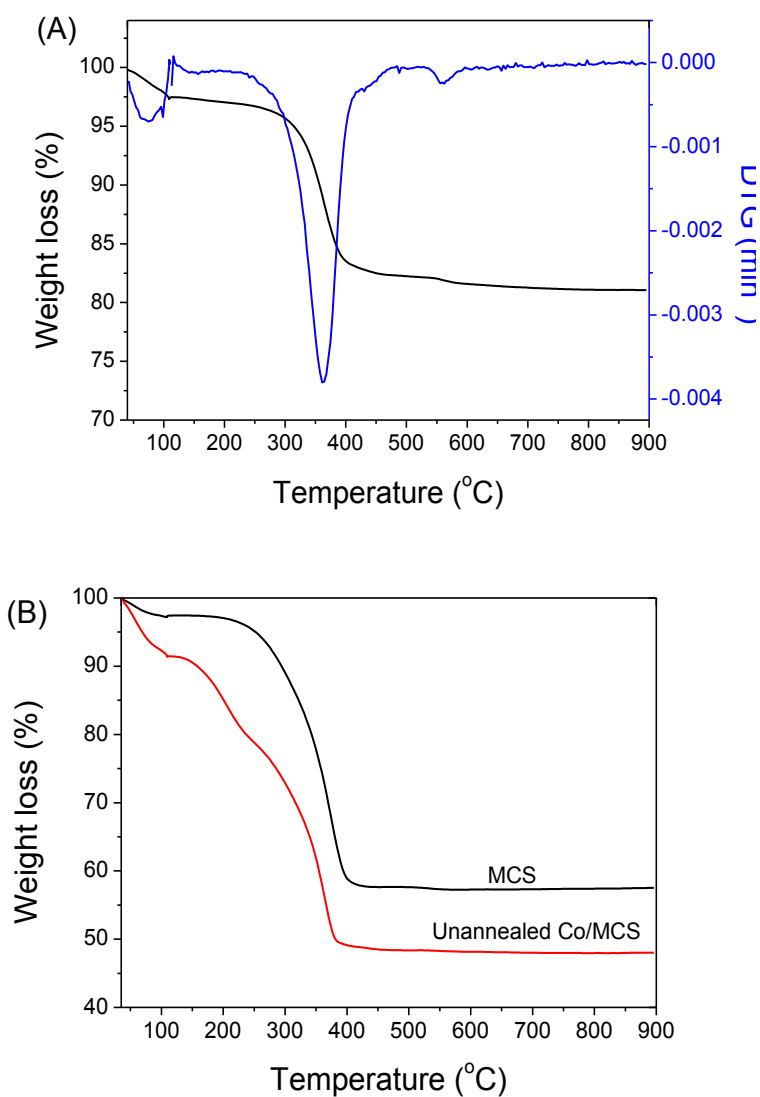


Figure 7.4 TGA curves of Co/MCS-300 and MCS.

FT-IR spectra in Fig. 7.5 are used to analyze the obtained MCS nanospheres. It was found that the strong IR band at 579 cm^{-1} is a characteristic signal of the Fe–O vibrations, the peaks at 1381 cm^{-1} and 1699 cm^{-1} are attributed to C–C and C=O vibrations, and the peak at 3449 cm^{-1} implies the existence of residual hydroxyl groups. Moreover, the peaks around $900\text{--}1300\text{ cm}^{-1}$ are attributed to the existence of C–O–C vibrations. Those hydrophilic functional groups result in the enhanced hydrophilics of the obtained composites (15). For the FT-IR spectra of the annealed Co/MCS nanocomposite, the curve is smoother than that of MCS due to the heat treatment. As seen, the peaks around $900\text{--}1300\text{ cm}^{-1}$ (C–O–C vibration) and the 1381 cm^{-1} (C–C vibration) disappeared after calcination, indicating that the surface feature of MCS was reconstructed after cobalt loading. The peaks at 1699 cm^{-1} and 3449 cm^{-1} of the annealed sample were weaker than the fresh one, showing that some of the C=O and –OH functional groups were removed during the heat treatment. In addition, a new peak appeared at 2150 cm^{-1} on the annealed Co/MCS sample, which is possibly due to the creation of $\text{C}\equiv\text{C}$ on the carbon surface during annealing process (15).

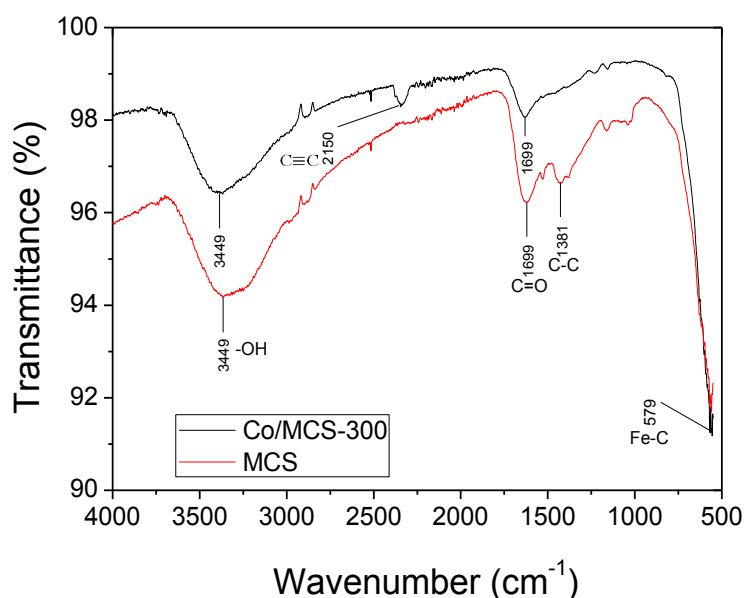


Figure 7.5 FT-IR spectra of Co/MCS-300 and MCS.

Above characterization suggested that the calcination in the preparation would significantly change the properties of the catalysts. Firstly, calcination would further

carbonize the fresh carbon spheres via the hydrothermal processes then desorb the organic compounds on the surface of the spheres. Secondly, calcination can increase the specific surface area and create porous structure for the catalysts. At last, the calcination is able to decompose and oxidize the cobalt precursor to produce cobalt oxide.

7.3.2 Adsorption and heterogeneous catalytic phenol degradation

Control experiments were carried out to evaluate adsorption, PMS self-oxidation and any catalytic performance of MCS. Fig. 7.6 shows phenol removal at different conditions. For the reaction conducted in the presence of PMS without any catalyst, negligible change in phenol concentration was observed. A change of less than 5% in phenol concentration was found after 180 min, suggesting that PMS itself in homogeneous solution could not induce significant phenol oxidation. A similar trend was observed in the reaction carried out with adsorption tests only using Co/MCS, in which phenol removal fluctuated for the first 60 min due to the adsorption/desorption balance of the nanocomposites. After that, phenol removal was relative steady as the adsorption/desorption approached equilibrium. The final phenol removal rate is less than 5% in 180 min, suggesting that phenol adsorption on Co/MCS is negligible. MCS without cobalt loading with PMS for phenol degradation produced less than 20% of phenol removal within 180 min, indicating that MCS using as a carrier of cobalt oxide would not make a significant contribution to phenol degradation. It was found that Co/MCS can significantly catalyze the phenol oxidation with sulfate radicals, with 100% degradation of phenol within 45 min. Compared with Co_3O_4 made from hydrothermal method (16), the as-synthesized Co/MCS catalyst showed a superior catalytic activity for phenol degradation.

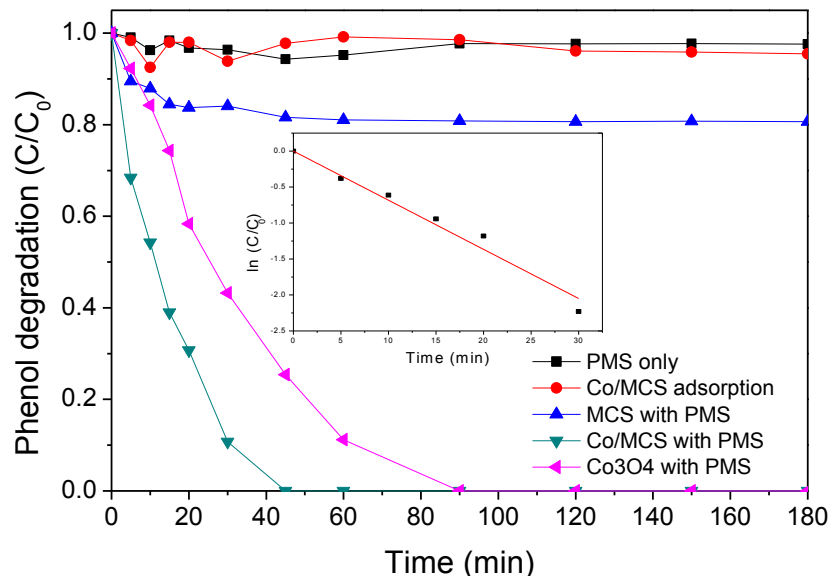


Figure 7.6 Phenol removal in various reaction conditions. Reaction conditions: $[\text{phenol}]_0 = 20 \text{ mg/L}$, catalyst loading = 0.2 g/L , Oxone[®] loading = 2.0 g/L , Temperature: $25 \text{ }^\circ\text{C}$.

The kinetics of phenol degradation was evaluated by the first-order kinetic model as listed below (Eq.7.1).

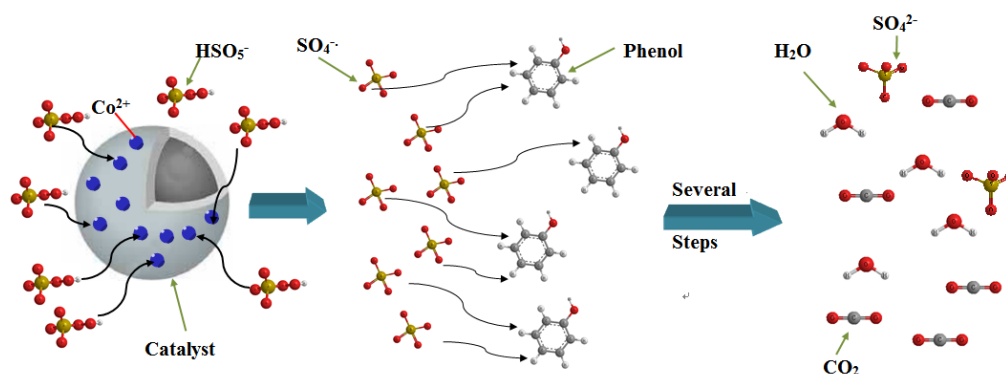
$$\ln\left(\frac{C}{C_0}\right) = kt \quad \text{Eq. 7.1}$$

Where, C and C_0 are the phenol concentrations at time (t) and $t=0$, respectively and k is the reaction rate constant.

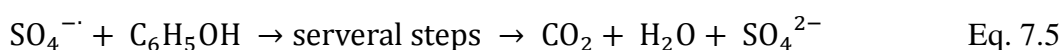
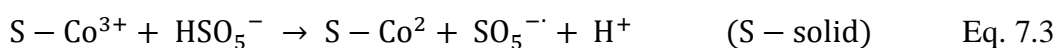
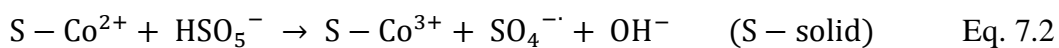
From the plot (inset of Fig.7.6), it is shown that phenol degradation curve was fitted with the first-order kinetics with high value of regressions coefficient. The rate constant of phenol oxidation by Co/MCS + PMS was evaluated as 0.0683 min^{-1} with a regression coefficient of 0.990.

Some researchers have investigated the kinetics of organic dye degradation in homogeneous Co/PMS system. Madhavan et al. (17) found the decolorization of acid

red 88 (AR88) follows first order kinetics in the Fe^{3+} /PMS system. Chen et al. (18) reported a pseudo first order decolorization of acid orange 7 (AO7) in aqueous solution induced by Co^{2+} /PMS. Shukla et al. (19) investigated phenol degradation on activated carbon supported Co with Oxone[®] and reported first order kinetics. This study presents similar kinetics to the above investigations. Scheme 2 illustrates the reaction mechanisms for homogeneous and heterogeneous phenol oxidation.



Scheme 7.2 Mechanism of catalytic oxidation of phenol on Co/MCS with PMS.



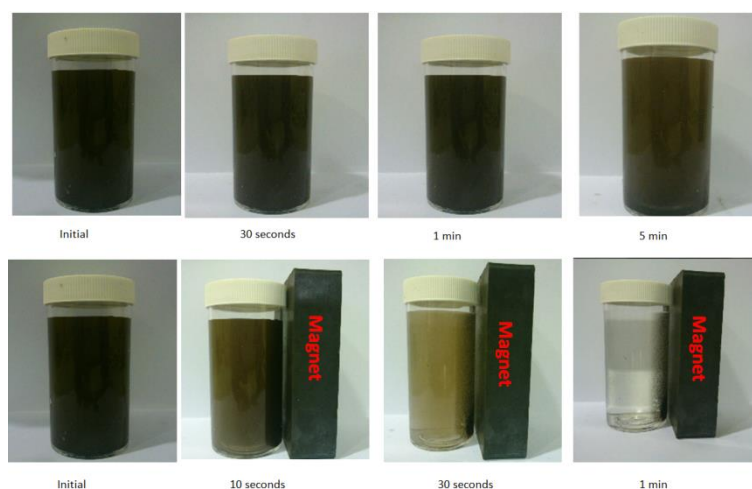


Figure 7.7 Photos of Co/MCS dispersion in water and their responses under an external magnetic field.

Fig.7.7 shows photographs of Co/MCS dispersion in water and their response under an external magnetic field. As illustrated in the photograph, by sonicating for 2 min, Co/MCS can be well dispersed in the deionized water and form a stable black suspension before magnetic separation. If a magnet was placed close to the glass vial containing the nanoparticles dispersed in deionized water, Co/MCS nanoparticles were attracted towards the magnet very quickly and accumulated to the side wall of the glass vial near the magnet. And the solution became clear and transparent within 1 min with the presence of the magnet. After removing the magnet and repeat the above sonicating procedure, Co/MCS was rapidly redispersed in water. Therefore, from the above simple experiments, the attraction and dispersion processes can be readily altered by placing or removing an external magnetic field, indicating good water dispersion and magnetic separation for effective water-solid separation.

7.3.3 Effects of reaction parameters on phenol degradation

In heterogeneous catalytic oxidation of phenol, parameters such as PMS concentration, catalyst loading and reaction temperature can influence phenol degradation rate in aqueous solution to different extents. This section will provide an investigation of these effects on phenol degradation.

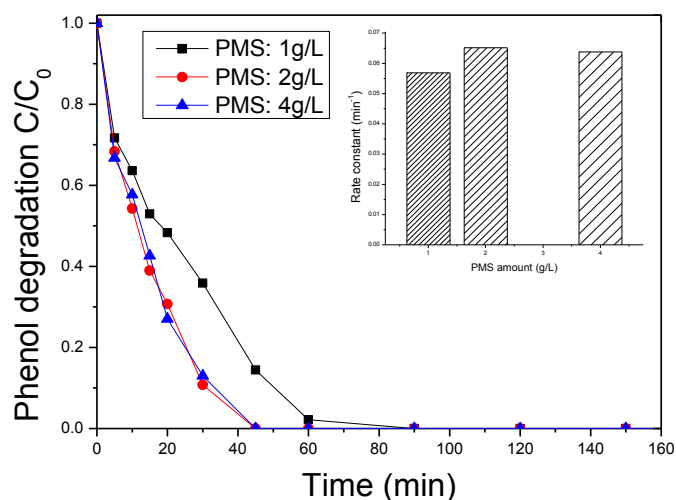


Figure 7.8 Effect of PMS amount on phenol degradation (inset: rate constants at different PMS amounts). Reaction conditions: $[\text{phenol}]_0 = 20 \text{ mg/L}$, catalyst loading = 0.2 g/L , Temperature: $25 \text{ }^\circ\text{C}$.

Fig. 7.8 depicts phenol degradation at varying concentrations of PMS. A general trend was that phenol degradation can be enhanced with the increase of PMS concentration. At 1 g/L PMS concentration, 100% phenol removal was achieved after 90 min. When PMS concentration was increased to 2 g/L , phenol could be fully removed within 45 min, which was half of the time at 1 g/L . Nevertheless, further increase of Oxone[®] concentration would result in lower degradation efficiency and rate constant. This was possibly due to the self-quenching of sulfate and hydroxyl radicals by PMS as follows (20).



The reduction potential of $\text{SO}_5^{\cdot-}/\text{HSO}_5^-$ is 0.95 V at pH 7. Meanwhile, $\text{SO}_4^{\cdot-}/\text{SO}_4^{2-}$ has an oxidation potential of $[2.5\text{--}3.1 \text{ V}]$ (21), which makes it possible that higher

concentration of HSO_5^- from PMS would consume the active $\text{SO}_4^{\bullet-}$, resulting in a lower degradation rate.

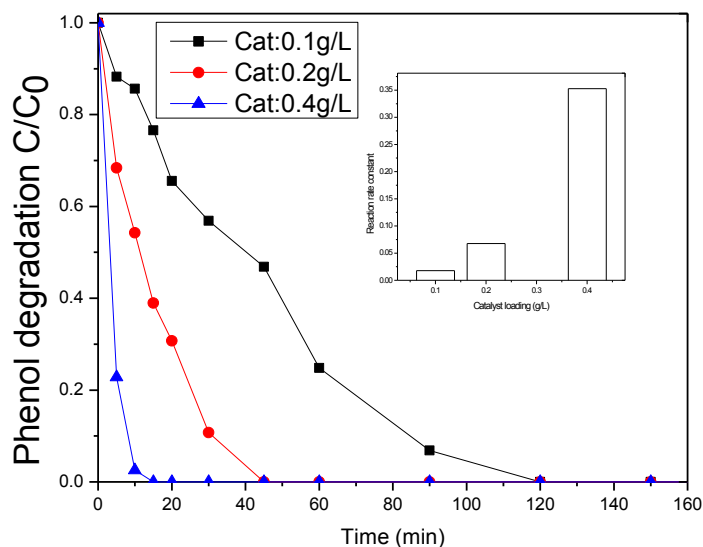


Figure 7.9 Effect of catalyst loading on phenol degradation. Reaction conditions: $[\text{phenol}]_0 = 20 \text{ mg/L}$, Oxone[®] loading = 2.0 g/L, Temperature: 25 °C.

The effect of catalyst concentration on phenol degradation efficiency is shown in Fig. 7.9. As shown, catalyst amount has a significant influence on phenol degradation. With the increase of catalyst concentration, phenol degradation efficiency would be dramatically enhanced. When catalyst concentration is 0.1 g/L, phenol was fully removed after 120 min, whereas catalyst concentration at 0.4 g/L resulted in 100% phenol degradation within 20 min. The increased efficiency is attributed to the increased availability of active sites in the solution for reaction with PMS thereby generating more sulfate radicals. Inset of Fig. 7.9 displayed that the reaction rate increased with catalyst loading.

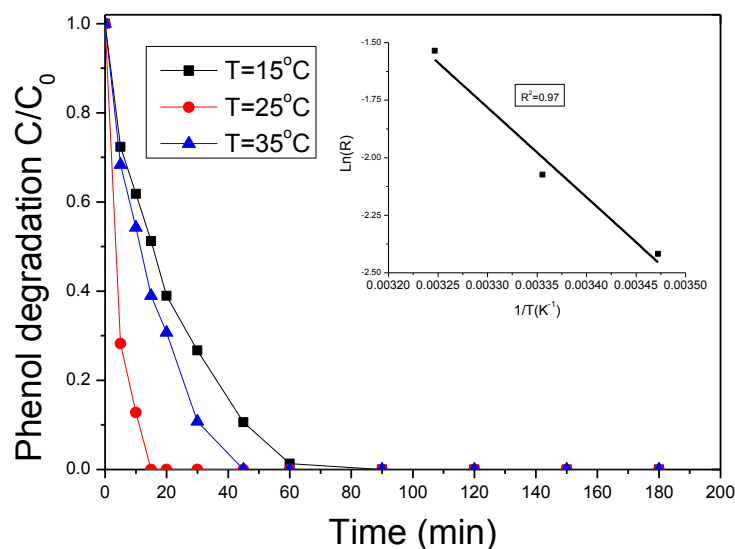


Figure 7.10 Effect of reaction temperature on phenol degradation and evaluation of activation energy. Reaction conditions: $[\text{phenol}]_0 = 20 \text{ mg/L}$, catalyst loading = 0.2 g/L , Oxone[®] loading = 2.0 g/L .

Fig. 7.10 reveals the performance of Co/MCS catalysts for heterogeneous oxidation of phenol at varying temperatures. It is seen that reaction temperature dramatically affected oxidation efficiency and degradation rate. When reaction took place at $15 \text{ }^\circ\text{C}$, phenol degradation would reach 100% in 90 min while the time would be reduced to be 45 min at $25 \text{ }^\circ\text{C}$. The duration would be dramatically reduced to be 10 min when reaction temperature was increased to $35 \text{ }^\circ\text{C}$. Based on the first-order kinetics, rate constants at varying temperatures were obtained and the relationship was found to follow the Arrhenius equation. The activation energy was then obtained as 49.1 kJ/mol .

For supported Co catalysts in reaction with PMS, a few investigations have reported the kinetics and activation energies. We have studied several heterogeneous Co catalysts in activation of PMS for phenol degradation and the activation energies obtained are presented in Table 7.1. As seen that Co/MCS presented lower activation energy than most of supported Co catalysts and the activation energy of Co/MCS is

similar to that of carbon xerogel (CX) supported Co catalyst. It is noteworthy that the activation energy only gives the dependence of reaction rate on the reaction temperature, and it cannot be related to the activity of catalysts before obtaining the identical pre-exponential factors.

Table 7.1 Activation energies of heterogeneous Co catalysts with PMS for phenol degradation.

Catalyst	Activation Energy (kJ/mol)	Reference
Co/SBA-15	67.4	(21)
Co/ZSM5	69.7	(19)
Co/SiO ₂	61.7-75.5	(22)
Co/CX	48.3-62.9	(23)
Co/AC	59.7	(24)
Co/CA	62.9	(25)
Co/RM	66.3	(26)
Co/MCS	49.1	This study

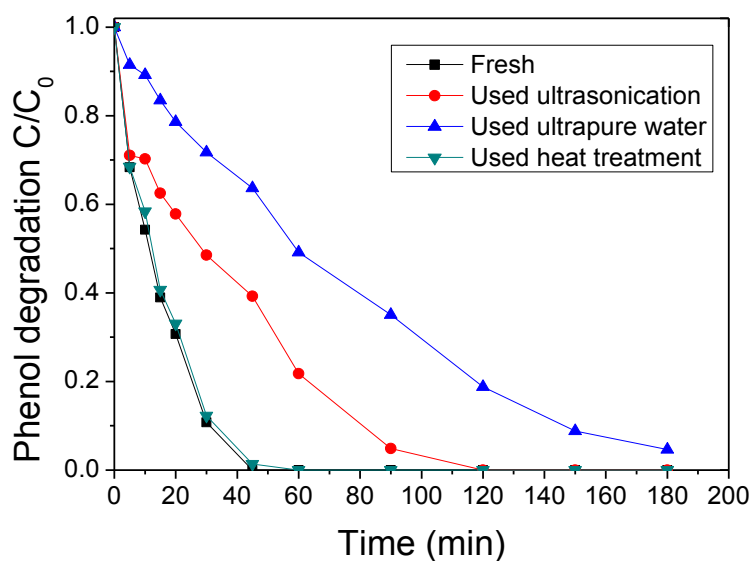


Figure 7.11 Regeneration studies of the used catalysts. Reaction conditions: [phenol]₀ = 20 mg/L, catalyst loading = 0.2 g/L, Oxone[®] loading = 2.0 g/L, Temperature:

25 °C.

It is known that the stability of the catalyst is very important in practical application. In order to improve the catalyst stability as well as to further investigate the causes of catalyst deactivation, the spent catalyst of Co/MCS was treated by three different regeneration methods, washing by ultrapure water, ultrasonication followed by washing with ultrapure water and annealing in air at 300 °C for 1 h. Fig.11 shows the phenol oxidation efficiency for used catalyst regenerated by the above methods. Catalyst regenerated by annealing in air provided the best stability and degraded 100% of phenol within 60 min, which was almost the same as the fresh catalyst. The excellent stability of this regeneration method indicated that, by annealing in air at 300 °C for 1 h, not only most of the reaction intermediates attached on the surface of the used catalyst were removed, but also the surface feature of the catalyst had been recovered. For catalyst regenerated by ultrasonication treatment, 100% phenol removal was achieved after 120 min, showing that ultrasonication partially removed the intermediates attached on the catalyst surface. Whereas regeneration by simple washing with ultrapure water provided the least compatible efficiency compared with others due to the least capability of removing reaction intermediates.

7.4 Conclusions

Magnetic carbon nanospheres ($\text{Fe}_3\text{O}_4/\text{CS}$) were synthesized via a hydrothermal method. And Co oxide loaded on these magnetic carbon nanospheres were prepared by an impregnation method. Co/MCS is a good catalyst for heterogeneous activation of Oxone[®] for oxidation of phenol. Meanwhile, Oxone[®] concentration posed a less effect than catalyst loading or reaction temperature on phenol degradation. Reaction temperature would significantly affect phenol degradation: the higher of temperature, the higher of degradation rate is. The kinetic studies suggested that the phenol oxidation on the heterogeneous system followed first order kinetics and the activation energy was 49.5 kJ/mol. Regeneration by calcination could fully recover the catalyst

activity. This chapter provided a feasible approach for removal of organic pollutants by magnetically separable catalysts.

References

1. Gong JL, Wang B, Zeng GM, Yang CP, Niu CG, Niu QY, et al. Removal of cationic dyes from aqueous solution using magnetic multi-wall carbon nanotube nanocomposite as adsorbent. *J. Hazard. Mater.* 2009;164(2–3):1517-22.
2. Chen L, Xu Z, Dai H, Zhang S. Facile synthesis and magnetic properties of monodisperse Fe₃O₄/silica nanocomposite microspheres with embedded structures via a direct solution-based route. *J. Alloys Compd.* 2010;497(1–2):221-7.
3. Kaminski MD, Nuñez L. Extractant-coated magnetic particles for cobalt and nickel recovery from acidic solution. *J. Magn. Mater.* 1999;194(1–3):31-6.
4. Chen C, Hu J, Shao D, Li J, Wang X. Adsorption behavior of multiwall carbon nanotube/iron oxide magnetic composites for Ni(II) and Sr(II). *Journal of Hazardous Materials.* 2009;164(2–3):923-8.
5. Lai G-S, Zhang H-L, Han D-Y. A novel hydrogen peroxide biosensor based on hemoglobin immobilized on magnetic chitosan microspheres modified electrode. *Sens. Actuators, B.* 2008;129(2):497-503.
6. Yao YJ, Xu C, Qin JC, Wei FY, Rao MN, Wang SB. Synthesis of Magnetic Cobalt Nanoparticles Anchored on Graphene Nanosheets and Catalytic Decomposition of Orange II. *Ind. Eng. Chem. Res.* 2013;52(49):17341-50.
7. Yao Y, Miao S, Liu S, Ma LP, Sun H, Wang S. Synthesis, characterization, and adsorption properties of magnetic Fe₃O₄@graphene nanocomposite. *Chem. Eng. J.* 2012;184(0):326-32.
8. Lu Z, Dai J, Song X, Wang G, Yang W. Facile synthesis of Fe₃O₄/SiO₂ composite nanoparticles from primary silica particles. *Colloids Surf., A.* 2008;317(1–3):450-6.
9. Cheng Y, Tan R, Wang W, Guo Y, Cui P, Song W. Controllable synthesis and magnetic properties of Fe₃O₄ and Fe₃O₄@SiO₂ microspheres. *J Mater Sci.* 2010;45(19):5347-52.
10. Dey R, Mukherjee N, Ahammed S, Ranu BC. Highly selective reduction of nitroarenes by iron(0) nanoparticles in water. *Chem. Commun.* 2012;48(64):7982-4.
11. Baby TT, Ramaprabhu S. SiO₂ coated Fe₃O₄ magnetic nanoparticle dispersed

multiwalled carbon nanotubes based amperometric glucose biosensor. *Talanta*. 2010;80(5):2016-22.

12. Liang H, Sun H, Patel A, Shukla P, Zhu ZH, Wang S. Excellent performance of mesoporous $\text{Co}_3\text{O}_4/\text{MnO}_2$ nanoparticles in heterogeneous activation of peroxymonosulfate for phenol degradation in aqueous solutions. *Appl. Catal., B*. 2012;127(0):330-5.

13. Xu C, Wang X, Zhu J, Yang X, Lu L. Deposition of Co_3O_4 nanoparticles onto exfoliated graphite oxide sheets. *J. Mater. Chem.* 2008;18(46):5625-9.

14. Wang J, Zheng S, Shao Y, Liu J, Xu Z, Zhu D. Amino-functionalized $\text{Fe}_3\text{O}_4@\text{SiO}_2$ core-shell magnetic nanomaterial as a novel adsorbent for aqueous heavy metals removal. *J. Colloid Interface Sci.* 2010;349(1):293-9.

15. Huang Y, Dong Z, Jia D, Guo Z, Cho WI. Preparation and characterization of core-shell structure $\text{Fe}_3\text{O}_4/\text{C}$ nanoparticles with unique stability and high electrochemical performance for lithium-ion battery anode material. *Electrochim. Acta*. 2011;56(25):9233-9.

16. Wang Y, Zhou L, Duan X, Sun H, Tin EL, Jin W, et al. Photochemical degradation of phenol solutions on Co_3O_4 nanorods with sulfate radicals. *Catal. Today*. 2015; 43 (9) 43-52.

17. Madhavan J, Maruthamuthu P, Murugesan S, Anandan S. Kinetic studies on visible light-assisted degradation of acid red 88 in presence of metal-ion coupled oxone reagent. *Appl. Catal., B*. 2008;83(1-2):8-14.

18. Chen X, Qiao X, Wang D, Lin J, Chen J. Kinetics of oxidative decolorization and mineralization of Acid Orange 7 by dark and photoassisted Co^{2+} -catalyzed peroxymonosulfate system. *Chemosphere*. 2007;67(4):802-8.

19. Shukla P, Wang S, Singh K, Ang HM, Tadé MO. Cobalt exchanged zeolites for heterogeneous catalytic oxidation of phenol in the presence of peroxymonosulphate. *Appl. Catal., B*. 2010;99(1-2):163-9.

20. Shukla P, Fatimah I, Wang S, Ang HM, Tadé MO. Photocatalytic generation of sulphate and hydroxyl radicals using zinc oxide under low-power UV to oxidise phenolic contaminants in wastewater. *Catal. Today*. 2010;157(1-4):410-4.

21. Shukla P, Sun H, Wang S, Ang HM, Tadé MO. Co-SBA-15 for heterogeneous oxidation of phenol with sulfate radical for wastewater treatment. *Catalysis Today*. 2011;175(1):380-5.

22. Shukla P, Sun H, Wang S, Ang HM, Tadé MO. Nanosized $\text{Co}_3\text{O}_4/\text{SiO}_2$ for heterogeneous oxidation of phenolic contaminants in waste water. *Sep. Purif. Technol.* 2011;77(2):230-6.

23. Sun H, Tian H, Hardjono Y, Buckley CE, Wang S. Preparation of cobalt/carbon-xerogel for heterogeneous oxidation of phenol. *Catal. Today.* 2012;186(1):63-8.
24. Shukla PR, Wang S, Sun H, Ang HM, Tadé M. Activated carbon supported cobalt catalysts for advanced oxidation of organic contaminants in aqueous solution. *Appl. Catal., B.* 2010;100(3–4):529-34.
25. Hardjono Y, Sun H, Tian H, Buckley CE, Wang S. Synthesis of Co oxide doped carbon aerogel catalyst and catalytic performance in heterogeneous oxidation of phenol in water. *Chem. Eng. J.* 2011;174(1):376-82.
26. Saputra E, Muhammad S, Sun H, Ang HM, Tadé MO, Wang S. Red mud and fly ash supported Co catalysts for phenol oxidation. *Catal. Today.* 2012;190(1):68-72.

Chapter 8: Conclusions and Perspectives

8.1 Conclusions

In this thesis, catalytic activation of peroxymonosulfate to produce free radicals on metal-based catalysts was carried out for oxidation of aqueous organic pollutants. With comprehensive studies, the main objectives as described in the previous chapters have been achieved satisfactorily. 1D and 3D hierarchically structured manganese oxides with different shapes have been successfully synthesized via the facile hydrothermal methods. Some low toxic, magnetically separable catalysts involving magnetic supported cobalt oxide catalysts, nano-Fe⁰ supported by carbonaceous material catalyst and 3D hierarchical ZnFe₂O₄/MnO₂ catalysts have been prepared for the ease of separation. All of these catalysts were characterized and tested for catalytic oxidation of phenol by activation of peroxymonosulfate to generate free radicals. Catalytic phenol degradation results revealed that the as-synthesized catalysts demonstrated promising catalytic activities as the alternatives to Co²⁺/PMS homogeneous system. And the reaction kinetics suggested that all of the reaction followed the first-order kinetic model. In addition, some reaction parameters such as the initial concentration of the target pollutant, oxidant loading, reaction temperature as well as catalysts usage would influence the catalytic degradation efficiency. Moreover, it was found by electron paramagnetic resonance (EPR) that both hydroxyl and sulfate radicals were produced and responsible for the degradation of organic pollutants during the PMS activation processes.

8.1.1 Catalytic activation of PMS utilizing 3D hierarchical structured manganese oxides

Corolla-like δ -MnO₂, prepared at a hydrothermal temperature of 100 °C, showed 2D compact layers of nanosheets on the surface. While 3D sea-urchin like α -MnO₂ was

prepared at 110 °C and consisting of 1D tetragonal nanorods. It was found that corolla-like δ -MnO₂ had a higher catalytic activity than 3D sea-urchin like α -MnO₂. Catalytic degradation of phenol was influenced by reaction temperature, PMS amount and catalyst loading. The kinetic studies suggested that the heterogeneous catalytic system followed first-order kinetics and the activation energy was 25.3 kJ/mol. The mechanism of catalytic reaction for PMS activation was investigated by EPR spectra showing that both of \cdot OH and $\text{SO}_4^{\cdot-}$ are produced in the activation processes, and $\text{SO}_4^{\cdot-}$ plays a more critical role in phenol oxidation.

8.1.2 Catalytic activation of PMS utilizing 1D manganese oxides in different shapes

1D α -MnO₂ catalysts with various shapes of nanorods, nanotubes and nanowires were prepared by a one-step hydrothermal method. Shape-dependent performance of 1D α -MnO₂ was observed in catalytic degradation of phenol solutions. And the catalytic activity follows the order of nanowires > nanorods > nanotubes. It was found that the catalytic activity of these 1D α -MnO₂ catalysts is the combination effect of surface area and the exposed active facet. The activation energies of α -MnO₂ nanorods, nanotubes and nanowires were calculated to be 39.3, 87.1 and 20.3 kJ/mol, respectively. EPR spectra and competitive radical tests illustrated that the hydroxyl radicals produced at the initial stage could initiate the generation of sulfate radicals which were the major reactive species responsible for the catalytic phenol oxidation.

8.1.3 Hierarchically structured magnetic ZnFe₂O₄/MnO₂ hybrid materials

3 D magnetic ZnFe₂O₄/MnO₂ hybrid materials, urchin-like and microsphere/nanosheet hierarchical nanostructures were synthesized by a hydrothermal method at varying temperatures. Their catalytic activities were investigated in terms of PMS activation for phenol degradation. ZnFe₂O₄/MnO₂ with microsphere/nanosheet hierarchical structure possessed a better catalytic activity than ur-

chin-like catalysts due to the higher BET surface area. The reactions were well fitted by the first order kinetic model. Catalyst stability tests suggested that deactivation of the catalysts occurred due to the blockage of active sites by the reaction intermediates. The mechanism of catalytic reaction for activation of PMS was illustrated by competitive radical tests and EPR spectra. Sulfate radicals were the major reactive species taking effect in this catalytic reaction and the generation of sulfate radicals could be induced by hydroxyl radicals produced at the initial stage.

8.1.4 Magnetic nano-Fe⁰ encapsulated in carbon sphere catalysts

A magnetic carbon encapsulated nano iron hybrid (nano Fe⁰/Fe₃C@CS) was synthesized via a novel one-pot hydrothermal method followed by self-reduction in N₂ atmosphere. Superior catalytic performance was observed by complete removal of 20 ppm phenol within 10 min. Moreover, Fe₃C catalysis for PMS activation was observed for the first time though detailed catalysis mechanism is still not very clear at current stage. The catalyst deactivation mechanism was also investigated and it was found that Fe₃C has a better catalytic stability than Fe⁰ in catalytic reaction. Magnetic separation was also remained even after five runs. The combination of EPR analysis and quenching tests showed that hydroxyl radicals were generated selectively against sulfate radicals within the PMS activation process and thus responsible for phenol oxidation.

8.1.5 Magnetic Fe₃O₄/carbon sphere/cobalt composites

Magnetic carbon nanospheres (Fe₃O₄/CS core/shell) and their supported Co₃O₄ nanoparticles were synthesized using a novel one-step hydrothermal method followed by heat treatment. Catalytic properties of the nanocomposites in activating Oxone[®] for oxidation of phenol solution were investigated. Fe₃O₄/CS supported Co₃O₄ nanoparticles exhibited high activity in Oxone[®] activation for phenol degradation with 100% conversion within 30 min. Regeneration by calcination could fully recover the

catalyst activity. This study provided a feasible approach for removal of organic pollutants by magnetically separable catalysts.

8.2 Perspective of Future Works

1. The work in this thesis focuses on metal-based catalytic activation of peroxymonosulfate for oxidation of aqueous organic pollutants. Although the metal-based catalysts demonstrated strong catalytic oxidation ability for phenol degradation, these catalysts need to be tested for other more recalcitrant and more complicated phenolic compounds with different substitutes such as dichlorophenol (DCP) and p-nitrophenol (PNP). In addition, the substitution groups on the aromatic ring will also affect the degradation efficiency due to the electron-donation and electron-withdrawing effects.

2. Apart from utilization in sulfate radical based AOPs, these metal-based catalysts are suggested to be employed for other AOPs such as catalytic ozonation and photocatalytic oxidation to evaluate their catalytic potentials for mineralization of toxic aqueous organic pollutants. Moreover, apart from these metal-based catalysts prepared in this thesis, other novel catalysts with the potential to integrate the catalytic activities for other types of the AOPs needed to be developed and tested to combine the advantages of each AOP whilst circumventing their shortcomings.

3. Due to the inevitable metal-ion leaching, it is recommended that more research attention should be focused on metal-free nanocarbons such as graphene, reduced graphene oxides and carbon nanotubes (CNTs). The application of these novel catalysts to the AOPs will eventually avoid the metal leaching and make the process more eco-friendly.

4. In current work included in this thesis, catalytic activity, stability and free radical generation and evolution processes were explored and investigated. However, little

research attention focused on the oxidation mechanism of the target pollutant. In the future work, in order to fully understand the oxidation process, the oxidation mechanism needs to be studied to investigate the reaction intermediates and the reaction pathways.

5. All of the as-mentioned research efforts were carried out in the lab-scale, in which ideal experimental conditions applied. In the practical wastewater processes, various types of the uncertain factors will influence the active species' behavior, performance of the catalysts and the degradation efficiency. For example, the industrial wastewater might contain different levels of salinity ranging from 0.1 g/L to as high as 100 g/L. It was reported that the existence of chloride ions would severely hinder the degradation efficiency of the sulfate radical-based AOPs by acting as scavengers for sulfate radicals. Moreover, due to the existence of high levels of salinity and other organic matters, the active sites on the catalysts would be affected. Additionally, the pH of the wastewater will affect the decomposition efficiency of the PMS. Therefore, before the industrial scale-up, further tests including the influences of the salinity level, solution pH and co-existence with other organics should be performed and their affecting mechanism should be clarified. Once the possible influences have been clarified, it is highly imperative to perform the industrial scale-up to test the degradation efficiency under practical condition and making these research efforts truly meaningful for environment remediation.

6. Utilizing catalytic PMS oxidation to generate sulfate based radicals for organic pollutants decomposition have been proved to be a high effective way with insignificant further contamination. In practice, this cost-effective method could be integrated with ozonation for treatment of industrial/municipal wastewater to decrease the COD.

7. In the current stage, several novel nano-sized catalysts have been synthesized and

proved to be catalytically active. However, experiments were carried out under lab-scale. Future studies would focus on synthesis of cost effective industrial-ready catalysts